

# Tailoring the Microstructure of Photoactive Ceramic Membranes Deposited by Suspension Plasma Spraying

Elnazsadat Ale ebrahim  
(Elnaz Alebrahim)

A Thesis  
In the Department  
of  
Mechanical, Industrial, and Aerospace Engineering

Presented in Partial Fulfillment of the Requirements for the Degree of  
Doctor of Philosophy (Mechanical Engineering) at  
Concordia University  
Montreal, Quebec, Canada

November 2023

© ELNAZSADAT ALEEBRAHIM, 2023

**CONCORDIA UNIVERSITY**

**School of Graduate Studies**

This is to certify that the thesis prepared

By: Elnazsadat Ale ebrahim

Entitled: **Tailoring the Microstructure of Photoactive Ceramic Membranes Deposited by Suspension Plasma Spraying**

And submitted in partial fulfillment of the requirements for the degree of

**Doctor of Philosophy (Mechanical Engineering)**

Complies with the regulations of the University and meets the accepted standards with respect to originality and quality.

Signed by the final examining committee:

_____	Chair
Dr. Alex De Visscher	
_____	External Examiner
Dr. Hanlin Liao	
_____	Examiner
Dr. Fariborz Haghighat	
_____	Examiner
Dr. Ali Dolatabadi	
_____	Examiner
Dr. Martin Pugh	
_____	Thesis Supervisor
Dr. Christian Moreau	

Approved by:

\_\_\_\_\_  
Dr. Muthukumaran Packirisamy, Graduate Program Director

\_\_\_\_\_  
Dr. Martin Pugh, Dean of Faculty

## ABSTRACT

### Tailoring the Microstructure of Photoactive Ceramic Membranes Deposited by Suspension Plasma Spraying

**Elnazsadat Ale ebrahim, Ph.D.**

**Concordia University, 2023**

The rise in the global water demand, coupled with the limited water resources readily usable on the planet, underscores the importance of developing cost-effective and modern approaches for safeguarding and reusing available water supplies. Consequently, membrane separation technologies have garnered increasing interest due to their ability to provide a sustainable, energy-efficient, and affordable solution for water treatment. Recently, ceramic membranes have been increasingly recognized in the commercial sphere due to their remarkable mechanical, thermal, and chemical stability, along with their hydrophilic properties, reduced fouling tendency, ease of cleaning, and sustained long-term flux. Nevertheless, the complex and costly manufacturing processes of these membranes limit their application to areas where polymer membranes are comparatively less efficient. Therefore, it is essential to investigate innovative membrane materials and manufacturing methods that can create cost-effective and high-performance membranes. One promising approach is the utilization of suspension plasma spray (SPS), a relatively new coating deposition technology that involves sub-micron to nano-sized feedstock materials. This single-step process holds the potential to offer a cost-effective solution for producing ceramic membranes. Additionally, the SPS process allows for the incorporation of photocatalysts like titanium dioxide ( $\text{TiO}_2$ ) into the feedstock, which can facilitate the degradation of organic contaminants on the membrane surface and enhance the anti-fouling properties of the membranes.

In this project, initially, the SPS process was used to produce porous  $\text{TiO}_2$  coatings with an average pore size of around 30 nm, which is in the range of ultrafiltration (UF) membranes, with pore sizes ranging from 2 to 100 nm. The coatings were then applied on the surface of the porous substrates to produce ultrafiltration membranes. The SPS membranes possess a distinct porous microstructure, where the porosity is mostly defined by the presence of unmelted feedstock particles retained within the matrix. The unmelted particles in the ultrafiltration membranes were deposited in the form of agglomerates of nanosized  $\text{TiO}_2$  particles found in the feedstock suspension. Therefore, the average pore size could be linked to the particle size of the original feedstock powder. The UF membranes exhibited a relatively high pure water flux, where the water flux decreased with increasing the thickness of the membranes. Furthermore, the SPS  $\text{TiO}_2$  membranes demonstrate photocatalytic properties under UV and visible light conditions due to the generation of oxygen vacancies in the lattice under SPS process

conditions. Additionally, the feasibility of tailoring the level of porosity in the structure of SPS coatings as a potential approach to control the porosity and permeability of the membranes was investigated by employing a dual suspension injection method. Two water-based suspensions of TiO<sub>2</sub> with different particle sizes were introduced into the plasma jet using injectors placed at two different radial distances from the plasma torch exit. The variation in the SPS parameters led to changes in the proportion of unmelted particles in the coatings originating from the injector located farther from the torch. As a result, the total porosity in the dual-injected coatings ranged from approximately 16% to about 36%. The proportion of the unmelted particles served as a reference for the fine porosity since the gaps among those particles were identified as the origin of nanosized pores. Among the spray parameters examined, it was found that the suspension feed rate and the distance between the injectors had the most notable impact on increasing the porosity levels in the coatings. Furthermore, based on previous work, microfiltration TiO<sub>2</sub> membranes with an average pore size of around 200 nm were deposited using the SPS process. The ultrafiltration and microfiltration TiO<sub>2</sub> membranes were characterized to assess their particle rejection ratio, where the membranes with high thickness and narrow pore size distribution showed a superior rejection efficiency. The influence of narrowing the pore size distribution of the membrane on the separation efficiency was confirmed after compacting the large pores in the membrane structure with the nanosized particles of the pristine SPS feedstock. Also, the membranes demonstrated self-cleaning properties under visible light.

## **Dedication**

*To my beloved parents, Maryam and Shahriar, whose unwavering love, support, and encouragement have been my guiding light throughout this journey. Your sacrifices and belief in me have been the source of my strength.*

*To my dear sisters, Yeganeh and Dornaz, for being my inspiration pillars and always cheering me on.*

*To my loving husband, Ashkan, for your unconditional love, understanding, and patience. Your unwavering support has been the rock on which I built my dreams.*

*And, to Aiden and Eileen, who have filled my heart with joy and purpose. You are my motivation to strive for excellence.*

## ACKNOWLEDGMENTS

I want to extend my heartfelt appreciation to my thesis advisor, Prof. Christian Moreau, for his unwavering guidance, encouragement, support, and patience throughout my Ph.D. journey. I am immensely grateful for the opportunity to be a part of his research group and for the valuable lessons learned from his vast knowledge, inspiring life experiences, dedication, creativity, and empathy during this research endeavor. Working with him has been an enriching and transformative experience that has shaped my academic and personal growth. I also express my heartfelt gratitude to Dr. Saifur Md. Rahaman, who was my co-supervisor during the initial phase of my research. His guidance and support were invaluable throughout that part of my journey.

I am grateful to Philippe Plamondon from Polytechnique Montréal and to Dr. Gwenaël Chamoulaud from Université du Québec à Montréal (UQAM) for permitting me to use the facilities in their laboratories. I want to thank Concordia University's research staff, particularly Robert Oliver, Mazen Samara, Dmytro Kevorkov, and administrative staff, including Leslie Hosein, Charlene Walde, Maureen Thuringer, and Arlene Zimmerman.

I would like to thank my dear colleagues and friends, Dr. Hedyeh Khatibnezhad and Dr. Ali Akbarnozari, who helped me through the difficulties of my research with their knowledge and support.

I sincerely thank Dr. Fadhel Ben Ettouil for his unwavering support, vast expertise, and constant availability. His invaluable assistance in conducting experiments and patiently addressing all my inquiries has been instrumental in successfully completing my research work.

I am filled with immense gratitude towards my wonderful friends at Concordia University and all the past and present members of the Thermal Spray research center, including Navid, Morvarid, Alexandre, Farzam, Saeed, Masiar, and Sadaf. Your support and camaraderie have made our team genuinely exceptional.

A special thanks go out to my esteemed thesis committee members, Dr. Fariborz Haghighat, Dr. Ali Dolatabadi, Dr. Martin Pugh, and Dr. Hanlin Liao. Your dedication to thoroughly reviewing my work, posing insightful and thought-provoking questions, and providing constructive feedback and suggestions have been invaluable to the success of my research. I am truly grateful for your time and expertise guiding me throughout this journey.

Finally, I extend my appreciation to Fonds de Recherche du Québec Nature et Technologies (FRQNT) for their financial support of my research.

## CONTRIBUTION OF AUTHORS

This thesis is written in a manuscript-based format. Chapters 1, 2, and 6 are the introduction, literature review, and conclusions of the thesis, respectively. The thesis includes coauthored works in Chapters 3, 4, 5, and Appendix 2 that were reprinted from papers published or submitted to scientific journals. The contribution of each coauthor is described below:

### Chapter 3:

Alebrahim, E., Rahaman, M. S., & Moreau, C. (2022). TiO<sub>2</sub> Photocatalytic Ultrafiltration Membrane Developed with Suspension Plasma Spray Process. *Coatings*, 12(11), 1764.

Elnaz Alebrahim, worked on the literature review, planning, and methodology, performed all SPS coating experiments, and collected the data. She conducted all characterization tests, analyses, and discussions about the results, wrote the original draft, and reviewed & edited the manuscript. C. Moreau and M.S. Rahaman supervised the research reviewed and revised the manuscript.

### Chapter 4:

Alebrahim, E., Akbarnozari, A., Ben Ettouil, F., & Moreau, C. “Tailoring the Porosity Level of the Suspension Plasma Sprayed Coatings Using a Dual Suspension Injection System”, submitted to the *Surface and Coatings Technology* journal.

Elnaz Alebrahim worked on the literature review, planning, and methodology, performed all SPS coating experiments, and collected the data, conducted the characterization tests, analyses, and discussions about the results, and wrote the original draft, and reviewed & edited the manuscript. F. Ben Ettouil assisted with the sample preparation and injection system development and optimization and reviewed the manuscript. A. Akbarnozari assisted with the plasma imaging process and reviewed the manuscript. C. Moreau supervised the research and reviewed and revised the manuscript.

### Chapter 5:

Alebrahim, E., & Moreau, C. (2023). A Comparative Study of the Self-Cleaning and Filtration Performance of Suspension Plasma-Sprayed TiO<sub>2</sub> Ultrafiltration and Microfiltration Membranes. *Membranes*, 13(9), 750.

Elnaz Alebrahim worked on the literature review, planning, and methodology, performed all SPS coating experiments, and collected the, conducted the characterization tests, analyses, and discussions about the results, wrote the original draft, and reviewed & edited the manuscript. C. Moreau supervised the research and reviewed and revised the manuscript.

## **Appendix 2:**

Alebrahim, E., Khatibnezhad, H., Bajgiran, M. M., Solomon, M., Liang, C., Sagan, S. M., ... & Moreau, C. (2023). A Comparative Study of the Antiviral Properties of Thermally Sprayed Coatings against Human Coronavirus HCoV-229E. *Catalysts*, 13(7), 1141.

This study was part of the collaborative research work among the members of the GreenSEAM NSERC Strategic Network (Concordia University, McGill University, University of Toronto, National Research Council of Canada, Metal 7 Inc., Hatch, and SprayWerx Technologies) funded through NSERC and Mitacs. This work was not performed directly in the context of this thesis. However, its results can be helpful in potential applications such as developing antiviral membranes. Therefore, it is included in the Appendix. Elnaz Alebrahim and Hediye Khatibnezhad contributed equally to this work. They were responsible for performing methodology, investigation, formal analysis, writing the original draft, and the following review and editing of the paper. Christian Moreau supervised the research and revised the manuscript. The rest of the authors assisted with preparing samples (APS and S-HVOF coatings) and helped the authors during the investigation and writing the manuscript.

## Table of contents

List of Figures .....	xii
List of Tables.....	xvi
Chapter 1 Introduction .....	1
1.1 Introduction.....	1
1.2 Research Objectives .....	2
1.3 Thesis Organization .....	3
Chapter 2 Literature Review .....	5
2.1 Classification of Ceramic Filtration Membranes .....	5
2.2 Microstructure and Conventional Fabrication Processes .....	6
2.3 Configuration.....	7
2.4 Operational Modes of Filtration Membranes .....	8
2.5 Characteristics and Performance of the Membranes .....	9
2.5.1 Porosity .....	9
2.5.2 Thickness.....	10
2.5.3 Surface Properties .....	11
2.6 Membrane Fouling .....	11
2.6.1 Passive Antifouling Approach .....	12
2.6.2 Active Antifouling Approach.....	12
2.7 Photocatalytic Property of TiO <sub>2</sub> .....	13
2.8 Important Parameters Affecting the Photocatalytic Activity of TiO <sub>2</sub> .....	14
2.8.1 Crystallin Composition .....	14
2.8.2 Photon Energy .....	15
2.8.3 Self-doping.....	16
2.9 Thermal Spray Process .....	16
2.10 Suspension Plasma Spray (SPS) Process.....	19
2.11 Membranes Produced with Thermal Spray Processes.....	21
2.12 Photocatalytic Property in the Thermal-Sprayed TiO <sub>2</sub> Coatings .....	25
Chapter 3 TiO <sub>2</sub> Photocatalytic Ultrafiltration Membrane Developed with Suspension Plasma Spray Process .....	27
3.1 Introduction.....	28
3.2 Materials and Methodology.....	30

3.2.1 Suspension Preparation.....	30
3.2.2 Plasma Spraying.....	31
3.2.3 Characterization .....	32
3.2.4 Membrane Performance .....	33
3.3 Results and Discussion .....	34
3.3.1 Optimization Process.....	34
3.3.2 Membrane Characterization.....	38
3.3.2.1 Microstructural Analysis.....	38
3.3.2.2 Phase Composition.....	41
3.3.2.3 Porosity Measurement.....	42
3.3.3 Membrane Performance .....	43
3.3.3.1 Clean Water Permeability Measurement.....	43
3.3.3.2 Photocatalytic Performance.....	46
3.4 Conclusion .....	49
Chapter 4 Tailoring the Porosity Level of the Suspension Plasma Sprayed Coatings Using a Dual Suspension Injection System .....	50
4.1 Introduction.....	51
4.2 Experimental .....	53
4.2.1 Plasma Spraying Process.....	53
4.2.2 Suspension Preparation.....	56
4.2.3 Coating Characterization .....	58
4.3 Results and Discussion .....	58
4.3.1 Microstructural Features .....	58
4.3.1.1 Surface Morphology and Roughness .....	63
4.3.1.2 Porosity .....	65
4.3.1.3 Influence of the Inflight Particle Velocity and Substrate Temperature .....	66
4.3.1.4 Influence of the Suspension Trajectory in the Plasma Jet.....	67
4.3.1.5 Influence of the Suspension Viscosity.....	69
4.3.2 Compositional Analysis.....	70
4.4 Conclusions.....	73
Chapter 5 A Comparative Study of the Self-Cleaning and Filtration Performance of Suspension Plasma-Sprayed TiO <sub>2</sub> Ultrafiltration and Microfiltration Membranes.....	75
5.1 Introduction.....	76
5.2 Materials and Methodology.....	78

5.2.1 Membrane Preparation .....	78
5.2.2 Membrane Characterization.....	79
5.2.3 Membrane Performance .....	80
5.3 Results and Discussion .....	82
5.3.1 Membrane Microstructure and Roughness (As-sprayed Membranes).....	82
5.3.2 Membrane Performance (As-sprayed Membranes) .....	85
5.3.2.1 Separation Performance .....	85
5.3.2.2 Self-cleaning and Recyclability .....	87
5.3.2.3 Contact Angle Measurement .....	90
5.3.3 Infiltration of the UF Membranes with Agglomerates of TiO <sub>2</sub> Nanoparticles (Filled Membranes) .....	91
5.3.3.1 Surface Roughness .....	91
5.3.3.2 Separation Performance .....	92
5.3.3.3 Molecular Weight Cut-off (MWCO).....	93
5.4 Conclusion .....	94
Chapter 6 Conclusions and Future Work .....	96
6.1 Summary and Conclusions .....	96
6.2 Contributions.....	97
6.3 Future Works.....	98
References .....	100
Appendix1: Supplementary Material to Chapter 5 .....	122
Appendix 2: A Comparative Study of the Antiviral Properties of Thermally Sprayed Coatings against Human Coronavirus HCoV-229E .....	125

## List of Figures

Figure 2.1 Classification of membranes based on the pore size. Adapted from [6].	5
Figure 2.2 (a) Schematic of the asymmetric microstructure of ceramic membrane in water and wastewater treatment [19], and (b) SEM image of the cross-section of a membrane with the top layer made of cobalt silica film and intermediate layer and substrate made of alumina [4].	6
Figure 2.3 Ceramic membrane with asymmetric non-layered structure produced by inversion process [23].	7
Figure 2.4 Examples of commercial ceramic membranes; top) flat sheets from KERAFOIL [21], bottom-left) hollow fiber membrane by Deltapore [28], and bottom-right) cylindrical from Pall Membralox [10].	8
Figure 2.5 Schematics of dead-end and crossflow filtration modes.	9
Figure 2.6 Schematic of direct and indirect bandgap.	15
Figure 2.7 Schematic of the thermal spray process and the main components of the coating [106].	17
Figure 2.8 is an overview of the inflight particles' temperatures and velocities in various thermal spray processes [110].	18
Figure 2.9 Overview of particle temperature versus particle velocity for various types of materials systems in thermal spray processes [110].	18
Figure 2.10 Schematic of The SPS system. Reproduced from [47].	20
Figure 2.11 The evolution of the suspension and inflight particles during the SPS process. Reproduced from [97].	20
Figure 2.12 The various types of microstructures typically obtainable using the SPS process, including (a) Fully dense [132], (b) Porous with vertical cracks [133], (c & d) porous with columnar features [133], and (e) uniformly porous [134] microstructures.	21
Figure 2.13 Metallic filtration membrane produced by wire arc spraying showing the influence of the standoff distance changing from 15 to 65 cm on the porosity in the membrane [43].	22
Figure 2.14 The SEM micrographs of (a) surface and (b) cross-section of TiO <sub>2</sub> membranes produced with the APS process [140].	23
Figure 2.15 SEM images of the (b) CFS membrane with powder feed, (c) CFS membrane with rod feed, and (d-f) APS Al <sub>2</sub> O <sub>3</sub> membranes [42].	23
Figure 2.16 (Top) The surface morphologies of membranes sprayed on dry and wet substrates, and (bottom) the influence of high temperature water vapor induced mechanism in splitting the splats [141].	24
Figure 2.17 SEM micrograph of the fractured cross- section of photocatalytic SPS TiO <sub>2</sub> filtration membrane including large pores (A), unmelted particles (B), re-solidified particles (C), and fully melted zones (D) [15].	25
Figure 3.1 (a) SEM micrograph of the TiO <sub>2</sub> powder, (b) agglomerate size distribution of the TiO <sub>2</sub> aqueous suspension, (c) schematic of the 3MB suspension plasma system.	30
Figure 3.2 Schematic of the photoreactor.	34
Figure 3.3 Optical microscope images of the cross-sections of samples 1, 2, 3 and 4 sprayed for the optimization process according to Table 3.2.	35
Figure 3.4 Photocatalytic degradation of MB solution for the optimization process samples sprayed according to Table 3.2 under UVA light.	37

Figure 3.5 Low- magnification SEM micrographs of M-2 (2 passes), M-4(4 passes), and M-8 (8 passes) membranes.....	38
Figure 3.6 (a) SEM micrograph of M-8 inside the large pores of the substrate and close to the surface of the substrate. Including 1: melted splats (light gray), 2: large pores(black), 3: loosely packed unmelted nanostructured agglomerates (dark gray), and 4: tightly packed unmelted nanostructured agglomerates (dark gray), (b) High-magnification SEM micrograph of the microstructure in the dark grey areas, and (c) Schematic of the asymmetric microstructure of ceramic membranes. ....	39
Figure 3.7 (a) SEM micrograph of a porous nanostructured agglomerate in the fractured cross-section of M-8, (b) high magnification SEM micrograph of the nanostructured agglomerates demonstrating the presence of unmelted/sintered TiO <sub>2</sub> nanoparticles.....	40
Figure 3.8 XRD patterns of the TiO <sub>2</sub> feedstock powder, M-2, M-4, and M-8 membranes.....	41
Figure 3.9 Pore size distribution of the membrane measured with mercury intrusion porosimetry. ....	43
Figure 3.10 (a) Clean water flux as a function of pressure for porous substrate, M-2, M-4, and M-8 membranes, and (b) Normalized water flux as a function of membrane thickness. ....	44
Figure 3.11 SEM micrographs of two positions on the polished cross-section of M-4 after the pure water permeability measurement.....	45
Figure 3.12 (a) Photocatalytic degradation of MB for M-2, M-4, and M-8 membranes under UVA, and (b) under visible light illumination.....	46
Figure 3.13 (a) UV–vis absorption spectra, (b) $(\alpha h\nu)^{0.5}$ - $h\nu$ , and (c) $(\alpha h\nu)^2$ - $h\nu$ plots of TiO <sub>2</sub> feedstock powder and M-4 membrane. ....	48
Figure 4.1 Schematic of the dual suspension injection system. Suspension 1, made by submicron-sized TiO <sub>2</sub> , was injected via injector 1, and suspension 2, made by nanosized TiO <sub>2</sub> , was injected via injector 2. Unmelted submicron-sized particles and unmelted nanosized particles in the coatings come from injector 1 and 2, respectively.....	54
Figure 4.2 (a) Particle size distribution of submicron-sized TiO <sub>2</sub> powder. (b) SEM micrograph of the submicron-sized TiO <sub>2</sub> powder. (c) particle size distribution of nano-sized TiO <sub>2</sub> powder. (d) SEM micrograph of the nano-sized TiO <sub>2</sub> powder.....	57
Figure 4.3 Low magnification SEM micrographs of control samples D1 (Submicron-sized TiO <sub>2</sub> injected through only injector 1), and D2 (Submicron-sized TiO <sub>2</sub> injected through injector 1, and water through injector 2) coatings. ....	59
Figure 4.4 SEM micrograph of the polished cross-section of sample D1, displaying (1) large pores, (2) splats from the melted particles, and (3) unmelted submicron-sized particles.....	60
Figure 4.5 SEM micrographs of samples D3 to D8 classified based on the spray parameters. Spray condition D9 resulted in a powdery deposition on the substrate (no coating was obtained).....	61
Figure 4.6 (a) SEM micrograph of a polished cross-section of the D5 coating showing: (1) large pores, (2) splats from the fully melted particles, and the co-existence of (3) submicron-sized particles from suspension and injector 1, and (4) nanosized particles from suspension and injector 2, (b) High magnification SEM micrograph of the submicron-sized particles, and (c) High magnification SEM micrograph of the nanosized particles. ....	62
Figure 4.7 ) SEM micrograph of a fractured cross-section of the coating D5 showing: (1) large pores, (2) splats from the fully melted particles, and the co-existence of (3) submicron-sized particles from suspension and injector 1, and (4) nanosized particles from suspension and injector 2.....	62
Figure 4.8 SEM micrographs of the surfaces of coatings D1 to D8.....	64

Figure 4.9 Ratio of the large pores, the unmelted submicron-sized particles from injector 1, and the unmelted agglomerates of nanosized particles from injector 2 in coatings D1 to D8. ....	65
Figure 4.10 Plasma imaging pictures of control samples D1 sprayed with a single injector (coating was produced by spraying suspension 1 through injector 1), D2 sprayed with two injectors (coating was produced by spraying suspension 1 through injector 1 and water through injector 2), and D5 (coating was sprayed by spraying suspension 1 through injector 1 and suspension 2 through injector 2). The spray parameters were the same, except for the presence of injector 2 spraying water and suspension .....	68
Figure 4.11 Suspension trajectory images of samples D7 and D8 showing the influence of increasing the distance between the two injectors, where submicron-sized and nanosized suspensions were sprayed through injectors 1 and 2, respectively. ....	69
Figure 4.12 Shear rate vs shear stress measurements of suspension 1, suspension 2-20 (suspension 2 with 20 wt.% TiO <sub>2</sub> ), and suspension 2-30 (suspension 2 with 30 wt.% TiO <sub>2</sub> ). The slope defines viscosity. ....	70
Figure 4.13 a) XRD patterns of f TiO <sub>2</sub> feedstock powders and samples D1 to D8. b) Rietveld refinement of XRD pattern of Powder 1, powder 2, and sample D8. (Powder 1 refers to the submicron-sized feedstock powder used to prepare suspension 1, and powder 2 to the nanosized feedstock powder used to prepare suspension 2.) .....	71
Figure 4.14 Raman spectra of the unmelted (identified in dark grey color in the microstructure) and melted areas (identified in light grey color in the microstructure), obtained from the cross-sections of coatings D1, D3, and D8.....	73
Figure 5.1 (a) SEM micrograph of the cross-section of the UF-2P membrane, (b) High magnification SEM micrograph of the red dashed zone in UF-2P membrane, (c) SEM micrograph of the cross-section of the UF-4P membrane, (d) SEM micrograph of the cross-section of the MF-12P membrane, and e) High magnification SEM micrograph of the red dashed zone in MF-12P membrane. In both UF and MF membranes, no.1 (light grey areas) shows the melted splats, no.2 (black areas) shows the large pores, no. 3 (dark grey areas) shows the agglomerates of unmelted nanosized TiO <sub>2</sub> particles in the UF membrane, and no.4 (dark grey areas) shows the u-melted submicron-sized TiO <sub>2</sub> particles in the MF membrane. ....	83
Figure 5.2 Confocal microscope images of UF-2P, UF-4P, and MF-12P membranes. ....	84
Figure 5.3 The SiO <sub>2</sub> particles rejection % of (a) UF membranes and (b) MF membranes. The separation efficiency was increased as a function of the thickness of the membranes .....	85
Figure 5.4 Fouling behavior of UF-2P, UF-4P, and MF-12P due to the pore blocking (obtained from RFRp) and cake formation (obtained from RFRc) phenomenon. A lower RFR value indicated a higher fouling resistance.....	86
Figure 5.5 Self-cleaning performance of UF-2P and MF-12P membranes repeated in three cycles showing partial flux recovery of the membranes due to the photocatalytic cleaning of the membranes. ....	88
Figure 5.6 Evolution of the flux recovery of UF-2P and MF-12P membranes after four hours of photocatalytic cleaning and back washing following the 3rd cycle of the self-cleaning experiment. ....	90
Figure 5.7 Confocal microscope image of UF-2P-F and UF-4P-F membranes.....	92
Figure 5.8 Comparing the rejection rates of the UF membranes before and after filling the large pores with agglomerates of TiO <sub>2</sub> nanoparticles for SiO <sub>2</sub> 200 nm and SiO <sub>2</sub> 400nm particles.....	93

Figure 5.9 Rejection rate as a function of the PEO molecular weight of the UF-4P and UF-4P-F membranes. The filling process made it possible to reduce the MWCO of the filled membrane to about 900 kDa. .... 94

Figure S1 Particle size distribution of the two SiO<sub>2</sub> particles used for characterizing the efficiency of the particle rejection in the membranes showing (a) the particle size distribution of SiO<sub>2</sub> powder with the average particle size of 200 nm, and (b) the particle size distribution of the SiO<sub>2</sub> powder with the average particle size of 400 nm. .... 123

## List of Tables

Table 3.1 Plasma torch operation parameters. ....	31
Table 3.2 Test matrix for the optimization process. ....	31
Table 3.3 The phase composition and anatase crystallite size of samples 1, 2, 3 and 4. ....	36
Table 3.4 Photocatalytic performance of the optimization process samples sprayed according to Table 3.2. ....	37
Table 3.5 Thickness and surface roughness of M-2, M-4, and M-8 membranes. ....	38
Table 3.6 Phase composition of M-2, M-4, and M-8 membranes. ....	42
Table 3.7 Clean water permeability of M-2, M-4, and M-8 membranes. ....	44
Table 3.8 Photocatalytic performance of M-2, M-4, and M-8 membranes under UVA and visible light. ....	47
Table 4.1 SPS parameters used to deposit TiO <sub>2</sub> coatings. ....	54
Table 4.2 Test matrix used to produce TiO <sub>2</sub> coatings. ....	55
Table 4.3 Surface roughness measurements (R <sub>a</sub> ) for coatings D1 to D8 obtained by confocal laser microscopy. ....	63
Table 4.4 Thickness, substrate temperature, and inflight particle velocity of the coatings D1 to D8. ....	66
Table 4.5 Phase composition of TiO <sub>2</sub> feedstock powders and samples D1 to D8 obtained from XRD analysis. Powder 1 refers to the submicron-sized feedstock powder used to prepare suspension 1, and powder 2 to the nanosized feedstock powder used to prepare suspension 2. ....	72
Table 5.1 Identification of the membranes. ....	79
Table 5.2 Thickness measurements of the UF and MF membranes. ....	84
Table 5.3 The surface roughness of UF-2P, UF-4P, and MF-12P membranes. ....	85
Table 5.4 Flux recovery ratio (FRR %) of the UF and MF membranes. ....	87
Table 5.5 Surface roughness of UF-2P-F and UF-4P-F. The membranes were filled with the agglomerates of nanosized TiO <sub>2</sub> . ....	92

## List of Abbreviations

Al <sub>2</sub> O <sub>3</sub>	Alumina
APS	Atmospheric Plasma Spray
CFS	Combustion Flame Spray
FESEM	Field Emission Scanning Electron Microscopy
FRR	Flux Recovery Ratio
h <sup>+</sup>	Hole
HA	Humic Acid
HVOF	High Velocity Oxygen Fuel
MB	Methylene Blue
MD	Membrane Desalination
MF	Microfiltration
MIP	Mercury Intrusion Porosimetry
MWCO	Molecular Weight Cut off
PEO	Polyethylene Oxide
RFR	Ratio of Fouling Resistance
ROS	Reactive Oxygen Species
SEM	Scanning Electron Microscopy
SiO <sub>2</sub>	Silicon Dioxide
SLPM/LPM	Standard Litre per Minute/ Litre per Minute
SOFC	Solid Oxide Fuel Cell
SPS	Suspension Plasma spray
SPPS	Solution Precursor Plasma Spray
TiO <sub>2</sub>	Titanium Dioxide
T <sub>m</sub>	Melting Temperature
UF	Ultrafiltration
UV	Ultraviolet
UV-vis	Ultraviolet/visible Absorption Spectroscopy
VPS	Vacuum Plasma Spray
XRD	X-ray Diffractometer
ZrO <sub>2</sub>	Zirconium Dioxide

# Chapter 1 Introduction

## 1.1 Introduction

In recent decades, the rapid growth of industrialization, climate change, population growth, and water contamination have become major challenges for sustainable development. The escalating scarcity of water resources has raised significant concerns, highlighting the urgent need for effective solutions to address this pressing issue [1,2]. To tackle these challenges, there is a pressing need to develop modern and affordable methods to protect and recycle available water supplies. Among the available methods is membrane filtration, which has emerged as an effective, sustainable, and cost-efficient solution to address the current water crisis [3].

The filtration membrane market has been predominantly controlled by polymeric membranes, mainly because of their affordability and moderate performance [4,5]. Nonetheless, the shortcomings of polymer membranes in certain aspects, such as their vulnerability to dissolution in various solvents and their limited applicability at high temperatures, have raised concerns about their reliability in aggressive environments. In contrast, ceramic-based membranes offer superior mechanical, thermal, and chemical stability, making them a promising alternative. Generally, these membranes can be cleaned through high-temperature sterilization or backwashing. As a result, the utilization of ceramic-based membranes represents a compelling solution to address some of the limitations associated with polymeric alternatives in various filtration applications [6,7]. Despite the advantageous characteristics of ceramic-based membranes, their widespread adoption is limited due to the complexity and high cost of their manufacturing processes. Therefore, their application is currently constrained to specific areas where their enhanced properties offer clear benefits over traditional polymer membranes. While ceramics present a promising solution for overcoming some of the limitations of polymeric alternatives, their full potential is yet to be realized, and further research and development efforts are required to make them more accessible and economically viable for broader filtration applications [8–11]. Aside from their higher cost, ceramic membranes also face challenges related to their weight, brittleness, and difficulty sealing them within metallic housings [10]. Additionally, there are critical areas of improvement needed for ceramic membranes, such as enhancing filtration precision, anti-fouling properties, and packing density. Moreover, optimization efforts are required for ceramic membranes to be viable for large-scale applications [12].

Given these limitations and areas for improvement, there is a pressing need to explore and develop novel membrane materials and manufacturing methods. The ultimate goal is to explore a novel approach to create cost-effective and efficient membranes offering improved performance and reliability. By addressing these issues, the development of innovative membrane technologies can significantly advance filtration applications, enabling their broader adoption and more effective use in diverse industries.

The application of suspension plasma spray (SPS) as a rather novel coating deposition technology, utilizing sub-micron to nano-sized feedstock material, could represent a promising approach for the cost-effective production of ceramic membranes [13]. Furthermore, the SPS process offers the opportunity to incorporate photocatalysts like titanium dioxide ( $\text{TiO}_2$ ) into the membranes, enabling the degradation of organic contaminants and improving the membrane's anti-fouling capabilities [14].

## 1.2 Research Objectives

Thermal spraying processes emerge as a promising novel avenue for membrane production. These coating deposition technologies are environmentally friendly and offer versatility and rapid processing capabilities, making them highly compatible with large-scale industrial applications. Previous studies have demonstrated the feasibility of producing  $\text{TiO}_2$  water-permeable membranes using the SPS process for filtration application. Titanium dioxide ( $\text{TiO}_2$ ) SPS porous membranes with an average pore size of around 180 nm were produced based on unmelted feedstock particles in a matrix built by melted splats. The SPS  $\text{TiO}_2$  membranes showed photocatalytic activity by discoloration of methylene blue (MB) solution under UVC illumination [15]. However, to unlock the full potential of these membranes, further investigation is crucial to optimize their microstructure in terms of pore size and porosity level, enabling the fabrication of diverse classes of membranes while enhancing fluid flow rates. Moreover, a comprehensive analysis of the membrane's performance is essential to understand its efficiency and potential real-world applications. This research aims to address these objectives and contribute to the advancement of SPS-based membrane technologies.

Here, the main objectives of this research respecting the sequence of the chapters of this thesis are outlined:

- Using the SPS coating deposition process to tailor the microstructure and develop photocatalytic ultrafiltration (UF) membranes with a pore size in the range of 2-100 nm with high water flux by optimizing the SPS process parameters.
- Investigating the feasibility of tailoring the porosity in porous coatings that could potentially be used for tailoring the porosity level in the structure of the SPS separation membranes. This was done by employing a dual suspension injection system to simultaneously introduce two suspensions into the plasma jet at different radial distances.

- A comprehensive characterization of the SPS ultrafiltration and microfiltration membranes' performance in terms of rejection efficiency, flux recovery, anti-fouling, and photocatalytic properties.

### **1.3 Thesis Organization**

This thesis comprises six chapters. Each chapter is briefly described herein.

**Chapter 1 (Introduction)** This chapter introduces the importance of membrane separation technologies, the advantages and limitations of ceramic membranes, their current fabrication technologies, and the research objectives of this study.

#### **Chapter 2 (Literature Review)**

This chapter provides background information about the membranes and their classifications, conventional fabrication methods of ceramic membranes, and the basic principle of photocatalytic oxidation using TiO<sub>2</sub>. Additionally, in Chapter 2, thermal spraying is introduced, and the technique used in this research, suspension plasma spraying (SPS), is briefly explained. In the end, a comprehensive review of the literature that employed thermal spraying to develop membranes and thermal-sprayed photocatalytic TiO<sub>2</sub> coatings is presented.

#### **Chapter 3 (Paper1)**

This chapter represents the systematic work to produce a TiO<sub>2</sub> photocatalytic ultrafiltration membrane with nanosized pores using the suspension plasma spray process.

#### **Chapter 4 (Paper2)**

This chapter represents a systematic approach for tailoring the porosity level of the suspension plasma sprayed coatings using a dual suspension injection system.

#### **Chapter 5 (Paper 3)**

This chapter represents a comparative study of the self-cleaning and filtration performance of suspension plasma sprayed TiO<sub>2</sub> ultrafiltration and microfiltration membranes.

#### **Chapter 6 (Conclusion and Future Work)**

This chapter presents a comprehensive overview of the primary findings, conclusions, and contributions of this research. It outlines the main outcomes achieved through the study and

highlights the significance of the results. Additionally, the chapter offers insights into potential areas for future research, providing recommendations for further investigations and advancements in the field.

# Chapter 2 Literature Review

## 2.1 Classification of Ceramic Filtration Membranes

In the context of separation or purification processes, the membrane is basically defined as “a selective barrier between two environments” with the ability to selectively control the passage of specific constituents [16]. Membranes are commonly categorized according to their pore sizes, resulting in four distinct classes: microfiltration (100-10,000 nm), ultrafiltration (2-100 nm), nanofiltration (0.5-2 nm), and reverse osmosis (less than 0.5 nm) [17,18]. Porous ceramic membrane development traces back to the 1940s when it was initially utilized for U235 enrichment [7]. By the 1980s, industrial applications began incorporating inorganic membranes for microfiltration and ultrafiltration [8]. Ceramic membranes utilized in water treatment applications typically consist of alumina ( $\text{Al}_2\text{O}_3$ ), silica ( $\text{SiO}_2$ ), titania ( $\text{TiO}_2$ ), and zirconia ( $\text{ZrO}_2$ ), along with silicon carbide ( $\text{SiC}$ ) or a combination of those, covering the range from microfiltration to nanofiltration [4,10,19,20]. In Figure 2.1, the membranes are categorized based on their pore size, and it shows the potential for rejecting various contaminants depending on the specific pore size of the membrane.

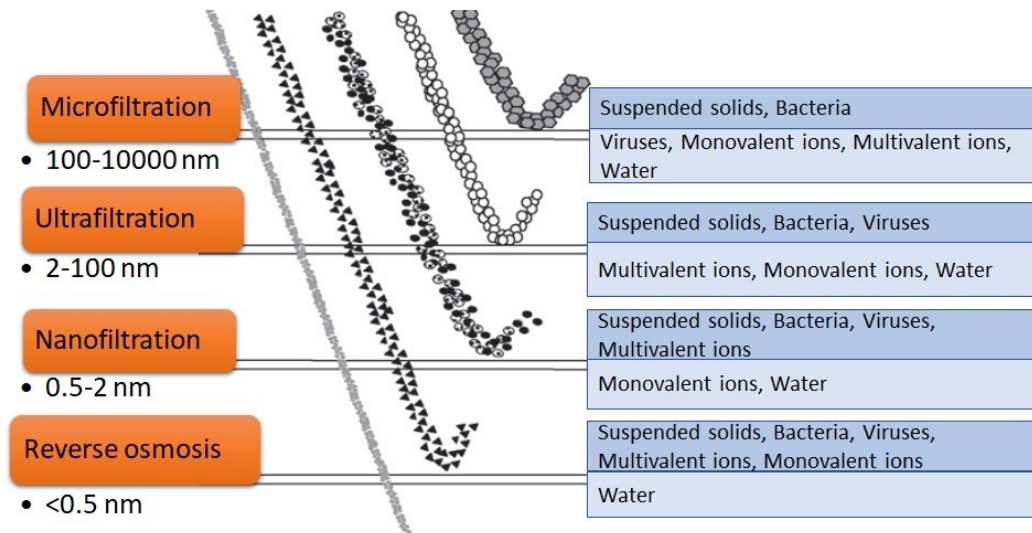


Figure 2.1 Classification of membranes based on the pore size. Adapted from [6].

## 2.2 Microstructure and Conventional Fabrication Processes

Ceramic filtration membranes are manufactured using a layered arrangement of porous materials, resulting in an asymmetric microstructure [5]. Each layer within the asymmetric structure exhibits variations in pore size and thickness. The few millimeters thick bottom layer with 1-10  $\mu\text{m}$  pore size serves as the substrate, imparting mechanical strength to the overall membrane system [4,20]. In certain cases, additional intermediate layers with a thickness of 1-100  $\mu\text{m}$  are incorporated to customize the overall pore size, porosity level, and mechanical strength of the membrane [4,5]. This design allows for a very thin active filtering layer, enabling higher flow rates to be achieved [21]. Finally, a thin top layer, with the smallest pore size among the layers, is responsible for the membrane's selectivity and separation efficiency [4]. Figure 2.2a presents a schematic diagram illustrating the asymmetric structure of a ceramic membrane. Figure 2.2b shows an example of an asymmetric membrane used in water and wastewater treatment applications.

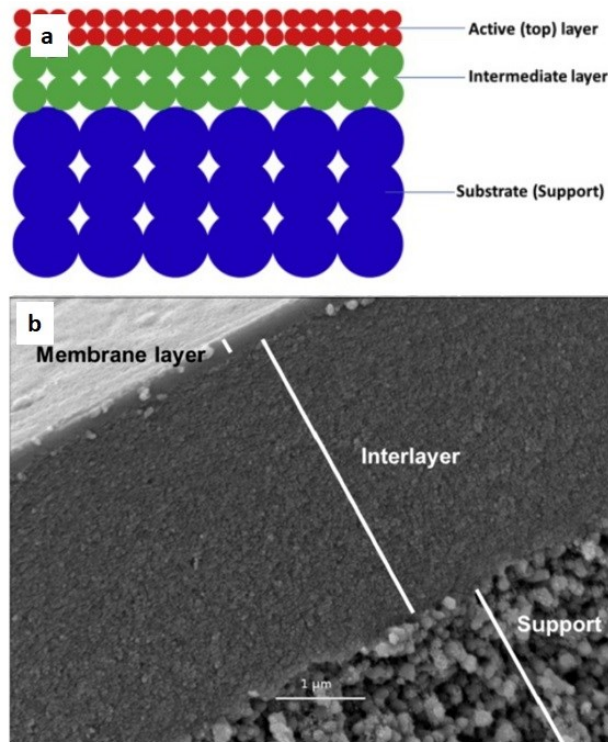


Figure 2.2 (a) Schematic of the asymmetric microstructure of ceramic membrane in water and wastewater treatment [19], and (b) SEM image of the cross-section of a membrane with the top layer made of cobalt silica film and intermediate layer and substrate made of alumina [4].

The typical techniques used to produce ceramic membranes include extrusion, sol-gel, slip-casting, phase inversion, and chemical vapor deposition [12,22]. A primary challenge linked to traditional manufacturing methods involves the high sintering temperature and long sintering time that impacts the quality and cost of the product. Therefore, alternative methods have been developed, such as combined phase inversion-sintering processes. In this method, an asymmetric

non-layered microstructure is developed, as shown in Figure 2.3. The pore size, morphology, and mechanical properties can be controlled through parameters such as the size distribution of the ceramic particles and the spinning process parameters, such as the viscosity of the suspension, ceramic to polymer ratio, and flow rate. However, the process is still time-consuming and needs a long and high-temperature sintering process, resulting in grain growth and densification of the finely porous sponge-like section [23–26].

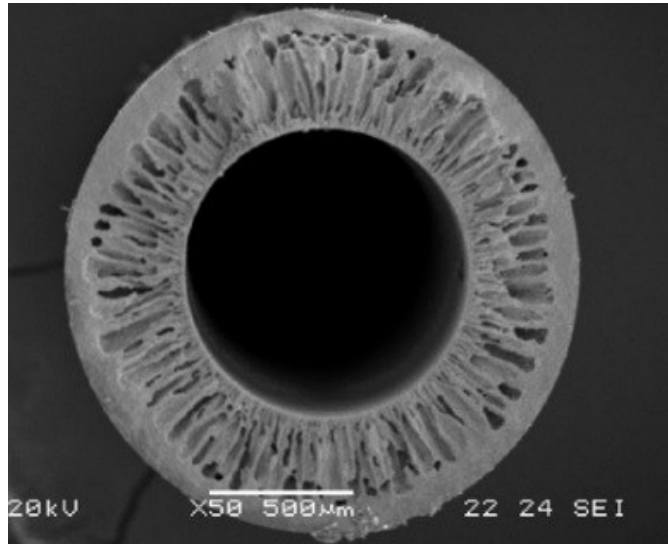


Figure 2.3 Ceramic membrane with asymmetric non-layered structure produced by inversion process [23].

## 2.3 Configuration

Commercial ceramic membranes used in water treatment applications are typically available in various modular forms. To increase the efficiency of the membrane setups, the membrane modules need to have a high packing density, enhanced hydrodynamic properties to decrease the effect of fouling and concentration polarization, low pressure drop during the filtration process, and minimal operational and maintenance cost [27]. Considering that, the most predominant commercial membrane configurations include flat-sheet type, tubular type, and hollow fiber set-ups. All these configurations feature multiple channels. Tubular membranes have garnered significant interest recently because of their advantageous high surface-to-volume ratio compared to flat-sheet membranes [4]. Some of the typical configurations of commercial ceramic membranes are presented in Figure 2.4.



Figure 2.4 Examples of commercial ceramic membranes; top) flat sheets from KERAFOIL [21], bottom-left) hollow fiber membrane by Deltapore [28], and bottom-right) cylindrical from Pall Membralox [10].

## 2.4 Operational Modes of Filtration Membranes

Membrane filtration is primarily conducted in dead-end and crossflow modes, as depicted in Figure 2.5. In the dead-end configuration, the feed flows perpendicular to the surface of the membrane. As a result, a filter cake layer made by the accumulated separated particles is built up on the surface of the membrane. The presence of the porous cake layer in the dead-end setup enhances the filtration efficiency. However, as the cake layer thickens, the filtration rate decreases. Eventually, cleaning or replacing the membrane becomes necessary when the cake layer reaches a certain thickness [29]. Due to the relatively fast decline in flux, dead-end setups are less used in industrial applications. Nevertheless, it finds effective applications in bench-scale and pilot-scale experiments [30].

In the crossflow setup, the feed flows parallel to the surface of the membrane. The continuous feed flow consistently removes the accumulated filtered species from the surface of the membrane, thereby diminishing the cake build-up. Eventually, the flux decline occurs in the crossflow mode as well. However, it is less severe than the dead-end mode [16,31].

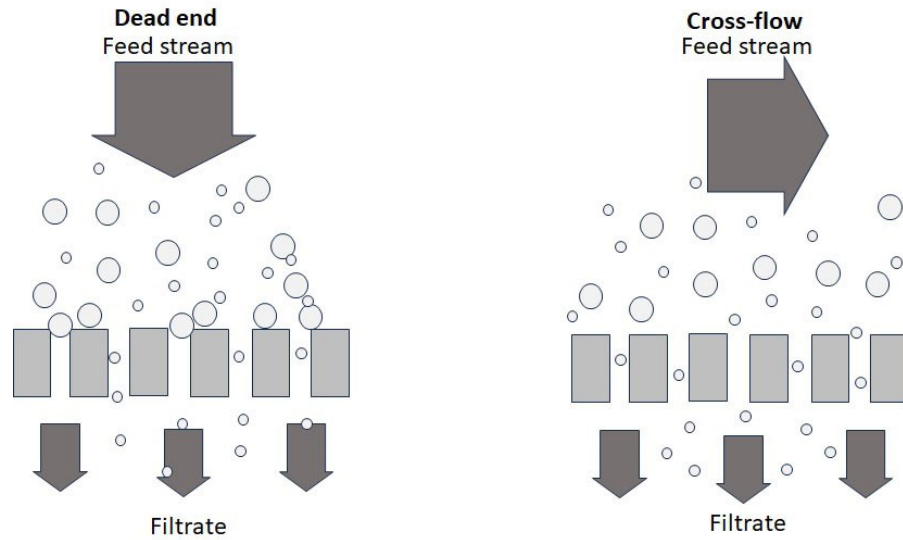


Figure 2.5 Schematics of dead-end and crossflow filtration modes.

## 2.5 Characteristics and Performance of the Membranes

The performance of the membranes in terms of rejecting the contaminants can be impacted by a range of factors tied to the characteristics of both the membrane and the feed. Here, we outline some key parameters related to the membrane itself.

### 2.5.1 Porosity

The permeability in the membranes is primarily affected by the pore size, pore size distribution, porosity, and the morphology of the pores in the structure [32]. Various methods are used to determine the pore size in the membranes. Here, some of the commonly used techniques are introduced.

- Direct determination of the pore size using the scanning electron microscopy (SEM)

In this method, SEM images of the surface and cross-section of the dry membranes are analyzed by image analysis software to quantify the pore size in the membrane [33].

- Bubble point pressure

This method determines the pore size and distribution by identifying the pressure needed to blow air through a porous membrane compacted with water. The diameters of the pores are determined using the Washburn equation (2.1) [34].

$$\Delta P = \frac{4\gamma \cos\theta}{d} \quad (2.1)$$

$\Delta P$  is the pressure,  $d$  is the pore diameter,  $\gamma$  is the surface tension of the liquid-liquid or air-liquid interface, and  $\theta$  is the wetting angle of water with the membrane. Since, in this method, the minimum pressure at which the bubbles appear is obtained, only the largest pore size in the pore size distribution is determined [35]. This method is typically used for the MF membranes, where relatively lower pressure is needed [36].

- Mercury Intrusion Porosimetry (MIP)

MIP is, in fact, a variation of the bubble point pressure method. This method is based on forcing mercury (a non-wetting liquid with a high surface tension) inside the pores by applying external pressure. The primary key to this technique is that it assumes a cylindrical shape for the pores. And the pore size is obtained through applying the Washburn equation (2.1) [37].

This equation relates the pressure required to fill the pores to the corresponding pore size by employing the surface tension of mercury and the contact angle between the surface and mercury. The volume of the pores at each size class is determined by measuring the volume of mercury that intrudes into the sample at each pressure point.

- Solute Retention Method

This method is the most commonly employed approach for evaluating the UF membranes. It basically relates the pore size of the UF membrane to the molecular weight of the solute it can reject by 90% [36]. The 90% rejection point is identified as the molecular weight cut off (MWCO) of the membrane since the UF membranes were primarily used to separate proteins and macromolecules identified by their molecular weights [38]. The common solutes used to define the MWCO include various proteins, dextrans, and polyethylene glycols [34,36,39]. However, parameters such as the form of the molecules, concentration, pressure, and temperature could influence the determination of the MWCO in membranes. Thus, it is not an absolute value [40]. As a rule of thumb, membrane manufacturers suggest choosing a membrane with MWCO that is three to six times smaller than the size of the solute to be rejected.

## 2.5.2 Thickness

The thickness of the membrane is a significant factor to consider during the fabrication process, as it inversely affects permeability [41]. On the other hand, the thicker the membrane layer, the higher the separation efficiency [42–44]. The optimal thickness for the filtration layer remains uncertain. An excessively thick layer is susceptible to cracking during the drying and sintering. In contrast, an overly thin layer is prone to incomplete formation, failing to cover the entire substrate surface [45]. Nevertheless, a recommended approach is for the thickness to exceed 50 times the diameter of the feedstock particles used for its fabrication [20].

### 2.5.3 Surface Properties

The surface properties of membranes can influence critical factors such as selectivity, fouling resistance, permeability, and overall separation efficiency. Surface roughness and wettability are two of the important surface characteristics in membranes.

- Surface Roughness

It has been reported that a high surface roughness can increase the fouling tendency of the membranes. A large surface area resulting from high roughness could provide more adherence sites for the contaminants. At the same time, the configuration of ridges and valleys could promote the gathering of the foulants on the surface, which also could result in lower permeate flux during the filtration process [46]. Furthermore, an increase in the surface roughness may alter the hydrophilic nature of the ceramic coatings [47].

- hydrophilicity/Hydrophobicity

To enhance the hydrophilic or hydrophobic properties in membranes, surface modification with functional groups is used. Some examples of the hydrophilic groups include -OH and -NH<sub>2</sub> [48,49]. Likewise, examples of the hydrophobic groups include methoxy (-OCH<sub>3</sub>) and ethoxy (-OC<sub>2</sub>H<sub>5</sub>), which can react with the hydroxyl groups on the surface of the ceramic membranes [50].

Enhancement of the hydrophilic properties is used to improve the fouling resistance in membranes. Most ceramic membranes are naturally hydrophilic [50]. Therefore, they have less tendency to irreversible fouling, and the foulants can be removed more effectively by physical washing [51].

Hydrophobic membranes are typically used for desalination applications. The membrane desalination (MD) process includes a hot feed side and a cold permeate side, where the driving force of the desalination is the vapor pressure difference between these two sides. Due to the hydrophobic property on the surface, the liquid is retained at the feed side, and only water vapor can be transported through the highly porous (>80%) membranes with pores smaller than 1 μm [50].

## 2.6 Membrane Fouling

Membrane fouling is a significant challenge in numerous applications, such as water treatment, wastewater purification, and industrial processes. It refers to the undesirable accumulation of materials on the surface or within the pores of a membrane, impeding its proper functioning. Fouling can result in reduced flow rates, compromised separation efficiency, increased energy consumption, and elevated maintenance requirements. Fouling can be caused by various reasons, including pore blocking, cake layer formation, adsorption of organic matter on the surface, and biological fouling [52]. Multiple strategies have been employed to reduce the fouling effect, such as pretreatment of the feed, physical cleaning of the membrane (sponge balls), intermittent reversal of the feed stream direction (backwashing), pulsing boosts in the axial flow rate, alteration in feed temperature or composition, washing and back washing with

cleaning agents, dynamic filtration using vibrating and rotating membranes, and ultrasonically cleaning [30,52–54]. However, constant employment of rigorous cleaning procedures can lead to a reduction in the longevity of the membranes. Therefore, other approaches to produce fouling-resistant membranes have been investigated to mitigate the fouling phenomenon. The methods to integrate antifouling characteristics into membrane technology can be categorized as passive and active strategies for preventing fouling [55–57].

### **2.6.1 Passive Antifouling Approach**

Passive antifouling strategies are designed to proactively deter fouling occurrences by impeding or minimizing the attachment of undesired substances onto the surface of membranes. This is achieved through modifications to the membrane's physical, chemical, and surface attributes. These alterations collectively discourage the adhesion of fouling agents, contributing to the prevention of fouling formation [52]. One main area of investigation has been developing membranes with hydrophilic and super hydrophilic surfaces. The hydrophilic surface can reduce fouling by creating a layer of water molecules on the surface. Hydrophilic polymer membranes have been produced by the incorporation of hydrophilic materials on the surface [55–57]. Some nanomaterials have also been used to improve the passive antifouling property of the membranes by mainly enhancing their hydrophilicity, including metal oxides such as  $\text{SiO}_2$ ,  $\text{TiO}_2$ ,  $\text{Al}_2\text{O}_3$ ,  $\text{ZrO}_2$ , [58–60], graphene oxide [61], and carbon nanotubes [62].

### **2.6.2 Active Antifouling Approach**

Active antifouling resistance is mainly defined by the capability of the membrane to actively degrade and eliminate undesirable substances that could lead to fouling, mainly organic and biological contaminants [52]. By actively participating in the degradation of contaminants, these membranes can maintain their performance efficiency, reduce time for cleaning and maintenance, and extend their operational lifespan. One strategy has been to prepare membranes that could release antimicrobial agents to kill the biofoulants [63]. Additionally, employing reactive oxygen species (ROSs) generated through catalytic/photocatalytic reactions has been explored as an alternative venue to decompose organic and biological matter.  $\text{TiO}_2$  is an abundant, stable, and affordable semiconductor recognized for its photocatalytic properties in water treatment applications.

A photocatalyst is a substance capable of absorbing light, resulting in the generation of electron-hole pairs that drive chemical changes among constituents [64]. One straightforward approach to harness the photocatalytic capability of titanium dioxide involves directly dispersing  $\text{TiO}_2$  nanoparticles within a solution and subjecting it to UV light exposure [65]. This method offers an economical solution while enhancing reactivity by utilizing a highly reactive surface area [14]. Nonetheless, retrieving the catalyst particles presents a challenge, necessitating the inclusion of an additional post-treatment process [65,66]. Various approaches have been investigated to address this issue. Ao et al. employed magnetic nanoparticles with an anatase coating, facilitating retrieval of the nanoparticles by applying a magnetic field [67]. In another work, Li et al. utilized sunken ceramic filters to gather  $\text{TiO}_2$  nanoparticles within a photoreactor employed for breaking down antibiotics [68]. Immobilizing  $\text{TiO}_2$  photocatalyst particles within a

membrane layer has the potential to simplify and economize water treatment by eliminating the requirement for the filtration of photocatalyst particles. This approach also has the added benefit of enhancing the membrane's separation efficiency through improved antifouling properties. As a result, various research works were directed toward modifying the surface of polymer membranes with TiO<sub>2</sub> nanoparticles to induce photocatalytic reactivity [69–73]. However, polymeric membranes are unsuitable for photocatalytic reactors due to their instability under UV irradiation [74]. To address this issue, TiO<sub>2</sub> particles coated commercial ceramic membranes were developed. Choi et al. coated alumina substrates with a nano-structured TiO<sub>2</sub> film with narrow pore size distribution via a sol-gel method with an anatase crystalline size of 9 nm [75]. The drawback of the immobilization of catalyst particles was the reduction of the active surface area [76]. Using a substrate with a catalyst coating also expands the application to gas-phase photocatalysis, for example, in air purification systems [65]. An additional technical challenge in using TiO<sub>2</sub> as a photocatalyst involves its bandgap energy of around 3-3.2 eV. This characteristic enables the creation of charge carriers when exposed to UV light, limiting the possibility of harnessing the less energetic visible light photons for driving photocatalytic reactions [66].

## 2.7 Photocatalytic Property of TiO<sub>2</sub>

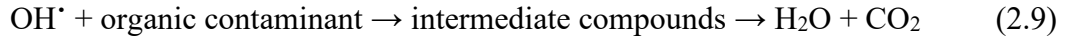
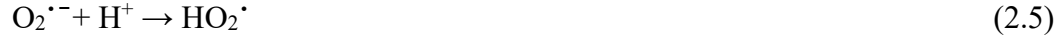
In 1972, Fujishima and Honda [77] introduced the concept of the photocatalytic ability of TiO<sub>2</sub>. This property enables the disintegration of organic contaminants and microorganisms into simpler compounds like carbon dioxide, water, and mineral acids. This breakdown process is facilitated by harnessing the energy of high-energy photons found in ultraviolet (UV) light. [78]. The process involves creating electrons and holes by excitation of the electrons from the valence band to the conduction band through the absorption of photons with energy equal to or greater than the bandgap energy [79].

TiO<sub>2</sub> exists in three different crystalline forms, known as anatase, rutile, and brookite. Brookite is known as an unstable polymorph of TiO<sub>2</sub>. Generally, anatase, which possesses a band gap energy of 3.2 eV, has been considered more efficient in terms of photocatalytic activity compared to rutile (with a band gap energy of 3 eV) [80]. When TiO<sub>2</sub> is exposed to photons with an energy greater than its band gap, an electron in the valence band is excited to the conduction band, and an electron-hole pair is created, as shown in Equation (2.2) [81]:



Followed by the creation of photogenerated electrons and holes and migration of these species to the surface of the catalyst, a series of various redox reactions could occur on the surface. Some of the common reactions are shown by Equations 2.3 to 2.9. [52,81,82]:





Powerful oxidizing species such as  $\text{OH}^{\cdot}$ ,  $\text{O}_2^{\cdot-}$ ,  $\text{HO}_2^{\cdot}$ , and  $\text{H}_2\text{O}_2$  have been suggested to be responsible for the degradation of organic contaminants.

## 2.8 Important Parameters Affecting the Photocatalytic Activity of $\text{TiO}_2$

The literature has pointed out several factors that can impact the photocatalytic property of  $\text{TiO}_2$ . Some of the most important parameters are discussed below.

### 2.8.1 Crystallin Composition

As mentioned earlier, anatase and rutile are the two main polymorphs of  $\text{TiO}_2$ . Generally, anatase has been considered to have superior photocatalytic performance to rutile [83–85]. This distinction arises from the lower recombination rate of electron-hole pairs in anatase and its stronger ability to attract and adsorb organic substances [80,86]. The lower electron-hole recombination rate in anatase has been linked to its indirect band gap. The schematic of the direct and indirect bandgaps is depicted in Figure 2.6. In the direct band gap, the momentum of electrons and holes aligns in both the conduction and valence bands, allowing electrons to emit photons directly. Conversely, in the indirect band gap, the emission of photons is hindered because electrons need to navigate an intermediary state and transfer momentum to the crystal lattice before photon emission can occur [87]. As a result, within semiconductors possessing a direct bandgap, the recombination of photoinduced electrons and holes takes place more readily. Consequently, even though anatase exhibits higher bandgap energy than rutile, it is proposed that anatase demonstrates enhanced photo reactivity attributed to the prolonged lifespan of photoexcited electron-hole pairs [83].

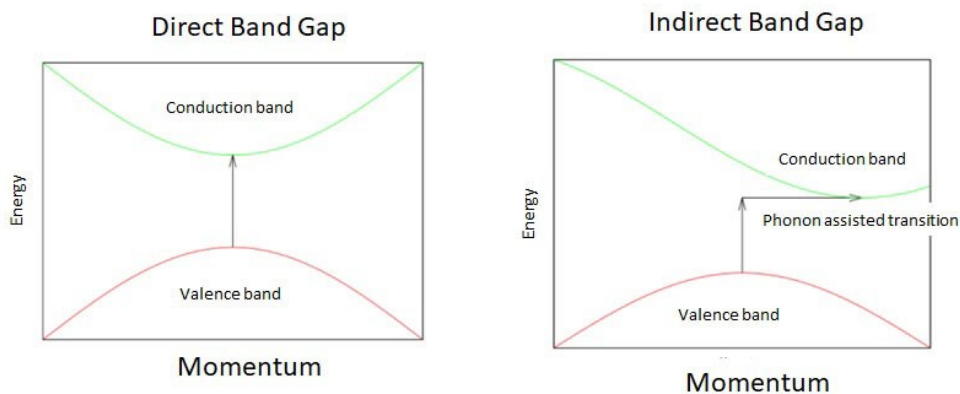


Figure 2.6 Schematic of direct and indirect bandgap.

While anatase has demonstrated notable efficiency as a standalone photocatalyst, a synergistic effect resulting from the combination of anatase, and rutile phases has been observed to yield higher photocatalytic activity [88]. A commonly acknowledged mechanism suggests that when anatase and rutile both exist in the photocatalyst, a preferred route for electron transfer from rutile to anatase is generated, promoting charge separation stability, and hindering the recombination [89,90].

### 2.8.2 Photon Energy

As mentioned earlier,  $\text{TiO}_2$  possesses a bandgap energy spanning from 3 eV for rutile to 3.2 eV for anatase. To excite an electron to jump from the valence band to the conduction band, photons with energies equal to or higher than that of the bandgap of the semiconductor are required. Therefore, for  $\text{TiO}_2$ , the wavelength of the light that can generate photos with adequate energy associates with  $\lambda < 400$  nm corresponding to the UV illumination [66]. Considering that a substantial proportion of solar radiation consists of visible light rather than UV light, the application of visible light-driven photolysis could offer a favorable alternative for reducing the energy demand associated with UV utilization [91]. Various approaches have been investigated to shift the photocatalytic reactivity in  $\text{TiO}_2$  toward the visible light range. Doping  $\text{TiO}_2$  with metallic atoms such as iron (Fe) enhanced photocatalytic activity by producing mid-gap energy levels that could trap the photo-generated charge carriers and hinder the electron-hole recombination rate [92]. Doping  $\text{TiO}_2$  with nonmetal atoms such as nitrogen has been used to create mid-gap levels over the valence band and oxygen vacancies by replacing some of the oxygen atoms in the lattice [93,94].

Khatibnezhad et al. showed that in  $\text{TiO}_2$  coatings produced by the suspension plasma spray (SPS), the bandgap energy is reduced by the inducement of oxygen vacancies, caused by a phenomenon known as self-doping. This adjustment enables the SPS  $\text{TiO}_2$  coatings to display photocatalytic reactivity when exposed to visible light [95].

### 2.8.3 Self-doping

The enhanced photocatalytic activity of the thermally sprayed TiO<sub>2</sub> coatings under visible light is attributed to a phenomenon referred to as self-doping [96]. The TiO<sub>2</sub> particles are subjected to very high temperatures in the plasma spray procedures, causing them to partially or entirely melt within low oxygen pressure or hydrogen-rich conditions. This process leads to the creation of oxygen vacancies within the solidified particles. [97–99] Oxygen vacancies in the lattice of TiO<sub>2</sub> anatase lead to the generation of sub-stoichiometric titanium dioxide (TiO<sub>2-x</sub>). While the TiO<sub>2</sub> powder is white, the sub-stoichiometric TiO<sub>2</sub> coating is dark blueish grey, absorbing more visible light [100]. Oxygen deficiencies in anatase provide mid-gap electronic states below the conduction band. Due to the generation of a narrower band gap, electron excitation to the mid-gap levels can occur by the lower energy photons of the visible light range. Further, the photo-generated electrons in these bands can jump to the conduction band, contributing to the photodegradation property of the photocatalyst [101]. Additionally, these sub-level states can act as charge carrier traps, hindering the recombination rate of the electrons and holes. Thus, oxygen-deficient titanium dioxide is regarded as a self-doped catalyst [96]. This allows the activation of the photodegradation process at lower photon energies of the visible illumination [101].

Additionally, other parameters such as concentration of the contaminant, PH, and temperature could also affect the photocatalytic efficiency of TiO<sub>2</sub> [102].

## 2.9 Thermal Spray Process

Thermal spray technology comprises a collection of coating deposition processes wherein the feedstock particles ranging from 1-100 μm are injected into a high-temperature jet, which can be generated by a combustion or non-combustion heat source. When the feedstock material interacts with the heat source, it undergoes partial or complete melting and is then propelled toward a substrate. As these molten or partially molten particles impact the substrate surface, they flatten and quickly solidify, forming thin layers called splats. The splats experience very high cooling rates. By repeating the process and accumulating more splats on the substrate and previously deposited splats, the coating is generated, and its thickness is increased [103,104]. In addition to powders, the feedstock material in the form of wire or rod is also used based on the specific coating process [105]. Based on the process parameters, the microstructures of thermal spray coatings may contain features such as pores, oxides, and intra and inter-lamellar cracks [42]. Figure 2.7 illustrates the schematic of the thermal spray process and the principal features of the produced coating [106].

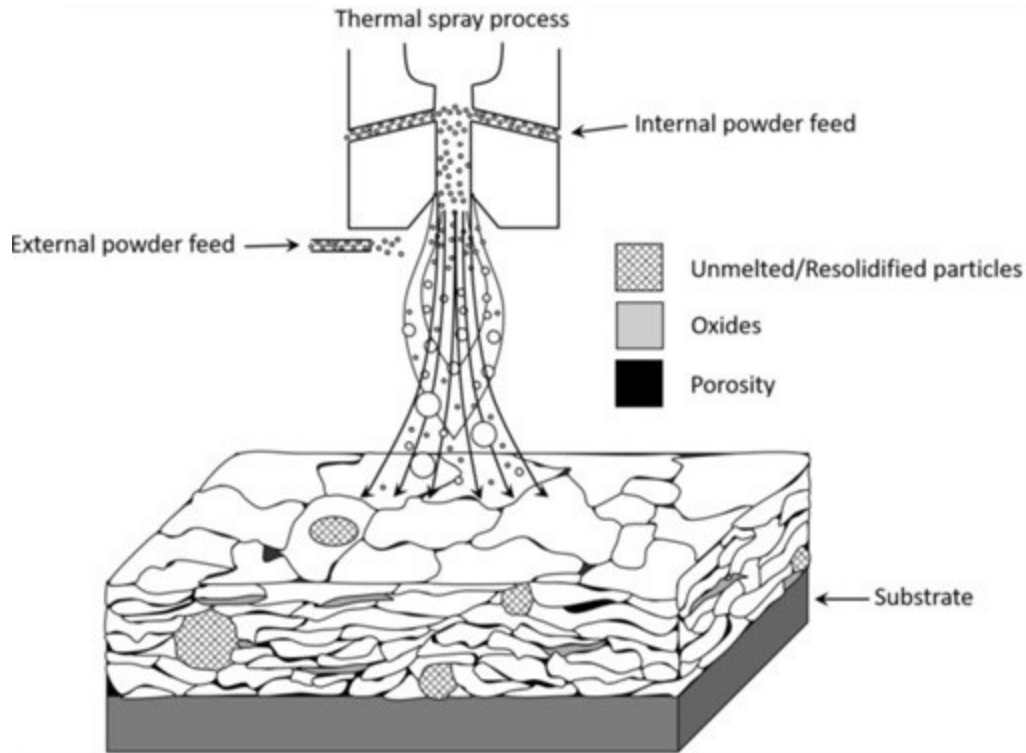


Figure 2.7 Schematic of the thermal spray process and the main components of the coating [106].

Thermal spray processes are performed over a range of temperatures and velocities that facilitate the application of a wide variety of materials, including metals, refractory alloys, ceramics, and cermets. The thermal spray techniques include flame spray, plasma spray, high-velocity oxygen-fuel (HVOF), and cold spray [107,108]. Figure 2.8 summarizes the various thermal spray processes based on the inflight particle temperatures and velocities.

The presence of a wide array of coating deposition methods and feedstock materials, offering the capability to generate coatings with diverse morphologies, surface textures, and distinct thermal and electrical attributes, has positioned thermal spraying as an intriguing option across various applications [106]. Furthermore, the scalability of the thermal spray process allows to coating large surface areas, and high coating deposition rates render it well-suited for extensive industrial applications. Additionally, they offer further benefits, including the flexibility to accommodate various substrates with varying shapes and sizes [109].

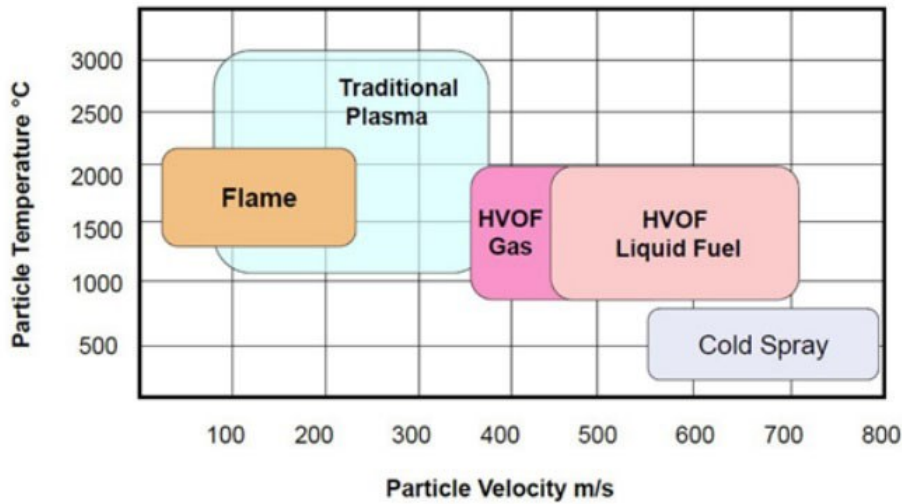


Figure 2.8 is an overview of the inflight particles' temperatures and velocities in various thermal spray processes [110].

The applications of thermal sprayed coatings cover a wide range, including but not limited to heat resistance coatings [111], corrosion resistant coatings [112], abrasible coatings [113], coatings used in electronics [114], and biomedical, antiviral and photocatalytic coatings [15,95,115–118]. The appropriate coating technique can be chosen by considering factors like feedstock characteristics, substrate properties, and desired coating attributes. Figure 2.9 illustrates the range of particle velocities and temperatures achievable during various thermal spray processes for different feedstock materials [110].

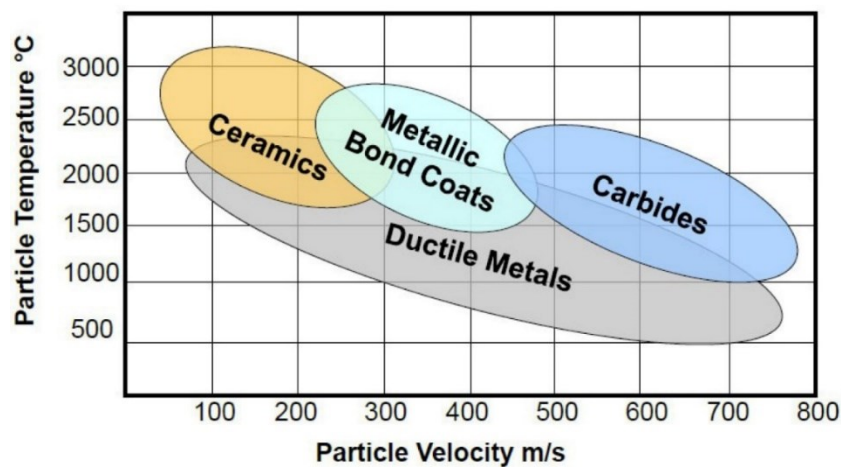


Figure 2.9 Overview of particle temperature versus particle velocity for various types of materials systems in thermal spray processes [110].

Among the thermal spray processes, atmospheric plasma spray (APS) is one of the widely used techniques for industrial applications. In APS, the heat source is a high-temperature, high-velocity plasma jet, where a mixture of gases (typically nitrogen and argon) is used to initiate the plasma [104]. The primary benefit of the APS process lies in its adaptability, allowing for the deposition of a diverse range of materials onto various substrate materials. Another significant advantage of this coating method is its cost-effectiveness compared to certain alternative surface engineering techniques [103,119]. Additionally, APS offers the advantage of minimal heat transfer to the substrate material; thereby, the characteristics of the substrate usually remain unaffected. However, In the APS process, the feedstock particle size cannot be smaller than around 10  $\mu\text{m}$ , and it normally is kept between 10 and 100  $\mu\text{m}$  to have a reasonable flowability of the powder [120] and prevent the clogging issues in the powder feeding system [47,121,122]. Therefore, submicron-sized and nanosized feedstock generally used to produce nanostructured coatings cannot be used in APS. Larger feedstock particles result in the generation of thicker splats in the coating. Thus, with this technique, typically macro-structured coatings can be produced, and the minimum thickness of the coatings that can be obtained with the APS method would also be limited. In addition to the issues mentioned above, very fine particles cannot easily penetrate the plasma jet. This implies that fine particles could potentially traverse the cooler segments of the plasma jet, encountering diminished heat exchange. Consequently, employing the APS technique to spray submicron-sized particles mandates a carrier gas flow rate reaching up to 80 slm. This elevated flow rate significantly disrupts and considerably reduces the temperature of the plasma jet [122,123]. Following that, the suspension plasma spray (SPS) process was developed to address the limitations associated with the APS technique.

## **2.10 Suspension Plasma Spray (SPS) Process**

The SPS process offers several advantages over conventional techniques, such as the direct deposition of very fine feedstock particles that can be used to produce thin (compared to the coatings obtained by conventional thermal spray methods) and nanostructured coatings, which are important for the membrane structure and performance [97]. The utilization of exceptionally fine feedstock particles enables thinner coatings with finer pores. In the SPS coatings, porosity originates from diverse factors, including gaps between columns, voids between splats, cracks, and deformed semi-melted and unmelted particles [15,124–126].

SPS is an emerging thermal spray technology that can produce thin and nanostructured coatings by employing a feedstock of particles ranging from submicron to nanometer size in diameters suspended in a solvent [127,128]. The typical solvents used in the SPS process include water or ethanol [129]. Figure 2.10 shows a schematic of the SPS process.

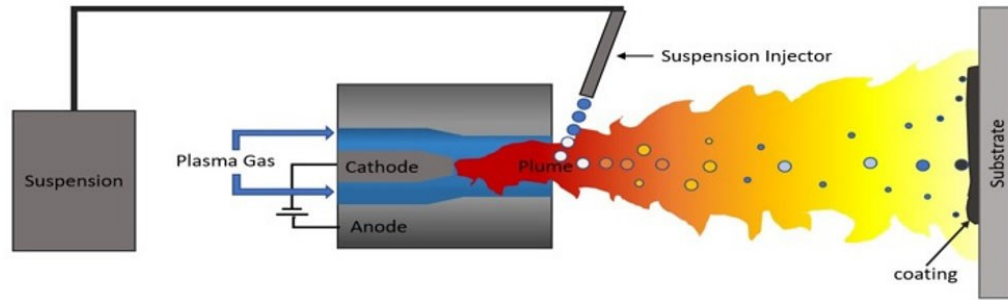


Figure 2.10 Schematic of The SPS system. Reproduced from [47].

In the SPS process, the suspension can be injected into the plasma jet either radially or axially. The evolution of the inflight particles in the SPS process from entering the plasma up to the formation of the splats on the substrate has been depicted in Figure 2.11. When the suspension hits the plasma, the droplets experience stages of successive breakup and atomization. Subsequently, the heat from the plasma causes the solvent enveloping the particles to evaporate, leaving behind agglomerates of the feedstock particles. These agglomerates, comprising fine particles, may undergo partial or complete melting or even remain unmelted based on their thermal and spatial history. Upon reaching the substrate, the molten and partially molten particles flatten to form splats [97,127]. Furthermore, in the SPS process, the standoff distance, denoting the space between the plasma torch exit and the substrate, is notably reduced compared to conventional thermal spray techniques. This reduction is a consequence of utilizing smaller feedstock in the SPS process. While these fine particles experience rapid acceleration and heating, they also undergo swift deceleration and cooling [130].

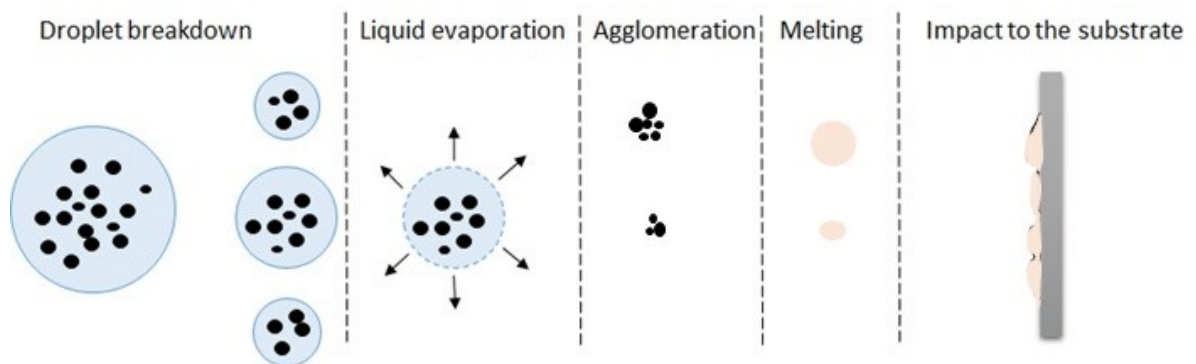


Figure 2.11 The evolution of the suspension and inflight particles during the SPS process. Reproduced from [97].

In thermal spray processes, including SPS, the coating structure is controlled by the feedstock and the process variables, defined as the spray parameters. In the literature, around 50 parameters have been reported to play a potential role in governing APS and SPS procedures, which, in turn, can define the coating structure [127,130,131]. This suggests that plasma spraying methods, including SPS, have the potential to generate a diverse array of microstructures and coatings.

Figure 2.12 summarizes a series of coating microstructures that can be obtained by the SPS process. These microstructures can vary from fully dense coatings [132] to porous coatings with vertical cracks, porous coatings with various forms of columnar features that appear in the form of bumps on the surface [133], and uniformly porous coatings [134]. This versatility allows producing coatings suitable for a wide range of applications, including finely porous coatings that could be used for filtration.

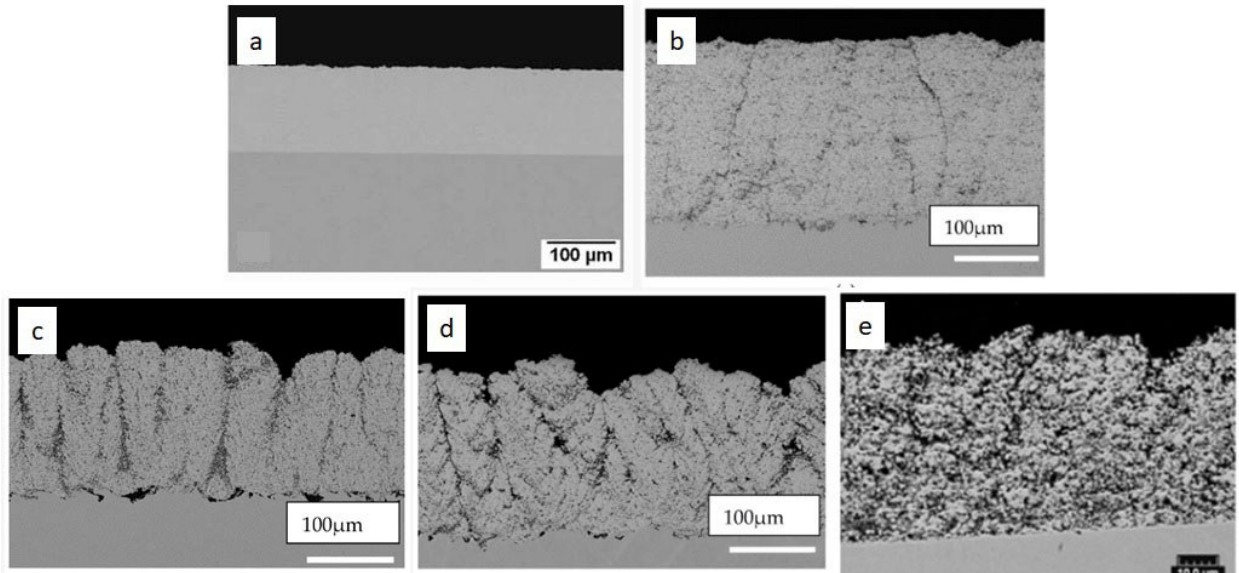


Figure 2.12 The various types of microstructures typically obtainable using the SPS process, including (a) Fully dense [132], (b) Porous with vertical cracks [133], (c & d) porous with columnar features [133], and (e) uniformly porous [134] microstructures.

## 2.11 Membranes Produced with Thermal Spray Processes

Coatings generated by thermal spray methods have been used in many industries, such as aerospace, automotive, biomedical, steel, pulp, and paper [104]. However, a limited number of studies investigated the capacity of this group of techniques for ceramic membrane manufacturing.

Thermal spray processes have been used to produce gas separation membranes. Gas separation layers need to be dense to decrease gas leakage and have ionic and electronic conductivity [121]. Kulkarni et al. used the APS and vacuum plasma spray (VPS) processes to produce dense YSZ gas separation membranes [135]. Fan et al. used the SPS process to generate dense lanthanum strontium cobalt ferrite membranes for oxygen separation with very low gas leakage. They were able to increase the density by optimizing the standoff distance and the plasma torch power [121].

Producing porous membrane-type layers as electrodes for solid oxide fuel cells (SOFC) using thermal spraying has also been the subject of investigation in several works. Ma et al. generated multiple layers in solid oxide fuel cells (SOFCs) using both APS and solution precursor plasma spray (SPPS) techniques. They applied the APS method to create a porous cathode layer, functioning as an oxygen/air electrode, where the macropores were due to the unmelted and semi-melted particles and the micropores were due to gas entrapment. They also

produced a highly porous anode layer with submicron-sized pores by the SPPS process, where, unlike the APS layer, the pores had a spherical form [136]. Hui et al. fabricated metal-supported solid oxide fuel cells using thermal spray methods, where the porous anode layer was deposited by the SPS process [137]. Fan et al. deposited a porous cathode layer for SOFCs by employing the SPS process, where They used a pore forming agent (carbon black) to enhance the formation of pores [138].

Furthermore, some research has focused on producing filtration membranes with thermal spray techniques. Madaeni et al. used wire arc spraying to produce relatively thick (0.5mm to 1.25mm) porous stainless-steel membranes with an average pore size of 5 to 7  $\mu\text{m}$  shown in Figure 2.13. They were able to increase the porosity by optimizing the standoff distance and reported an increase in the rejection efficiency of the membranes by increasing the thickness [43].

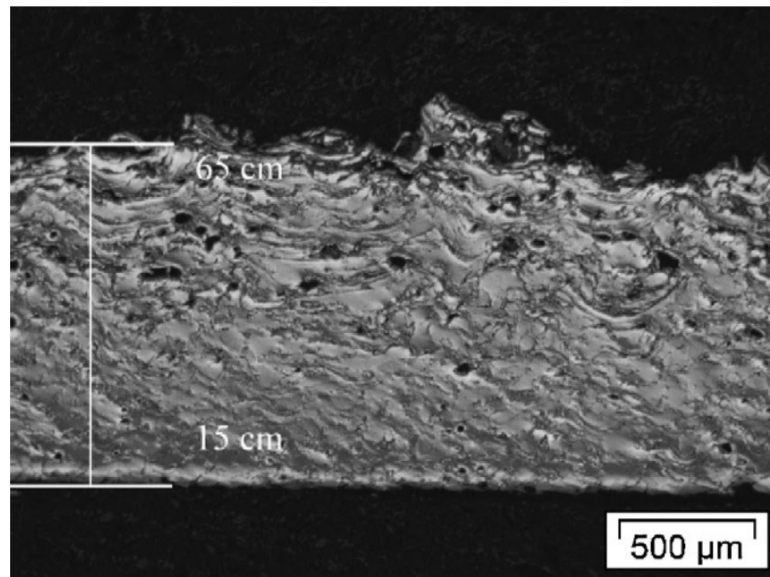


Figure 2.13 Metallic filtration membrane produced by wire arc spraying showing the influence of the standoff distance changing from 15 to 65 cm on the porosity in the membrane [43].

Tung et al. used APS to generate  $\text{Al}_2\text{O}_3/\text{Ni-Cr}$  cermet microfiltration membranes, where Ni-Cr powder was used to enhance the binding between the  $\text{Al}_2\text{O}_3$  particles. They obtained a variety of pore sizes and water flux of 0.2–0.4  $\mu\text{m}$  and 100-500  $\text{L m}^{-2} \text{h}^{-1} \text{bar}^{-1}$ , respectively, at various standoff distances and torch powers [139]. Lin et al. employed the APS to fabricate photocatalytic microfiltration  $\text{TiO}_2$  membranes with a pore size of 0.35  $\mu\text{m}$  and water flux of 2300  $\text{L m}^{-2} \text{h}^{-1}$ , shown in Figure 2.14. They also characterized the fouling mechanism of the membranes for various model foulants [140].

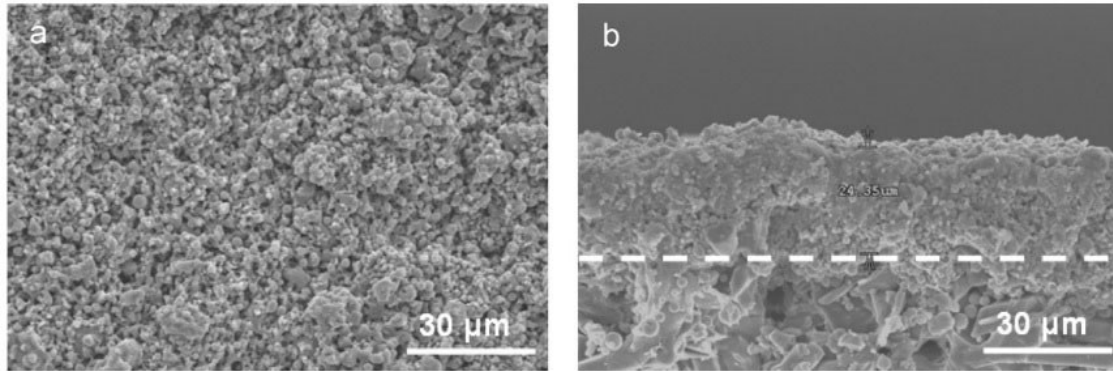


Figure 2.14 The SEM micrographs of (a) surface and (b) cross-section of  $\text{TiO}_2$  membranes produced with the APS process [140].

Ramakrishnan et al. used APS and combustion flame spray (CFS) processes to produce  $\text{Al}_2\text{O}_3$  microfiltration membranes with pore size and porosity in the range of 0.8-2.6  $\mu\text{m}$  and 8.5-30%, respectively (Figure 2.15). This study investigated the influence of the type of feed used in the CFS process and the impact of spray distance and plasma power in the APS process on the pore size and porosity of the membranes. They also showed that the water flux decreases by increasing the thickness of the membranes. A pure water flux of around 5500  $\text{L m}^{-2} \text{h}^{-1}$  was obtained at the lowest membrane thickness [42].

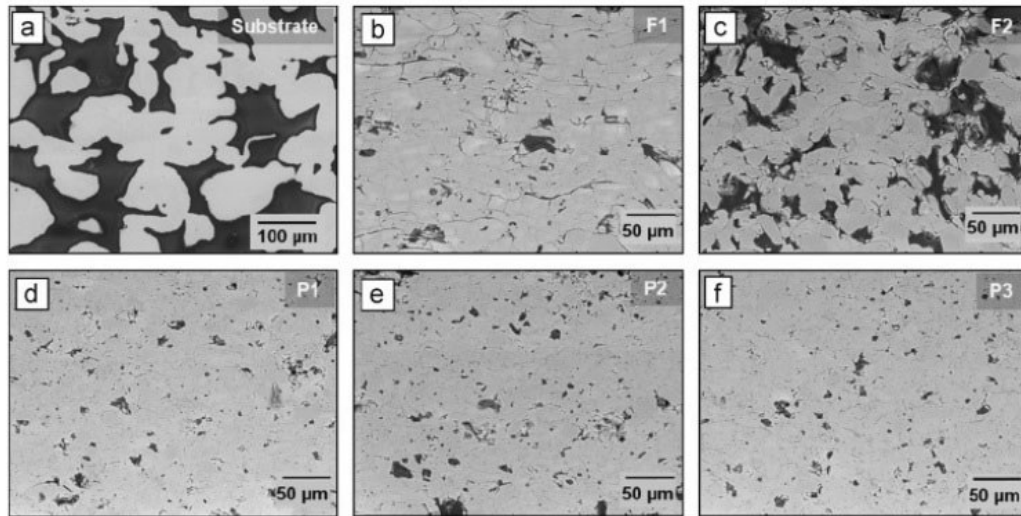


Figure 2.15 SEM images of the (b) CFS membrane with powder feed, (c) CFS membrane with rod feed, and (d-f) APS  $\text{Al}_2\text{O}_3$  membranes [42].

Tung et al. reported the fabrication of an  $\text{Al}_2\text{O}_3$  microfiltration membrane, where the porosity was increased by using water-filled porous substrates. The origin of the pores in the case of the dry substrate was identified as the inter-splat cracks. On the other hand, in the case of the wet substrate, the pores resulted due to the vapor pressure dispersing the melted particles that formed splats on the substrate. The surfaces of the membranes produced on dry and wet substrates, as well as the schematic of the pore formation due to the hot vapor pressure, are shown in Figure 2.16. [141].

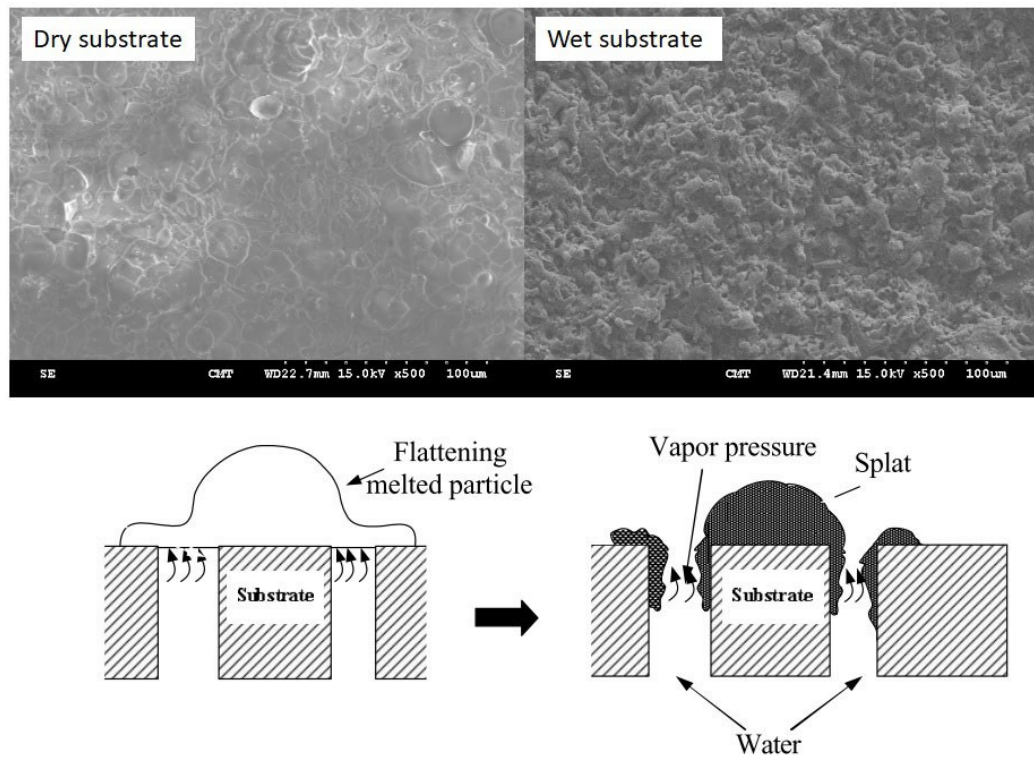


Figure 2.16 (Top) The surface morphologies of membranes sprayed on dry and wet substrates, and (bottom) the influence of high temperature water vapor induced mechanism in splitting the splats [141].

Islam et al. used the APS process to fabricate YSZ filtration. After optimizing the process parameters, including the plasma power, plasma gas flow rate, powder feed rate, and standoff distance, they produced membranes with 30% porosity and a pore size of  $< 2\mu\text{m}$ . They reported an inverse relation between the membrane thickness and the water flux, with a maximum flux of around  $400 \text{ L m}^{-2} \text{ h}^{-1} \text{ bar}^{-1}$ , and the salt rejection efficiency of the membranes was characterized [44].

Due to the fabrication process, the pores in porous membranes produced with conventional thermal spray techniques mainly result from interlamellar pores, intra-splat cracks, and gas entrapment, and in a lower degree, from the retained unmelted feedstock [42][35]. Alebrahim et al. used the SPS process to produce a photocatalytic microfiltration  $\text{TiO}_2$  membrane with around 15% porosity and a pore size under  $0.2 \mu\text{m}$ , which was relatively close to the feedstock particle size. The unique microstructure, shown in Figure 2.17, resulted from the pile-up of unmelted and re-solidified particles in a matrix of fully melted splats, and a water flux of around  $480 \text{ L m}^{-2} \text{ h}^{-1} \text{ bar}^{-1}$  was obtained. The main origin of the pores was the space among the unmelted and resolidified particles within the structure [15].

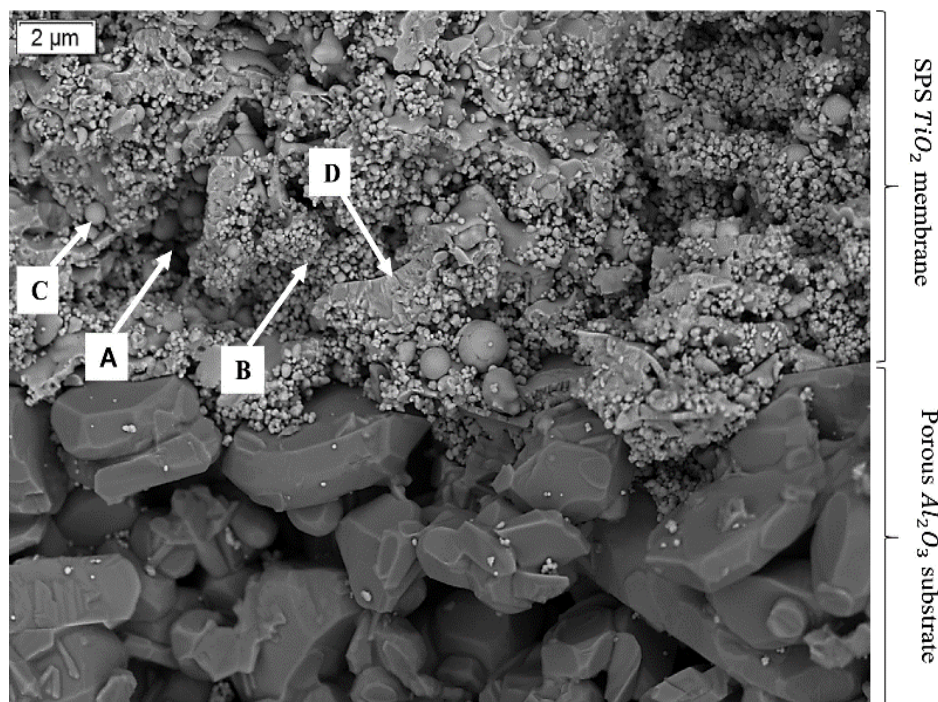


Figure 2.17 SEM micrograph of the fractured cross-section of photocatalytic SPS TiO<sub>2</sub> filtration membrane including large pores (A), unmelted particles (B), re-solidified particles (C), and fully melted zones (D) [15].

## 2.12 Photocatalytic Property in the Thermal-Sprayed TiO<sub>2</sub> Coatings

As stated earlier, the pivotal role of photocatalytic reactivity in mitigating membrane fouling by enhancing the degradation of organic contaminants is widely recognized. In this regard, TiO<sub>2</sub> stands out as one of the most frequently employed photocatalysts to achieve this specific objective. The thermal spray process has been used to investigate the production of TiO<sub>2</sub> coatings with photocatalytic properties in many studies. Through this set of fabrication methods, the catalyst particles naturally form an immobilized layer on the substrate's surface by a one-step manufacturing procedure.

As mentioned earlier, the efficiency of the photocatalytic activity of TiO<sub>2</sub> is commonly linked to its anatase proportion. Various literature addressing the photocatalytic efficiency of thermally sprayed TiO<sub>2</sub> coatings has similarly shown increased photoreactivity by increasing the anatase content within the coatings [117,142]. Maintaining the anatase phase within the high-temperature plasma poses a notable challenge in thermal spray techniques. Various research endeavors have been undertaken to generate TiO<sub>2</sub> coatings using SPS with the primary objective of retaining the anatase phase in the coating. This specific TiO<sub>2</sub> phase is considered crucial for effective photocatalytic applications [97,143,144]. In contrast to conventional thermal spray methods that generally utilize dry powders as feedstock, in the SPS processes that involve water as a solvent, the anatase phase from the original powder can be more likely to be preserved within the coating due to the relatively high vaporization enthalpy of water [117,145]. Nonetheless, it's worth noting that the literature also points to additional factors influencing the photocatalytic behavior of thermally sprayed coatings, supported by the evidence where thermal-sprayed rutile coatings have displayed photocatalytic activity [97,146,147]. The efficiency of the photocatalytic activity of TiO<sub>2</sub> is controlled by light absorbance, surface hydroxylation, electron-

hole separation, and reactive surface area [80]. Literature suggests that the photocatalytic property of SPS TiO<sub>2</sub> coatings could be influenced by characteristics such as the level of porosity, surface roughness, and thickness of the coatings [97,100]. Moreover, the presence of rutile in thermally sprayed coatings might enhance photocatalytic performance by hindering electron-hole recombination, as previously indicated [84,148].

Additionally, during the plasma spraying process, sub-stoichiometric titanium dioxide (TiO<sub>2-x</sub>) with oxygen vacancies is generated in the coating by heating the feedstock to high temperatures in a low oxygen pressure or a hydrogen environment [97,149,150]. Consequently, the rather white color of the TiO<sub>2</sub> powder turns to various shades of grey color in the coatings resulting in an enhanced absorbance in the visible spectrum. When hydrogen interacts with TiO<sub>2</sub>, oxygen vacancies and electrons are generated. Following that, Ti<sup>3+</sup> ions can be formed by entrapment of electrons in the lattice sites of Ti<sup>4+</sup> ions [151]. The darker color appears due to a higher concentration of Ti<sup>3+</sup> ions [100,152]. With oxygen vacancies in the lattice of TiO<sub>2</sub>, electronic states below the conduction band are created. Thus, instead of under UV light, the electrons can get excited at lower photon energies of the visible illumination [101].

## Chapter 3 TiO<sub>2</sub> Photocatalytic Ultrafiltration Membrane Developed with Suspension Plasma Spray Process

### **Preface**

As mentioned in previous sections, the primary origin of the pores in SPS membranes was identified as the presence of the unmelted and resolidified particles of the feedstock powder in the membrane structure. It was also observed that due to the unmelted particles in the structure, the average pore size in the membrane was very close to the size of the starting sub-micron-sized powder particles.

The main objective of this work was to investigate the possibility of using SPS to customize a porous microstructure with nanosized pores (smaller than 100 nm), in the range of ultrafiltration membranes (2-100 nm) with improved water permeability.

**Abstract:** The suspension plasma spray process was used to fabricate photocatalytic ultrafiltration membranes for potential water and wastewater treatment applications. An aqueous suspension of 30 wt.% titanium dioxide with an average individual particle size of around 30 nm was used as feedstock material. The spray parameters, such as suspension solid content, suspension feed rate, and spray distance, were optimized using an Ar/H<sub>2</sub> plasma to retain a fraction of unmelted feedstock nanoparticles as the source of fine pores in the membrane microstructure. The microstructure, porosity, phase composition, and pure water permeability of the membranes were characterized comprehensively. The average pore size of the membrane was around 40 nm, which was very close to the particle size of the pristine titanium dioxide powder. The membranes demonstrated a high water permeability between 2000 and 7200 L m<sup>-2</sup> h<sup>-1</sup> bar<sup>-1</sup>, which was inversely proportional to the thickness. They also exhibited significant photocatalytic activity under visible light.

**Keywords:** suspension plasma spray; ceramic membrane; ultrafiltration; titanium dioxide; nanoparticles; nanostructured agglomerates; photocatalyst

### 3.1 Introduction

Filtration technologies based on membrane separation are becoming popular by offering a low-cost, sustainable, and highly energy-efficient solution in water and wastewater treatment [153].

Currently, polymeric membranes mainly dominate the liquid separation market. However, ceramic microfiltration (MF) and ultrafiltration (UF) membranes are gaining emerging commercial attention due to their significant mechanical, thermal, and chemical stability, hydrophilic nature, lower fouling, ease of cleaning, stable long-term flux, and relatively higher permeability compared to polymer membranes [50]. UF membranes, with a pore size of 1-100 nm, are one of the most widely used technologies owing to the ability to remove contaminants with molecules larger than 10 nm at low applied pressures of around 0.1-5 bars through a sieving mechanism [41,154–156]. Ceramic membranes are mainly synthesized in a multi-layered asymmetric structure, including a thick, porous substrate for mechanical support, an intermediate layer to reduce the pore size, and a top filtration layer [157]. Although ceramic membranes demonstrate a reliable performance, their application in water treatment is still limited due to the high costs mainly linked to the multi-step fabrication techniques, including shaping, sintering, and surface modification [50,158]. Recently, authors introduced the suspension plasma spray (SPS) process, an emerging thermal spray process, as a novel single-step fabrication method for MF membranes [15]. In that work, the space between the unmelted submicron-sized particles was presented as the source of porosity in the membrane structure, and the pore size was very close to the feedstock powder particle size [15]. In the SPS process, a feedstock of sub-micron sized to nano-sized particles suspended in a liquid allows the deposition of thin nano-structured coatings [97]. Using a nano-sized feedstock would be advantageous in inducing agglomerates of

unmelted nano-sized particles in the coating [159], which could be the source of nano-sized pores in the range of ultrafiltration. Other advantages of the SPS process to the membrane technology include high scalability, high deposition rate, relatively low operating cost, rather low thermal input into substrates, and the possibility of deposition of the membrane layer on various surfaces, including porous ceramic and metallic substrates [97,135]. The potential advantages of the SPS process compared to conventional manufacturing methods of ceramic membranes and conventional thermal spray (TS) methods were described elsewhere [15]. Typically, feedstock powders finer than 10  $\mu\text{m}$  cannot be thermally sprayed with conventional technologies due to clogging the feeding system and destabilizing the plasma jet [160]. However, conventional TS processes such as atmospheric plasma spray (APS) and high-velocity oxy-fuel (HVOF) have been used to produce nano-structured coatings for structural, biomedical, and thermal barrier applications, using agglomerated sintered feedstock powders in the range of over 10  $\mu\text{m}$  [160]. Recently, agglomerates of submicron to nano-sized powders, produced by the ball milling process, have also been used to deposit nanocrystalline high entropy alloy coatings and thermal barrier coatings using APS and HVOF processes [161,162]. However, these coatings were produced with a low degree of porosity, which is not suitable for filtration [160–162].

Titanium dioxide ( $\text{TiO}_2$ ) nanoparticles in a suspension are one of the most frequently used photocatalysts employed in water treatment applications because of their low cost, availability, and thermal and chemical stability [69,163–165]. When  $\text{TiO}_2$  absorbs photons with energies more than its bandgap energy (3.2 eV), the excitation of an electron from the valence band to the conduction band results in the generation of an electron-hole pair which further produces oxidizing radicals capable of degrading organic pollutants into water and  $\text{CO}_2$  [82]. Immobilizing  $\text{TiO}_2$  particles in the form of a membrane layer on a porous substrate may reduce the efficiency of the photocatalyst by decreasing the active surface area. However, it may also reduce the complexity and maintenance costs of the water treatment system by eliminating the post-filtration process to separate the photocatalyst particles [69]. The photocatalytic property in a filtration membrane has been shown to improve the separation performance by enhancing the antifouling property [71]. However, the large bandgap energy of  $\text{TiO}_2$  requires UV illumination to activate its photocatalytic property, which requires relatively high energy consumption and adapted safety measures in interior applications.

Moreover, external applications of  $\text{TiO}_2$  as a photocatalyst are of limited efficiency since more than 52% of the sunlight is visible light while only around 3% is UV [91]. Thus, developing active photocatalytic membranes under UV and visible light could lead to a more efficient, sustainable filtration process. The SPS method allows the deposition of sub-stoichiometric  $\text{TiO}_{2-x}$  coatings due to the inducement of oxygen vacancies and  $\text{Ti}^{3+}$  ions in the coating. Consequently, the SPS coating shows photocatalytic activity under visible light due to narrowing the bandgap, which allows the excitation of photogenerated electrons and holes under lower photon energies [95,166]. Miao et al. reported around 1.3 times higher photocatalytic degradation of rhodamine B in  $\text{TiO}_{2-x}/\text{TiO}_2$  composite compared to  $\text{TiO}_2$  under visible light. In that work, the  $\text{TiO}_{2-x}/\text{TiO}_2$  composite was produced by a hydrothermal method [167].

The considerable attention to ceramic filtration technology, including UF membranes, requires exploring new fabrication methods [50]. In this work, the novel SPS process for

membrane fabrication [15] was used to produce membranes with nano-sized pores to extend the application to the range of UF. Furthermore, the process parameters were optimized to preserve a significant fraction of the pristine TiO<sub>2</sub> agglomerates of nanoparticles in the membrane microstructure as the origin of nano-sized pores. In addition, microstructural characteristics and the photocatalytic activity of the membranes under both UVA and visible illumination were investigated, and the influence of membrane thickness on pure water permeability was studied.

### 3.2 Materials and Methodology

#### 3.2.1 Suspension Preparation

A 100 wt.% anatase TiO<sub>2</sub> powder (Pi-Kem Co, Tamworth, UK) was used to prepare the aqueous suspensions. The size and morphology of TiO<sub>2</sub> powder nanoparticles were examined using a scanning electron microscope (FESEM Hitachi Regulus 8230, Mississauga, ON, Canada) that was set in the secondary electron mode. Figure 3.1a shows the morphology of TiO<sub>2</sub> powder in the feedstock. The nanoparticles formed agglomerates, where the average diameter of the individual TiO<sub>2</sub> powder particles was measured to be  $27 \pm 10$  nm.

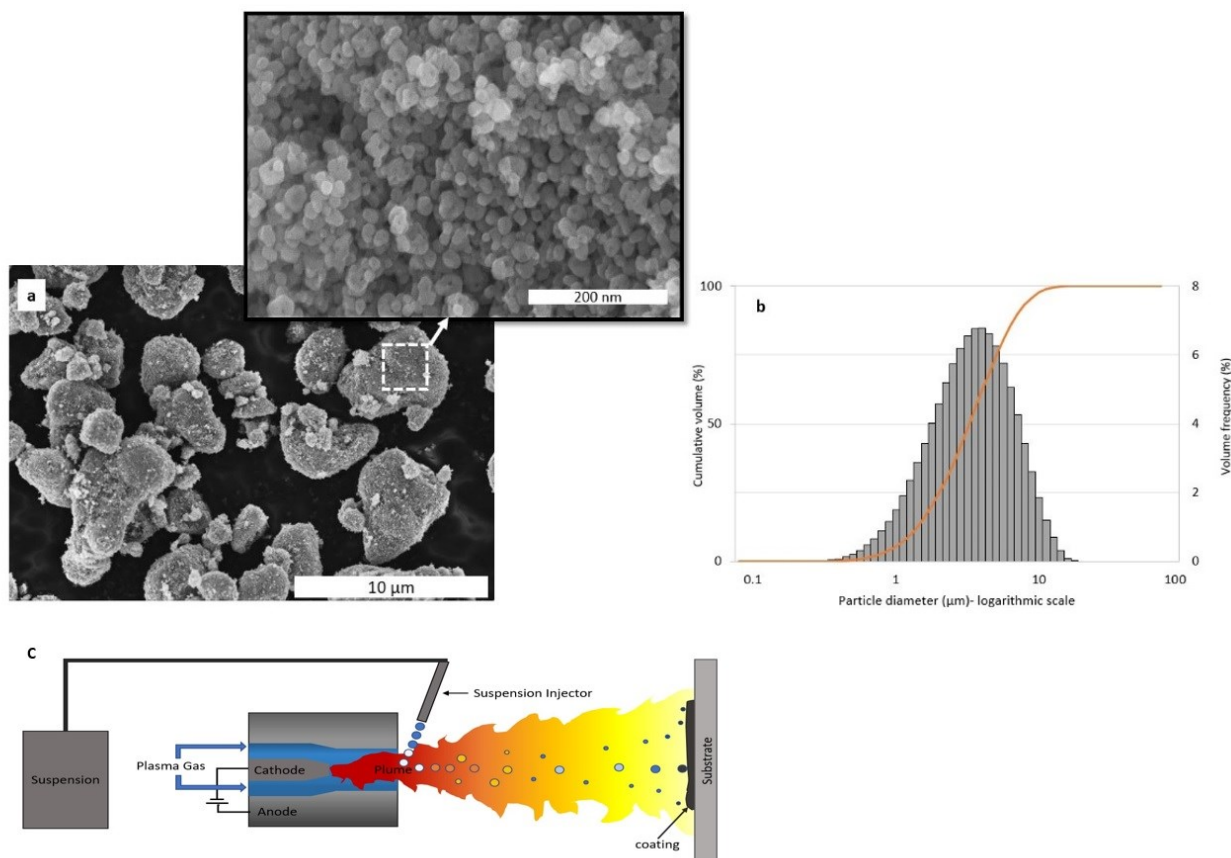


Figure 3.1 (a) SEM micrograph of the TiO<sub>2</sub> powder, (b) agglomerate size distribution of the TiO<sub>2</sub> aqueous suspension, (c) schematic of the 3MB suspension plasma system.

Figure 3.1b shows the agglomerate size distribution of the TiO<sub>2</sub> suspension measured by a Spraytec system (Malvern Instruments, Malvern, UK) having  $d_{10} = 1.4 \mu\text{m}$ ,  $d_{50} = 3.1 \mu\text{m}$ , and  $d_{90} = 6.3 \mu\text{m}$ .

For the SPS coating deposition process, suspensions of TiO<sub>2</sub> powder were prepared by dispersion and homogenization of 20 wt.% and 30 wt.% solid content in 80 wt.% and 70 wt.% distilled water, respectively. The suspensions were stabilized by adding 3 wt.% (corresponding to the weight of TiO<sub>2</sub>) sodium tripolyphosphate (Sigma-Aldrich Chemicals, Oakville, ON, Canada) and adjusting the pH to around 10 by adding NaOH (Sigma-Aldrich Chemicals, Oakville, ON, Canada). The suspensions were prepared by adding the TiO<sub>2</sub> nanoparticles to water agitated with a magnetic stirrer (Huanghua faithful instrument Co., Huanghua, China) and a probe sonicator (QSonica, LLC, Newtown, CT, US).

### 3.2.2 Plasma Spraying

The SPS process was utilized to fabricate the membranes in this study. The coating deposition process was carried out by a 3 MB plasma torch (Oerlikon Metco, Wohlen, Switzerland) with Ar/H<sub>2</sub> plasma. A schematic of the SPS system is shown in Figure 3.1c. Details of the suspension feeding system were described elsewhere [15]. The suspension flow rate and density remained relatively stable during the deposition process. The density of the suspensions with 20 wt.% and 30 wt.% solid content was measured as 1.165 g/mL and 1.273 g/mL, respectively.

The plasma torch operation parameters are summarized in Table 3.1.

Table 3.1 Plasma torch operation parameters.

Ar (LPM)	H <sub>2</sub> (LPM)	Current (A)	Voltage (V)	Power (kW)	Torch Velocity (m/s)
60	5	500	60	30	1

According to Table 3.2, a preliminary test matrix was designed to optimize the other spray parameters for the desired photocatalytic filtration membranes

Table 3.2 Test matrix for the optimization process.

Sample	Solid content (Wt. %)	Suspension feed rate (mL/min)	Spray distance (mm)	Injector diameter (mm)	No. of passes
1	20	45	50	0.254	30
2	30	45	50	0.254	24
3	20	20	50	0.15	29
4	20	20	40	0.15	30

As previously shown, the presence of unmelted particles in the membrane structure plays an essential role in the formation of pores in the membrane structure [15]. In addition, it is reported that the quantity of anatase improves the photocatalytic activity of the TiO<sub>2</sub> coatings [117]. Furthermore, a finely porous coating with a uniform microstructure to increase the water permeability of the produced membranes was desired. Thus, the spray parameters were varied to increase the number of unmelted particles as the primary source of fine pores and anatase content in the coatings. For this purpose, we compared the microstructure of the coatings at two levels of solid content, suspension feed rate and spray distance.

Dense 304 stainless steel substrates with the dimension of 25 × 25 × 5 mm<sup>3</sup> were used for the optimization process. Before the coating deposition process, the dense steel substrates were grit-blasted with Al<sub>2</sub>O<sub>3</sub> particles (80 grit) and cleaned by sonication in acetone. The resulting surface roughness was measured as  $R_a = 3.5 \pm 0.5 \mu\text{m}$ . Further details about the optimization process are discussed later in Section 3.3.1.

In this work, the term "membrane" refers to the optimized coatings sprayed on porous stainless steel substrates. The membranes were sprayed on porous 316 L stainless steel discs with a diameter of 38 mm and thickness of 1.6 mm designed for filtering particles with sizes down to 2 μm (9446T35, McMaster-Carr, Elmhurst, IL, US). Porous substrates were used without grit blasting. The surface roughness of porous substrates was  $R_a = 9.6 \pm 1 \mu\text{m}$ . The temperature of the substrates was monitored with an infrared camera (A310, FLIR, Wilsonville, OR, US). The average substrate/coating temperature during the spray process was around 300 °C.

### 3.2.3 Characterization

The surface roughness of the samples was measured with a confocal laser microscope (LEXT OLS4000 Olympus, Toronto, ON, Canada), and the arithmetic average surface roughness ( $R_a$ ) has been reported. In addition, the morphology of the powder, as well as the polished and fractured cross-sections of the samples, was observed with an optical microscope (VHX-S550E, Keyence Corporation, Osaka, Japan) and a field emission scanning electron microscope (FESEM JSM 7600TFE, JEOL, Tokyo, Japan, and FESEM Hitachi Regulus 8230, Mississauga, ON, Canada).

The phase analysis of the samples was carried out by the X-ray diffraction (XRD) technique (X'Pert pro-MRD, Malvern PANalytical, Malvern, UK) in a range of 20–80° with Cu K $\alpha$  radiation and a step size of 0.02°. HighScore Plus software (Malvern PANalytical, Malvern, UK) was used to quantify the phase content by Rietveld refinement analysis.

The porosity of the samples was measured with a mercury intrusion porosimeter (MIP) (Autopore IV, Micrometric, Norcross, GA, US) on free-standing coatings deposited on 15 × 25 × 5 mm<sup>3</sup> flat dense 304 stainless steel substrates. For MIP analysis, the coatings were separated from the substrate by mechanically bending the substrate.

The optical absorption spectra of the feedstock powder and as-sprayed membrane were obtained using a UV–Vis–NIR spectrometer (Lambda 750, Perkin Elmer, Waltham, MA, USA). The measurements were carried out in the range of 340–600 nm with a resolution of 1 nm. Bandgap energies of the coatings were measured according to Equations. (3.1), and (3.2) [82,168]:

$$(\alpha E_{\text{photon}})^n = A(E_{\text{photon}} - E_g) \quad (3.1)$$

$$E_{\text{photon}} (\text{eV}) = h\nu = \frac{1239}{\lambda} \quad (3.2)$$

Where  $E_{\text{photon}}$  is the photon energy at each wavelength  $\lambda$ ,  $\alpha$  is the absorption coefficient,  $A$  is the slope of the linear region in plot  $(\alpha E_{\text{photon}})^n - E_{\text{photon}}$ ,  $E_g$  is the bandgap energy obtained from extrapolation of  $E_{\text{photon}}$ , to  $\alpha = 0$ , and  $n$  is the characteristic of the optical transition process type. The value of  $n$  for direct and indirect bandgap equals 2 and 0.5, respectively.

### 3.2.4 Membrane Performance

A dead-end stirred cell (Sterlitech, HP4750, Auburn, WA, US) was used to determine the water permeation of the membranes using deionized (DI) water. Water permeate flux was calculated according to Equation (3.3) [154]:

$$J = \frac{V}{B \times t} \quad (3.3)$$

Where  $J$  is the permeation flux ( $\text{L m}^{-2} \text{h}^{-1}$ ),  $V$  is the permeation volume (L),  $t$  is the permeation time (h), and  $B$  is the effective surface area of the membrane ( $\text{m}^2$ ). The slope of the line in the permeate flux-pressure plot corresponds to the pure water permeability of the membrane in ( $\text{L m}^{-2} \text{h}^{-1} \text{bar}^{-1}$ ).

In this work, the photocatalytic performance of the samples was evaluated by measuring the discoloration of methylene blue (MB) (Sigma- Aldrich Chemicals, Oakville, ON, Canada) under both UVA (Fisher Scientific, Ottawa, ON, Canada) and visible light irradiation. Two UVA ( $\lambda = 365 \text{ nm}$ ) lamps with a power of 15 W each provided an irradiance of  $0.408 \text{ mW cm}^{-2}$ . Visible light irradiation was provided with two xenon arc lamps with the power of 35 W, each with an irradiance of  $2.16 \text{ mW cm}^{-2}$ . A UV cut-off filter (54056, Edmund Optics, Barrington, NJ, USA) was used to measure photocatalytic performance under visible light. The experiment was carried out under a fume hood at room temperature.

A schematic of the photoreactor is shown in Figure 3.2. In both UVA and visible light illumination conditions, the samples were placed in a test cell consisting of a Petri dish containing around 30 mL of MB solution with an initial MB concentration of  $2 \times 10^{-5} \text{ M}$ , and the distance between the lamps and the top of the samples was adjusted to around 3 cm. The solution samples taken every 30 minutes were used to monitor the MB degradation (discoloration). The MB discoloration degree was analyzed with UV-vis spectrophotometer (Cary 8454, Agilent, Mississauga, ON, Canada) at the fixed wavelength of 664 nm corresponding to the maximum absorbance of MB. The test cell was cooled using a water bath and an electric fan.

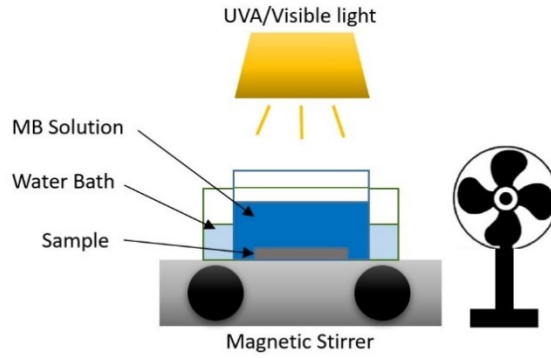


Figure 3.2 Schematic of the photoreactor.

Each sample was immersed in MB solution in the dark for 60 min before exposure to UVA or visible light illumination to complete the adsorption equilibrium [169].

The variation in MB concentration with time is determined by assuming a first-order kinetic equation, which applies to low concentrations [146], according to Equation (3.4):

$$-\frac{dc}{dt} = kC \quad (3.4)$$

which after integration results in Equation (3.5):

$$\ln \frac{C_0}{C} = kt \quad (3.5)$$

Where  $C$  is the MB concentration (ppm) at each time interval,  $C_0$  its initial concentration (ppm) after residence time in the dark,  $t$  is the irradiation time (min), and  $k$  is the apparent rate constant of photocatalytic activity ( $\text{min}^{-1}$ ).

The MB degradation efficiency was determined with Equation. (3.6):

$$\text{degradation (\%)} = \left(1 - \frac{C}{C_0}\right) \times 100 \quad (3.6)$$

### 3.3 Results and Discussion

#### 3.3.1 Optimization Process

In the SPS process, several spray parameters may influence the quality of the coatings. For the filtration application, coatings with high porosity are desired. As mentioned earlier, in an SPS membrane, the porosity depends on the presence of unmelted particles in the structure [15]. Therefore, in this work, the spray parameters chosen to optimize the portion of melted and unmelted particles were the suspension solid content, suspension feed rate, and standoff distance, according to Table 3.2. By increasing the suspension solid content and feed rate, we intended to

introduce more feedstock into the plasma jet to decrease the heat transfer to the inflight particles [170]. Mainly two goals were followed through this approach: i) to retain anatase from the feedstock powder in the membrane by avoiding the anatase to rutile transformation [117], and ii) to produce a significant proportion of fine pores in the membrane corresponding to the space between the unmelted nanoparticles. In addition, the standoff distance may influence the microstructure of the coating through the temperature and residence time of the particles in the plasma jet [171].

The main criteria for choosing the optimized coating for the membrane were homogeneity of the microstructure, porosity, low surface roughness, anatase quantity, and photocatalytic performance. The importance of these parameters is discussed in the following paragraphs.

To study the microstructural homogeneity and distribution of pores in the coatings, which may result in a higher permeation flux and a uniform filtering performance [20], the polished cross-sections of the produced coatings were analyzed by the optical microscope. Figure 3.3 shows the microstructure of the four coatings produced based on the spray parameters listed in Table 3.2. The detachment of the coating from the substrate observed in samples 1 and 2 is due to the low adhesion of these coatings to the dense substrate. However, detachment did not occur in the case of the membranes deposited on the porous substrates.

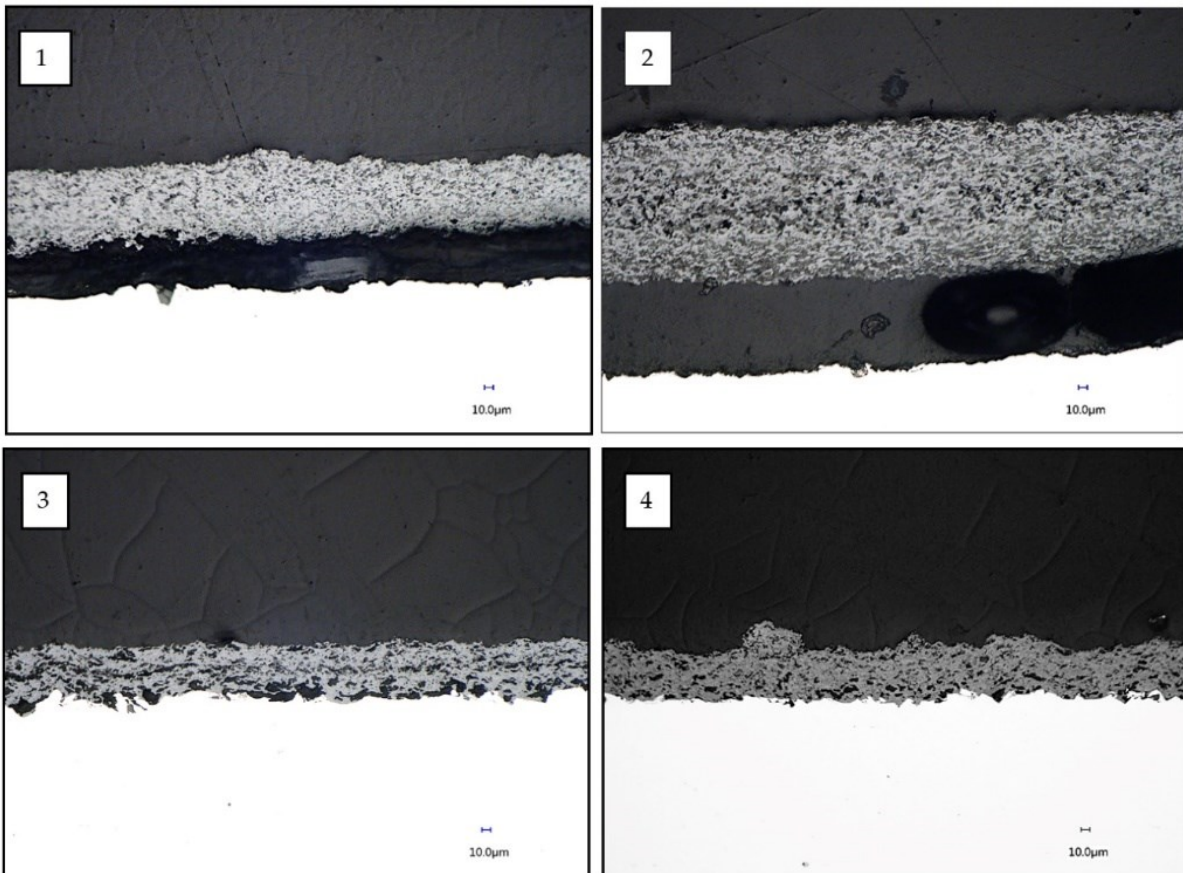


Figure 3.3 Optical microscope images of the cross-sections of samples 1, 2, 3 and 4 sprayed for the optimization process according to Table 3.2.

In samples 1 and 2, a relatively homogenous distribution of dark grey regions corresponding to the finer pores can be seen in the microstructure. However, in samples 3 and 4, the microstructure seems less porous, and a higher number of large pores (black regions) can be observed.

Fouling is one of the most challenging aspects of the membrane filtration process [20,172]. Among other parameters, lower surface roughness in the membranes could result in better fouling control through a more effective cleaning process. The surface roughness of samples 1, 2, 3, and 4 were obtained as  $R_a = 2.6 \pm 0.3 \mu\text{m}$ ,  $R_a = 2.4 \pm 0.1 \mu\text{m}$ ,  $R_a = 3.3 \pm 0.4 \mu\text{m}$ , and  $R_a = 5.3 \pm 0.7 \mu\text{m}$ , respectively. The bumps on the surface of sample 4 are common features observed in SPS coatings but were not desired for this work. A detailed description of the membrane microstructure is discussed in Section 3.3.2.1.

The phase composition of the samples in terms of the mass fraction is listed in Table 3.3, showing that the coatings contain both anatase and rutile phases.

*Table 3.3 The phase composition and anatase crystallite size of samples 1, 2, 3 and 4.*

<b>Sample</b>	<b>Anatase (%)</b>	<b>Rutile (%)</b>
1	50.5	49.5
2	52.4	47.6
3	40.3	59.7
4	33.4	66.6

As mentioned before, the photocatalytic performance of  $\text{TiO}_2$  was one of the main reasons for choosing this material for the filtration application. The photocatalytic property may assist in mitigating the membrane fouling, allowing a higher flux and decomposition of the organic contaminants [61]. For the optimization process, the photocatalytic activity of the samples was measured under UVA illumination for 90 minutes (Figure 3.4). The MB degradation after 90 min, the rate constant of the reaction ( $k$ ), and the correlation coefficient ( $R^2$ ) are summarized in Table 3.4. A blank test without coating showed very limited MB photolysis under UVA irradiation.

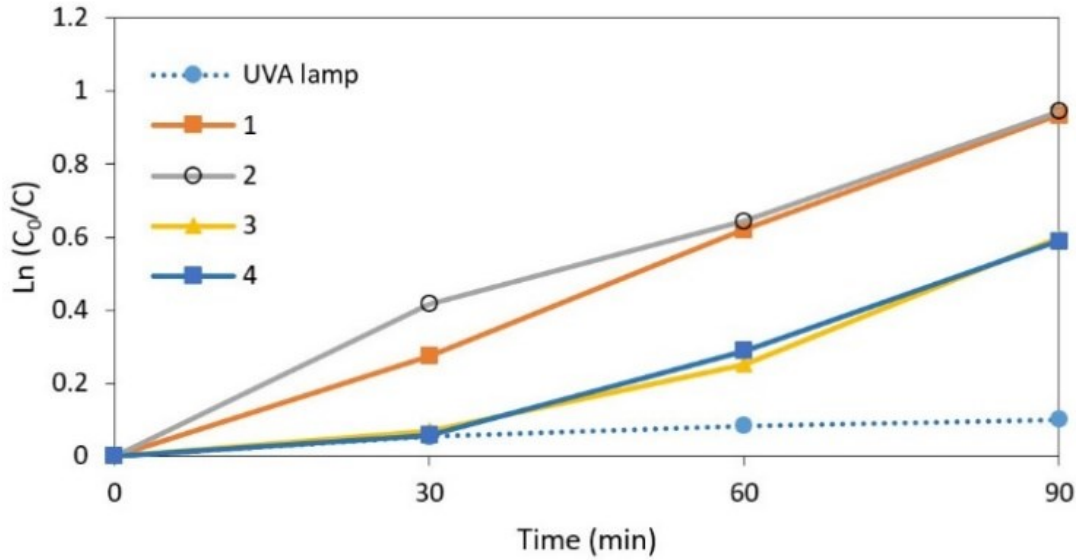


Figure 3.4 Photocatalytic degradation of MB solution for the optimization process samples sprayed according to Table 3.2 under UVA light.

Table 3.4 Photocatalytic performance of the optimization process samples sprayed according to Table 3.2.

Sample	MB Degradation after 90 min (%)	Rate Constant (k) $\times 10^{-2}$ (min <sup>-1</sup> )	Correlation Coefficient (R <sup>2</sup> )
UVA lamp (without coating)	9.6	0.01	0.93
1	53	1.0	1.00
2	61	1.1	0.99
3	45	0.06	0.88
4	44	0.06	0.9

The photocatalytic performance of TiO<sub>2</sub> depends on the light absorbance, surface hydroxylation, and electron-hole recombination rate [80]. The higher anatase content in the coatings may improve the photocatalytic activity due to the higher levels of radicals adsorbed on its surface and lower electron-hole recombination rate [117]. The literature also suggests that in thermally sprayed coatings, other parameters such as porosity, surface properties, and coating thickness may play a role in the photocatalytic performance of the coatings [97].

After optimization, the desired spray parameters corresponding to sample 2 were chosen to deposit the filtration membrane with three different thicknesses. The thickness of the membranes was controlled through the number of passes of the spray raster. In this work, M-2, M-4, and M-8 correspond to the membranes sprayed with 2, 4, and 8 spray passes.

### 3.3.2 Membrane Characterization

#### 3.3.2.1 Microstructural Analysis

Figure 3.5 illustrates the low-magnification SEM micrographs of membranes M-2, M-4 and M-8 sprayed on porous stainless steel substrates. By increasing the number of spray passes by a factor of two, the thickness of the membranes showed an increase by a factor of around two. The thickness and surface roughness of the membranes are listed in Table 3.5.

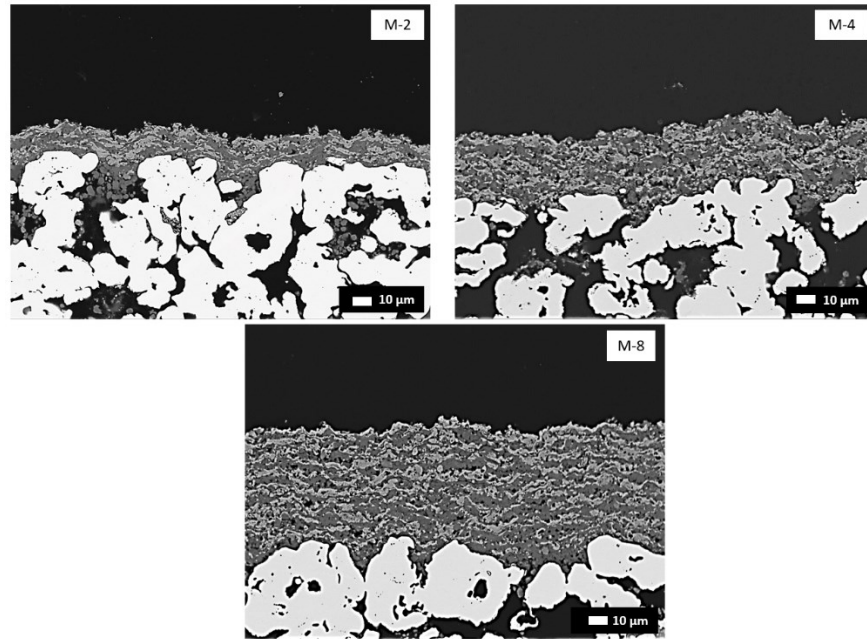


Figure 3.5 Low- magnification SEM micrographs of M-2 (2 passes), M-4(4 passes), and M-8 (8 passes) membranes.

Table 3.5 Thickness and surface roughness of M-2, M-4, and M-8 membranes.

Sample	Thickness ( $\mu\text{m}$ )	Surface Roughness ( $R_a$ ) ( $\mu\text{m}$ )
M-2	$17.1 \pm 1$	$5.7 \pm 0.7$
M-4	$30.5 \pm 0.8$	$3 \pm 0.2$
M-8	$65.4 \pm 1$	$3.5 \pm 0.3$

The general overview of the membranes in all three cases shows a microstructure including layers of light gray and dark gray regions and some black regions indicating the presence of large pores. Since the microstructures of the three membranes mentioned above were similar, sample M-8 was chosen as a reference for a more detailed analysis. As explained in section 3.3.2.2, anatase and rutile are the only phases present in the membranes. Considering that titanium and oxygen are the only elements present in the membranes, the color difference between light and dark gray regions does not attribute to the difference in the mean atomic number but either existence of a significant number of small pores or a difference in the densities

[173]. Evidence of the presence of a significant number of fine pores in the dark gray areas is discussed in this section.

Figure 3.6a shows specific details of the microstructure in an area close to the surface of the substrate. The microstructure of the membrane consists of four main zones: (1) light gray areas corresponding to melted regions, (2) black areas corresponding to large pores, (3) dark gray areas corresponding to loosely packed unmelted/sintered agglomerates of the feedstock, and (4) dark gray areas corresponding to tightly packed unmelted/sintered agglomerates of the feedstock. The loosely packed agglomerates are mainly present inside the pores of the stainless steel substrate, while tightly packed agglomerates can be observed in the microstructure from the surface of the substrate toward the top surface of the membrane. A detailed microstructural inspection of both loosely and tightly packed zones, shown in the dashed areas in Figure 3.6a, revealed that the porous agglomerates in both zones were formed by nanosized  $\text{TiO}_2$  particles seen in Figure 3.6b. Figure 3.7a shows a close-up of a nanostructured agglomerate in the fractured cross-section of the membrane. Moreover, in the higher magnification image of the agglomerates in Figure 3.7b, the presence of  $\text{TiO}_2$  particles similar to the nanosized  $\text{TiO}_2$  particles of the starting powder presented previously in Figure 3.1a can be observed. The space between the nanoparticles is indeed the origin of the fine pores in the membrane structure. The composite layered microstructure could be explained by the plasma temperature heterogeneity and the size of the inflight particles [174–176].

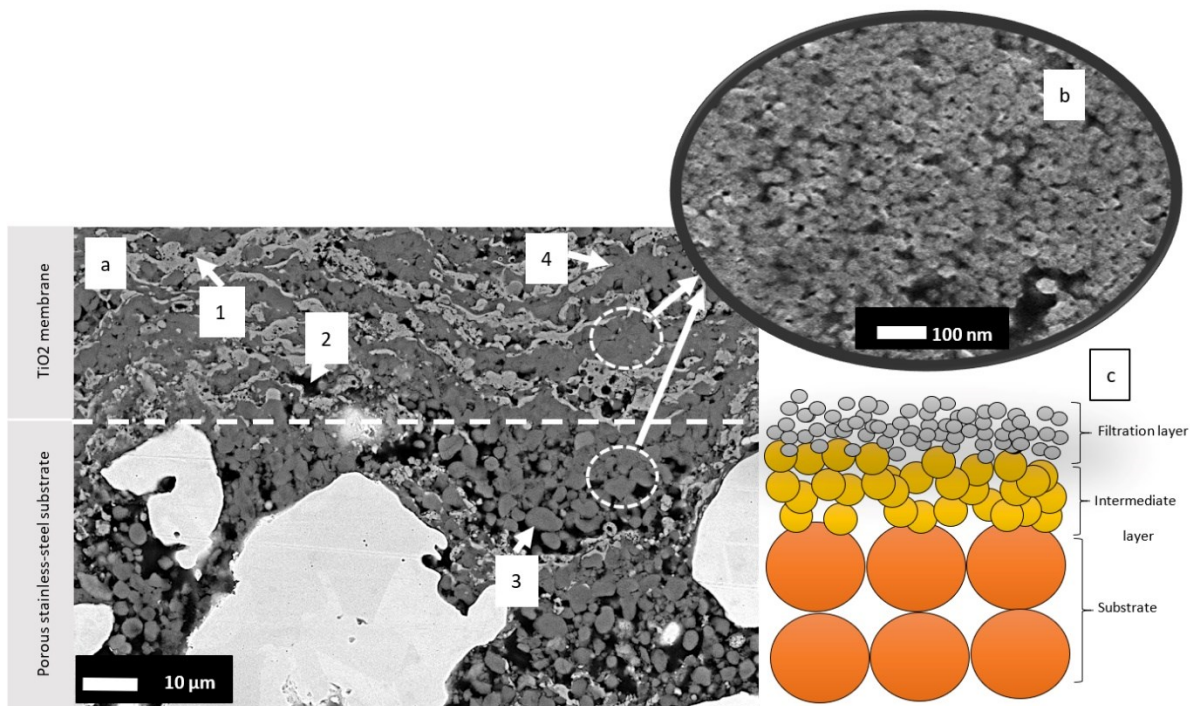


Figure 3.6 (a) SEM micrograph of M-8 inside the large pores of the substrate and close to the surface of the substrate. Including 1: melted splats (light gray), 2: large pores (black), 3: loosely packed unmelted nanostructured agglomerates (dark gray), and 4: tightly packed unmelted nanostructured agglomerates (dark gray), (b) High-magnification SEM micrograph of the microstructure in the dark gray areas, and (c) Schematic of the asymmetric microstructure of ceramic membranes.

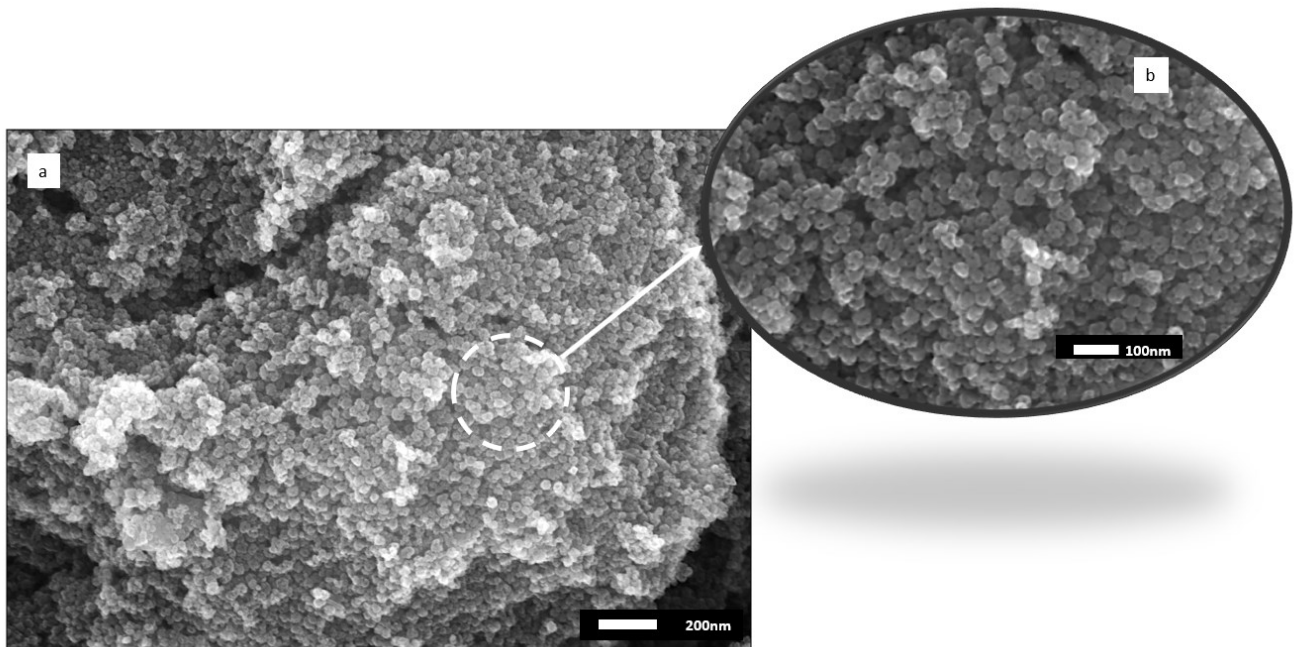


Figure 3.7 (a) SEM micrograph of a porous nanostructured agglomerate in the fractured cross-section of M-8, (b) high magnification SEM micrograph of the nanostructured agglomerates demonstrating the presence of unmelted/sintered  $\text{TiO}_2$  nanoparticles.

In general, when the suspension is radially injected into the plasma jet, it is subjected to intense shear stress from the plasma plume, and fragmentation to smaller droplets occurs [130,133]. The inflight particles include molten  $\text{TiO}_2$  particles and droplets of suspension that may agglomerate after full or partial water evaporation. Additionally, some particles and agglomerates that experience high enough temperatures may sinter without melting. Sintering could occur due to traveling in the plasma periphery, where they experience a lower heat transfer from the plasma jet or larger agglomerate size [97]. Using water as a solvent may also promote the preservation of unmelted particles by reducing the heat transfer to the large droplets carrying the agglomerates of nanoparticles due to the relatively high water vaporization enthalpy ( $2.3 \times 10^6 \text{ J kg}^{-1}$ ) [118].

The presence of loosely packed nanostructured agglomerates inside the pores of the substrate could be explained through the influence of the particle size on the normal velocity component of the inflight particles. The size of these nanostructured agglomerates (around 1 to 5  $\mu\text{m}$ ) is close to the diameter of the particle agglomerates ( $d_{50} = 3.1 \mu\text{m}$ ) in the starting suspension, as shown in Figure 3.1b. Therefore, these large agglomerates do not easily deviate from the normal flow in the vicinity of the substrate and impact the substrate with a higher normal velocity component. By increasing the distance from the plasma torch, the velocity of the agglomerates decreases [177]. Hence, inside the pores of the substrate, the agglomerates may not have sufficient momentum upon impact to become fully packed. Thus, the large pores of the substrate would be mostly bridged with relatively loosely packed agglomerates. Following the filling of the large pores of the substrate with the loosely packed agglomerates, a new surface with much less roughness compared to the original porous substrate is created.

The layered microstructure of the membranes, which was built mainly on top of this newly formed surface, could be explained through the different temperature histories of the inflight particles traveling in the plasma jet. During the deposition process, when the plasma torch begins to scan the surface, the particles and agglomerates within the peripheral regions of the plasma jet impact the surface. In this region, the agglomerates experience lower temperatures than the core of the plasma. Thus, they may remain unmelted and/or experience some degree of sintering. However, they may receive high enough momentum to become fully packed upon impingement to the substrate. Upon the movement of the torch, the fully molten particles closer to the centerline of the plasma jet will impact upon previously deposited tightly packed agglomerates. These fully molten particles were exposed to the highest temperature and momentum transfer and impacted the surface, forming dense lamellae (light gray) [128]. The alternation between unmelted porous and melted dense zones leads to the formation of a layered microstructure, as shown in Figures 3.5 and Figure 3.6. The large pores (1 to 5  $\mu\text{m}$  black) seem to be formed due to a random pile-up of the molten particles and the porous agglomerates of unmelted/sintered nanoparticles. Moreover, some large pores may also result from gas entrapment in the splats [178] and inter-splat boundaries.

An interesting feature in the SPS membrane is the deposition of an intermediate layer in the microstructure. A schematic of the asymmetric microstructure of the conventional ceramic membranes is illustrated in Figure 3.6c. In this configuration, the thick substrate with the largest pores provides mechanical strength for the membrane system. The role of the intermediate layer(s) with medium pore size is to prepare a relatively smooth surface for applying the filtering layer and adjusting the pressure gradient through the membrane system. The top filtration layer has the smallest pore size [157,179]. Interestingly, as seen in Figure 3.6a, the preferential build-up of the loosely packed nano-structured agglomerates inside the pores of the stainless-steel substrate has created a natural intermediate layer preventing the membrane structure from collapsing into the large pores of the substrate.

### 3.3.2.2 Phase Composition

Figure 3.8 illustrates the XRD patterns of membranes and the  $\text{TiO}_2$  feedstock powder. As listed in Table 3.6, the phase composition of the three membranes is relatively similar, containing anatase and rutile, with ICDD code numbers 00-021-1272 and 00-021-1276, respectively [180]. This result was expected since the spray conditions of the membranes were similar.

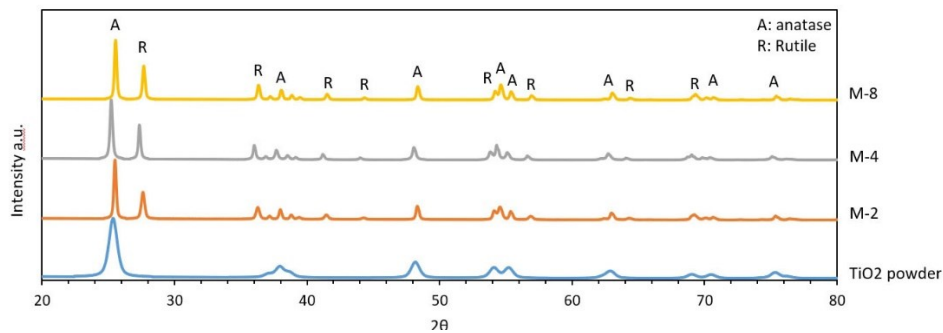


Figure 3.8 XRD patterns of the  $\text{TiO}_2$  feedstock powder, M-2, M-4, and M-8 membranes.

Table 3.6 Phase composition of M-2, M-4, and M-8 membranes.

Sample	Anatase (%)	Rutile (%)
M-2	55.2	44.8
M-4	57.7	42.3
M-8	54.3	45.7

In thermal sprayed coatings, anatase may correspond to unmelted and partially melted feedstock anatase powder [117,181] and nucleation from the molten particles [35,50]. Thermodynamically, rutile has lower free energy than anatase. Therefore, rutile is the stable polymorph at all pressures and temperatures in TiO<sub>2</sub>. However, in thermally sprayed coatings, with a high degree of undercooling, the nucleation of anatase from the liquid phase may also occur. In a rapid solidification condition, rutile nucleation occurs at temperatures from 0.88 T<sub>m</sub> up to T<sub>m</sub> (T<sub>m</sub> is the melting temperature of TiO<sub>2</sub>). On the other hand, at temperatures below 0.88 T<sub>m</sub>, due to the lower interfacial energy between anatase and liquid, anatase may nucleate from the molten phase [143,183].

The narrower XRD peaks in the membranes than those of the TiO<sub>2</sub> powder observed in Figure 3.8 correspond to the crystallite size. The anatase crystallite size in the feedstock powder was 13.3 nm. However, an increase in the anatase crystallite size to 24.7 nm was observed in the membranes. The increase in the crystallite size could be due to the recrystallization of some of the in-flight nanoparticles that get heated but do not melt [184]. It also could correspond to the presence of re-solidified anatase in the melted zones under rapid solidification condition, which might grow below the transformation temperature

In thermally sprayed TiO<sub>2</sub> coatings, some authors have linked the melting degree with the phase composition [95,181]. Looking at Figure 3.6a, one origin of the anatase in the membrane could most probably be related to the significant number of unmelted particles observed in the dark gray regions, whereas rutile may correspond to the fully melted areas [95,181]. In this work, the substrate temperature during the spray process was measured at around 300 °C, decreasing the influence of substrate temperature on anatase to rutile transformation [143]. In addition, we must consider that a significant fraction of the in-flight droplets was most likely not in the molten state at the deposition point and may have limited the possibility of phase transformation on the surface of the substrate.

Moreover, one reason for observing a color difference between light and dark gray regions in the structure of the membrane could be due to the difference in the densities. Rutile shows about 10% higher density than anatase. Therefore, combined with the presence of fine pores in the dark gray areas, it can be assumed that lighter areas may mostly correspond to rutile [173]. However, as explained before, the presence of anatase in the fully melted regions is also possible due to the rapid quenching of molten particles in thermally sprayed coatings [95].

### 3.3.2.3 Porosity Measurement

The porosity of the membrane was measured as 27%. Figure 3.9 illustrates a multi-modal pore size distribution for the membrane. In this plot, the vertical axis shows the

differential pore volume intrusion [185]. The black regions corresponding to inter-agglomerate and intra-splat pores with the size of around 1 to 5  $\mu\text{m}$ , shown in Figure 3.6, could be the source of the peak observed at point A. The next peak, at point B, could correspond to smaller intra-splat and inter-lamellar pores [42]. Finally, the peaks at point C could indicate the fine porosity due to the space between the unmelted nanoparticles. The average pore diameter was measured as 36 nm. In addition, most of the pores are in the range of 10 to 50 nm.

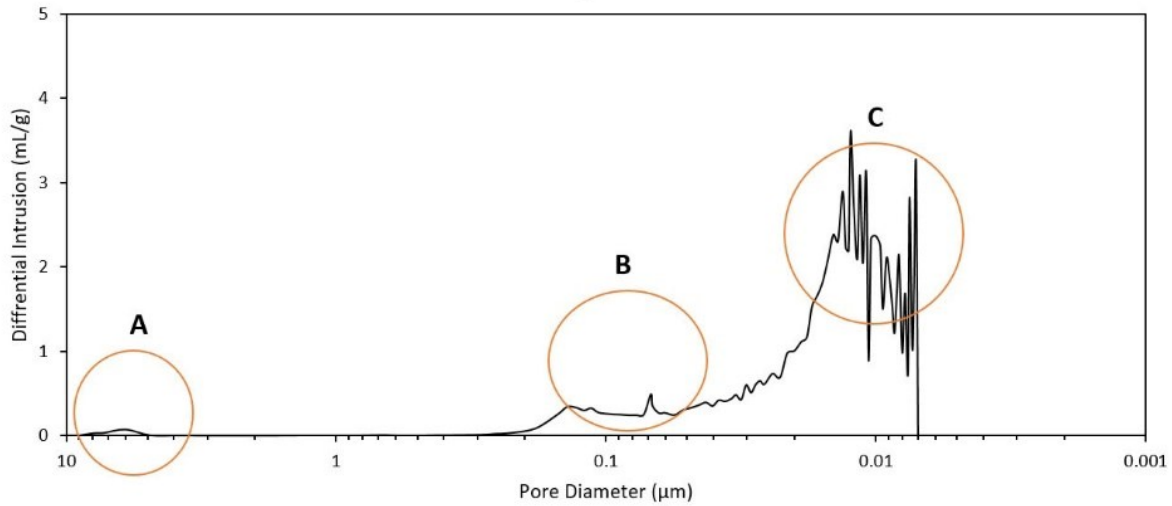


Figure 3.9 Pore size distribution of the membrane measured with mercury intrusion porosimetry.

According to the results, the average pore size of the membrane is very close to the individual  $\text{TiO}_2$  powder particles in the feedstock powder (shown in Figure 3.1a). This outcome seems consistent with a relatively large number of unmelted nano-sized particles observed in the microstructure. This result is similar to our previous work [15], which used submicron-sized  $\text{TiO}_2$  powder to deposit the MF membranes. In that work, the pore size of the microfiltration SPS  $\text{TiO}_2$  membrane was very close to the particle size of the submicron-sized feedstock [15].

### 3.3.3 Membrane Performance

#### 3.3.3.1 Clean Water Permeability Measurement

Figure 3.10a shows the experimental measurements of clean water flux for the porous substrate, M-2, M-4, and M-8 membranes. The water flux was measured as a function of pressure. It can be seen that the flux increases almost linearly with the pressure, implying the mechanical stability of the membranes [169]. The pure water permeability of the membranes has been listed in Table 3.7.

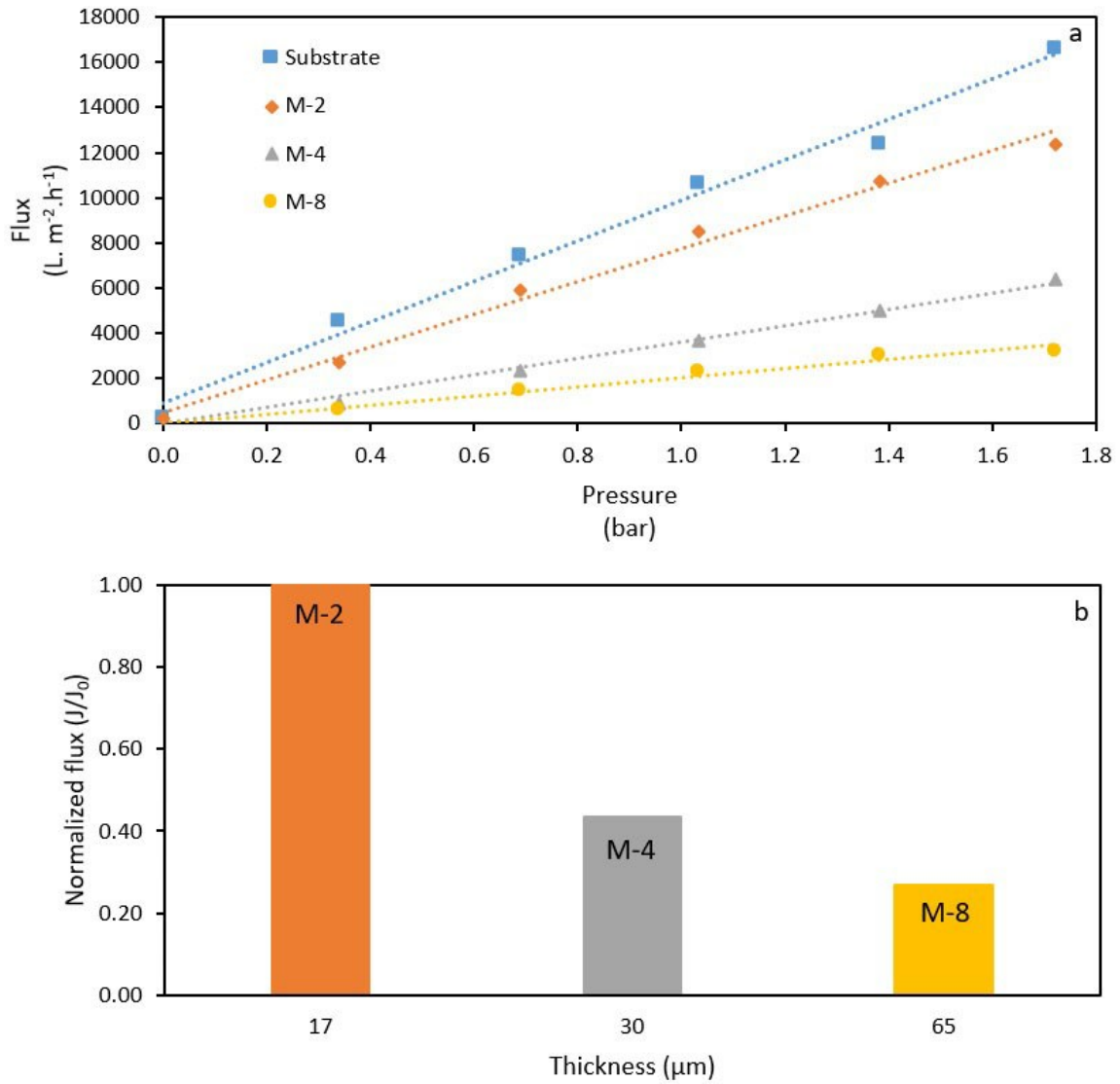


Figure 3.10 (a) Clean water flux as a function of pressure for porous substrate, M-2, M-4, and M-8 membranes, and (b) Normalized water flux as a function of membrane thickness.

Table 3.7 Clean water permeability of M-2, M-4, and M-8 membranes.

Sample	Water permeability (L m <sup>-2</sup> h <sup>-1</sup> bar <sup>-1</sup> )
Porous substrate	9000
M-2	7270
M-4	3619
M-8	2025

The water permeability of the membranes has been reported to be inversely proportional to their thickness [41,43,186]. Figure 3.10b shows the correlation between the thickness of the membranes and the normalized water flux ( $J/J_0$ ) at 1 bar,  $J_0$  being the pure water flux of the M-2. As seen in Figure 3.10b, by an approximately two-fold increase in the thickness of M-4 compared to M-2, the water flux dropped by a factor of about 2.3. Similarly, by almost doubling the thickness in M-8 compared to M-4, a flux decrease of about 1.7 was observed.

The practical water flux for commercial ultra-filtration ceramic membranes reaches around  $1800 \text{ L m}^{-2} \text{ h}^{-1} \text{ bar}^{-1}$  [187]. Ben Ali et al. reported a pure water flux of  $2263 \text{ L m}^{-2} \text{ h}^{-1}$  at 1 bar for UF ceramic membranes with 27% porosity and an average pore size of  $0.09 \mu\text{m}$  for natural kaolino-illitic clay membranes fabricated by the dip-coating method [188]. Yu et al. used the phase inversion method to produce alumina micro sheet membranes with a thickness of 0.5 mm, a pore size of 80-120 nm, and a porosity of 50-80%. They reported a pure water flux of around  $13000 \text{ L m}^{-2} \text{ h}^{-1} \text{ bar}^{-1}$  and oil/water emulsion flux of around  $2300 \text{ L m}^{-2} \text{ h}^{-1} \text{ bar}^{-1}$  [189].

In this work, the relatively high water permeability in the membranes could be attributed to the 27% porosity corresponding to the significant number of cross-linked pores produced by the presence of nanostructured porous agglomerates providing a more efficient water passage through the thickness of the membrane. Also, the multi-modal pore distribution of the membrane and the presence of some larger pores could serve toward more effortless water flow across the membrane.

Figure 3.11 shows two different positions on the cross-section of M-4 after measuring the pure water flux. The details of the microstructure were thoroughly discussed in section 3.3.2.1. Compared to the original microstructure of M-4 shown in Figure 3.5, no significant damage to the microstructure was observed after the water flux measurement. Therefore, a similar microstructure before and after the water flux measurement test could be another indication of the mechanical stability of the SPS membrane. However, investigating the durability of the membranes requires a more intensive study through measuring the flux recovery, antifouling activity, and a detailed microstructural assessment after the long-term working condition, which has been planned in our future work.

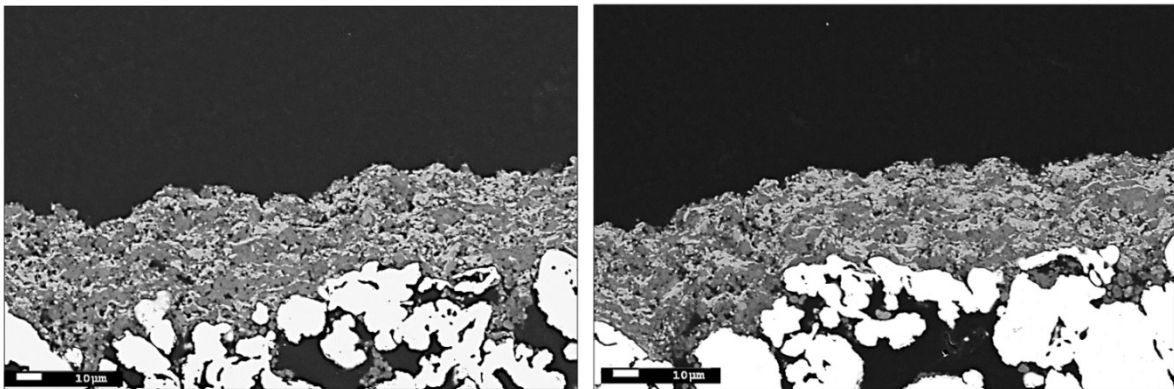


Figure 3.11 SEM micrographs of two positions on the polished cross-section of M-4 after the pure water permeability measurement.

### 3.3.3.2 Photocatalytic Performance

The photocatalytic activity of the membranes under UVA and visible light illuminations are illustrated in Figure 3.12a, b, respectively. The MB degradation after 90 min, the rate constant of the reaction ( $k$ ), and the correlation coefficient ( $R^2$ ) are listed in Table 3.8. The blank test without the membrane shows minor photolysis of MB solution under UVA and visible light irradiation. After 90 minutes, M-2, M-4, and M-8 membranes demonstrated a rather similar degradation of the dye solution under UVA. The maximum difference in the degradation by the three membranes is roughly 9% under UVA illumination. Likewise, the degradation of dye solution under visible light was also relatively similar for the three membranes, with maximum variability of around 12%.

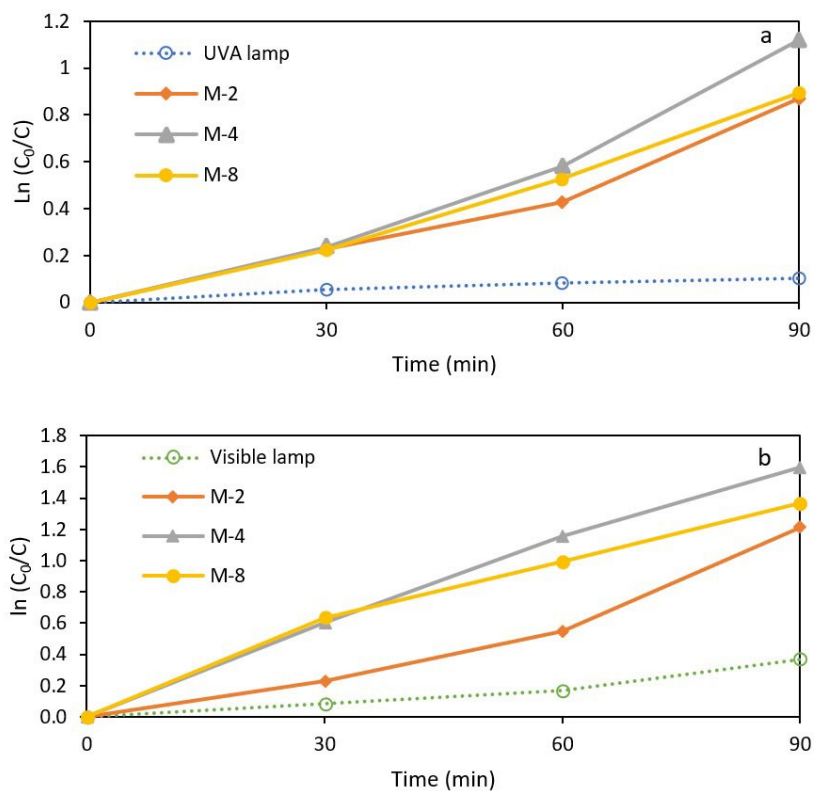


Figure 3.12 (a) Photocatalytic degradation of MB for M-2, M-4, and M-8 membranes under UVA, and (b) under visible light illumination.

Table 3.8 Photocatalytic performance of M-2, M-4, and M-8 membranes under UVA and visible light.

	Sample	MB degradation	Rate constant (k) ×10 <sup>-2</sup>	R <sup>2</sup>
		after 90 min (%)	(min <sup>-1</sup> )	
UVA	M-2	58.1	0.91	0.985
	M-4	67.4	1.1	0.982
	M-8	59.1	0.95	0.996
Visible	M-2	70.2	1.2	0.924
	M-4	82	1.8	0.997
	M-8	74.5	1.7	0.997

Toma et al. reported around 20-30% degradation of methylene blue (MB) for suspension-HVOF TiO<sub>2</sub> coatings obtained by internal and external suspension injection [190] and around 15% degradation of MB for suspension-HVOF TiO<sub>2</sub> coatings treated with direct laser interference patterning [191] after 3 hours under UVA irradiation. Fu et al. reported around 60% and 80% MB degradation in Onion-like carbon (OLC) modified TiO<sub>2</sub> coating produced by SPS under UV and visible light, respectively, after 6 hours [166]. Compared to thermally sprayed coatings above, SPS TiO<sub>2</sub> membranes in our work show higher photocatalytic activity.

Generally, the species responsible for the photodegradation of organic compounds are presumed to be hydroxyl radicals (OH·) due to their high oxidation capacity. The photocatalytic activity in TiO<sub>2</sub> is based on the diffusion of charge carriers to the surface. When TiO<sub>2</sub> is exposed to photons with energies exceeding its bandgap, photocatalytic activity is triggered by generating electrons and holes in the conduction and valence bands, respectively. Electrons and holes diffuse to the surface of the catalyst, where the photogenerated holes may oxidize the OH<sup>-</sup> and H<sub>2</sub>O to produce OH·. Furthermore, the photo-excited electrons may react with the oxygen molecules on the surface to produce superexcited anions (O<sub>2</sub><sup>-</sup>), which may prevent electron-hole recombination. O<sub>2</sub><sup>-</sup> may also go through a number of reactions to produce H<sub>2</sub>O<sub>2</sub>, which then, in reaction with electrons or O<sub>2</sub><sup>-</sup>, generates more OH· [78,97,163].

As mentioned before, one of the critical factors for the degradation of MB is the absorption of energetic photons. The bandgap energy of TiO<sub>2</sub> is within the range of 3.0-3.2 eV, allowing the absorption of photons in the UV range [97]. The photocatalytic reactivity of the thermally sprayed TiO<sub>2</sub> coatings under visible light is due to a phenomenon known as self-doping, which decreases the bandgap energy of the semiconductors [95,96]. In the plasma spray process, TiO<sub>2</sub> particles are heated to their melting temperatures in a low oxygen pressure or a hydrogen environment, resulting in oxygen vacancies in the solidified splats and generation of sub-stoichiometric TiO<sub>2-x</sub> [97,99,149,151]. Moreover, by entrapment of electrons in Ti<sup>4+</sup> lattice sites, Ti<sup>3+</sup> ions are generated [151]. While the TiO<sub>2</sub> powder is white, the sub-stoichiometric TiO<sub>2-x</sub> membrane is dark blueish gray due to a high concentration of Ti<sup>3+</sup> ions. Hence, the membrane absorbs more visible light allowing the activation of the photodegradation process at lower photon energies of the visible illumination [100,192,193].

Figure 3.13a shows the UV–vis absorption spectra of the M-4 membrane and the original TiO<sub>2</sub> powder. Membrane M-4, which showed a slightly higher photocatalytic reactivity under UVA and visible light, was used as a reference for absorbance measurements. While TiO<sub>2</sub> powder does not have any absorption in the visible range, a shift of the absorbance edge toward the visible range and a much higher absorption in the visible range can be detected in the membrane suggesting a decrease in the bandgap energy. The indirect and direct bandgaps of TiO<sub>2</sub> powder and M-4 membrane were obtained respectively from extrapolation of the linear section of the  $(\alpha h\nu)^{0.5}$ - $h\nu$  and  $(\alpha h\nu)^2$ - $h\nu$  plots as shown in Figures 3.13b, c. The indirect and direct bandgap energies in TiO<sub>2</sub> powder were measured as 3.02 eV and 3.22 eV, respectively. The indirect and direct bandgap energies in the membrane were decreased to 1.94 eV and 2.81 eV, respectively. Therefore, photo-induced charge carriers could be formed in the membrane in the range of visible illumination.

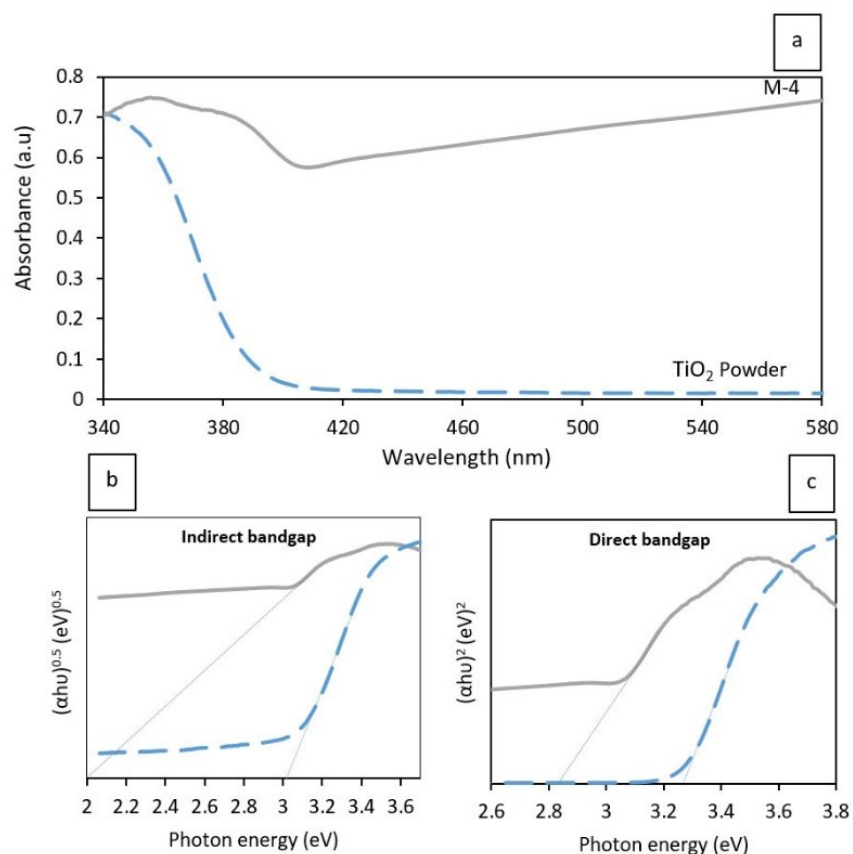


Figure 3.13 (a) UV–vis absorption spectra, (b)  $(\alpha h\nu)^{0.5}$ - $h\nu$ , and (c)  $(\alpha h\nu)^2$ - $h\nu$  plots of TiO<sub>2</sub> feedstock powder and M-4 membrane.

Another factor in the efficiency of photocatalytic activity is the recombination rate of the charge carriers [82]. Literature suggests that in TiO<sub>2-x</sub>, the Ti<sup>3+</sup> ions and oxygen vacancies introduce sub-level energy states below the conduction band, which decreases the recombination rate and enhances the excitation of electrons from the valence to the conduction band, thus improving the photocatalytic performance [151,192].

As can be seen in Table 3.8, the membranes show a rather similar rate constant under both visible and UVA illuminations. Although, the illumination of the visible light used in this

work is around 5.3 higher than the UVA. Therefore, the photocatalytic activity of the membranes under visible illumination is, in fact, lower than that under UVA illumination. However, it shall be considered that the fraction of visible illumination in the sunlight is around 17 times more than UV illumination [91], making the membranes more efficient in photocatalytic performance under direct sunlight as a sustainable energy source.

### 3.4 Conclusion

This study showed:

- SPS technology can be used to produce UF membranes with pore size smaller than 100 nm by using a nano-sized feedstock and optimizing the process parameters.
- The unmelted agglomerates of nano-sized feedstock are essential to introduce nano-sized porosity and a network of cross-linked pores in the SPS UF membrane.
- Since the pores mainly originate from the space between the unmelted particles, there is a relatively close correlation between the feedstock particle size and the membrane pore size. Therefore, the pore size and porosity of the membrane can be tailored by retaining a balanced fraction of unmelted agglomerates of nano-sized feedstock in the microstructure. This outcome is also in agreement with the results of our previous work [15].
- The permeability of the membranes can be adjusted by optimizing the thickness and porosity.

Furthermore, these membranes could offer an attractive solution for outdoor filtration/photocatalysis applications under sunlight with approximately 52% visible illumination by proposing a more efficient use of solar energy as a renewable energy source. Therefore, our future work mainly focuses on the performance assessment of the SPS membranes. More specifically, the filtration efficiency, the self-cleaning and photocatalytic, and the long-term stability of the membranes in filtering/cleaning cycles will be characterized in detail.

## Chapter 4 Tailoring the Porosity Level of the Suspension Plasma Sprayed Coatings Using a Dual Suspension Injection System

### **Preface to Chapter 4**

The previous chapter demonstrated the possibility of using SPS to produce a porous microstructure with nanosized pores. The main objective of this chapter was to investigate the feasibility of customizing the porosity in porous coatings that could be used for tailoring the porosity level in the structure of the SPS separation membrane. This was done by employing a novel approach using a dual suspension injection system to simultaneously introduce two suspensions into the plasma jet at different radial distances.

**Abstract:** This study investigated the feasibility of tailoring the porosity in suspension plasma sprayed (SPS) coatings using a dual suspension injection system. Two titanium dioxide water-based suspensions with different particle sizes were injected into the plasma jet through two injectors located at different radial distances from the exit of the plasma torch. By varying the spray parameters, the fraction of unmelted particles in the coatings coming from the injector located farther from the torch changed. The total porosity was evaluated to range from approximately 16% to 36%, and the variation was related principally to the gaps between the unmelted particles. Among the selected spray parameters, the suspension feed rate and distance between the injectors were found to have the most significant effect on increasing the porosity. The samples were analyzed using SEM, XRD, and Raman spectroscopy.

**Keywords:** Suspension plasma spray; dual suspension injection; unmelted particles; porosity

## 4.1 Introduction

Thermal spray technology is a group of processes involving the melting and spraying of particles ranging typically from 1-80  $\mu\text{m}$  at high temperatures and velocities to deposit coatings. When the molten or partially molten inflight particles hit the surface of the substrate, they rapidly solidify, forming thin layers known as splats. The process continues as more splats accumulate and mechanically bond to produce well-adhered deposits [194]. Suspension plasma spray (SPS) is a relatively recent thermal spray deposition process that was primarily developed to facilitate the introduction of fine sub-micron to nanosized particles into the plasma jet to produce finely structured coatings with enhanced structural and functional properties. In the SPS process, submicron and nano-sized particles are suspended in a slurry using ethanol or water. Introducing very fine particles into the plasma in the form of suspension enhances the flowability of those particles, which cannot be obtained in the other conventional thermal spray techniques [127,195,196].

Typically, SPS coatings with diverse microstructures such as dense, segmented, columnar, and porous can be produced by controlling the process parameters that could be used for a wide array of applications [197]. In SPS, it is possible to produce thinner coatings with finer pores due to the possibility of using very fine feedstock particle size. Porosity can be generated from various sources such as inter-columnar gaps, inter-splat and intra-splat voids, cracks, and deformed semi-melted and unmelted particles [124–126].

Porous SPS coatings can be used for various applications. The functionality of SPS thermal barrier coatings (TBCs) relies on the presence of pores and segmentation cracks or columns in their microstructure. In TBCs, the porosity allows for effective thermal insulation, while the presence of cracks or columns provides the coating with a higher strain tolerance [124,125]. The SPS process is also being investigated for producing the electrode layers in

solid oxide fuel cells. Specifically, for the cathode [198] and anode [170], the SPS process appears to be a viable option, as it allows the production of coatings with high porosity levels combined with fine pore sizes. Recently, authors have introduced SPS as a potential fabrication method for ceramic filtration membranes with submicron and nanosized pores. Fine pores in the SPS membrane structure were identified as the gaps between unmelted feedstock particles embedded in a matrix formed by the splats. Therefore, the average pore size in the membranes was very close to the feedstock particle size, providing a way to control the pore size for specific filtration applications [15,199].

The existence of pores holds crucial significance in SPS coatings, underscoring the importance of effectively controlling the porosity proportion. In SPS filtration membranes, the porosity can determine the level of permeability. Generally, in thermal spray coatings, the porosity is controlled by adjustment of the spray parameters [200,201]. However, considering the voids between the unmelted particles as one possible origin of fine pores, another approach could be keeping a controlled fraction of unmelted feedstock in the coating structure by simultaneously injecting two suspensions at two radial distances from the plasma torch exit.

Different studies investigated the use of the dual feedstock injection system in the thermal spray process. Cuglietta et al. used a hybrid suspension and powder system to plasma spray anodes for solid oxide fuel cells, where they introduced a suspension of CuO, Co<sub>3</sub>O<sub>4</sub>, and NiO axially, and samaria-doped ceria (SDC) powder radially into the plasma jet. Depending on the spray parameters, they obtained structures with layered or mixed SDC and metal phases [202]. Bolelli et al. co-injected MCrAlY powder with Al<sub>2</sub>O<sub>3</sub> suspension at the same point in the plasma jet using a dual injection system to produce a sliding wear-resistant composite at high temperatures [203]. Hazel et al. invented a suspension injection method with multiple injection points, where the injectors were located normally to the plasma axis around a circle at various angles [204]. Bjorklund et al. proposed the concept of axial and radial co-spraying of micron-sized powder and submicron-sized suspensions in the same spot in the plasma jet to produce composite and layered coatings [205]. Nowakowaska et al. simultaneously sprayed alumina (Al<sub>2</sub>O<sub>3</sub>) and titanium dioxide (TiO<sub>2</sub>) suspensions with two injectors at the same point in the plasma to produce highly porous coatings with columnar structure with a gradient of TiO<sub>2</sub> content [206].

Although the co-injection of feedstock material has been studied in thermal spraying for various applications, to our knowledge, the concept of co-injection of the suspensions in the plasma jet at two radial distances has not been investigated. The primary purpose of this study was to use the unmelted feedstock particles in the SPS coating to regulate the porosity level and pore size for photocatalytic filtration membrane application, which was developed in our previous works [15,199]. In addition, in photocatalytic TiO<sub>2</sub> coatings, anatase content is believed to be one of the important factors enhancing photocatalytic reaction efficiency. One significant contributor to anatase content in thermal spray coatings is the preserved anatase from the unmelted original feedstock. [100,145]. The dual injection approach could provide the possibility of retaining a controlled level of anatase in the SPS coatings, which could influence the photocatalytic and self-cleaning properties of the SPS membranes. Another potential application could be to embed and control the level of heat-sensitive feedstock, such as

graphene, in the coatings to improve photocatalytic or wear resistance performance [207,208] or to obtain controlled oxidation of feedstocks such as Cu to produce antiviral coatings [116].

In this study, a dual suspension injection system was employed to investigate the potential of customizing the quantity of unmelted feedstock particles and, consequently, the porosity levels in SPS coatings. By adjusting the spray parameters, samples with varying degrees of porosity were produced, and the impact of different spray conditions and suspension trajectory on the microstructure was discussed. Furthermore, the findings were analyzed using image analysis, X-ray diffraction (XRD), and Raman spectroscopy.

## **4.2 Experimental**

### **4.2.1 Plasma Spraying Process**

Coatings were fabricated using the suspension plasma spray process (SPS) utilizing a 3MB plasma torch (Oerlikon Metco, Switzerland) with a gas mixture of Ar and H<sub>2</sub>. A dual-suspension injection system, illustrated in Figure 4.1, was developed to introduce two suspensions simultaneously into the plasma jet. The suspensions were sprayed radially at two distances from the exit of the torch. In this work, the injector located closer to the exit of the plasma gun is designated as injector 1, while the suspension sprayed using injector 1 is referred to as suspension 1. Similarly, the injector situated farther from the torch exit is labeled as injector 2, and the corresponding suspension is referred to as suspension 2. The primary aim of this setup was to investigate the feasibility of generating porous microstructures and tailoring the porosity by introducing unmelted particles downstream into the plasma jet. It was assumed that injecting suspension closer to the exit of the plasma torch would result in creating a matrix composed of melted splats. This was attributed to the particles in suspension 1 being exposed to the high-temperature regions of the plasma jet. A matrix of fully melted splats would enhance the mechanical strength of the porous coating structure. Conversely, injecting suspension 2 farther from the plasma jet could potentially introduce a portion of unmelted or sintered particles into the matrix due to the reduced exposure to the hot core of the plasma jet [209]. Previous findings by the authors have demonstrated that including unmelted particles in the coating plays a significant role in generating porosity, where the pores originate from the vacant spaces among these unmelted particles [15,199].

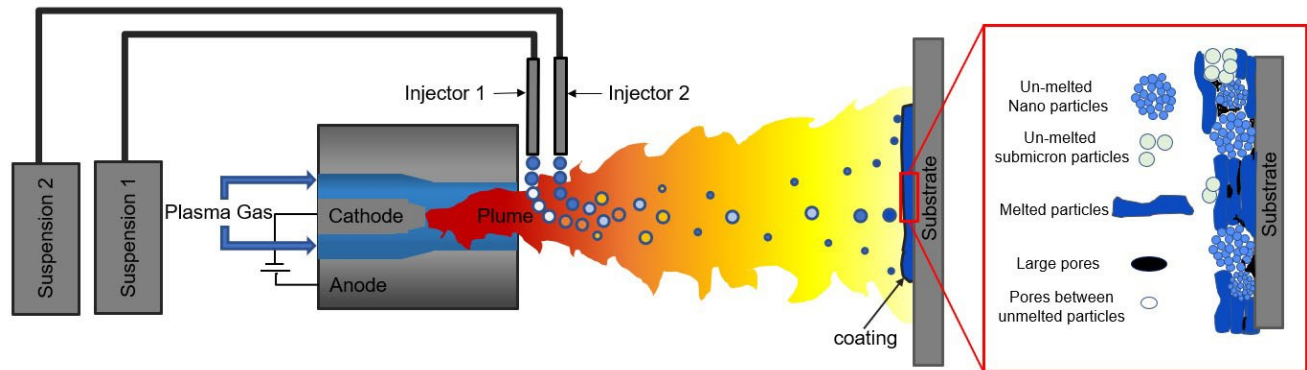


Figure 4.1 Schematic of the dual suspension injection system. Suspension 1, made by submicron-sized  $\text{TiO}_2$ , was injected via injector 1, and suspension 2, made by nanosized  $\text{TiO}_2$ , was injected via injector 2. Unmelted submicron-sized particles and unmelted nanosized particles in the coatings come from injector 1 and 2, respectively.

Table 4.1 shows the SPS parameters used to produce the  $\text{TiO}_2$  coatings. To enhance the formation of a strong matrix and promote the melting of particles from suspension 1 during the production of  $\text{TiO}_2$  coatings, a 3MB torch with high power was employed. Additionally, to preserve a high level of unmelted particles, the injection of suspension 2 was carried out downstream, where the temperature and speed of the plasma were lower.

Table 4.1 SPS parameters used to deposit  $\text{TiO}_2$  coatings.

Ar (SLPM)	H <sub>2</sub> (SLPM)	Current (A)	Voltage (V)	Power (kW)	Torch velocity (m/s)	Injector diameter (mm)	Spray distance (mm)
60	5	600	60	36	1	0.2	50

Table 4.2 summarizes the test matrix used to produce nine coatings by varying three spray parameters: the distance between injector 1 and injector 2, the solid content of suspension 2, and the feed rate of suspension 1. In all cases, a two-step process was employed to position the combined suspension jet approximately at the center of the plasma jet. Initially, suspension 1 was introduced at a specific feed rate, followed by the introduction of suspension 2 in the second step. During this stage, the feed rate of suspension 2 was adjusted to ensure that both suspensions remained in close proximity to the centerline of the plasma jet. This alignment was confirmed by visually inspecting through the Accura spray system camera. Throughout the entire experiment, the distance from the center of injector 1 to the exit of the torch was consistently maintained at approximately 8 mm. The distance between the two injectors was changed by adjusting the position of injector 2. By increasing the distance between the two injectors, suspension 2 was introduced into the plasma at a longer distance from the torch exit. It was assumed that this increased distance would result in less heating of inflight particles from injector 2 [210], which

in turn could increase the likelihood of retaining unmelted particles from suspension 2 within the coating. An increase in the solid content of the suspension and suspension feed rate could potentially lead to higher porosity due to promoting the incomplete melting of the inflight particles since less energy is available to evaporate the solvent and melt the feedstock powder [211,212].

To gain a deeper understanding of the impact of incorporating the second injector on the microstructure of the coatings, control samples D1 and D2 were prepared to be used as baseline conditions. These control samples served as reference points to compare and analyze the specific effects resulting from the inclusion of the second injector. In the case of D1, the coating was deposited with only suspension 1 injected using injector 1. In addition, for sample D2, water was sprayed through injector 2 instead of suspension. Sample D9 did not yield a mechanically stable coating due to the spray parameters used, resulting in an excessive amount of unmelted feedstock particles [212]. Consequently, in the case of D9, a powdery coating was deposited. Therefore, this sample was excluded from the subsequent discussion and analysis.

*Table 4.2 Test matrix used to produce TiO<sub>2</sub> coatings.*

<b>Sample</b>	<b>Distance between the injectors (mm)</b>	<b>Solid content Suspension 2 (%)</b>	<b>Feed rate Suspension 1 (mL/min)</b>	<b>Feed rate Suspension 2 (ml/min)</b>
D1	-	No suspension/ water	30	-
D2	16	Water	30	29
D3	16	20	30	25
D4	20	20	30	25
D5	16	30	30	29
D6	20	30	30	29
D7	16	20	25	25
D8	25	20	25	25
D9	25	20	30	29

Dense 304 stainless steel coupons measuring 25 × 25 × 5 mm<sup>3</sup> were used as substrates. Before the coating deposition, the substrates underwent grit blasting using Al<sub>2</sub>O<sub>3</sub> particles (80 grit) and were subsequently cleaned by sonication in acetone. The resulting surface roughness was measured to be R<sub>a</sub> = 3.0 ± 0.5 μm. The substrates were fixed on a stationary substrate holder with no cooling. Coatings were deposited by 30 passes of a full spray raster with an overlay distance of 3 mm.

Accuraspray 4.0 system (Tecnar, Saint-Bruno-de-Montarville, QC, Canada), with a 3% accuracy for the particle velocity measurement, was used to determine the inflight particle velocity during the SPS process. The velocity was measured at the spray distance of 50 mm. Due

to technical limitations, the Accuraspray system cannot accurately measure the temperature of TiO<sub>2</sub> particles in the suspension. The substrate temperature during the SPS process was measured using an infrared camera (A310, FLIR, Wilsonville, OR, USA), and the average temperature was reported.

The setup details used for imaging the suspension trajectory and the inflight particles during the SPS process have been described elsewhere [213]. In summary, a high-speed camera (Photron, FASTCAM SA1.1, HIS Inc., Uxbridge, ON, Canada) with a maximum resolution of 1024 × 1024 pixels equipped with a Nikon lens (AF-S Micro NIKKOR 105mm f/2.8, Nikon Canada Inc., Mississauga, ON, Canada) was employed to capture the images. The number of captured frames was set at 15000 f/s. The inflight particles were illuminated by a 5 Hz pulse laser, creating a laser sheet with a thickness of 500 μm. A prism was placed in front of the laser to position the laser sheet in front of the camera. The camera and laser positions remained unchanged throughout the experiments. To effectively eliminate plasma radiation, a set of three filters was employed. These filters included a bandpass filter with a 1 nm bandwidth to allow the passage of the 532 nm wavelength, a gray filter with an optical density (OD) of 1.2 to reduce intensity across all wavelengths, and a short pass filter to block wavelengths ranging from 610 to 1000 nm. The images covered a field of view with an area of approximately 40 × 30 mm<sup>2</sup>. The number of images captured for each set of spray parameters was 5-6, which were superimposed to obtain a single image using the Image J open-access software.

#### 4.2.2 Suspension Preparation

In alignment with our previous works for developing of photocatalytic SPS membranes, TiO<sub>2</sub> was used as the feedstock material due to its photocatalytic properties [15,199]. To facilitate the distinction between the unmelted particles originating from each suspension in the microstructure of the coating, TiO<sub>2</sub> powders with two distinct particle sizes were utilized in the preparation of the suspensions. These powders exhibited different morphologies and sizes, allowing for clear recognition within the coating. Figure 4.2 presents the particle size distribution and the SEM images of the TiO<sub>2</sub> powders used in this work. A commercially available 100 wt% anatase submicron-sized powder (KS-203A/B, TKB Trading, US) was used to prepare the 20 wt.% water-based suspension 1. The concentration of suspension 1 was constant in all conditions. Furthermore, a 100 wt.% anatase nanosized powder (Pi-Kem Co., Tamworth, UK) was used to prepare the 20 wt.% and 30 wt.% water-based suspensions 2. The decision to use water as a solvent is supported by the fact that the total amount of heat needed to vaporize water is higher than that of other common solvents like ethanol [214]. This higher heat requirement increases the chances of a portion of the inflight particles retaining their solid, unmelted state in the coating. The particle size distribution of the TiO<sub>2</sub> suspensions was obtained by a Spraytec system (Malvern Instruments, Malvern, UK). The submicron-sized TiO<sub>2</sub> exhibited a particle size distribution with  $d_{10} = 0.15 \mu\text{m}$ ,  $d_{50} = 0.28 \mu\text{m}$ , and  $d_{90} = 0.6 \mu\text{m}$ . Also, the average particle size of the submicron-sized TiO<sub>2</sub> was measured as  $137 \pm 40 \text{ nm}$ . On the other hand, the nanosized

TiO<sub>2</sub> showed a particle size distribution with  $d_{10} = 1.4 \mu\text{m}$ ,  $d_{50} = 3.1 \mu\text{m}$ , and  $d_{90} = 6.3 \mu\text{m}$ . Furthermore, the average particle size of the nanosized TiO<sub>2</sub> powder was obtained as  $27 \pm 10 \text{ nm}$ . The variation observed between the particle size observed in SEM images and the measurements obtained from the Spraytec system was attributed to the agglomeration tendency of nanosized materials in suspensions, which affects the particle size distribution [210]. Nanoparticles are difficult to disperse due to their high specific surface. They tend to form micron-sized agglomerates that have been previously shown to promote the introduction of nanosized pores in the membrane microstructure. During the SPS process, the density of suspension 1, containing submicron-sized TiO<sub>2</sub> particles, was determined to be approximately 1.173 g/mL. As for suspension 2, which contained nanosized TiO<sub>2</sub> particles, the density was around 1.170 g/mL for a solid content of 20 wt.% and 1.280 g/mL for a solid content of 30 wt.%. The density and flow rate of the suspensions remained relatively constant during the spray process as determined by a Coriolis flow meter (Endress+Hauser, Canada).

The details of the suspension preparation process for the submicron-sized TiO<sub>2</sub> powder [15] and the nanosized TiO<sub>2</sub> powder [199] were previously described.

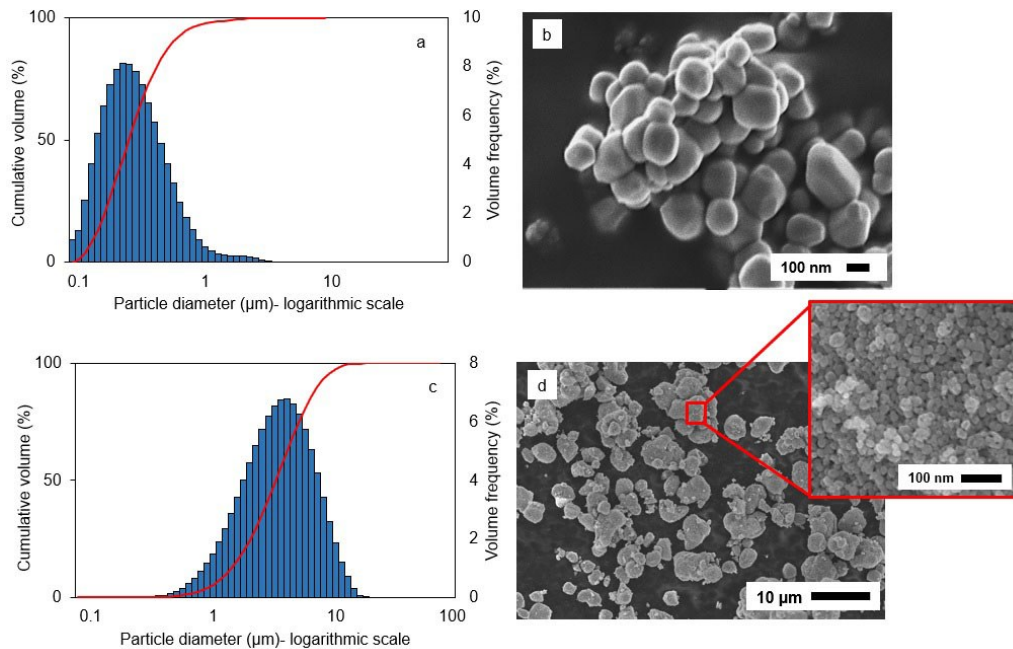


Figure 4.2 (a) Particle size distribution of submicron-sized TiO<sub>2</sub> powder. (b) SEM micrograph of the submicron-sized TiO<sub>2</sub> powder. (c) particle size distribution of nanosized TiO<sub>2</sub> powder. (d) SEM micrograph of the nanosized TiO<sub>2</sub> powder.

The viscosity of suspensions was measured using a viscosimeter system (DNVext, Brookfield Amatek, US).

### 4.2.3 Coating Characterization

The surface roughness of the samples was assessed using a confocal laser microscope (LEXT OLS4000 Olympus, Toronto, ON, Canada), and the reported values were the arithmetic average surface roughness (Ra). The powder morphology, as well as the polished cross-sections and coating surfaces, were examined using field-emission scanning electron microscopes (FESEM JSM 7600TFE, JEOL, Tokyo, Japan, and FESEM Hitachi Regulus 8230, Mississauga, ON, Canada). The thickness of the coating was measured at sixteen points on the cross-sectional backscattered images of the coatings with a magnification of 2000x. The phase composition of the coatings was analyzed to determine anatase content, which is important for photocatalytic membrane application. Phase analysis of the samples was conducted using the X-ray diffraction (XRD) technique (X'Pert pro-MRD, Malvern PANalytical, Malvern, UK) over a range of 20–80° with Cu K $\alpha$ , a step size of 0.02°, the scan step time of 2 s, with the voltage of 45 kV, and the current of 35 mA. The phase content and crystallite size of anatase and rutile was quantified using Rietveld refinement analysis performed with HighScore Plus software (Malvern PANalytical, Malvern, UK).

In general, one main source of anatase in the thermal spray coatings is believed to be from the unmelted or partially melted zones [145]. To better understand the source of anatase in the coatings, Raman spectroscopy was carried out on the melted and unmelted zones of the coatings. Raman analysis was conducted on the polished cross-section of the coatings using a Raman spectrometer (inVia Reflex, UK). The spectrometer utilized a laser with a wavelength of 532 nm and a spot size of approximately 2  $\mu$ m. The objective magnification was set to 50x, and the exposure time for each measurement was 10 seconds. Prior to the analysis, the system was calibrated using a silicon reference.

In the coatings, the proportion of large pores, unmelted submicron particles introduced through injector 1, and unmelted agglomerates of nanosized particles introduced through injector 2 were assessed by image analysis using the Olympus Stream basic software. The variations in the fraction of unmelted agglomerates of nanosized TiO<sub>2</sub> particles injected through injector 2 were associated with the development of nanosized porosity within the coatings, where the nanosized pores were attributed to the gaps between the unmelted/sintered nanosized TiO<sub>2</sub> particles in the coatings [199]. Therefore, in this work, increasing the fraction of unmelted agglomerates of nanosized particles would be translated to an increase in the porosity of the coatings. Five SEM images of the polished cross-sections of each coating, captured using a backscatter electron detector at a magnification of 2000 $\times$ , were utilized for the image analyzing process.

## 4.3 Results and Discussion

### 4.3.1 Microstructural Features

Figure 4.3 illustrates low-magnification images of the control samples D1 and D2, providing a general overview of their microstructure. These coatings exhibit three similar distinct regions, visually distinguished by grey level: black, light grey, and dark grey. Furthermore, Figure 4 presents a high-magnification image of sample D1, demonstrating the presence of these

regions in greater detail. The black areas, identified by number 1, correspond to large pores, while the light grey areas, identified by number 2, are fully dense splats formed from melted particles. On the other hand, the dark grey areas, labeled by number 3, indicate the presence of unmelted particles retained from the feedstock powder and/or resolidified particles. Indeed, filling larger inter-splats pores with unmelted particles of the pristine feedstock leads to forming a network of fine pores within the coating[15,199]. The splats were formed from the melted inflight particles traveling closer to the centreline of the plasma jet, where the plasma temperature was highest. On the other hand, the particles that remained unmelted likely traveled through the outer regions of the plasma jet, encountering lower momentum and less heat transfer from the plasma. [212,215,216].

Sample D1, sprayed using the submicron-sized particles through only injector 1, exhibits a distinctive columnar microstructure found typically in SPS coatings due to a phenomenon known as the shadow effect. During the coating deposition in the SPS process, the larger inflight particles mainly move in a direction perpendicular to the substrate surface, while the plasma drag influences the trajectory of the smaller particles. As a result, the smaller particles tend to travel almost parallel to the surface near the substrate and become attached to the sides of the surface asperities and irregularities. The lateral and vertical growth of the coating leads to the formation of columnar features and porous bands between the columns as the underlying surfaces are shielded from the impact of new particles [217,218].

Compared to D1, in sample D2, where water was sprayed through injector 2, the coating thickness was reduced by approximately 50%. The columnar features were still visible in the structure but were less pronounced. Furthermore, the overall microstructure appeared more densely packed, with a decreased presence of large pores (indicated by black regions) and unmelted submicron-sized particles (dark grey areas).

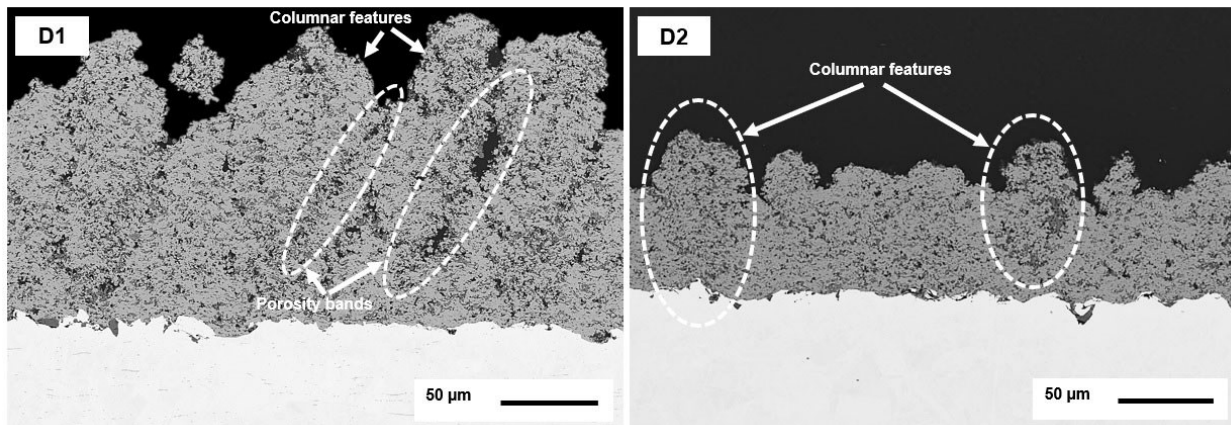


Figure 4.3 Low magnification SEM micrographs of control samples D1 (Submicron-sized  $TiO_2$  injected through only injector 1), and D2 (Submicron-sized  $TiO_2$  injected through injector 1, and water through injector 2) coatings.

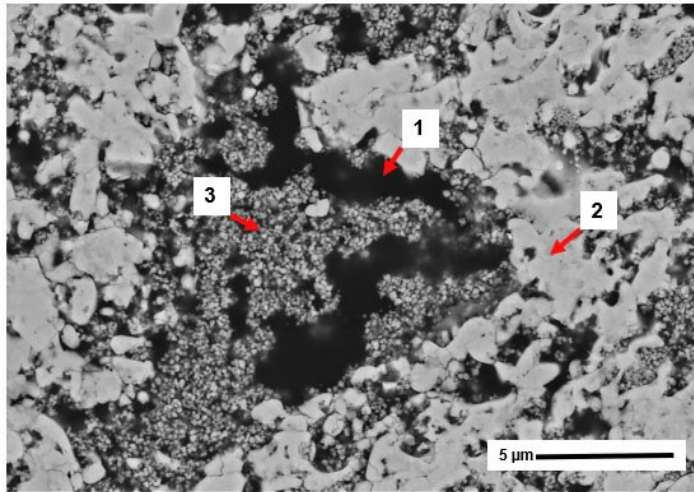


Figure 4.4 SEM micrograph of the polished cross-section of sample D1, displaying (1) large pores, (2) splats from the melted particles, and (3) unmelted submicron-sized particles.

SEM micrographs of samples D3 to D8 are presented in Figure 4.5, based on the variation in the spray parameters. Figure 5 shows a comparable coating thickness to the control sample D2. The effect of the spray parameters on the porosity level in the coatings is discussed in the following sections. All coatings displayed a firm mechanical bond to the substrate, and no detachment was observed.

Like the control samples, these samples exhibit three distinct regions: black, light grey, and dark grey areas. Also, some columnar features in the form of bumps can be observed on the top sections of the coatings.

Among these samples, D5 was selected for a more detailed examination of the microstructure, as depicted in Figure 6. Like in the control samples, the black regions (number 1) correspond to the large pores, and the light grey areas labeled by number 2, are the splats. Moreover, the high magnification SEM images of sample D5 reveal that the unmelted regions appear in two different shades of grey, which can be distinguished by the size of the unmelted particles. The lighter grey sections, identified by number 3, correspond to the unmelted submicron-sized particles introduced through injector 1. In comparison, the darker grey areas, shown by number 4, correspond to the unmelted agglomerates of nanosized particles injected via injector 2. Figure 4.7 displays the fractured cross-section of D5, providing a detailed representation of the co-existence of the unmelted submicron-sized and nanosized particles from injectors 1 and 2, respectively. The unmelted particles may result from the deposition of agglomerated submicron or nanosized particles or the impact of suspension droplets in which all the water was not evaporated in flight. The remanent water was evaporated on the hot substrate, leaving the unmelted feedstock particles deposited on the substrate surface. Indeed, most of the individual submicron particles likely do not reach the substrate due to their low mass.

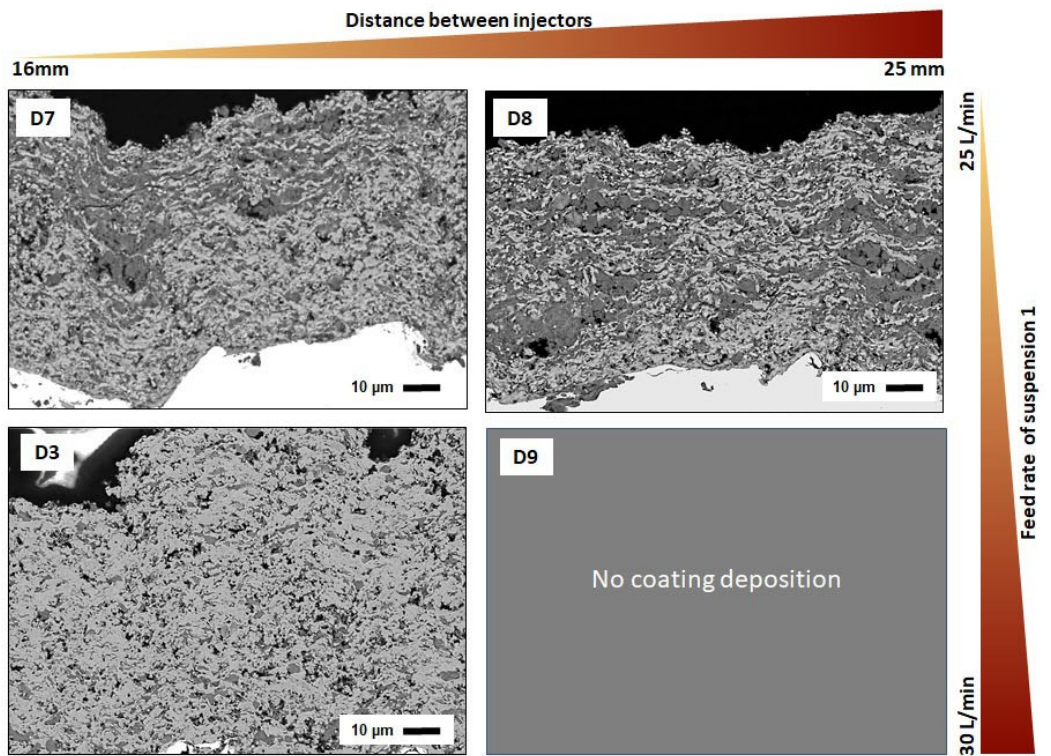
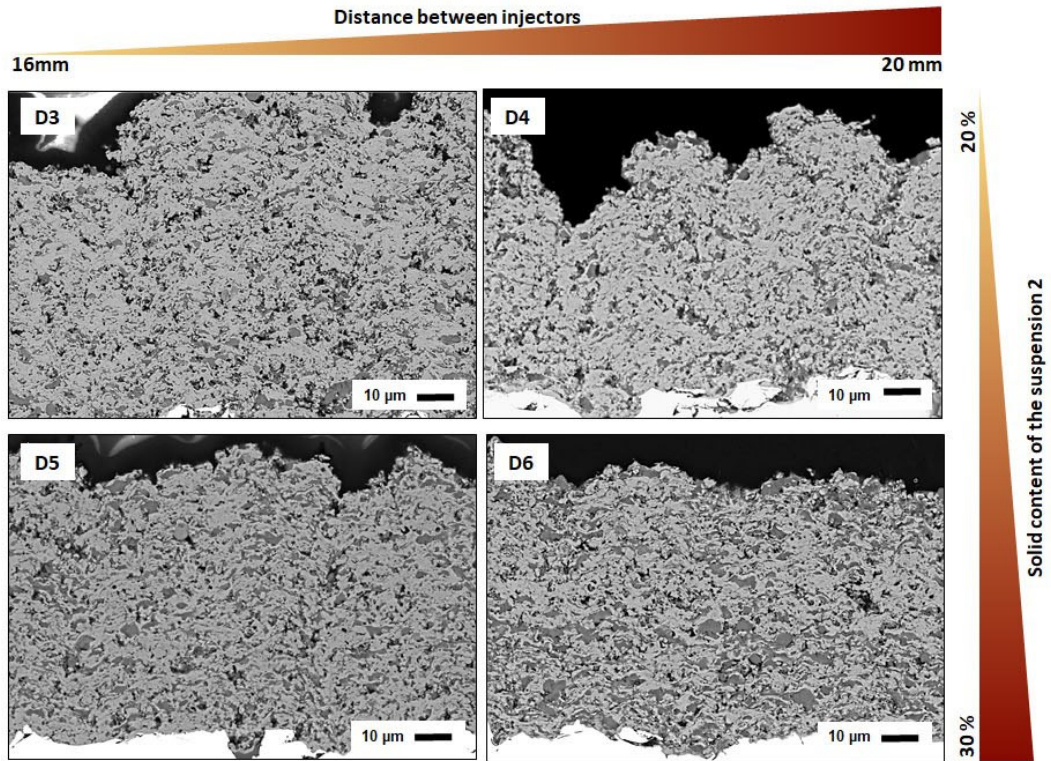


Figure 4.5 SEM micrographs of samples D3 to D8 classified based on the spray parameters. Spray condition D9 resulted in a powdery deposition on the substrate (no coating was obtained).

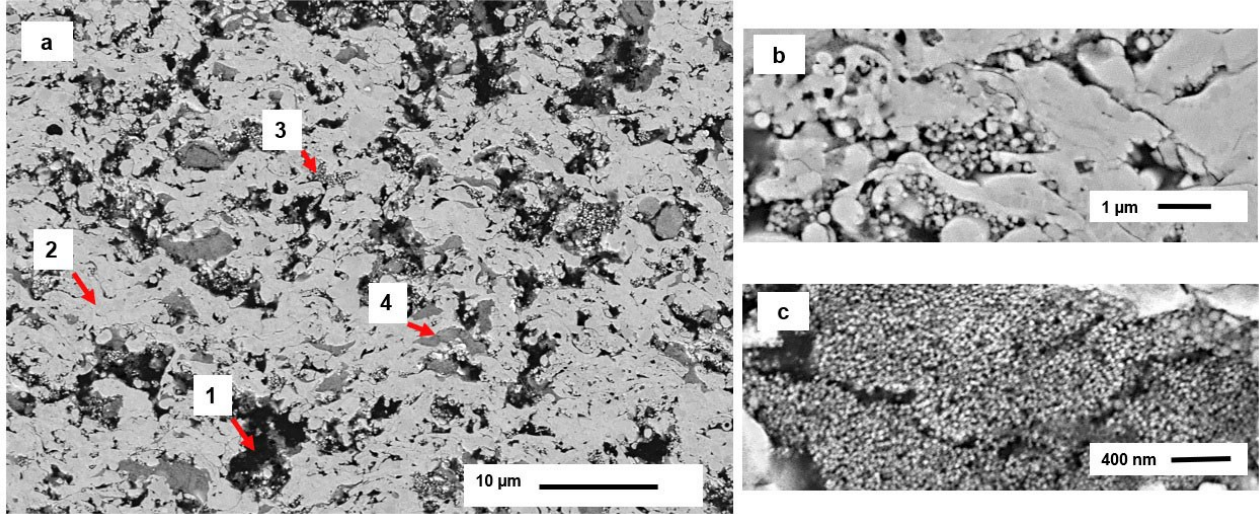


Figure 4.6 (a) SEM micrograph of a polished cross-section of the D5 coating showing: (1) large pores, (2) splats from the fully melted particles, and the co-existence of (3) submicron-sized particles from suspension and injector 1, and (4) nanosized particles from suspension and injector 2, (b) High magnification SEM micrograph of the submicron-sized particles, and (c) High magnification SEM micrograph of the nanosized particles.

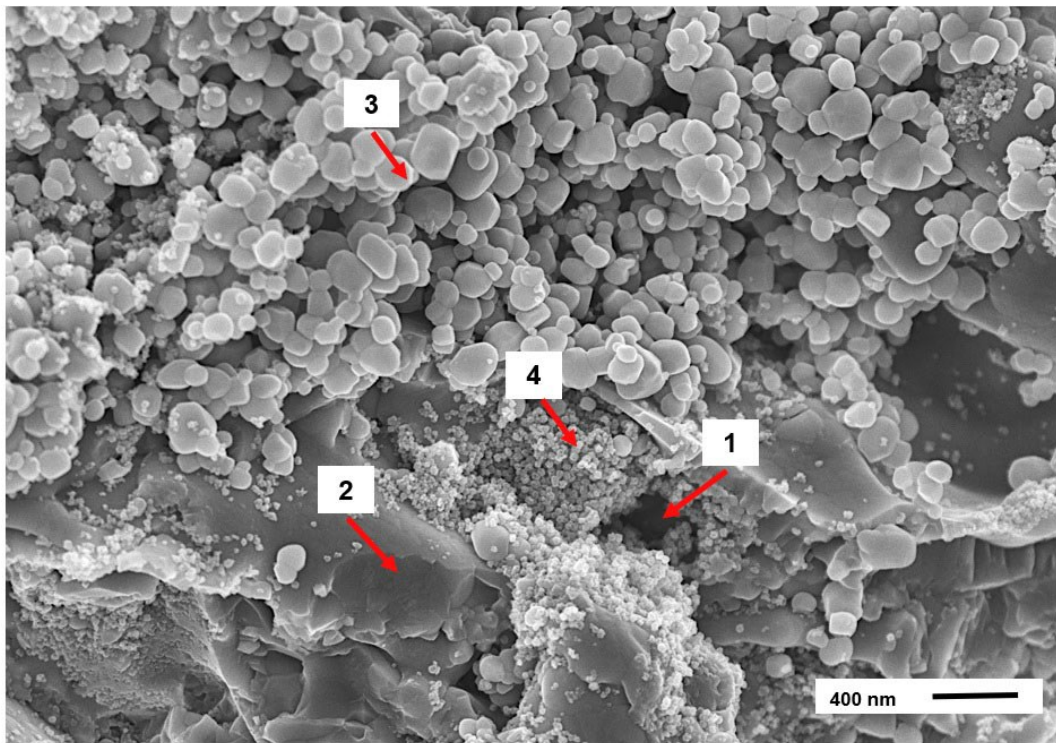


Figure 4.7) SEM micrograph of a fractured cross-section of the coating D5 showing: (1) large pores, (2) splats from the fully melted particles, and the co-existence of (3) submicron-sized particles from suspension and injector 1, and (4) nanosized particles from suspension and injector 2.

#### 4.3.1.1 Surface Morphology and Roughness

Table 4.3 summarizes the surface roughness measurements represented as  $R_a$  values. The data shows that D1, sprayed with one injector, exhibits the highest  $R_a$  value, while D5 and D8 demonstrate the lowest  $R_a$  values among the samples. The remaining samples exhibit surface roughness values falling between these extremes. Figure 4.8 displays the surface morphology of samples D1 to D8, where various degrees of columnar features in the form of bumps are seen on the surfaces of the coatings. In alignment with the  $R_a$  measurements in Table 3, the most significant columnar feature appears on the surface of D1. At the same time, D5 and D8 exhibit a much smoother surface structure compared to the other coatings. The possible reasons for the generation of the columnar shapes on the surface of these coatings are discussed in the following sections.

Table 4.3 Surface roughness measurements ( $R_a$ ) for coatings D1 to D8 obtained by confocal laser microscopy.

Sample	D1	D2	D3	D4	D5	D6	D7	D8
<b>Ra (<math>\mu\text{m}</math>)</b>	15.7 $\pm$ 0.2	6.3 $\pm$ 0.1	7.4 $\pm$ 0.1	8.1 $\pm$ 0.1	5.2 $\pm$ 0.1	7 $\pm$ 0.1	8.1 $\pm$ 0.2	4.1 $\pm$ 0.2

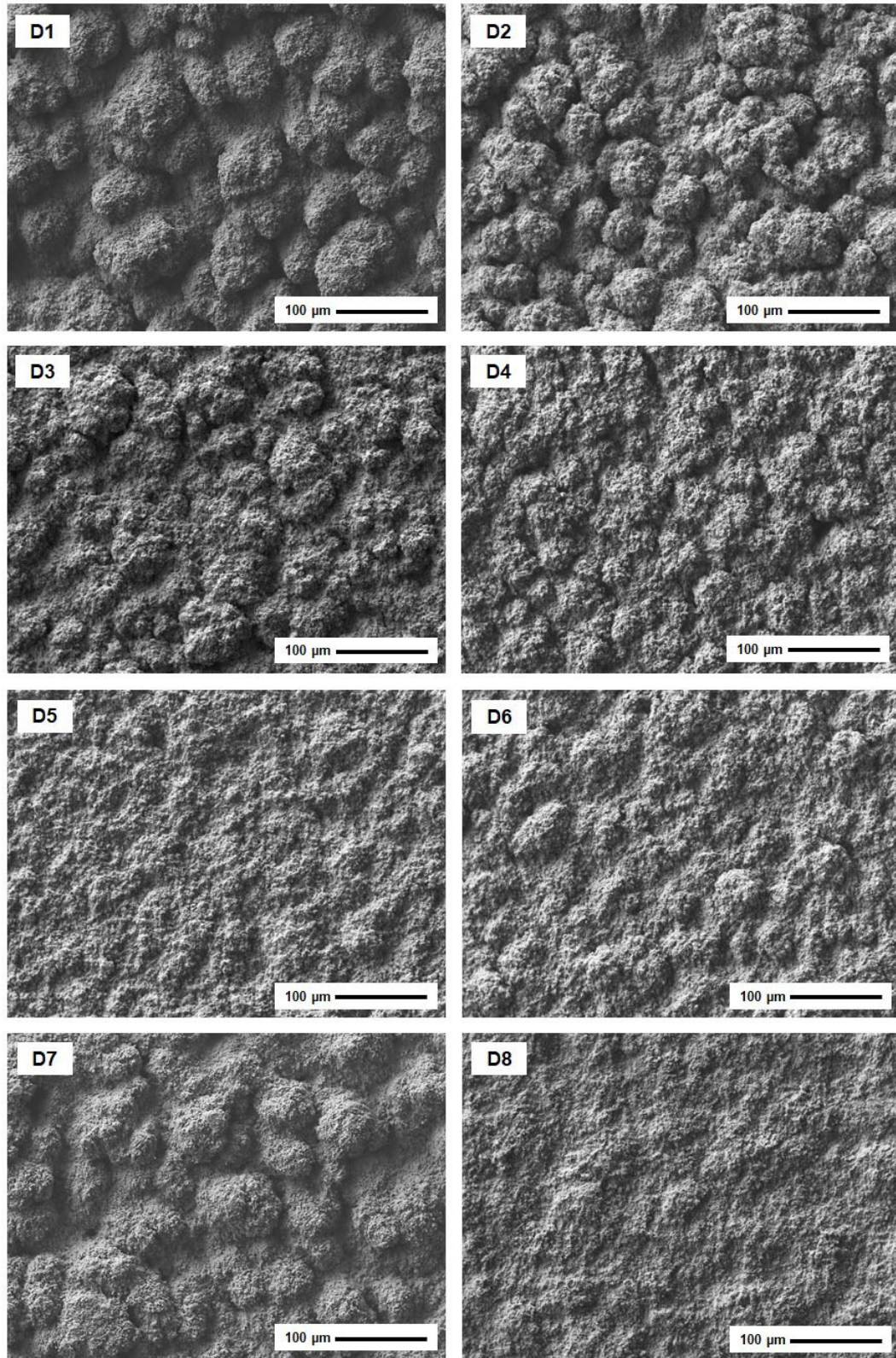


Figure 4.8 SEM micrographs of the surfaces of coatings D1 to D8.

#### 4.3.1.2 Porosity

Figure 4.9 shows the fraction of large pores (black regions in the microstructures), unmelted submicron-sized particles, and unmelted nanosized particles (indicated by two shades of grey color in the microstructures) in the coatings obtained from the image analyzing results. Comparing D1 and D2 (control samples), it is seen that the portion of large pores and unmelted submicron-sized pores were decreased in D2 when water was injected through injector 2. Notably, in samples D3 to D8, the proportion of the large pores and unmelted submicron-sized particles from injector 1 was relatively similar, suggesting that the variation of porosity level of coatings D3 to D8 is mainly related to the gaps between the unmelted nanosized particles from injector 2. Indeed, the porosity level increases with the percentage of unmelted particles/agglomerates introduced in the coating through injector 2 and suspension 2. The fraction of unmelted nanosized particles varies from around 10% to about 45%. Therefore, the increase in the fraction of unmelted nanosized particles in samples D3 to D8, with the exception of sample D4, indicates that the porosity level can be tailored by using a dual suspension injecting system. Considering the packing factor of around 60% for the randomly packed spheres [219], the total porosity of the dual-injected coatings could be estimated as the sum of the large pores and 40% of the unmelted submicron-sized and nanosized particle area. Therefore, the approximate value for the total porosity can be obtained between 16 % for D4 and 36 % for D8.

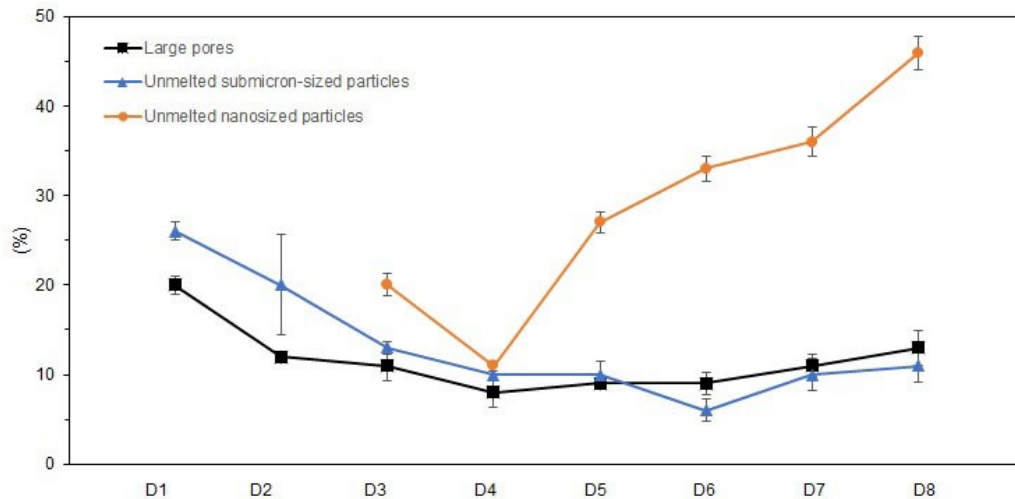


Figure 4.9 Ratio of the large pores, the unmelted submicron-sized particles from injector 1, and the unmelted agglomerates of nanosized particles from injector 2 in coatings D1 to D8.

By examining Figure 4.5 and Figure 4.9, the effect of different spray parameters utilized in this study on the porosity level of the coatings can be discussed. As anticipated, increasing the distance between the two injectors led to an increase in porosity. By increasing the distance between the injectors, suspension 2 was introduced into the plasma jet further away from the

torch exit. As a result, the agglomerates composed of nanosized TiO<sub>2</sub> particles had less exposure to the hotter regions of the plasma plume, and their residence time within the plasma jet was reduced. Consequently, the large agglomerates of suspension 2, which were a few microns in size, could not receive sufficient heat to fully melt, leading to the presence of unmelted agglomerates of nanoparticles within the coatings. However, an unexpected decrease in unmelted nanosized particles was observed in sample D4. The reason behind the observed decrease in porosity in D4 compared to D3 remains uncertain at this point. We expected a higher portion of unmelted nanosized particles from suspension 2 in D4, given that in D4, suspension 2 was injected at a longer distance into the plasma. This aspect warrants further investigation, and the experiment can be replicated to delve deeper into this phenomenon.

In addition, increasing the solid content of suspension 2 and decreasing the feed rate of suspension 1 increased the porosity level. The most prominent increase in porosity in sample D8 was observed when both the suspension feed rate was decreased and the distance between the injectors was increased. Comparing D3 and D7, one possible speculation could be that reducing the feed rate of suspension 1 may result in the deposition of fewer unmelted submicron-sized particles and melted splats from suspension 1, which could be the reason for the lower thickness of sample D7 compared to D3. On the other hand, a lower feed rate of suspension 1 could potentially lead to deeper penetration of suspension 2 in the plasma jet in sample D7. Therefore, in D7, suspension 2 can take higher advantage of the atomization and momentum of the plasma to deposit more efficiently in the coating. The subsequent sections discuss the factors that may impact the microstructure of the coatings and the variation of the proportion of unmelted agglomerates from suspension 2 within the coatings, consequently affecting the level of porosity in the coatings.

#### 4.3.1.3 Influence of the Inflight Particle Velocity and Substrate Temperature

Table 4.4 displays the thickness of the coatings, substrate temperature, and the velocity of the inflight particles for samples D1 to D8. It can be seen that by injecting water and suspension through injector 2, the thickness of the coatings, the substrate temperature, and the velocity of the inflight particles were decreased.

Table 4.4 Thickness, substrate temperature, and inflight particle velocity of the coatings D1 to D8.

Sample	Coating Thickness ( $\mu\text{m}$ )	Substrate temperature ( $^{\circ}\text{C}$ )	Inflight particle velocity (m/s)
D1	145.6 $\pm$ 2.8	450	298
D2	76 $\pm$ 1.2	380	227
D3	92.5 $\pm$ 1.9	350	232
D4	62.1 $\pm$ 1.5	300	281
D5	73.2 $\pm$ 1.3	330	261
D6	72.1 $\pm$ 1.6	300	233
D7	73.6 $\pm$ 1.7	350	235
D8	61.6 $\pm$ 1.3	290	230

Upon examining Figure 4.3 and Figure 4.5, it is observed that when water or suspension was injected into the plasma jet through injector 2, the thickness of the coatings was reduced significantly. With the exception of sample D3, which demonstrated a relatively smaller decrease, the thickness of the coatings in the remaining samples was reduced by approximately 50% compared to the control sample D1. The data indicate that when water or suspension was introduced into the plasma jet, the temperature of the substrate decreased. This is expected since adding water and suspension through injector 2 cools down the plasma [220]. Although the submicron-sized particles of suspension 1 may heat up rapidly in the plasma jet, they also lose their temperature faster than the larger particles. Therefore, some of the particles coming from suspension 1 could resolidify due to the decrease in the plasma temperature and probably not attach to the surface of the substrate, resulting in a deposition of coatings with lower thickness.

Furthermore, Figure 4.5 also reveals that the dark grey regions in the coatings, primarily consisting of agglomerates formed by nanosized particles introduced through injector 2, exhibit a relatively globular shape. This observation could be attributed to the fact that suspension 2 was injected further downstream of the plasma jet, leading to thermal and kinetic energy loss in the inflight particles. As a result, the velocity and momentum of the particles may not be sufficient to flatten the original form of the agglomerates [221]. The reduced velocity of the inflight particles might have contributed to the lower deposition efficiency observed in samples D2 to D9. As a result, even some of the melted particles from suspension 1 might not have acquired sufficient kinetic energy to partially flatten and effectively participate in the coating build-up process. It also should be considered that in samples D7 and D8, the decrease in the suspension feed rate could also have contributed to reducing the thickness of the coatings.

#### *4.3.1.4 Influence of the Suspension Trajectory in the Plasma Jet*

Figure 4.10 compares the suspension trajectory for samples D1, D2, and D5. As mentioned in Table 2, sample D1 was sprayed with only submicron-sized suspension through injector 1, and D2 was sprayed with submicron-sized suspension through injector 1 and water through injector 2. Sample D5 was sprayed with the same spray parameters as D2, except that nanosized suspension was sprayed through injector 2. Sample D5 was chosen for this comparison as the higher solid content for suspension 2 was used in this condition. Figure 10 shows that water and suspension 2 (even at the higher suspension concentration) penetrate well in the plasma jet. Additionally, it is seen that adding injector 2 had a limited effect on the trajectory of suspension 1 injection through injector 1.

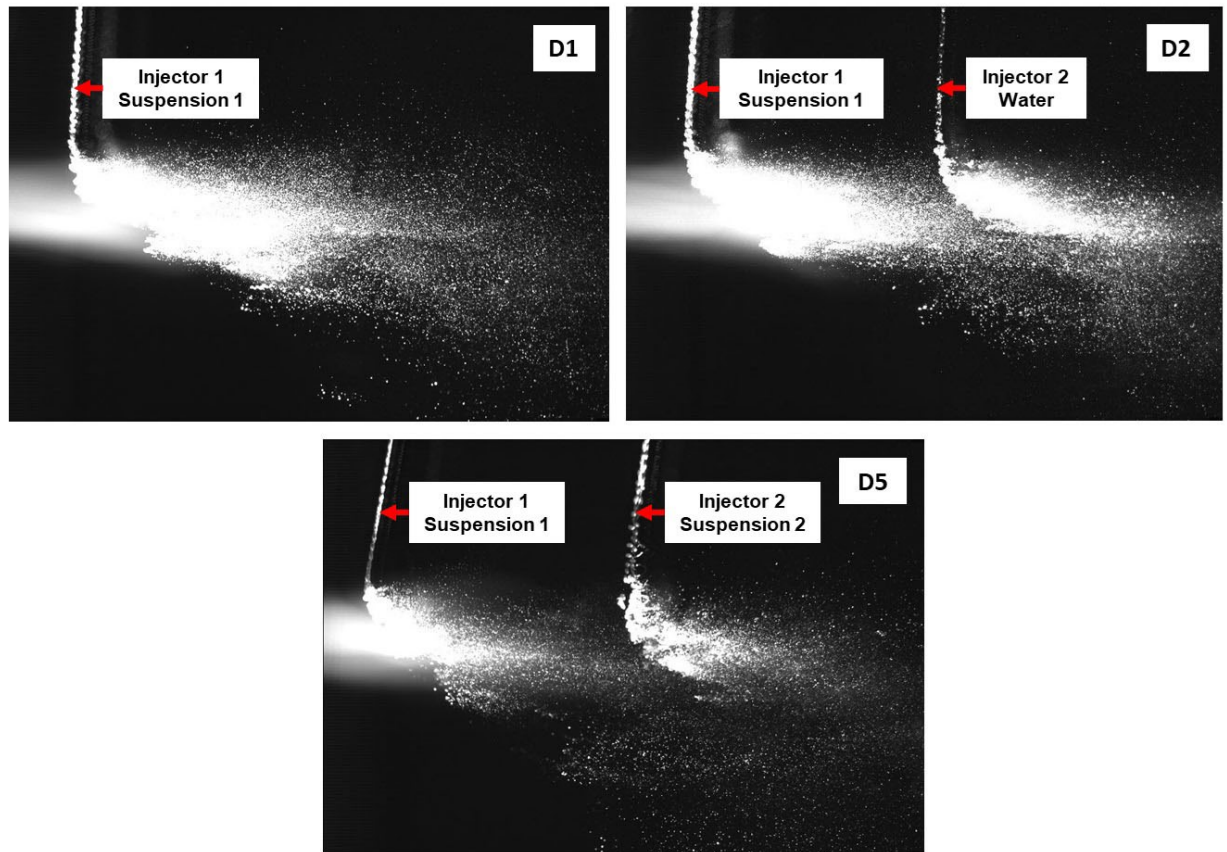


Figure 4.10 Plasma imaging pictures of control samples D1 sprayed with a single injector (coating was produced by spraying suspension 1 through injector 1), D2 sprayed with two injectors (coating was produced by spraying suspension 1 through injector 1 and water through injector 2), and D5 (coating was sprayed by spraying suspension 1 through injector 1 and suspension 2 through injector 2). The spray parameters were the same, except for the presence of injector 2 spraying water and suspension

Figure 4.11 shows the images of the suspension trajectory in the plasma jet for samples D7 and D8, showing the influence of the distance between the injectors. It is seen that in both cases the inflight particles originating from suspension 2 followed a trajectory that was relatively close to the plasma axis, confirming a good penetration of suspension 2 in the plasma jet. The penetration of suspension 2 into the plasma allows taking advantage of the atomization provided by the plasma at that point.

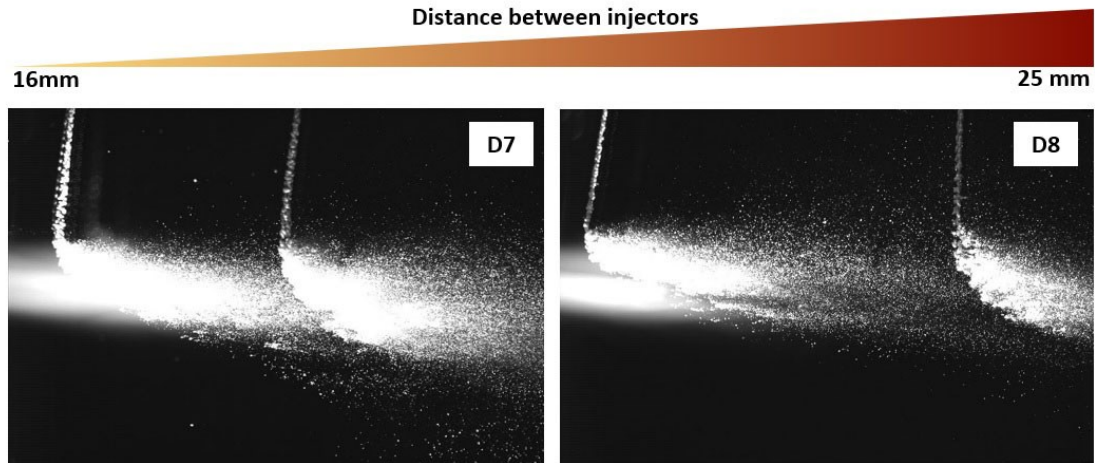


Figure 4.11 Suspension trajectory images of samples D7 and D8 showing the influence of increasing the distance between the two injectors, where submicron-sized and nanosized suspensions were sprayed through injectors 1 and 2, respectively.

The cooling effect of suspension 2 on removing the smaller particles of suspension 1 and its influence on the microstructure has already been discussed. Additionally, it is worth noting that by introducing suspension 2, the displacement of particles from suspension 1 could also be possible. It can be assumed that injecting water or suspension through injector 2 might have forced some smaller particles out of the plasma. This would be consistent with Joulia et al. who were able to remove the columnar features and produce very dense SPS yttria-stabilized zirconia coatings by altering the trajectory of very fine inflight particles in the vicinity of the substrate by employing a gas cooling system [132]. However, in this work the displacement of the particles was not evident in the images, which could be associated with the limited number of the inflight particle images that were captured.

#### 4.3.1.5 Influence of the Suspension Viscosity

Figure 4.12 shows the shear stress-shear rate measurements for suspension 1, suspension 2-20, and suspension 2-30 (20 and 30 indicate the wt.% of TiO<sub>2</sub> in suspension 2). Viscosity can be obtained from the slope of the lines. Suspension 1 exhibits a viscosity of nearly half of that observed in suspension 2-20 and suspension 2-30.

When the suspensions come in contact with the plasma jet, crossflow atomization takes place. The atomization process generates smaller droplets from suspension 1 with lower viscosity [133,210,222]. Consequently, smaller molten particles may be produced from the smaller droplets of suspension 1, which are more susceptible to get deviated close to the substrate due to the shadow effect [133,223]. Additionally, suspension 1 was injected in the plasma jet where the temperature and velocity are much higher, favoring fine atomization. Compared to suspension 1, suspension 2 included larger agglomerates of nanoparticles (a few micron-sized). Larger particles with larger inertia are less affected by the plasma drag forces. In addition, suspension 2 was injected downstream of the plasma jet, where the droplets

experienced lower temperature and momentum than droplets from suspension 1 [177]. Combined with the higher viscosity of suspension 2, this could lead to a less effective atomization of suspension 2. Therefore, larger droplets of suspension 2 would more likely hit the substrate with less deviation from the normal angle [217,223]. Hence, it could be assumed that the columnar features are more likely the product of suspension 1 injected from injector 1. On the other hand, the embedded large agglomerates of suspension 2 in the coating may increase the roughness on the surface of the deposited coating as the coating thickness increases during the deposition process, which could also enhance the likelihood of the generation of cauliflower-like clusters observed on the surface of the coatings in Figure 4.8 [15].

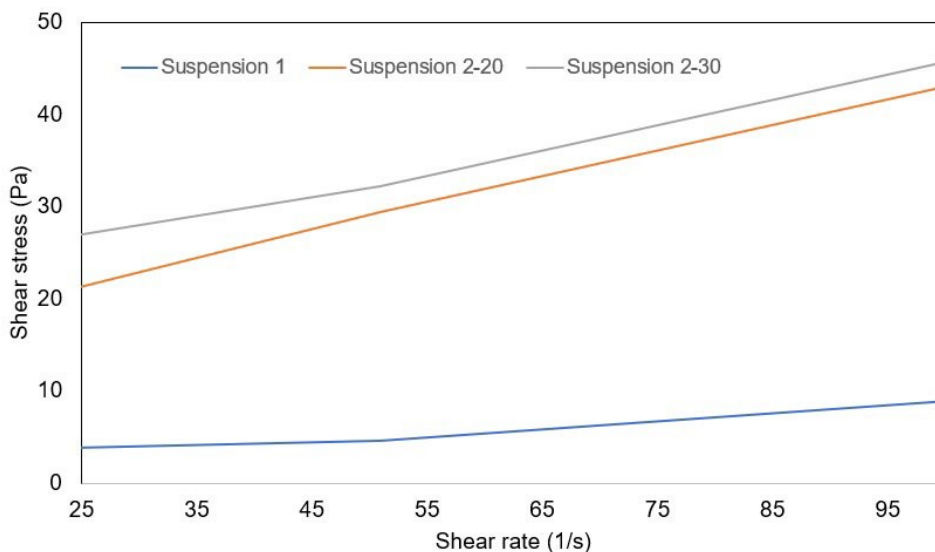


Figure 4.12 Shear rate vs shear stress measurements of suspension 1, suspension 2-20 (suspension 2 with 20 wt.%  $\text{TiO}_2$ ), and suspension 2-30 (suspension 2 with 30 wt.%  $\text{TiO}_2$ ). The slope defines viscosity.

### 4.3.2 Compositional Analysis

As mentioned earlier, the original purpose of this work was to explore a novel approach to tailor the porosity and the pore size for the SPS photocatalytic filtration membranes developed in other works by the authors. The fraction of the anatase phase in the  $\text{TiO}_2$  membranes plays an important role in photocatalytic efficiency. Therefore, analyzing the compositional characteristics of the SPS  $\text{TiO}_2$  coatings created using the dual injection system is important. The XRD patterns of the feedstock  $\text{TiO}_2$  powders and samples D1 to D8 are displayed in Figure 13 a. Furthermore, the Rietveld refinement for the two  $\text{TiO}_2$  powders and sample D8 with the highest porosity is shown in Figure 13 b as the reference for the quality of the measurements. Figure 13 b shows a good fit of the experimental and calculated results. The peaks match with the anatase pattern in powders 1 and 2 and anatase and rutile patterns in sample D8, with ICDD code number 00-021-1272 for anatase, and 00-021-1276 for rutile [180]. Table 5 shows that the compositional analysis of the coatings demonstrated various levels of anatase and rutile, indicating the transformation of a portion of the anatase in the feedstock powders into rutile during the coating process.

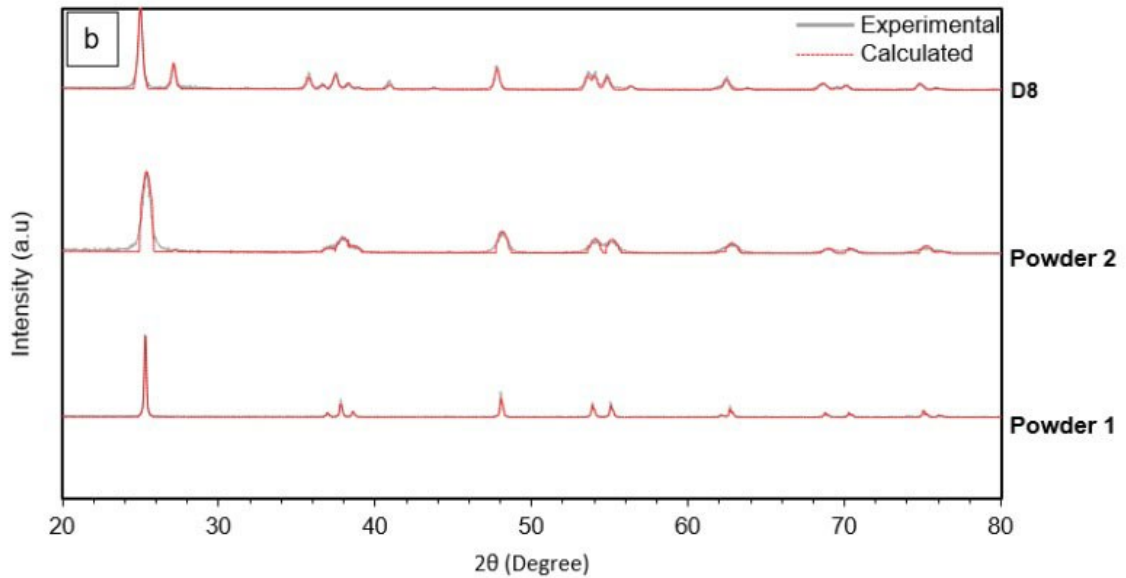
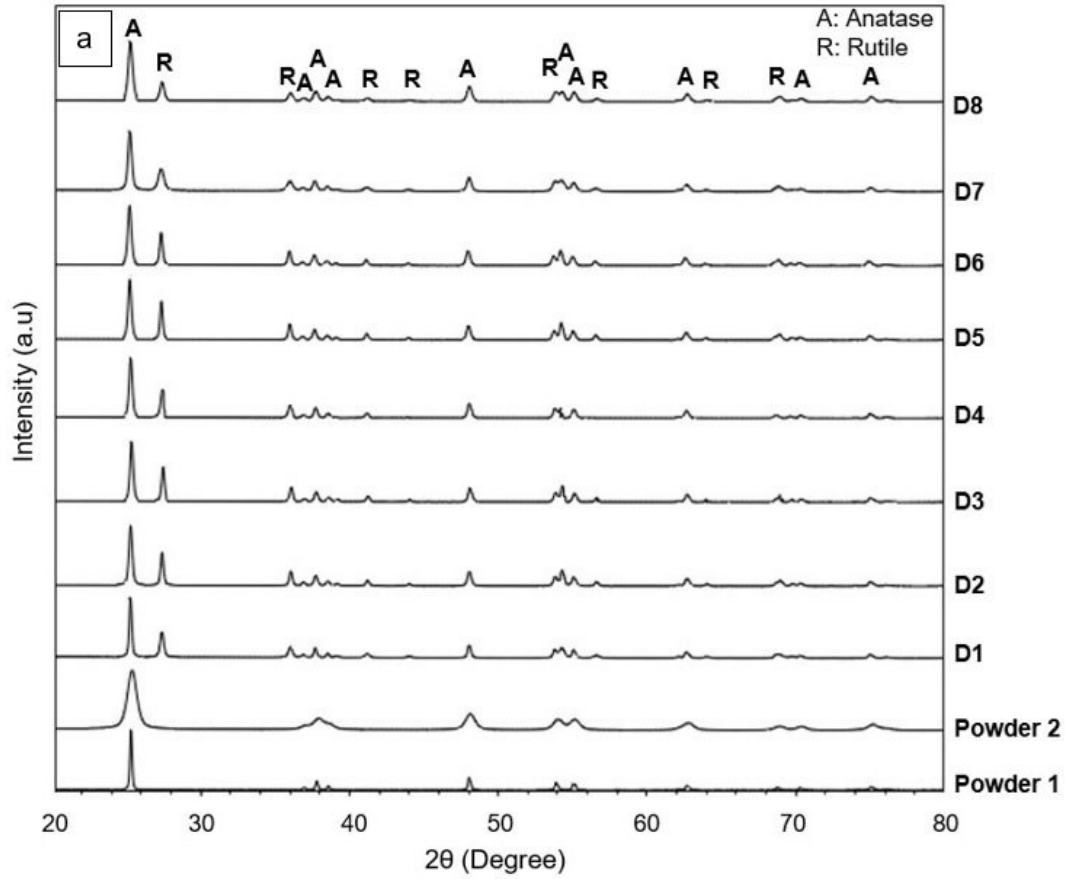


Figure 4.13 a) XRD patterns of  $\text{TiO}_2$  feedstock powders and samples D1 to D8. b) Rietveld refinement of XRD pattern of Powder 1, powder 2, and sample D8. (Powder 1 refers to the submicron-sized feedstock powder used to prepare suspension 1, and powder 2 to the nanosized feedstock powder used to prepare suspension 2.)

Table 4.5 Phase composition of TiO<sub>2</sub> feedstock powders and samples D1 to D8 obtained from XRD analysis. Powder 1 refers to the submicron-sized feedstock powder used to prepare suspension 1, and powder 2 to the nanosized feedstock powder used to prepare suspension 2.

Sample	Anatase (%)	Rutile (%)
Powder 1	100	-
Powder 2	100	-
D1	53.8	46.2
D2	56.7	43.3
D3	55.8	44.2
D4	59.1	40.9
D5	58.5	41.5
D6	61.6	38.4
D7	63.3	36.7
D8	70.2	29.8

Figure 4.13 also reveals the presence of broader peaks in powder 2 resulting from the smaller crystallite size in the nanosized TiO<sub>2</sub> powder compared to that in powder 1 (submicron-sized powder). The crystallite size of anatase in powders 1 and 2 was obtained at around 80 nm and 11 nm, respectively. Additionally, the coatings show peak widths that are relatively broader than those of powder 1 but narrower than those of powder 2. This could be due to the signal coming from both melted and unmelted regions in the coatings originating from both the submicron-sized and nanosized feedstocks. The anatase and rutile crystallite sizes in the coatings ranged from approximately 30 to 61 nm and 23 to 70 nm, respectively. The increase in the crystallite size could result from recrystallization taking place in certain nanoparticles during the coating process, which, while heated, do not undergo melting [184]. On the other hand, the crystallite size of the re-solidified anatase in the melted regions of the coatings generated due to the rapid solidification could decrease. In addition, in the melted regions, anatase size growth could be possible, on the hot substrate and below the anatase to rutile transformation temperature.

To better understand the phase composition of melted and unmelted regions in the coatings, Raman spectroscopy was performed on a selected number of coatings. The Raman spectra were obtained for D1 (produced by only suspension 1), D3 (produced with dual injectors with a rather low fraction of unmelted particles), and D8 (produced with dual injectors with a high fraction of unmelted particles). Figure 4.14 shows the Raman spectra of the unmelted and melted sections of the mentioned coatings. Peaks at 144, 197, 399, 513, 519, and 639 cm<sup>-1</sup> are recognized as the characteristic peaks for anatase, and peaks at 143, 236, 447, and 613 cm<sup>-1</sup> are associated with rutile [147]. The dark grey zones in the coatings (observed in Figures 4.5 and 4.6), where the unmelted particles from suspensions 1 and 2 were detected, are mainly composed of anatase. On the other hand, the light grey sections identified by the splats formed by the melted inflight particles coming from suspensions 1 and 2 consist of anatase and rutile.

At equilibrium solidification conditions, the irreversible transformation of anatase to rutile (the thermodynamically stable titania polymorph) occurs [224]. Thus, the melted in-flight particles (originated from anatase feedstock) are most likely to deposit as rutile. The influence of the latent heat of solidification from the adjacent splats has also been noted as a possible route for promoting anatase to rutile transformation within the coating [225]. Moreover, looking at the Raman spectra of the unmelted zones, very small humps can be observed at around 447, and 613  $\text{cm}^{-1}$  (the characteristic peaks of rutile), which could suggest that probably a small fraction of the unmelted in-flight particles could also heat up to the anatase to rutile transformation temperature without melting.

A fraction of the anatase observed in the coatings has originated from the remaining unmelted feedstock particles in the structure [117]. The presence of unmelted particles in our coatings was confirmed in the microstructural analysis in section 4.3.1. In addition, anatase may also nucleate from the molten phase that experiences high cooling rates [143,224]. In the SPS process, quenching of the splats increases the likelihood of higher degrees of undercooling, which could result in anatase nucleation from the molten phase [225]. Also, the lower substrate temperature could promote the formation of anatase as it may increase the cooling rate and limit the transformation of solidified anatase to rutile [143]. In this work, the injection of suspension 2 resulted in decreasing the substrate temperature, which amongst other possibilities mentioned above, could have increased the likelihood of anatase formation in the melted zones. The similar phase composition of the unmelted section of the coatings to that of the pristine feedstock powders may confirm the possibility of using the dual suspension injection system to control and retain the characteristics of the original feedstock in the final coatings.

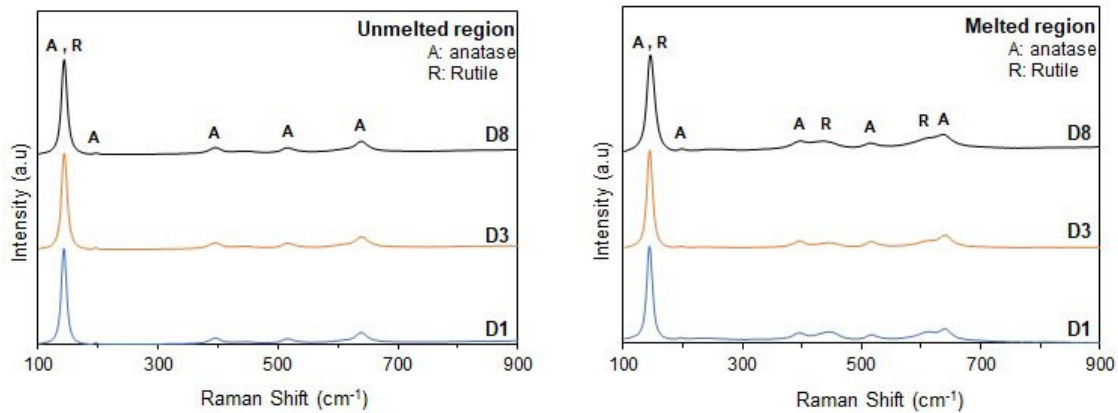


Figure 4.14 Raman spectra of the unmelted (identified in dark grey color in the microstructure) and melted areas (identified in light grey color in the microstructure), obtained from the cross-sections of coatings D1, D3, and D8.

## 4.4 Conclusions

This study investigated the feasibility of regulating the porosity in SPS coatings by an innovative approach, which consists of simultaneously injecting two feedstock suspensions at two radial distances from the plasma torch into the plasma jet. The possibility to tailor the porosity level and the pore size distribution is of potential interest for different applications such

as filtration membranes and multiphase composite coatings. The porosity was mainly linked to the fraction of the unmelted particles from the suspension sprayed through the injector located farther from the torch exit by relating it to the gaps among the unmelted particles. Our results showed that:

- In the dual injection system, it is possible to tailor the fraction of the unmelted inflight particles in the coating through introducing the second suspension injected into the plasma at a farther radial distance from the torch.
- Among the chosen spray parameters in this work, the distance between the two injectors and the suspension feed rates had a significant impact the proportion of unmelted particles in the coatings, which consequently affected the coating microstructure and porosity.

The results of this study can be used to regulate the porosity in SPS coatings, which could be a helpful means to adjust the parameters such as permeability and heat transfer of the deposited coatings or membranes. Moreover, it can potentially be used as a way to control and preserve the quantity of heat-sensitive feedstock in the nanostructured composite SPS coatings by limiting their exposure to high plasma temperatures. However, further optimizations need to be applied to the injection mechanism and the spray parameters to better control the injection system and the coating deposition process.

To more precisely define the trend describing the relation between the various spray parameters and the resulting microstructure, we intend to implement a comprehensive DoE approach in our future work. Incorporating a broader range of conditions in the coating deposition process is expected to yield more robust insights, contributing to a more accurate and comprehensive understanding of how different spray parameters impact the final microstructure in the dual-injected SPS coatings.

# Chapter 5 A Comparative Study of the Self-Cleaning and Filtration Performance of Suspension Plasma-Sprayed TiO<sub>2</sub> Ultrafiltration and Microfiltration Membranes

## **Preface**

The main objective of this chapter was to delve deeper into the performance aspects of the SPS ultrafiltration and microfiltration membranes. To better understand the benefits and limitations of SPS ceramic membranes, the filtration and self-cleaning characteristics of the SPS MF and UF membranes was studied. The UF membranes used in this chapter were deposited using a single suspension injection process detailed in chapter 3, since a more uniform microstructure was obtained compared to the dual injection approach.

**Abstract:** This study investigated the performance of photocatalytic titanium dioxide microfiltration membranes with an average pore size of approximately 180 nm and ultrafiltration membranes with an average pore size of around 40 nm fabricated with the suspension plasma spray process. The membranes were evaluated for their filtration performance using SiO<sub>2</sub> particles of different sizes and polyethylene oxide with molecular weights of 20 kDa to 1000 kDa, and the fouling parameters were characterized. The rejection rate was enhanced by increasing the thickness of the membranes. This effect was more pronounced with the ultrafiltration membranes. The rejection rate of the ultrafiltration membrane was improved significantly after filling the larger pores on the surface with agglomerates of titanium dioxide nanoparticles. The self-cleaning performance of the membranes was assessed under visible light. Both ultrafiltration and microfiltration membranes showed a flux recovery under visible light illumination due to the photocatalytic activity of titanium dioxide. The membranes also show a flux recovery of more than 90%.

**Keywords:** suspension plasma spray; ceramic membrane; ultrafiltration; microfiltration; fouling; self cleaning

## 5.1 Introduction

Over the past few decades, the significant expansion of industrialization, coupled with climate change, population growth, and water contamination, has emerged as a critical concern for sustainable development due to the increasingly severe scarcity of water resources [1,2]. Therefore, affordable and highly efficient membrane-based technologies with low energy consumption, modular nature, and small footprint have become increasingly popular for water and wastewater treatment [3,226]. Among these technologies, microfiltration (MF) membranes with a pore size ranging from 100 nm to 10  $\mu$ m and ultrafiltration (UF) membranes with a pore size of 2-100 nm are widely utilized due to their ability to remove contaminants with large molecules at low pressure [227].

Due to their superior mechanical strength, resistance to fouling, and high chemical and thermal resistance, ceramic membranes are regarded as favorable candidates for water treatment [228]. However, when it comes to the extensive utilization of ceramic membranes, capital cost and efficiency are critical considerations and present notable challenges. To overcome these challenges, new materials, production processes, and performance-improving techniques have been explored [229]. Despite the numerous advantages offered by the MF and UF processes in membrane technology, the challenge of membrane fouling persists and influences the development of membrane applications [230]. The performance of the membranes can be easily affected by fouling, which may occur by organic and inorganic substances and bio-contaminants [52,231]. Subsequently, fouling causes a reduction in membrane flux, separation efficiency, and lifespan while also increasing cost and energy consumption [52,232]. Various approaches have been employed to mitigate membrane fouling, including physical and chemical cleaning, pretreatment of the feed, combining membrane technologies and processes, and development of

antifouling and self-cleaning membranes [52,230]. Typically, the fouling caused by organic colloids on membranes is addressed by pre-treating the feed and optimizing process parameters. Therefore, the development of self-cleaning and anti-fouling membranes is focused on reducing the fouling effect of organic contaminants [52]. Integrating photocatalysis properties with the filtration process is an ever-growing approach that could enhance the purification efficiency of the membrane by providing a self-cleaning potential. Titanium dioxide ( $\text{TiO}_2$ ) is a semiconductor that can degrade organic contaminants due to photocatalytic reactivity. When exposed to UV light, the photo-generated electron-hole pair may react with water and oxygen to produce highly oxidizing reactive oxygen species (ROSs) such as  $\text{HOO}^\cdot$ ,  $\text{O}_2^{\cdot-}$ , and  $\text{OH}^\cdot$  radicals. Further, ROSs contribute to the decomposition of organic contaminants [3,233]. Humic acid (HA) is a model organic contaminant widely used to characterize membrane processes [52]. Humic substances, including humic acids, are formed through the natural processes of the microbiological or chemical decomposition of organic matter and are found in soil and surface water [234,235]. HA is substantially used in the fertilizer production industry. The presence of a high dosage of HA in water could result in the generation of toxic material during the chlorination process [236]. Thus, removing HA is essential to the water treatment process before disinfection.

The rejection properties and anti-fouling/self-cleaning of the  $\text{TiO}_2$  incorporated membranes have been discussed in many studies. Teow et al. [237] investigated the influence of surface morphology on the anti-fouling property of PVDF/ $\text{TiO}_2$  membranes against HA under UVA illumination, with an enhanced flux recovery for the membranes with lower surface roughness. Zhang et al. [238] investigated the influence of hydrogenation on the HA removal efficiency of  $\text{TiO}_2$  membranes prepared by spinning and partial sintering processes under UVA light. Li et al. [239] studied the influence of surface modification of ceramic membranes coated with  $\text{TiO}_2$ -GO composition on photocatalytic reactivity to remove HA, where pore-blocking was the primary fouling mechanism. Lin et al. [140] characterized the fouling mechanisms in  $\text{TiO}_2$  MF membranes produced by the atmospheric plasma spray (APS) process using silicon dioxide ( $\text{SiO}_2$ ), HA, and dextran. In their study, pore-blocking and cake formation resistance were the dominant mechanisms influencing the photolysis-filtration of HA and dextran solutions.

Recently, suspension plasma spray (SPS) technology was introduced by the authors as a novel method to fabricate  $\text{TiO}_2$  membranes with average pore sizes in the range of MF and UF, with a rather high pure water permeability and photocatalytic activity under UV and visible light [15,199]. SPS is a developing thermal spray coating deposition process that can produce thin nanostructured coatings due to using a feedstock of submicron to nanometer-sized particles suspended in a solvent. In SPS, the suspension of very fine particles is injected in a high-temperature and high-velocity plasma jet, where the temperature in the core of the plasma jet exceeds 8000K [128]. Due to the aerodynamic drag forces in the plasma jet, the suspension droplets break into smaller fragments and get accelerated toward the surface of a substrate [240]. In an ideal process, when all the fragmentation occurs close to the plasma core, the solvent that carries the inflight particles may evaporate completely, and the particles melt before impacting the substrate surface and get deposited in the form of splats [214]. However, the inflight particles that travel in the fringes of the plasma, gaining lower temperature and momentum, may get partially melted or remain unmelted [128]. Subsequently, the coating is formed layer by layer

through the repeated impact of the melted, partially melted, and unmelted particles onto the substrate. In addition, the thickness of the SPS coating can be adjusted by the number of times the plasma torch scans the surface of the substrate. Furthermore, coatings with various microstructures can be produced by adjusting the feedstock properties and the spray parameters. These microstructures can vary from fully dense coatings [24] to porous coatings with vertical cracks [133], porous coatings with various forms of columnar features that appear in the form of bumps on the surface [25–28], and uniformly porous coatings [134]. This versatility allows producing coatings suitable for a wide range of applications.

The SPS membranes own a unique porous microstructure, where the porosity depends on the presence of the retained unmelted feedstock particles within the structure, and the average pore size relates to the particle size of the pristine feedstock powder. Additionally, the SPS TiO<sub>2</sub> membranes exhibit photocatalytic properties under UV and visible light [15,199]. The photocatalytic activity of TiO<sub>2</sub> membranes under visible light is due to the generation of sub-stoichiometric TiO<sub>2-x</sub> under the SPS conditions [241]. The presence of oxygen vacancies in the lattice of TiO<sub>2-x</sub> in the membrane, known as self-doping, leads to lower bandgap energy [199]. Consequently, the SPS TiO<sub>2</sub> membranes can absorb lower energy photons in the range of visible illumination. Visible light-driven photolysis could introduce a promising alternative to decrease the energy requirement for UV utilization.

Other advantages of the SPS method over conventional ceramic membrane fabrication techniques and other thermal spray processes could be outlined as flexibility and efficiency, which align well with industrial requirements [242]. The primary emphasis of our earlier works was to investigate the feasibility of creating porous structures with pore sizes in the range of UF and MF membranes suitable to use as filtration membranes. [15,199]. In this study, we aimed to build upon those previous efforts and delve deeper into the performance aspects of the SPS membranes. To better understand the benefits and limitations of SPS ceramic membranes, this work investigates the filtration and self-cleaning characteristics of the SPS MF and UF membranes produced in our previous works. The inorganic contaminants (SiO<sub>2</sub> particles) were used to characterize the rejection efficiency of the SPS membranes. In addition, organic pollutants (humic acid (HA) and methylene blue (MB)) were used to study the self-cleaning performance and recyclability of the membranes. Furthermore, the fouling mechanisms of the model contaminants were characterized.

## **5.2 Materials and Methodology**

### **5.2.1 Membrane Preparation**

The suspension plasma spray (SPS) process was used to produce the TiO<sub>2</sub> membranes. The membranes were sprayed on porous stainless-steel discs (diameter:38 mm, thickness:1.6 mm). The thickness of the membranes was controlled by the number of times the plasma torch passed over the surface of the stainless-steel substrates (spray passes).

The membranes were identified based on the number of spray passes, according to Table 5.1. Membranes UF-2×4P and MF-2×12P were built by stacking two UF-4P and two MF-12P,

respectively. The stacked configuration was achieved by placing one membrane over another and securing them together using silicon glue.

Table 5.1 Identification of the membranes.

Sample name	No. of spray passes
UF-2P	2
UF-4P	4
UF-2×4P	stacking two UF-4P
MF-12P	12
MF-2×12P	stacking two MF-12P

The details of the fabrication process for the SPS microfiltration (MF) membranes [15] and ultrafiltration (UF) membranes [199] and comprehensive discussions regarding the microstructures and some particular properties of the UF and MF membranes have been published in our previous works. For a clearer understanding and to contextualize the findings in this current manuscript, here, a concise overview of the UF and MF membrane characteristics based on our previous research is presented.

The UF membranes were produced using a nanosized TiO<sub>2</sub> powder. The average TiO<sub>2</sub> particle size was 27±10 nm. However, the TiO<sub>2</sub> nanosized particles formed natural agglomerates with d<sub>50</sub>= 3.1µm in the feedstock suspension used in the SPS process. The presence of these agglomerates showed to be essential to produce nanosized pores within the structure [199]. On the other hand, the MF membrane was produced using a submicron-sized TiO<sub>2</sub> powder, where the average TiO<sub>2</sub> particle size was 137±40 nm, and the SPS feedstock suspension showed d<sub>50</sub>=280 nm [15]. The average pore size and the pore size distribution of the UF and MF membranes were obtained using the mercury intrusion porosimetry method. The average pore size of the UF membranes was around 36 nm, which was in the range of ultrafiltration. However, the pore size exhibited a multi-modal distribution due to the presence of some large pores in the range of a few micrometers [199]. Alternatively, the average pore size of the MF membranes was around 180 nm, with a relatively narrow pore size distribution [15]. A brief description of some of the features of the SPS membranes can be found in the supplementary materials section (Appendix 1).

## 5.2.2 Membrane Characterization

The surface roughness of the membranes was measured with a confocal laser microscope (LEXT OLS4000 Olympus, Toronto, ON, Canada). Three-dimensional surface images were obtained by stitching 25 single images of the surface in three spots. The arithmetic average surface roughness (R<sub>a</sub>) and the mean height difference between the highest peak and five lowest valleys (R<sub>z</sub>) [243] have been reported. In addition, the morphology of polished cross-sections of the membranes was observed with an ultra-high resolution scanning electron microscope (SEM) (Hitachi Regulus 8230, Mississauga, ON, Canada).

The water contact angles on the surface of the membranes were obtained using a contact angle measuring system (VCA, AST products Inc., Billerica, MA, USA).

### 5.2.3 Membrane Performance

The separation efficiency of the membranes was determined using 1wt.% aqueous colloidal suspensions of SiO<sub>2</sub> (PiKem Co., Tamworth, UK) with average particle diameters of 200 and 400 nm. The particle size distribution of the two SiO<sub>2</sub> powders was measured using a Zetasizer Nano ZS system (Malvern Panalytical, Malvern, UK). It was noted that the SiO<sub>2</sub> powder with an average particle size of 200 nm displayed a broader particle size distribution (Appendix 1, Supplementary Materials, Figure S1).

The filtration was carried out in a dead-end vacuum filtration device. A mixing device was added to the filtration system to keep the feed agitated during the process. The transmembrane pressure for all the performance measurement tests was around 0.3 bar. The concentration of the SiO<sub>2</sub> particles in the filtrate and feed was measured using a turbidity meter (Oakton T-100, Cole-Palmer, Quebec, QC, Canada). It has been reported that turbidity is directly related to the total suspended solid concentration of slurries [244,245]. Calibration curves were produced to obtain the concentrations of suspended SiO<sub>2</sub> in the filtrate. In both 200 nm and 400 nm SiO<sub>2</sub> suspensions, the concentration showed linearity with the turbidity. The concentration of the SiO<sub>2</sub> particles in the filtrate was measured by collecting about 10 ml of filtrate after around 30 min of filtration.

The separation efficiency was calculated by Equation (5.1) [246]:

$$R (\%) = \left(1 - \frac{C_f}{C_0}\right) \times 100 \quad (5.1)$$

Where  $C_f$  and  $C_0$  are the concentration of the contaminant in the filtrate and feed, respectively.

The permeation flux was calculated by Equation (4.2) [237]:

$$J = \frac{V}{A \cdot t} \quad (5.2)$$

Where  $J$  is the permeation flux ( $L \text{ m}^{-2} \text{ h}^{-1}$ ),  $V$  is the permeation volume (L),  $t$  is the permeation time (h), and  $A$  is the surface area of the membrane ( $\text{m}^2$ ).

The flux recovery ratio (FRR) was calculated using Equation (5.3) [246,247]:

$$\text{FRR} (\%) = \frac{J_c}{J_0} \times 100 \quad (5.3)$$

Where  $J_c$  is the permeation flux of DI water after back-washing or self-cleaning ( $L \text{ m}^{-2} \text{ h}^{-1}$ ), and  $J_0$  is the initial permeation flux of DI water ( $L \text{ m}^{-2} \text{ h}^{-1}$ ). The membranes were back washed with 1000 mL of DI water at the transmembrane pressure of 0.3 bar.

The analysis of the fouling characteristics of the membranes during the SiO<sub>2</sub> particles separation was conducted by evaluating the ratio of fouling resistance (RFR) using Equation (5.4) -(5.6) [237,247,248]:

$$\text{RFR}_t (\%) = \left(1 - \frac{J_t}{J_0}\right) \times 100 \quad (5.4)$$

$$RFR_p(\%) = \left(1 - \frac{J_p}{J_0}\right) \times 100 \quad (5.5)$$

$$RFR_c(\%) = RFR_t(\%) - RFR_p(\%) \quad (5.6)$$

Where  $RFR_t$  is the total ratio of fouling resistance due to pore-blocking and cake formation.  $J_t$  is the flux of the SiO<sub>2</sub> suspension (L m<sup>-2</sup> h<sup>-1</sup>),  $J_0$  is the initial permeation flux of DI water (L m<sup>-2</sup> h<sup>-1</sup>),  $RFR_p$  is the ratio of fouling resistance due to pore blocking,  $J_p$  is the DI water flux measured after removing the SiO<sub>2</sub> cake layer (L m<sup>-2</sup> h<sup>-1</sup>), and  $RFR_c$  is the ratio of fouling resistance due to cake formation.

The SPS TiO<sub>2</sub> membranes exhibited absorbance and photocatalytic activity under visible light [199]. Therefore, the self-cleaning performance and recyclability of the membranes were investigated in three cycles using a dead-end vacuum filtration device under visible light condition [246]. The surface of the membrane was illuminated with two xenon arc lamps with a power of 35 W, each with an irradiance of 2.16 mWcm<sup>-2</sup>. No optical filter was used. The distance between the surface of the membrane and the light source was set at around 5 cm, and an electric fan was used to cool the setup. A 2 ppm solution of humic acid (68131-04-4, Sigma-Aldrich, St. Louis, MO, USA) with the pH adjusted at around seven was used to characterize the membranes' self-cleaning performance [237,249]. Each cycle consisted of three steps: i) filtering DI water for 15 min in the dark, ii) filtering HA solution for 15 min in the dark, and iii) filling with DI water and exposing the surface of the membranes to visible light for 150 min with no pressure. The evolution of the normalized flux was monitored as an indicator of the self-cleaning property of the membranes. The volume of the HA solution was maintained at around 30 mL throughout the duration of the experiment. In order to evaluate the extent of flux recovery after the self-cleaning process, following the 3<sup>rd</sup> cycle, around 30 ml of DI water was added to the system, and the membranes were exposed to visible light for 4h and then were back washed with 1000 mL of DI water and were rinsed thoroughly with DI water. The membrane DI water flux was measured after the 4 h exposure to visible light and after the hydraulic cleaning. Additionally, the recyclability of the UF-2P and UF-12P membranes in terms of the photo-degradation of the dye solution was investigated in three static cycles of 120 min using a 6 ppm methylene blue (MB) solution. After each cycle, the membrane was cleaned by immersing it in ethanol for around 12 h on the magnetic stirrer, flushing and rinsing thoroughly with DI water, and exposing it to UVC light for 12 h. The details of the test and the experimental setup for the MB degradation experiment have been described elsewhere [199].

The molecular weight cutoff (MWCO) was determined using 1wt.% polyethylene oxide (PEO) with molecular weights of 20, 100, 300, and 1000 kDa obtained from Sigma-Aldrich. The concentration of PEO was measured with a UV-vis spectrophotometer (Cary 8454, Agilent, Mississauga, ON, Canada) at the fixed wavelength of 535 nm [250,251]. For PEO, the molecular weight (MW) was converted into the pore diameter (nm) using Equation (5.7) [252]:

$$d_{50} = 0.11 MW_{50}^{0.46} \quad (5.7)$$

Where  $MW_{50}$  indicates the molecular weight of the organic molecule that can be rejected by 50%.

The Stokes radius of PEO was obtained using Equation (5.8) [253]:

$$a = 10.44 \times 10^{-3} (MW)^{0.587} \quad (5.8)$$

Where  $a$  is the Stokes radius (nm), and  $MW$  is the molecular weight of the PEO.

This study also utilized an infiltration process of nanoparticles into the structure of UF membranes to explore potential enhancements in the performance of UF membranes. Therefore, the manuscript presents two sets of results: first, the results for the untreated membranes, referred to as "as-sprayed" membranes, and following that, from section 5.3.3, the results obtained for the membranes subjected to infiltration, referred to as "filled membranes." The paper discusses the outcomes obtained from both sets of membranes in detail.

## 5.3 Results and Discussion

### 5.3.1 Membrane Microstructure and Roughness (As-sprayed Membranes)

Figure 5.1 illustrates the SEM micrographs of UF-2P, UF-4P, and MF-12P membranes. An overview of the cross-sections of UF-2P, UF-4P, and MF-12P membranes are shown in Figures 1a, 1c, and 1d, respectively. The main features of the SPS membranes include (1) light grey areas made of the melted splats, (2) black areas, which are the large pores in between the randomly stacked melted splats and/or agglomerates of nanosized TiO<sub>2</sub> particles, and dark grey areas, which in UF membranes are made of (3) agglomerates of unmelted nanosized TiO<sub>2</sub> particles, and in MF membranes are made of (4) unmelted submicron-sized TiO<sub>2</sub> particles. The dark grey zones in UF and MF membranes are finely porous regions. In the UF membranes, these pores are of nanoscale size and result from unmelted nanosized TiO<sub>2</sub> particles deposited as micron-sized agglomerates. In contrast, the dark grey regions in MF filtration membranes exhibit submicron-sized porosity, which arises from the gaps between unmelted submicron-sized TiO<sub>2</sub> particles. Additionally, the few micron-sized pores in the UF membranes, which closely aligned with the average size of the agglomerates of nanosized particles in the feedstock suspension, were linked to the large inter-agglomerate and inter-splats gaps, indicated by no.2, observed in Figures. 5.1a and 5.1c [199]. Figure 1b,e provide a detailed representation of the regions described earlier, namely regions 1 to 4. Microstructures of UF-2P and UF-4P membranes shared similar detailed features. Thus, it is expected that the detailed features presented in Figure 5.1b for UF-2P to be consistent in UF-4P. A comprehensive discussion regarding the microstructures of UF and MF membranes produced with the SPS process can be found elsewhere [15,199].

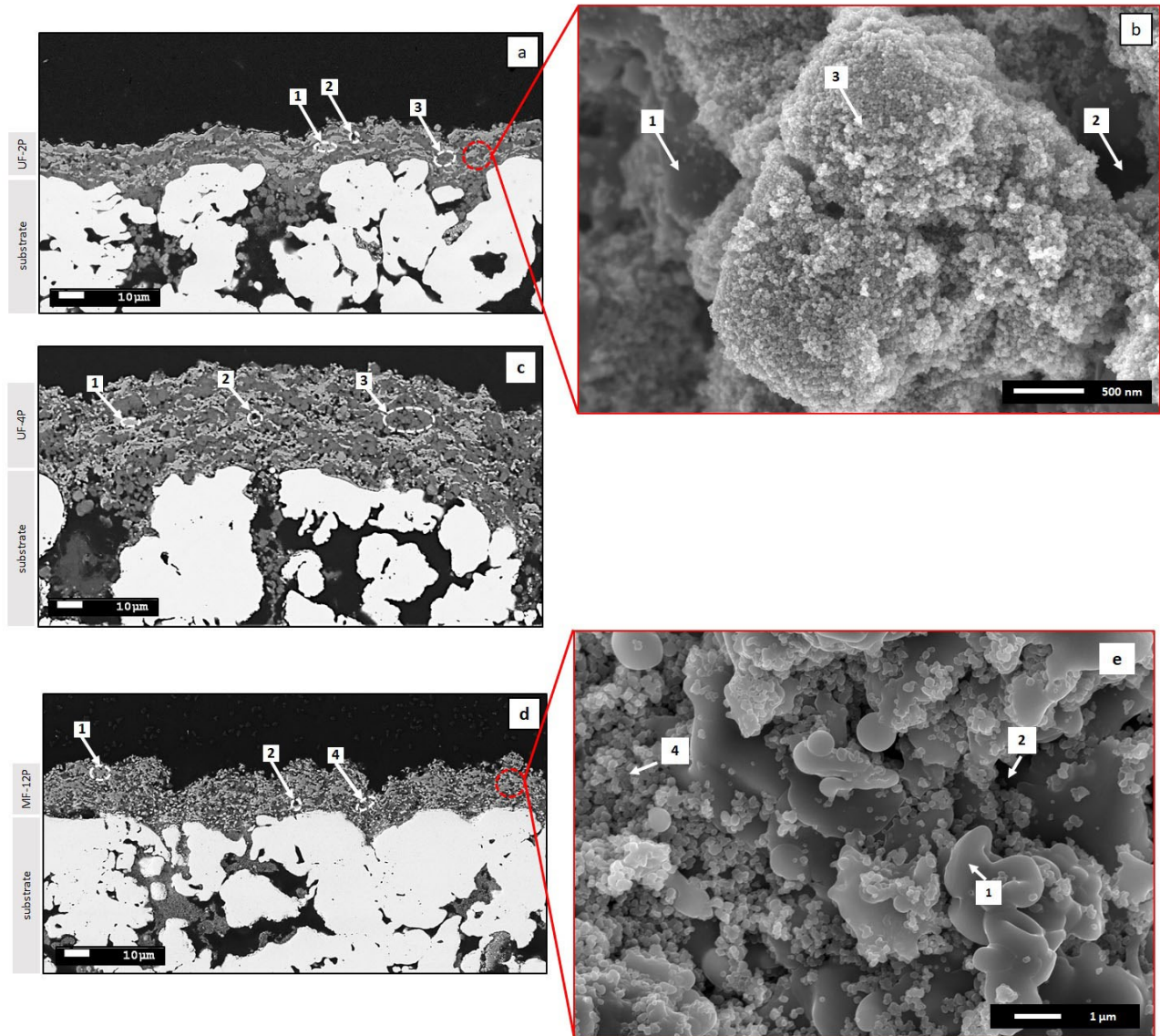


Figure 5.1 (a) SEM micrograph of the cross-section of the UF-2P membrane, (b) High magnification SEM micrograph of the red dashed zone in UF-2P membrane, (c) SEM micrograph of the cross-section of the UF-4P membrane, (d) SEM micrograph of the cross-section of the MF-12P membrane, and (e) High magnification SEM micrograph of the red dashed zone in MF-12P membrane. In both UF and MF membranes, no.1 (light grey areas) shows the melted splats, no.2 (black areas) shows the large pores, no. 3 (dark grey areas) shows the agglomerates of unmelted nanosized TiO<sub>2</sub> particles in the UF membrane, and no.4 (dark grey areas) shows the u-melted submicron-sized TiO<sub>2</sub> particles in the MF membrane.

Table 5.2 displays the thickness of the UF and MF membranes. The thicknesses of UF-2×4P and MF-2×12P were estimated to be twice that of UF-4P and MF-12, respectively.

Table 5.2 Thickness measurements of the UF and MF membranes.

Sample name	Thickness ( $\mu\text{m}$ )
UF-2P	$17.2 \pm 0.8$
UF-4P	$37 \pm 1$
MF-12P	$20.5 \pm 0.9$

The confocal microscope images of UF-2P, UF-4P, and MF-12P membranes in Figure 5.2 reveal the surface roughness of these membranes, while Table 5.3 provides the corresponding  $R_a$  and  $R_z$  roughness values. It is evident that the UF membranes have a lower roughness compared to the MF membranes. Furthermore, within the UF membranes, increasing thickness leads to decreased surface roughness. As mentioned earlier, higher surface roughness could make the membrane more susceptible to fouling. On the other hand, an increased roughness could probably enhance the photocatalytic performance by providing a larger reactive surface area. The higher surface roughness observed in the MF-12P membrane is attributed to the presence of columnar features or bumps on its surface (a brief description can be found in the Supplementary Materials section). Additionally, the larger pores on the surface of the stainless-steel substrate and the presence of smaller inflight species in the MF membrane feedstock, compared to the larger agglomerates in the UF membrane feedstock, could contribute to the higher roughness of the MF membrane.

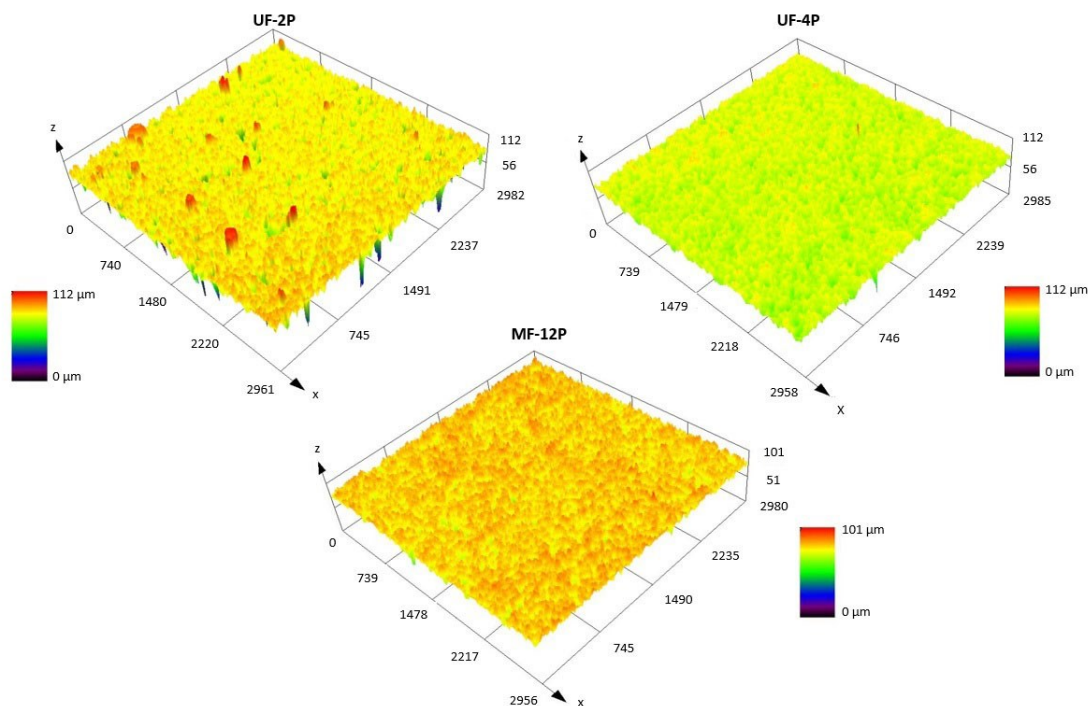


Figure 5.2 Confocal microscope images of UF-2P, UF-4P, and MF-12P membranes.

Table 5.3 The surface roughness of UF-2P, UF-4P, and MF-12P membranes.

Sample	Roughness (Ra) ( $\mu\text{m}$ )	Roughness (Rz) ( $\mu\text{m}$ )
UF- 2P	$5.3 \pm 0.3$	$41 \pm 2.6$
UF- 4P	$3.4 \pm 0.1$	$25.3 \pm 2.2$
MF-12P	$6.4 \pm 0.1$	$43.6 \pm 1.2$

### 5.3.2 Membrane Performance (As-sprayed Membranes)

#### 5.3.2.1 Separation Performance

Figure 5.3 shows the particle rejection efficiency of the UF and MF membranes. Both UF and MF membranes exhibit an enhancement in particle rejection as the membrane thickness increases. Similar findings regarding the impact of membrane thickness on rejection have been reported by Ramakrishnan et al. for thermally sprayed MF membranes [42] and by Ding et al. for the  $\text{TiO}_2$  UF membranes fabricated using a wet chemical method [45]. Wang et al. [254] also reported an increase in the rejection efficiency of two-dimensional graphene carbon nitride nanosheet membranes at higher thicknesses. Figure 5.3 also showed that overall, the MF membranes demonstrate superior particle rejection compared to UF membranes, and specifically, the UF-2 $\times$ 4P membrane exhibits particle rejection rates comparable to the MF-12P membrane. The higher rejection of the MF membrane can be explained due to its narrow pore size distribution with an average pore size of around 180 nm [15]. On the other hand, although the average pore size of the UF membrane was about 40 nm, the pore size distribution was multimodal, with some larger pores in the range of a few micrometers corresponding to the inter-agglomerates and inter-splat pores [199]. The presence of large pores can be the reason for the lower particle rejection in the case of UF membranes [255]. Additionally, it is worth noting that the broader range of particle sizes observed in the feed made with  $\text{SiO}_2$  with an average particle size of 200 nm might have played a role in enhancing the separation efficiency of the membranes when that particular feed was used. The improved separation efficiency for feeds containing mixed molecular weight solutes could be attributed to pore blocking, where larger particles that can still penetrate the pores may reduce the pore size. Reducing the pore size may result in a higher separation for the smaller particles in the feed [256].

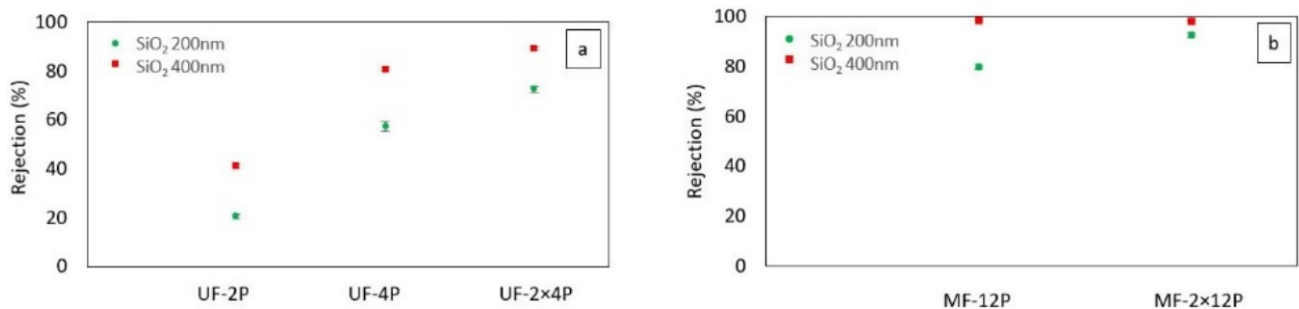


Figure 5.3 The  $\text{SiO}_2$  particles rejection % of (a) UF membranes and (b) MF membranes. The separation efficiency was increased as a function of the thickness of the membranes

During the filtration process, both UF and MF membranes underwent a substantial flux reduction (Appendix 1, Supplementary Materials, Figure S2). The flux decline during filtration occurs due to the fouling of the membranes through pore fouling and cake formation [237,246,249]. Also, employing a dead-end filtration system could have played a role in reducing the flux. By continuing the filtration in the dead-end mode, the thickness of the porous cake layer on the surface increases, leading to a decrease in the filtration rate. The formation of the cake layer may also improve the filtration efficiency. However, after a certain point, the excessive cake thickness interrupts the filtration process, and the membranes need to be cleaned [29]. Among the five membranes evaluated, it seems that the MF-2×12P demonstrated the most favorable performance, exhibiting relatively the lowest drop in flux and the highest particle rejection rates.

During the SiO<sub>2</sub> separation processes, fouling occurs due to two main mechanisms: pore-blocking and cake formation. In this work, the ratio of fouling resistance (RFR) was used to characterize the fouling behavior of the membranes. Figure 5.4 illustrates the fouling behavior of UF-2P, UF-4P, and MF-12P membranes. In Figure 5.4, the ratio of pore blocking is represented by the RFR<sub>p</sub>, and the ratio of cake formation is defined by RFR<sub>c</sub>. The RFR was not calculated for the UF-2×4P and MF-2×12P membranes since the cake layer could not be removed effectively from the surface of the stacked samples.

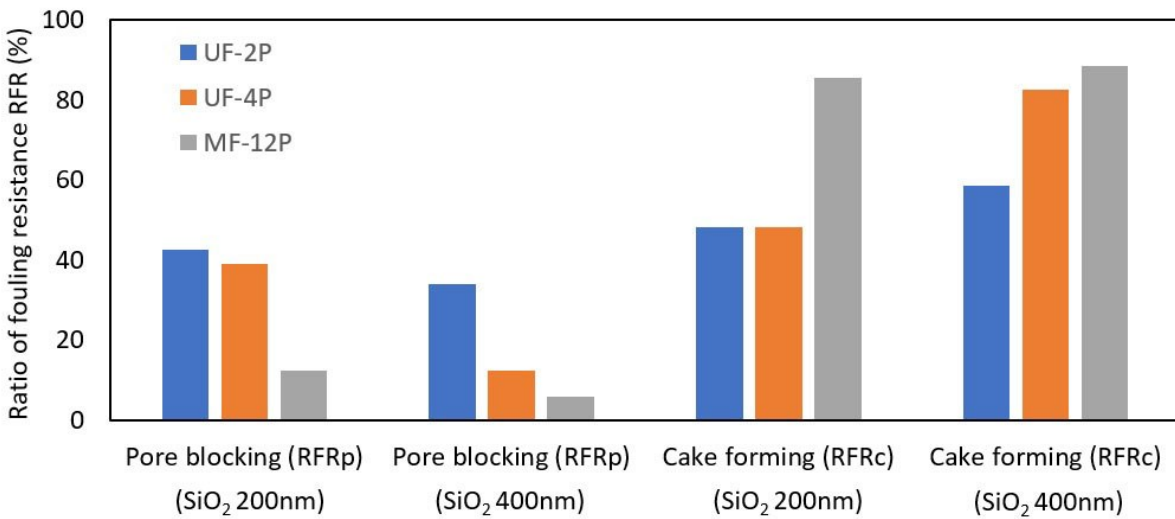


Figure 5.4 Fouling behavior of UF-2P, UF-4P, and MF-12P due to the pore blocking (obtained from RFR<sub>p</sub>) and cake formation (obtained from RFR<sub>c</sub>) phenomenon. A lower RFR value indicated a higher fouling resistance.

A lower RFR generally means a higher fouling resistance [237]. The primary fouling mechanism observed in the MF-12P membrane for both SiO<sub>2</sub> particle sizes is forming a cake layer. Moreover, the MF-12P membrane demonstrates a significantly higher resistance to pore-blocking than UF membranes. Furthermore, the findings suggest that increasing the thickness of UF membranes, especially at the larger foulant size, reduces their tendency to pore-blocking fouling. The influence of pore-blocking and cake formation seems comparable for the UF membranes at the smaller foulant size.

The multimodal nature of the pore size distribution and the presence of some large pores in the UF membranes has probably made them more susceptible to fouling due to pore-blocking. While the larger particles are rejected by the sieving mechanism, smaller particles could infiltrate the pores and decrease the pore size by deposition on the pore walls and narrowing the pores [231,257]. Therefore, the UF membranes are more prone to pore-blocking fouling than the MF membranes, which have a narrow pore size distribution, and the pore size is close to or smaller than the SiO<sub>2</sub> particle size. It also could be the potential reason for increased resistance to pore-blocking fouling with increasing the thickness of UF membranes. In UF-4P, the narrowing of the pore close to the surface of the thicker UF membrane could probably prevent further fouling by creating a narrower pore size distribution. The fouling mechanism may convert to cake formation following the generation of smaller pores on the surface. The pore-blocking fouling is more pronounced in the case of smaller SiO<sub>2</sub> particle size, where a more significant difference exists between the foulant particle size and membrane pore size. Additionally, the flux reduction of the UF membranes could be attributed to their increased tendency to pore blocking, corresponding to their relatively wide pore size distribution. In the SPS UF membranes, the presence of some larger pores contributes to a high initial flux. Consequently, the foulants may penetrate easier into the pores and cause a more severe flux decline due to the pore-blocking phenomena [30]. These observations may suggest that the average pore size does not solely determine the SiO<sub>2</sub> particle rejection efficiency of the SPS membrane, and the presence of a narrow pore size distribution also appears to play a significant role in influencing the separation performance [258].

Table 5.4 summarizes the flux recovery ratio (FRR) of the UF and the MF membranes. UF-2P, UF-4P, and MF-12P membranes showed FRR over around 95%. The UF-2×4P and MF-2×12P membranes demonstrated a lower FRR than the other membranes. UF-2×4P and MF-2×12P membranes were backflushed while preserving their stacked arrangement without any separation. Therefore, the lower FRR of UF-2×4P and MF-2×12P could correspond to the less efficient cleaning through the backwashing process due to the attachment of the membranes.

Table 5.4 Flux recovery ratio (FRR %) of the UF and MF membranes.

Sample	FRR (%)	
	SiO <sub>2</sub> (200 nm)	SiO <sub>2</sub> (400 nm)
UF-2P	96.8	98.1
UF-4P	96.5	95.1
UF-2×4P	76.9	79.7
MF-12P	94.5	98.1
MF-2×12P	80.9	82.7

### 5.3.2.2 Self-cleaning and Recyclability

Figure 5.5 illustrates the self-cleaning performance of the UF-2P and MF-12P membranes. The selection of UF-2P was based on its similarity in terms of thickness and surface roughness to that of MF-12P, allowing a more direct comparison between the two membranes. The self-cleaning trend observed in both UF-2P and MF-12P membranes was relatively similar

during the three cycles of the experiment. Initially, during the filtration stage involving HA, a sharp decline in flux is observed, attributed to membrane fouling. The fouling could occur due to a combined effect of accumulation of the foulants on the surface of the membranes, forming a cake layer and pore blocking throughout the membrane thickness [249].

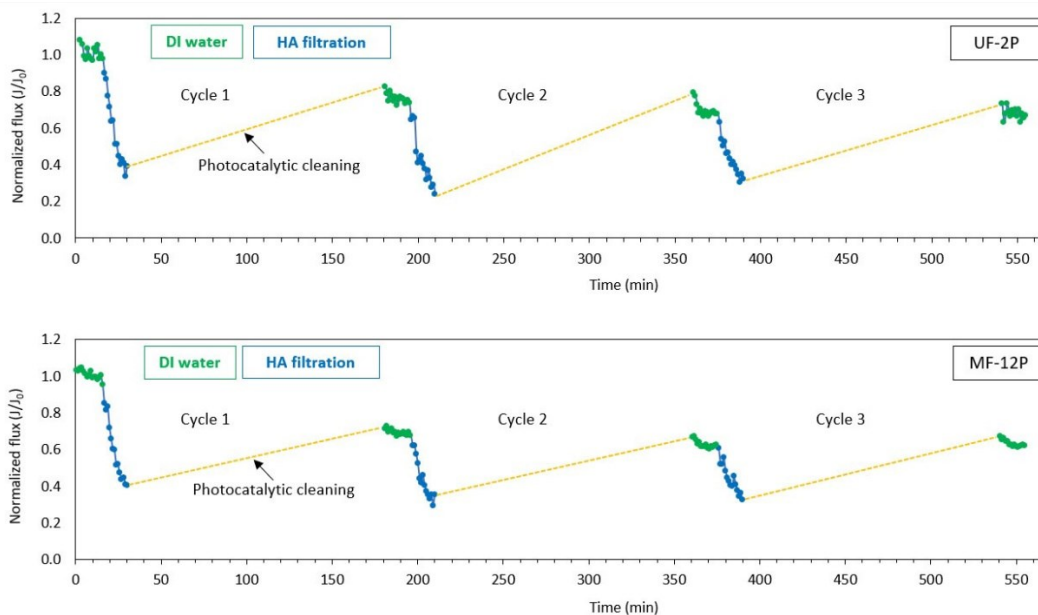


Figure 5.5 Self-cleaning performance of UF-2P and MF-12P membranes repeated in three cycles showing partial flux recovery of the membranes due to the photocatalytic cleaning of the membranes.

The self-cleaning property in a membrane is a parameter that can influence the lifespan of the membranes significantly. In this work, a series of dark and photocatalysis experiments were used to study the self-cleaning characteristics of UF-2P and MF-12P membranes in terms of HA removal.

After the photocatalytic cleaning in the 1st cycle, the membranes partially recover their initial flux, showing the removal of the foulants from the surface. However, the DI water flux does not fully return to its initial value before fouling occurs. This could be attributed to the pore-blocking phenomena due to the wide range of molecular weights in the HA solution [237,249]. Nystrom et al. [259] reported a more significant HA fouling in membranes with larger pores due to pore-blocking. Another possibility could be that the foulants were not completely decomposed during the photocatalytic cleaning process. It has been reported that the photocatalytic degradation of HA in the presence of  $\text{TiO}_2$  could initially be hindered due to the photo-depolymerization of large aromatic structures in HA. Subsequently, the photodegradation of HA follows the pseudo-first-order kinetics, resulting in the mineralization of HA into by-products [260,261]. Additionally, the depolymerization process lowers the molecular weight of the HA. Reduction in the molecule size could result in a decrease in the membrane flux due to narrowing the pore size [257]. On the other hand, smaller molecules can also pass more easily through the pores and potentially contribute to flux recovery as well. Therefore, the observed

partial increase in the flux could have occurred probably even without a complete degradation of the foulant. A similar trend was observed during the 2nd and 3rd cycles of the experiments, with a slight decrease in the DI water flux toward the end of the experiment. The flux recovery ratio during the three cycles of experiments is 75%, 68%, and 67% for the UF membrane and 69%, 61%, and 62% for the MF membrane, indicating the recyclability of the de-fouling process. It is also worth noting that the kinetics of the photodegradation of HA by TiO<sub>2</sub> can be influenced by various factors related to the properties of the HA substance itself. These factors include the origin of the HA, the method of extraction, its interactions with the environment, and age [262]. Furthermore, other parameters, such as the morphological characteristics of TiO<sub>2</sub>[233], the chemistry of water [263], and the experimental parameters, such as the wavelength and the intensity of the light, also influence the photocatalytic degradation process.

The photocatalytic activity of the SPS TiO<sub>2</sub> membranes under visible light is due to the generation of oxygen vacancies in the lattice of TiO<sub>2</sub>, known as self-doping. As a result, the band gap energy of the SPS TiO<sub>2</sub> membrane is reduced, allowing the photo generation of electron-hole pairs under visible light [199,241].

The photodegradation of HA occurs due to the breakup of the large aromatic species followed by mineralization [260,261]. Corin et al. determined the formation of carboxylic acids with lower molecular weight compared to that of HA due to the direct photolysis of HA [264]. It has also been reported that in the presence of TiO<sub>2</sub> as the photocatalyst, the photodepolymerization of the adsorbed HA molecules could occur through the successive oxidation of the carboxylate or phenolate surface groups [260]. During the photocatalytic reaction, the photogenerated electron-hole pairs in TiO<sub>2</sub> form powerful oxidizing species through interaction with water and oxygen. Holes may react with H<sub>2</sub>O to produce H<sup>+</sup> and OH<sup>·</sup> (hydroxyl radicals). Meanwhile, electrons react with O<sub>2</sub> to generate O<sub>2</sub><sup>·-</sup>, which can further yield OH<sup>·</sup> radicals. Furthermore, hydrolyses of water molecules on the surface of the TiO<sub>2</sub> photocatalyst leads to the generation of free radicals and OH<sup>·</sup> groups. [233]. The highly reactive hydroxyl radicals break down molecules of HA through chemical reactions involving hydroxyl addition or hydrogen extraction and eventually decompose HA or HA intermediate molecules [237].

After completing the 3<sup>rd</sup> cycle, the flux recovery of UF-2P and MF-12P membranes was measured. This assessment involved measuring the flux recovery following a 4-hour photocatalytic cleaning process followed by a hydraulic cleaning stage, as shown in Figure 5.6. A higher flux recovery was observed in both membranes after the four 4-hour photocatalytic cleaning stage. Additionally, after the hydraulic cleaning, a final flux recovery of 94% and 92% were obtained for UF-2P and MF-12P membranes, respectively. It also seems that the pore-blocking fouling was more dominant in the UF membrane, as observed in section 3.2.1.

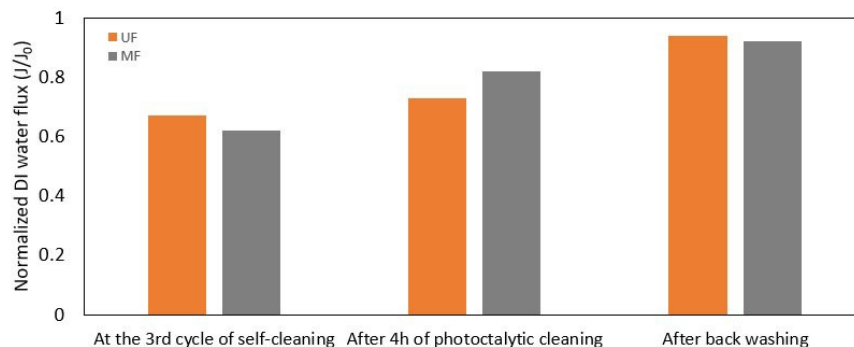


Figure 5.6 Evolution of the flux recovery of UF-2P and MF-12P membranes after four hours of photocatalytic cleaning and back washing following the 3rd cycle of the self-cleaning experiment.

Additionally, the measurement of the photocatalytic efficiency of the UF-2P and MF-12P membranes in degrading a MB solution over the course of 3 cycles showed a minor variation in the performance of the membranes. The maximum change of 6.5% for the UF-2P membrane and 5% for the MF-12P membrane was observed (Appendix 1, Supplementary Materials, Figure S3). This indicates that the photocatalytic property of the membranes remains relatively consistent throughout the recycling process. MB, with the chemical formula  $C_{16}H_{18}ClN_3S$ , is a cationic dye that dissolves in water and finds extensive application in the textile industry [265]. Various degradation pathways for MB have been determined. According to Houas et al., the degradation of MB in the presence of the  $TiO_2$  photocatalyst could occur by de-cyclization and mineralization of molecules through continuous interactions with the hydroxyl radicals. As a result, the dye molecules get oxidized efficiently with an almost total mineralization of carbon, nitrogen, and sulfur heteroatoms, resulting in the formation of  $CO_2$ ,  $NH_4^+$ ,  $NO_3^-$  and  $SO_4^{2-}$  [266].

### 5.3.2.3 Contact Angle Measurement

The as-sprayed UF and MF membranes exhibit super hydrophilic surfaces with a contact angle of  $0^\circ$ . When a water droplet touches the surface of the as-sprayed membranes, it instantly gets absorbed into the surface. The surface of the UF-2P and MF-12P remained unchanged, with super hydrophilic properties after the HA self-cleaning process. However, the contact angle was slightly increased to  $7^\circ$  and  $5.5^\circ$  at the 2nd and 3rd cycles of photocatalytic degradation of MB for the UF-2P. Likewise, an increase to  $3.3^\circ$  and  $7.5^\circ$  was observed at the 2nd and 3rd cycles of photocatalytic degradation of MB for the MF-12P. Despite this slight contact angle increase, the surface maintains its hydrophilic characteristics. In theory, hydrophilic membranes are considered to be less susceptible to fouling. The higher anti-fouling property could arise from the presence of hydrophilic OH species on the surface of  $TiO_2$  and the consequent water-shielding phenomena [267,268]. However, as mentioned earlier, other parameters may also impact the fouling property of the membranes.

### 5.3.3 Infiltration of the UF Membranes with Agglomerates of TiO<sub>2</sub> Nanoparticles (Filled Membranes)

As described in section 5.3.2.1, the SPS UF exhibited a rather poor separation efficiency that could have been linked to the wide pore size distribution in those membranes. Thus, it was decided to investigate the possibility of improving the separation performance of the UF membranes by producing a narrower pore size distribution. Chung et al. [258] suggested a method to reduce the pore size distribution of the ceramic membranes by packing nano-sized particles into the pre-existing pores of the membrane, following a calcination process to enhance the mechanical strength of the membranes. In this work, a similar approach was utilized to fill the larger pores in the UF-2P and UF-4P membranes. The heat treatment process was not carried out in our study to avoid potential oxidation and densification of the metallic substrate [269].

The as-sprayed UF-2P and UF-4P membranes were filtered with around 30 ml of 1 wt.% TiO<sub>2</sub> (PiKem, Tamworth UK) aqueous suspension to eliminate the large pores. The TiO<sub>2</sub> powder used to fill the pores was identical to the powder used to fabricate the UF membranes in the SPS process with a particle size of 27±10 nm and agglomerate size with  $d_{50} = 3.1\mu\text{m}$ , described in section 5.2.1 [199]. The primary purpose was to decrease the pore size distribution of the membrane by embedding the agglomerates of nanosized TiO<sub>2</sub>, identical to those present in the microstructure of the suspension plasma sprayed UF membranes, in the larger pores on the surface. The UF membranes filled with TiO<sub>2</sub> nanoparticles have been referred to as filled membranes and are identified as UF-2P-F and UF-4P-F.

#### 5.3.3.1 Surface Roughness

Figure 5.7 shows the confocal microscope image of the surface UF-4P membrane after filling with TiO<sub>2</sub> nanoparticles. Combined with the measurements seen in Table 5.5, it was observed that in both cases,  $R_a$  and  $R_z$  values were decreased due to filling up the pores on the surface of the membranes with TiO<sub>2</sub> agglomerates. The decrease in the roughness is more significant in the UF-2P-F sample, which had a higher initial roughness.

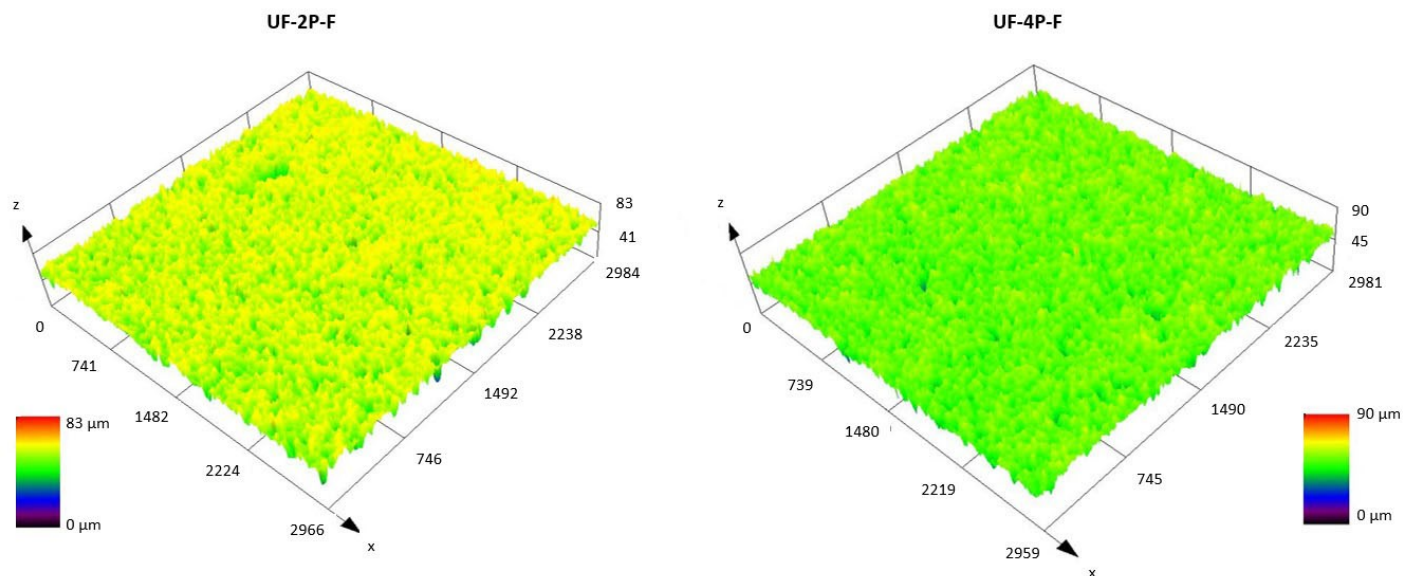


Figure 5.7 Confocal microscope image of UF-2P-F and UF-4P-F membranes.

Table 5.5 Surface roughness of UF-2P-F and UF-4P-F. The membranes were filled with the agglomerates of nanosized TiO<sub>2</sub>.

Sample	Roughness (R <sub>a</sub> ) (μm)	Roughness (R <sub>z</sub> ) (μm)
UF- 2P-F	3.5 ± 0.05	20.8 ± 0.4
UF- 4P-F	2.9 ± 0.1	18.9 ± 0.7

### 5.3.3.2 Separation Performance

The UF-2P-F and UF-4P-F membranes were cleaned before rejection measurement. Following the filling of the membranes with TiO<sub>2</sub> nanoparticles, the surface of the membranes was rinsed with DI water to remove the loose particles on the surface. After that, the membranes were compacted with DI water until obtaining the turbidity of 0 NTU for the filtrate. The compaction with DI water was to remove the residual loose agglomerates of nanoparticles.

Figure 5.8 shows the particle rejection efficiency of the filled UF membranes. After filling the UF membranes with the agglomerates of TiO<sub>2</sub> nanoparticles, the rejection rates of UF-2P-F and UF-4P-F were increased compared to UF-2P and UF-4P. Compared to UF-2P, for both 200 nm and 400 nm SiO<sub>2</sub> particles, the rejection rates of the UF-2P-F membranes were improved by a factor of approximately two. On the other hand, the UF-4P-F membrane reached rejection rates of over 97% for 200 nm and 400 nm SiO<sub>2</sub> particles, showing the importance of the membrane's thickness on the separation efficiency.

The membrane's performance remained stable during the filtration process. However, the agglomerates of TiO<sub>2</sub> nanoparticles were removed during the backwashing process, requiring a refilling process.

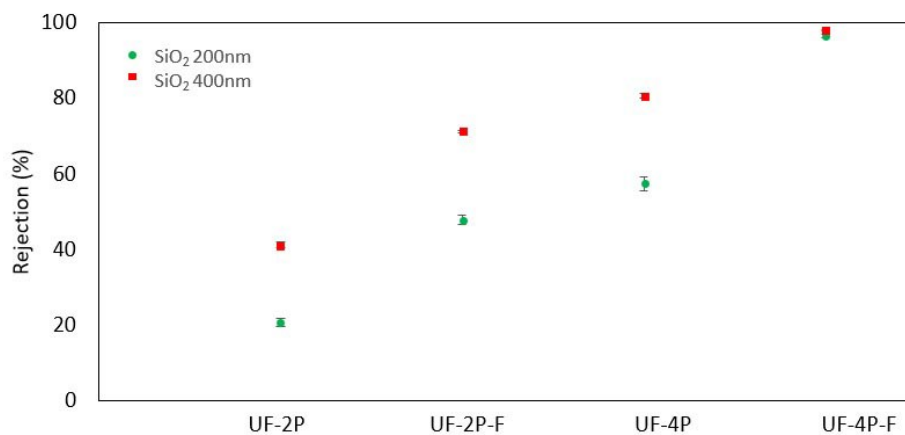


Figure 5.8 Comparing the rejection rates of the UF membranes before and after filling the large pores with agglomerates of TiO<sub>2</sub> nanoparticles for SiO<sub>2</sub> 200 nm and SiO<sub>2</sub> 400nm particles.

### 5.3.3.3 Molecular Weight Cut-off (MWCO)

To further investigate the impact of incorporating TiO<sub>2</sub> nanoparticles into the packing of ultrafiltration membranes for narrowing the pore size distribution, the Molecular Weight Cut-Off (MWCO) of UF-4P and UF-4P-F membranes was assessed. The evaluation of MWCO is a method to determine the rejection efficiency of UF membranes. The MWCO of the membranes corresponds to the molecular weight at which 90% rejection by the membrane was achieved [36].

Figure 5.9 presents the MWCO measurements for UF-4P and UF-4P-F, indicating a decrease in the MWCO of the UF-4P-F. In this experiment, due to the range of PEO materials used, it was not possible to determine the 90% rejection point (MWCO) for the UF-4P sample (as-sprayed membrane). Since the as-sprayed UF membranes, especially at lower thickness, did not demonstrate favorable separation efficiency, higher molecular weight PEO materials were not employed to determine the MWCO of those membranes. Despite this limitation, the results clearly show that the MWCO of UF-4P is lower than that of UF-4P-F, which aligns with the particle rejection measurements of the as-sprayed and filled membranes. The MWCO of UF-4P-F was determined to be approximately 900 kDa, equivalent to a PEO molecule with a stokes radius of roughly 33 nm. This suggests that the filled UF membrane could potentially remove molecules with a diameter of around 70 nm. However, it is worth noting that the MWCO is not an absolute determinant of the potential size of the particles that can be rejected since not all the foulants molecules and particles are spherical [36]. Furthermore, the shape of the pores could also influence the rejection efficiency [252,255]. In one case, the penetration of organic

molecules over 30 times larger than the membrane pore size was reported by Arkhangelsky et.al [270].

The application of Equation (5.7) estimated the  $d_{50}$  of the UF-4P membrane to be approximately 37.5 nm, aligning with the average pore diameter of roughly 36 nm obtained using the mercury intrusion porosimetry [199]. Furthermore, the estimated  $d_{50}$  of the UF-4P-F membrane was calculated to be about 29 nm. Filling the larger pores could lead to a sharper MWCO curve and improved rejection that could be due to a narrower pore size distribution [271]. Additionally, a stronger correlation was observed between the membrane's pore size and the particle size of  $\text{TiO}_2$  feedstock powder used in the SPS process to produce the membranes [199].

These results indicate that the filling process can improve the performance of the SPS UF membranes. However, optimizing the SPS process parameters is necessary to produce UF membranes with a narrow pore size distribution. An alternative approach could be to increase the thickness of the UF membranes.

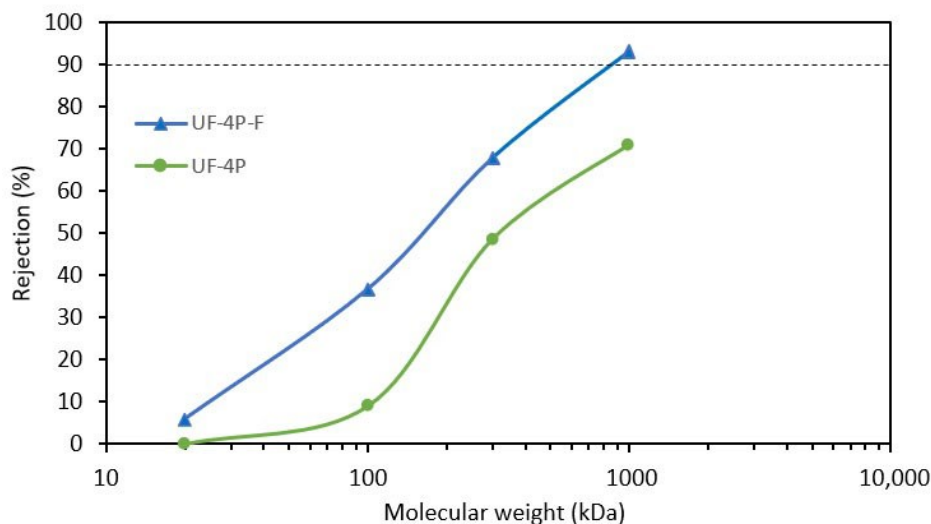


Figure 5.9 Rejection rate as a function of the PEO molecular weight of the UF-4P and UF-4P-F membranes. The filling process made it possible to reduce the MWCO of the filled membrane to about 900 kDa.

## 5.4 Conclusion

This study evaluated the efficiency of  $\text{TiO}_2$  UF and MF membranes produced by the SPS process regarding their rejection rate, self-cleaning property, and recyclability. It was shown that:

- The rejection efficiency of the MF and UF membranes can be tuned by adjusting the thickness of the membrane. Increasing the thickness of the membranes led to higher

rejection rates, indicating the importance of membrane thickness in determining filtration performance.

- The SPS UF membrane exhibited enhanced rejection rates by effectively filling its larger pores with agglomerates of TiO<sub>2</sub> nanoparticles. This modification improved the effective rejection of smaller particles which could be attributed to the decrease in the average pore size and the total pore size distribution. This finding highlights the potential of incorporating nanoparticles to enhance the performance of ceramic membranes. Additionally, it suggests that the rejection efficiency of the membranes is influenced by both the average pore size and a uniform and narrow pore size distribution.
- both SPS MF and UF membranes demonstrated recyclable self-cleaning properties under visible light, which is desirable for maintaining long-term filtration efficiency.
- Enhancing the performance of the UF membrane requires better optimization of its structure, focusing on achieving a more uniform membrane structure and narrow pore size distribution to enable more efficient filtration. The optimization can be carried out by adjusting the SPS process parameters.

Overall, the findings of this study provide valuable insights into the capabilities and limitations of the SPS process as a novel approach for manufacturing ceramic membranes. These understandings can be used to improve the structure and performance quality of SPS membrane technologies for various filtration applications. Furthermore, exploring the possible pathways to generate narrow pore size distribution in the SPS membranes by optimizing the SPS process parameters can be considered as a future task. Also, a comprehensive evaluation of the quality of the filtered water and optimization of the cleaning process can be conducted to provide a more thorough assessment of the performance efficiency of the membranes.

## Chapter 6 Conclusions and Future Work

### 6.1 Summary and Conclusions

The main objective of this work was to develop and refine a novel one-step fabrication approach for producing various classes of high-performance hybrid filtration/ photocatalysis ceramic membranes and tailoring their microstructure. Thermal spray processes including the SPS process, present an ideal approach for coating large surfaces due to their capacity to operate under atmospheric conditions, scalability, and capability to deposit a variety of functional engineering ceramics. Therefore, the SPS process was selected as it could present a venue to overcome the shortcomings of commercial ceramic membrane fabrication processes. Using the SPS process, it was possible to produce photoreactive and porous coatings with acceptable efficiency under UV and visible light that could be used for filtration applications.

Initially, the SPS process was employed to produce porous membranes with nanosized pores in the range of UF. To that end, a nanosized TiO<sub>2</sub> anatase powder was used to prepare the feedstock suspension. A systematic optimization process was conducted to find the suitable spray parameters based on the porosity and the photocatalytic performance. In the optimized coating, the multi-modal pore distribution exhibited an average pore size relatively close to the particle size of the feedstock powder due to the presence of a significant number of unmelted particles in the structure. Furthermore, the optimized parameters were used to deposit membranes on the porous substrates. The examination of the membrane microstructure unveiled notable quantities of unmelted nanoparticles, forming porous nanostructured agglomerates that matched those present in the feedstock suspension. Additionally, an inherent intermediate layer was formed on the surface of the porous substrate due to the rapid, selective filling of the larger pores on the substrate with the in-flight nanostructured agglomerates. The membranes showed a relatively high pure water permeability, which inversely correlated with the thickness. Additionally, the membranes showed photocatalytic activity under both UVA and visible lights. The photocatalytic activity under visible light was linked to the generation of oxygen vacancies and Ti<sup>3+</sup> ions, which led to decreasing the bandgap energy and introducing sub-level energy states under the conduction band, reducing the required energy to initiate the photocatalytic process and the recombination rate of the photogenerated electron-hole pairs.

Additionally, a systematic investigation was conducted to study the feasibility of tailoring the porosity level of the suspension plasma sprayed membranes/coatings using a dual suspension injection system. The objective was to assess the potential for controlling the porosity of SPS coatings by simultaneously introducing two feedstock suspensions at different radial distances from the plasma torch into the plasma jet. A matrix of experiments was designed to study the effect of various spray parameters on the porosity of the coatings. Porosity levels were found to be associated with the proportion of unmelted particles from the suspension sprayed farther away from the torch exit, which was correlated with the gaps among these unmelted

particles. Notably, the distance between the two injectors and the feed rates of the suspensions appeared to have a substantial influence on the ratio of unmelted particles present in the coatings. Additionally, the utilization of the dual injection system could influence the structural configuration of the coatings due to cooling the plasma and reducing its velocity. By offering a potential solution to customize the porosity, the radial dual suspension injecting system could serve as a promising avenue to fine-tune parameters like permeability and heat transfer in membranes and coatings. Furthermore, this approach could serve as a method to govern the amount of heat-sensitive feedstock within composite SPS coatings by mitigating their exposure to elevated plasma temperatures.

Finally, a comparative analysis was undertaken for a more profound comprehension of the potential and limitations of the SPS process as an innovative technique for producing ceramic membranes. This study aimed to examine the attributes of UF and MF membranes manufactured through the SPS process, specifically focusing on self-cleaning capability and filtration efficiency. To this end, the membranes' ability to reject particles was evaluated using SiO<sub>2</sub> particles. Notably, as membrane thickness increased, rejection rates also elevated. This observation emphasized the significant role of membrane thickness in influencing filtration performance. Furthermore, although the MF membranes had a larger average pore size, they exhibited superior rejection efficiency. This was attributed to their narrower pore size distribution compared to the UF membranes. Moreover, the rejection efficiency was enhanced by compacting the UF membranes, which had a multi-modal pore size distribution, using agglomerates of nanosized TiO<sub>2</sub> particles, the same as those used in the SPS feedstock. This highlighted the significance of pore size distribution in the overall separation performance. Both the SPS MF and UF membranes showcased reusable self-cleaning attributes when exposed to visible light. This characteristic is valuable for ensuring sustained, long-term filtration efficiency.

The collection of the results and conclusions presented here suggest that SPS can be a promising novel approach for manufacturing ceramic membranes with a customizable porosity and pore size. These insights offer a foundation to enhance the architecture and performance standards of SPS membrane technologies, catering to diverse filtration requirements. Additionally, investigating potential strategies to achieve a more confined pore size distribution within SPS membranes through optimizing process parameters could be seen as a prospective avenue for further exploration.

## 6.2 Contributions

The main contributions of this research can be summarized as follows.

- A hybrid filtration/photocatalysis ultrafiltration membrane with nanosized pores and high permeability was developed by employing the SPS process as an innovative ceramic membrane development process. The membrane exhibited a unique microstructure where the nanosized pores resulted from the preservation and entrapment of naturally formed agglomerates of unmelted nanosized feedstock particles within the matrix built by the splats originated from the fully melted particles. This agglomeration of nanosized particles yielded a membrane structure with finely tuned nanoscale porosity, rendering it exceptionally effective for applications where precision in pore size and permeability is required.

- An innovative method was devised to finely control the porosity levels within SPS coatings. This was achieved by implementing a radial dual suspension injection system, which involves injecting two distinct suspensions at varying distances from the plasma jet. By doing so, certain quantities of unmelted particles from the injector positioned farther away from the torch became embedded within the coating. This process resulted in the generation of fine pores within the coatings. These fine pores, responsible for the controlled porosity, stem from the spaces that arise between the retained unmelted particles integrated within the coating's structure. This technique could potentially offer a sophisticated means of engineering coatings with specific porosity profiles and coatings, including heat-sensitive components.
- Thoroughly characterizing the SPS membranes resulted in a comprehensive grasp of both the strengths and limitations inherent in the SPS process for manufacturing porous filtration membranes. The SPS membranes exhibited self-cleaning properties exposed to visible light. Additionally, the importance of the membrane thickness and pore size distribution on the contaminant separation performance was confirmed.

### 6.3 Future Works

Based on the results of the present research study, the following suggestions are proposed for future research.

Further optimization of the SPS spray parameters to remove the large pores and generate a more uniform and narrow pore size distribution in the UF membranes. The main origin of the large pores is the empty spaces among the deposited agglomerates of nanosized TiO<sub>2</sub> particles. Therefore, smaller-sized agglomerates in the membranes could potentially lead to smaller inter-agglomerate gaps. One possible approach could be to optimize the suspension properties to decrease the size of the agglomerates in the feedstock suspension. Another suggestion could be optimizing the atomization of the suspension in the plasma jet to produce smaller inflight droplets, resulting in the generation of the smaller agglomerates of nanosized particles. Additionally, the spray parameters can be optimized to reduce/avoid the formation of columns in SPS membranes, resulting in smoother surface which could be cleaned easier.

- All the membranes produced and studied in this work were deposited on flat substrates. However, for most potential applications in membrane technology, the target surfaces are curved and tubular. It is important to optimize the spray process for curved substrates as the surface curvature might potentially influence the microstructure and characteristics of the SPS coatings.
- A comprehensive evaluation of the filtered water quality and optimization of the membrane cleaning process can be conducted to provide a more thorough assessment of the performance efficiency of the membranes.
- The performance and stability of the membranes can be studied in long-term experiments, under various filtration modes, temperatures, and pH, and possibly in outdoor

environments as the efficiency of the membranes could be influenced. Another area for performance assessment could be for the filtration of fines particles in hot gas flow to reduce the environmental impact of industrial processes.

- The dual injection system mechanism needs to be further optimized to obtain a stable suspension stream to enhance the reproducibility of the process.
- In the dual injection system, a full DoE can be designed to more precisely define the trend describing the relation between the various spray parameters and the resulting microstructure.
- The possibility of tailoring the porosity/unmelted feedstock portion in porous/composite SPS coatings by a combined radial-axial suspension injection system can be investigated.
- In the dual injection system, further optimization of the microstructures can be investigated by studying the influence of parameters such as the robot speed and using a rotating substrate holder.

## References

- [1] S. Al Aani, T.N. Mustafa, N. Hilal, Ultrafiltration membranes for wastewater and water process engineering: A comprehensive statistical review over the past decade, *Journal of Water Process Engineering*. 35 (2020) 101241. <https://doi.org/10.1016/j.jwpe.2020.101241>.
- [2] A. Samadi, L. Gao, L. Kong, Y. Orooji, S. Zhao, Waste-derived low-cost ceramic membranes for water treatment: Opportunities, challenges and future directions, *Resour Conserv Recycl*. 185 (2022) 106497. <https://doi.org/10.1016/j.resconrec.2022.106497>.
- [3] Y. Wen, X. Yang, Y. Li, L. Yan, Y. Zhao, L. Shao, Progress reports of metal-phenolic network engineered membranes for water treatment, *Sep Purif Technol*. 320 (2023) 124225. <https://doi.org/10.1016/j.seppur.2023.124225>.
- [4] A.K. Fard, G. McKay, A. Buekenhoudt, H. Al Sulaiti, F. Motmans, M. Khraisheh, M. Atieh, Inorganic membranes: Preparation and application for water treatment and desalination, *Materials*. 11 (2018) 74. <https://doi.org/10.3390/ma11010074>.
- [5] Z. He, Z. Lyu, Q. Gu, L. Zhang, J. Wang, Ceramic-based membranes for water and wastewater treatment, *Colloids Surf A Physicochem Eng Asp*. 578 (2019) 123513. <https://doi.org/10.1016/j.colsurfa.2019.05.074>.
- [6] H.E. Johnson, B.L. Schulman, Assessment of the potential for refinery applications of inorganic membrane technology: An identification and screening analysis. Final report, (1993). <https://www.osti.gov/servlets/purl/10182536> (accessed May 14, 2018).
- [7] R. Mallada, M. Menéndez, *Inorganic membranes: synthesis, characterization and applications*, 13th ed., Elsevier, 2008.
- [8] M.M. Pendergast, E.M.V. Hoek, A review of water treatment membrane nanotechnologies, *Energy Environ Sci*. 4 (2011) 1946–1971. <https://doi.org/10.1039/c0ee00541j>.
- [9] T.T. More, S. Yan, R.D. Tyagi, R.Y. Surampalli, Applications of membrane processes for concentrated industrial wastewater treatment, in: *Membrane Technology and Environmental Applications*, 2012: pp. 217–238. <https://doi.org/10.1061/9780784412275.ch07>.
- [10] R.W. Baker, *Membrane technology and applications*, John Wiley and Sons, England, 2007. <https://doi.org/10.1002/0470020393>.
- [11] S. Luque, D. Gómez, J.R. Álvarez, Industrial Applications of Porous Ceramic Membranes (Pressure-Driven Processes), *Membrane Science and Technology*. 13 (2008) 177–216. [https://doi.org/10.1016/S0927-5193\(07\)13006-0](https://doi.org/10.1016/S0927-5193(07)13006-0).
- [12] S.M. Samaei, S. Gato-Trinidad, A. Altaee, The application of pressure-driven ceramic membrane technology for the treatment of industrial wastewaters – A review, *Sep Purif Technol*. 200 (2018) 198–220. <https://doi.org/10.1016/j.seppur.2018.02.041>.
- [13] A. Killinger, R. Gadow, G. Mauer, A. Guignard, R. Vaßen, D. Stöver, Review of New Developments in Suspension and Solution Precursor Thermal Spray Processes, *Journal of Thermal Spray Technology*. 20 (2011) 677. <https://doi.org/10.1007/s11666-011-9639-8>.

- [14] C. Xu, G.P. Rangaiah, X.S. Zhao, Photocatalytic Degradation of Methylene Blue by Titanium Dioxide: Experimental and Modeling Study, *Ind Eng Chem Res.* 53 (2014) 14641–14649. <https://doi.org/10.1021/ie502367x>.
- [15] E. Alebrahim, F. Tarasi, M.S. Rahaman, A. Dolatabadi, C. Moreau, Fabrication of titanium dioxide filtration membrane using suspension plasma spray process, *Surf Coat Technol.* 378 (2019). <https://doi.org/10.1016/j.surfcoat.2019.124927>.
- [16] M. Mulder, *Basic principles of membrane technology*, (1991) 564. [https://doi.org/10.1524/zpch.1998.203.part\\_1\\_2.263](https://doi.org/10.1524/zpch.1998.203.part_1_2.263).
- [17] J. Finley, Ceramic membranes: A robust filtration alternative, *Filtration and Separation.* 42 (2005) 34–37. [https://doi.org/10.1016/S0015-1882\(05\)70695-9](https://doi.org/10.1016/S0015-1882(05)70695-9).
- [18] A.G. Fane, R. Wang, Y. Jia, *Membrane Technology: Past, Present and Future*, in: *Membrane and Desalination Technologies*, Humana Press, Totowa, NJ, 2011: pp. 1–45. [https://doi.org/10.1007/978-1-59745-278-6\\_1](https://doi.org/10.1007/978-1-59745-278-6_1).
- [19] S.M. Samaei, S. Gato-Trinidad, A. Altaee, The application of pressure-driven ceramic membrane technology for the treatment of industrial wastewaters – A review, *Sep Purif Technol.* 200 (2018) 198–220. <https://doi.org/10.1016/j.seppur.2018.02.041>.
- [20] J. Kim, B. Van Der Bruggen, The use of nanoparticles in polymeric and ceramic membrane structures: Review of manufacturing procedures and performance improvement for water treatment, *Environmental Pollution.* 158 (2010) 2335–2349. <https://doi.org/10.1016/j.envpol.2010.03.024>.
- [21] M. Lee, Z. Wu, K. Li, *Advances in ceramic membranes for water treatment*, in: *Advances in Membrane Technologies for Water Treatment: Materials, Processes and Applications*, Elsevier Inc., 2015: pp. 43–82. <https://doi.org/10.1016/B978-1-78242-121-4.00002-2>.
- [22] M.B. Asif, Z. Zhang, Ceramic membrane technology for water and wastewater treatment: A critical review of performance, full-scale applications, membrane fouling and prospects, *Chemical Engineering Journal.* 418 (2021) 129481. <https://doi.org/10.1016/j.cej.2021.129481>.
- [23] B.F.K. Kingsbury, K. Li, A morphological study of ceramic hollow fibre membranes, *J Memb Sci.* 328 (2009) 134–140. <https://doi.org/10.1016/j.memsci.2008.11.050>.
- [24] X. Tan, S. Liu, K. Li, Preparation and characterization of inorganic hollow fiber membranes, *J Memb Sci.* 188 (2001) 87–95. [https://doi.org/10.1016/S0376-7388\(01\)00369-6](https://doi.org/10.1016/S0376-7388(01)00369-6).
- [25] C.C. Wei, O.Y. Chen, Y. Liu, K. Li, Ceramic asymmetric hollow fibre membranes-One step fabrication process, *J Memb Sci.* 320 (2008) 191–197. <https://doi.org/10.1016/j.memsci.2008.04.003>.
- [26] X. Tan, N. Liu, B. Meng, S. Liu, Morphology control of the perovskite hollow fibre membranes for oxygen separation using different bore fluids, *J Memb Sci.* 378 (2011) 308–318. <https://doi.org/10.1016/j.memsci.2011.05.012>.

- [27] H. Strathmann, Membrane separation processes: Current relevance and future opportunities, *AIChE Journal*. 47 (2001) 1077–1087. <https://doi.org/10.1002/aic.690470514>.
- [28] Deltapore, Deltapore hollow fiber ceramic membranes, <Http://Deltapore.Com/En/Ceram/>. (2019) (accessed 04 Nov 2019). <http://deltapore.com/en/hollow-fiber-ceramic-membranes/> (accessed January 7, 2020).
- [29] R.R. Bhave, *Cross-Flow Filtration*, 2nd ed., William Andrew Publishing, 1996. <https://doi.org/10.1016/B978-081551407-7.50010-6>.
- [30] G. Belfort, R.H. Davis, A.L. Zydney, The behaviour of suspensions and macromolecular solutions filtration, *J Memb Sci*. 96 (1994) 1–58.
- [31] K.P. Lee, *Fabrication and Applications of Nanoporous Alumina Membranes*, (2013) 250.
- [32] P. Wu, Y. Xu, Z. Huang, J. Zhang, A review of preparation techniques of porous ceramic membranes, *Journal of Ceramic Processing Research*. 16 (2015) 102–106. [http://jcpr.kbs-lab.co.kr/file/JCPR\\_vol.16\\_2015/JCPR16-1/\\_202014-131\\_102-106.pdf](http://jcpr.kbs-lab.co.kr/file/JCPR_vol.16_2015/JCPR16-1/_202014-131_102-106.pdf) (accessed April 17, 2019).
- [33] F. Martínez-Villa, J.I. Arribas, F. Tejerina, Quantitative microscopic study of surface characteristics of track-etched membranes, *J Memb Sci*. 36 (1988) 19–30. [https://doi.org/10.1016/0376-7388\(88\)80003-6](https://doi.org/10.1016/0376-7388(88)80003-6).
- [34] A. Hernández, J.I. Calvo, P. Prádanos, F. Tejerina, Pore size distributions in microporous membranes. A critical analysis of the bubble point extended method, *J Memb Sci*. 112 (1996) 1–12. [https://doi.org/10.1016/0376-7388\(95\)00025-9](https://doi.org/10.1016/0376-7388(95)00025-9).
- [35] G.R. Li, B.W. Lv, G.J. Yang, W.X. Zhang, C.X. Li, C.J. Li, Relationship Between Lamellar Structure and Elastic Modulus of Thermally Sprayed Thermal Barrier Coatings with Intra-splat Cracks, *Journal of Thermal Spray Technology*. 24 (2015) 1355–1367. <https://doi.org/10.1007/s11666-015-0292-5>.
- [36] R. Singh, *Introduction to Membrane Technology*, 2015. <https://doi.org/10.1016/b978-0-444-63362-0.00001-x>.
- [37] H. Giesche, Mercury porosimetry: A general (practical) overview, *Particle and Particle Systems Characterization*. 23 (2006) 9–19. <https://doi.org/10.1002/ppsc.200601009>.
- [38] M.N. Sarbolouki, Properties of asymmetric polyimide ultrafiltration membranes. I. Pore size and morphology characterization, *J Appl Polym Sci*. 29 (1984) 743–753. <https://doi.org/10.1002/APP.1984.070290303>.
- [39] ASTM, *Standard Test Method for Molecular Weight Cutoff Evaluation of Flat Sheet E1343*, Technology (Singap World Sci). 90 (2008) 1–9.
- [40] *Basic Principles of Membrane Technology* - Marcel Mulder - Google Books, (n.d.). [https://books.google.ca/books?hl=en&lr=&id=SP2\\_GYvL384C&oi=fnd&pg=PA1&dq=M.+Mulder,+Basic+Principles+of+Membrane+Technology,+Kluwer+Academic+Publishers,+Holland,+1997.&ots=GtH46hV600&sig=lsrkZV1NOqjY4Cf7b\\_\\_MfjBESPg#v=onepage&q&f=false](https://books.google.ca/books?hl=en&lr=&id=SP2_GYvL384C&oi=fnd&pg=PA1&dq=M.+Mulder,+Basic+Principles+of+Membrane+Technology,+Kluwer+Academic+Publishers,+Holland,+1997.&ots=GtH46hV600&sig=lsrkZV1NOqjY4Cf7b__MfjBESPg#v=onepage&q&f=false) (accessed August 21, 2023).

- [41] L.J. Zeman, A.L. Zydney, *Microfiltration and Ultrafiltration Principles and Applications*, Marcel Dekker, INC, New York, 2017.
- [42] G. Ramakrishnan, G. Dwivedi, S. Sampath, A. Orlov, Development and optimization of thermal sprayed ceramic microfiltration membranes, *J Memb Sci.* 489 (2015) 106–111. <https://doi.org/10.1016/j.memsci.2015.03.094>.
- [43] S.S. Madaeni, M.E. Aalami-Aleagha, P. Daraei, Preparation and characterization of metallic membrane using wire arc spraying, *J Memb Sci.* 320 (2008) 541–548. <https://doi.org/10.1016/j.memsci.2008.04.051>.
- [44] A. Islam, B. Praveen Chakkravarthy Raghupathy, M. V. Sivakumaran, A. Kumar Keshri, Ceramic membrane for water filtration: Addressing the various concerns at once, *Chemical Engineering Journal.* 446 (2022). <https://doi.org/10.1016/j.cej.2022.137386>.
- [45] X. Ding, Y. Fan, N. Xu, A new route for the fabrication of TiO<sub>2</sub> ultrafiltration membranes with suspension derived from a wet chemical synthesis, *J Memb Sci.* 270 (2006) 179–186. <https://doi.org/10.1016/j.memsci.2005.07.003>.
- [46] S.H. Woo, J. Park, B.R. Min, Relationship between permeate flux and surface roughness of membranes with similar water contact angle values, *Sep Purif Technol.* 146 (2015) 187–191. <https://doi.org/10.1016/J.SEPPUR.2015.03.048>.
- [47] N. Sharifi, M. Pugh, C. Moreau, A. Dolatabadi, Developing hydrophobic and superhydrophobic TiO<sub>2</sub> coatings by plasma spraying, *Surf Coat Technol.* 289 (2016) 29–36. <https://doi.org/10.1016/j.surfcoat.2016.01.029>.
- [48] V. Freger, J. Gilron, S. Belfer, TFC polyamide membranes modified by grafting of hydrophilic polymers: an FT-IR/AFM/TEM study, *J Memb Sci.* 209 (2002) 283–292. [https://doi.org/10.1016/S0376-7388\(02\)00356-3](https://doi.org/10.1016/S0376-7388(02)00356-3).
- [49] H. Zou, Y. Jin, J. Yang, H. Dai, X. Yu, J. Xu, Synthesis and characterization of thin film composite reverse osmosis membranes via novel interfacial polymerization approach, *Sep Purif Technol.* 72 (2010) 256–262. <https://doi.org/10.1016/J.SEPPUR.2010.01.019>.
- [50] T. Arumugham, N.J. Kaleekkal, S. Gopal, J. Nambikkattu, R. K, A.M. Aboulella, S. Ranil Wickramasinghe, F. Banat, Recent developments in porous ceramic membranes for wastewater treatment and desalination: A review, *J Environ Manage.* 293 (2021) 112925. <https://doi.org/10.1016/j.jenvman.2021.112925>.
- [51] A. Murić, I. Petrinić, M.L. Christensen, Comparison of ceramic and polymeric ultrafiltration membranes for treating wastewater from metalworking industry, *Chemical Engineering Journal.* 255 (2014) 403–410. <https://doi.org/10.1016/j.cej.2014.06.009>.
- [52] R. Zhang, Y. Liu, M. He, Y. Su, X. Zhao, M. Elimelech, Z. Jiang, Antifouling membranes for sustainable water purification: Strategies and mechanisms, *Chem Soc Rev.* 45 (2016) 5888–5924. <https://doi.org/10.1039/c5cs00579e>.

- [53] S.M. Finnigan, J.A. Howell, The effect of pulsed flow on ultrafiltration fluxes in a baffled tubular membrane system, *Desalination*. 79 (1990) 181–202. [https://doi.org/10.1016/0011-9164\(90\)85005-U](https://doi.org/10.1016/0011-9164(90)85005-U).
- [54] S. Wroński, E. Molga, L. Rudniak, Dynamic filtration in biotechnology, *Bioprocess Engineering*. 4 (1989) 99–104. <https://doi.org/10.1007/BF00369757>.
- [55] Y.F. Zhao, L.P. Zhu, Z. Yi, B.K. Zhu, Y.Y. Xu, Improving the hydrophilicity and fouling-resistance of polysulfone ultrafiltration membranes via surface zwitterionization mediated by polysulfone-based triblock copolymer additive, *J Memb Sci*. 440 (2013) 40–47. <https://doi.org/10.1016/j.memsci.2013.03.064>.
- [56] Q. Shi, Y. Su, W. Chen, J. Peng, L. Nie, L. Zhang, Z. Jiang, Grafting short-chain amino acids onto membrane surfaces to resist protein fouling, *J Memb Sci*. 366 (2011) 398–404. <https://doi.org/10.1016/j.memsci.2010.10.032>.
- [57] J.F. Hester, P. Banerjee, A.M. Mayes, Preparation of Protein-Resistant Surfaces on Poly(vinylidene fluoride) Membranes via Surface Segregation, *Macromolecules*. 32 (1999) 1643–1650. <https://doi.org/10.1021/ma980707u>.
- [58] J. nan Shen, H. min Ruan, L. guang Wu, C. jie Gao, Preparation and characterization of PES-SiO<sub>2</sub> organic-inorganic composite ultrafiltration membrane for raw water pretreatment, *Chemical Engineering Journal*. 168 (2011) 1272–1278. <https://doi.org/10.1016/j.cej.2011.02.039>.
- [59] A. Sotto, A. Boromand, S. Balta, J. Kim, B. Van Der Bruggen, Doping of polyethersulfone nanofiltration membranes: Antifouling effect observed at ultralow concentrations of TiO<sub>2</sub> nanoparticles, *J Mater Chem*. 21 (2011) 10311–10320. <https://doi.org/10.1039/c1jm11040c>.
- [60] N. Maximous, G. Nakhla, W. Wan, K. Wong, Effect of the metal oxide particle distributions on modified PES membranes characteristics and performance, *J Memb Sci*. 361 (2010) 213–222. <https://doi.org/10.1016/j.memsci.2010.05.051>.
- [61] R. Yue, B. Raisi, J. Rahmatinejad, Z. Ye, B. Barbeau, M.S. Rahaman, A photo-Fenton nanocomposite ultrafiltration membrane for enhanced dye removal with self-cleaning properties, *J Colloid Interface Sci*. 604 (2021) 458–468. <https://doi.org/10.1016/J.JCIS.2021.06.157>.
- [62] P. Daraei, S.S. Madaeni, N. Ghaemi, M.A. Khadivi, B. Astinchap, R. Moradian, Enhancing antifouling capability of PES membrane via mixing with various types of polymer modified multi-walled carbon nanotube, *J Memb Sci*. 444 (2013) 184–191. <https://doi.org/10.1016/j.memsci.2013.05.020>.
- [63] L. Tang, K.J.T. Livi, K.L. Chen, Polysulfone membranes modified with bioinspired polydopamine and silver nanoparticles formed in situ to mitigate biofouling, *Environ Sci Technol Lett*. 2 (2015) 59–65. <https://doi.org/10.1021/acs.estlett.5b00008>.
- [64] M.R. Hoffmann, S.T. Martin, W. Choi, D.W. Bahnemann, Environmental Applications of Semiconductor Photocatalysis, *Chem Rev*. 95 (1995) 69–96. <https://doi.org/10.1021/cr00033a004>.

- [65] S. Riaz, S.J. Park, An overview of TiO<sub>2</sub>-based photocatalytic membrane reactors for water and wastewater treatments, *Journal of Industrial and Engineering Chemistry*. 84 (2020) 23–41. <https://doi.org/10.1016/j.jiec.2019.12.021>.
- [66] H. Dong, G. Zeng, L. Tang, C. Fan, C. Zhang, X. He, Y. He, An overview on limitations of TiO<sub>2</sub>-based particles for photocatalytic degradation of organic pollutants and the corresponding countermeasures, *Water Res*. 79 (2015) 128–146. <https://doi.org/10.1016/j.watres.2015.04.038>.
- [67] Y. Ao, J. Xu, D. Fu, L. Ba, C. Yuan, Deposition of anatase titania onto carbon encapsulated magnetite nanoparticles, *Nanotechnology*. 19 (2008). <https://doi.org/10.1088/0957-4484/19/40/405604>.
- [68] Q. Li, R. Jia, J. Shao, Y. He, Photocatalytic degradation of amoxicillin via TiO<sub>2</sub> nanoparticle coupling with a novel submerged porous ceramic membrane reactor, *J Clean Prod*. 209 (2019) 755–761. <https://doi.org/10.1016/j.jclepro.2018.10.183>.
- [69] A. Abdal-Hay, A.S. Hamdy Makhlouf, K.A. Khalil, Novel, Facile, Single-Step Technique of Polymer/TiO<sub>2</sub> Nanofiber Composites Membrane for Photodegradation of Methylene Blue, *ACS Appl Mater Interfaces*. 7 (2015) 13329–13341. <https://doi.org/10.1021/acsami.5b01418>.
- [70] Y. Gao, M. Hu, B. Mi, Membrane surface modification with TiO<sub>2</sub>-graphene oxide for enhanced photocatalytic performance, *J Memb Sci*. 455 (2014) 349–356. <https://doi.org/10.1016/j.memsci.2014.01.011>.
- [71] J. Grzechulska-Damszel, M. Tomaszewska, A.W. Morawski, Integration of photocatalysis with membrane processes for purification of water contaminated with organic dyes, *Desalination*. 241 (2009) 118–126. <https://doi.org/10.1016/J.DESAL.2007.11.084>.
- [72] R. Molinari, M. Mungari, E. Drioli, A. Di Paola, V. Loddo, L. Palmisano, M. Schiavello, Study on a photocatalytic membrane reactor for water purification, *Catal Today*. 55 (2000) 71–78. [https://doi.org/10.1016/S0920-5861\(99\)00227-8](https://doi.org/10.1016/S0920-5861(99)00227-8).
- [73] R.-X. Zhang, L. Braeken, P. Luis, X.-L. Wang, B. Van Der Bruggen, Novel binding procedure of TiO<sub>2</sub> nanoparticles to thin film composite membranes via self-polymerized polydopamine, *J Memb Sci*. 437 (2013) 179–188. <https://doi.org/10.1016/j.memsci.2013.02.059>.
- [74] S.S. Chin, K. Chiang, A.G. Fane, The stability of polymeric membranes in a TiO<sub>2</sub> photocatalysis process, *J Memb Sci*. 275 (2006) 202–211. <https://doi.org/10.1016/j.memsci.2005.09.033>.
- [75] H. Choi, E. Stathatos, D.D. Dionysiou, Sol-gel preparation of mesoporous photocatalytic TiO<sub>2</sub> films and TiO<sub>2</sub>/Al<sub>2</sub>O<sub>3</sub> composite membranes for environmental applications, *Appl Catal B*. 63 (2006) 60–67. <https://doi.org/10.1016/j.apcatb.2005.09.012>.
- [76] R. Molinari, F. Pirillo, M. Falco, V. Loddo, L. Palmisano, Photocatalytic degradation of dyes by using a membrane reactor, *Chemical Engineering and Processing: Process Intensification*. 43 (2004) 1103–1114. <https://doi.org/10.1016/j.cep.2004.01.008>.
- [77] U.I. Gaya, A.H. Abdullah, Heterogeneous photocatalytic degradation of organic contaminants over titanium dioxide: A review of fundamentals, progress and problems, *Journal of*

- Photochemistry and Photobiology C: Photochemistry Reviews. 9 (2008) 1–12. <https://doi.org/10.1016/J.JPHOTOCHEMREV.2007.12.003>.
- [78] M.R. Hoffmann, S.T. Martin, W. Choi, D.W. Bahnemann, Environmental Applications of Semiconductor Photocatalysis, Chem Rev. 95 (1995) 69–96. <https://doi.org/10.1021/cr00033a004>.
- [79] H. Khatibnezhad, M.A.F. Sani, Preparation and characterization of nanostructured TiO<sub>2</sub> thin film codoped with nitrogen and vanadium on glass surface by sol-gel dip-coating method, Research on Chemical Intermediates. 41 (2015) 7349–7361. <https://doi.org/10.1007/s11164-014-1816-1>.
- [80] L.-B. Xiong, J.-L. Li, B. Yang, Y. Yu, Ti<sup>3+</sup> in the Surface of Titanium Dioxide: Generation, Properties and Photocatalytic Application, J Nanomater. 2012 (2012) 13. <https://doi.org/10.1155/2012/831524>.
- [81] M. Gong, S. Xiao, X. Yu, C. Dong, J. Ji, D. Zhang, M. Xing, Research progress of photocatalytic sterilization over semiconductors, RSC Adv. 9 (2019) 19278–19284. <https://doi.org/10.1039/c9ra01826c>.
- [82] F.L. Toma, L.M. Berger, I. Shakhverdova, B. Leupolt, A. Potthoff, K. Oelschlägel, T. Meissner, J.A.I. Gomez, Y. de Miguel, Parameters Influencing the Photocatalytic Activity of Suspension-Sprayed TiO<sub>2</sub> Coatings, Journal of Thermal Spray Technology. 23 (2014) 1–17. <https://doi.org/10.1007/s11666-014-0090-5>.
- [83] T. Luttrell, S. Halpegamage, J. Tao, A. Kramer, E. Sutter, M. Batzill, Why is anatase a better photocatalyst than rutile? - Model studies on epitaxial TiO<sub>2</sub> films, Sci Rep. 4 (2015). <https://doi.org/10.1038/srep04043>.
- [84] D.A.H. Hanaor, C.C. Sorrell, Review of the anatase to rutile phase transformation, J Mater Sci. 46 (2011) 855–874. <https://doi.org/10.1007/s10853-010-5113-0>.
- [85] J. Zhang, P. Zhou, J. Liu, J. Yu, New understanding of the difference of photocatalytic activity among anatase, rutile and brookite TiO<sub>2</sub>, Physical Chemistry Chemical Physics. 16 (2014) 20382–20386. <https://doi.org/10.1039/c4cp02201g>.
- [86] G. Odling, N. Robertson, Why is anatase a better photocatalyst than rutile? the importance of free hydroxyl radicals, ChemSusChem. 8 (2015) 1838–1840. <https://doi.org/10.1002/cssc.201500298>.
- [87] L.D. Yuan, H.X. Deng, S.S. Li, S.H. Wei, J.W. Luo, Unified theory of direct or indirect band-gap nature of conventional semiconductors, Phys Rev B. 98 (2018) 1–10. <https://doi.org/10.1103/PhysRevB.98.245203>.
- [88] W.R. Siah, H.O. Lintang, M. Shamsuddin, L. Yuliaty, High photocatalytic activity of mixed anatase-rutile phases on commercial TiO<sub>2</sub> nanoparticles, in: IOP Conf Ser Mater Sci Eng, IOP Publishing, 2016: p. 012005. <https://doi.org/10.1088/1757-899X/107/1/012005>.
- [89] D.C. Hurum, A.G. Agrios, K.A. Gray, T. Rajh, M.C. Thurnauer, Explaining the enhanced photocatalytic activity of Degussa P25 mixed-phase TiO<sub>2</sub> using EPR, Journal of Physical Chemistry B. 107 (2003) 4545–4549. <https://doi.org/10.1021/jp0273934>.

- [90] D.O. Scanlon, C.W. Dunnill, J. Buckeridge, S.A. Shevlin, A.J. Logsdail, S.M. Woodley, C.R.A. Catlow, M.J. Powell, R.G. Palgrave, I.P. Parkin, G.W. Watson, T.W. Keal, P. Sherwood, A. Walsh, A.A. Sokol, Band alignment of rutile and anatase TiO<sub>2</sub>, *Nat Mater.* 12 (2013) 798–801. <https://doi.org/10.1038/nmat3697>.
- [91] Yamasaki RS, Intensity variations of ultraviolet, visible, and near infrared bands of terrestrial solar radiation, *J Paint Technol.* 43 (1971) 75–83.
- [92] R. Dagherir, P. Drogui, D. Robert, Modified TiO<sub>2</sub> for environmental photocatalytic applications: A review, *Ind Eng Chem Res.* 52 (2013) 3581–3599. <https://doi.org/10.1021/ie303468t>.
- [93] T. Ihara, M. Miyoshi, Y. Iriyama, O. Matsumoto, S. Sugihara, Visible-light-active titanium oxide photocatalyst realized by an oxygen-deficient structure and by nitrogen doping, *Appl Catal B.* 42 (2003) 403–409. [https://doi.org/10.1016/S0926-3373\(02\)00269-2](https://doi.org/10.1016/S0926-3373(02)00269-2).
- [94] T. Lindgren, J.M. Mwabora, E. Avandaño, J. Jonsson, A. Hoel, C.G. Granqvist, S.E. Lindquist, Photoelectrochemical and optical properties of nitrogen doped titanium dioxide films prepared by reactive DC magnetron sputtering, *Journal of Physical Chemistry B.* 107 (2003) 5709–5716. <https://doi.org/10.1021/jp027345j>.
- [95] H. Khatibnezhad, F. Ambriz-Vargas, F. Ben Ettouil, C. Moreau, An investigation on the photocatalytic activity of sub-stoichiometric TiO<sub>2-x</sub> coatings produced by suspension plasma spray, *J Eur Ceram Soc.* 41 (2021) 544–556. <https://doi.org/10.1016/J.JEURCERAMSOC.2020.08.017>.
- [96] A. Kubacka, M. Fernández-García, G. Colón, Advanced nanoarchitectures for solar photocatalytic applications, *Chem Rev.* 112 (2012) 1555–1614. <https://doi.org/10.1021/cr100454n>.
- [97] S. Kozerski, F.-L. Toma, B. Leupolt, L. Latka, L.-M. Berger, Suspension plasma sprayed TiO<sub>2</sub> coatings using different injectors and their photocatalytic properties, *Surf Coat Technol.* 205 (2010) 980–986. <https://doi.org/10.1016/J.SURFCOAT.2010.04.068>.
- [98] A. Ohmori, H. Shoyama, K. Ohashi, K. Moriya, C. Li, A Study of the Photo-Catalytic Character of Plasma Sprayed TiO<sub>2</sub> Coatings (Physics, Processes, Instruments & Measurements), *Transactions of JWRI.* 28 (1999) 21–26.
- [99] N. Branland, E. Meillot, P. Fauchais, A. Vardelle, F. Gitzhofer, M. Boulos, Relationships between microstructure and electrical properties of RF and DC plasma-sprayed titania coatings, *Journal of Thermal Spray Technology.* 15 (2006) 53–62. <https://doi.org/10.1361/105996306X92596>.
- [100] P. Vu, N. Otto, A. Vogel, F. Kern, A. Killinger, R. Gadow, Efficiently quantifying the anatase content and investigating its effect on the photocatalytic activity of titania coatings by suspension plasma spraying, *Surf Coat Technol.* 371 (2019) 117–123. <https://doi.org/10.1016/j.surfcoat.2018.07.064>.
- [101] I. Justicia, G. Garcia, G.A. Battiston, R. Gerbasi, F. Ager, M. Guerra, J. Caixach, J.A. Pardo, J. Rivera, A. Figueras, Photocatalysis in the visible range of sub-stoichiometric anatase films prepared by MOCVD, *Electrochim Acta.* 50 (2005) 4605–4608. <https://doi.org/10.1016/j.electacta.2004.10.096>.

- [102] S. Malato, P. Fernández-Ibáñez, M.I. Maldonado, J. Blanco, W. Gernjak, Decontamination and disinfection of water by solar photocatalysis: Recent overview and trends, *Catal Today*. 147 (2009) 1–59. <https://doi.org/10.1016/j.cattod.2009.06.018>.
- [103] P. Fauchais, M. Vardelle, A. Vardelle, L. Bianchi, Plasma spray: Study of the coating generation, *Ceram Int*. 22 (1996) 295–303. [https://doi.org/10.1016/0272-8842\(95\)00106-9](https://doi.org/10.1016/0272-8842(95)00106-9).
- [104] R. Herman, Herbert and Sampath, Sanjay and McCune, Thermal Spray: Current Status and Future Trends, *MRS Bull*. 25 (2000) 17–25. <https://doi.org/10.1557/mrs2000.119>.
- [105] S. Amin, H. Panchal, A. Professor, A Review on Thermal Spray Coating Processes, *International Journal of Current Trends in Engineering & Research Scientific Journal Impact Factor*. 2 (2016) 556–563. <http://www.ijcter.com>.
- [106] D. Tejero-Martin, M. Rezvani Rad, A. McDonald, T. Hussain, Beyond Traditional Coatings: A Review on Thermal-Sprayed Functional and Smart Coatings, *Journal of Thermal Spray Technology* 2019 28:4. 28 (2019) 598–644. <https://doi.org/10.1007/S11666-019-00857-1>.
- [107] M.I. Boulos, P.L. Fauchais, J.V.R. Heberlein, *Thermal Spray Fundamentals*, 2021. <https://doi.org/10.1007/978-3-030-70672-2>.
- [108] S.K. Sundaram, *Surface Engineering, Advanced Materials and Processes*. 180 (2022) 14–21.
- [109] L. Du, T.W. Coyle, K. Chien, L. Pershin, T. Li, M. Golozar, Titanium Dioxide Coating Prepared by Use of a Suspension-Solution Plasma-Spray Process, *Journal of Thermal Spray Technology*. 24 (2015) 915–924. <https://doi.org/10.1007/s11666-015-0251-1>.
- [110] A.S.M. Thermal, S. Society, Overview of Thermal Spray Technology, *Thermal Spray Technology*. (2022) 1–9. <https://doi.org/10.31399/asm.tb.tstap.t56040001>.
- [111] G. Mauer, M.O. Jarligo, D.E. Mack, R. Vaßen, Plasma-sprayed thermal barrier coatings: New materials, processing issues, and Solutions, *Journal of Thermal Spray Technology*. 22 (2013) 646–658. <https://doi.org/10.1007/s11666-013-9889-8>.
- [112] P. Fauchais, A. Vardelle, Thermal Sprayed Coatings Used Against Corrosion and Corrosive Wear, in: *Advanced Plasma Spray Applications*, IntechOpen, 2012. <https://doi.org/10.5772/34448>.
- [113] C.U. Hardwicke, Y.C. Lau, Advances in thermal spray coatings for gas turbines and energy generation: A review, *Journal of Thermal Spray Technology*. 22 (2013) 564–576. <https://doi.org/10.1007/S11666-013-9904-0/FIGURES/11>.
- [114] S. Sampath, Thermal spray applications in electronics and sensors: Past, present, and future, *Journal of Thermal Spray Technology*. 19 (2010) 921–949. <https://doi.org/10.1007/s11666-010-9475-2>.
- [115] L. Sun, C.C. Berndt, K.A. Gross, A. Kucuk, Material fundamentals and clinical performance of plasma-sprayed hydroxyapatite coatings: A review, *J Biomed Mater Res*. 58 (2001) 570–592. <https://doi.org/10.1002/jbm.1056>.

- [116] E. Alebrahim, H. Khatibnezhad, M.M. Bajgiran, M. Solomon, C. Liang, S.M. Sagan, R.S. Lima, J.O. Berghaus, M. Aghasibeig, C. Moreau, A Comparative Study of the Antiviral Properties of Thermally Sprayed Coatings against Human Coronavirus HCoV-229E, *Catalysts*. 13 (2023) 1141.
- [117] F.L. Toma, G. Bertrand, D. Klein, C. Meunier, S. Begin, Development of photocatalytic active TiO<sub>2</sub> surfaces by thermal spraying of nanopowders, *J Nanomater.* 2008 (2008) 58. <https://doi.org/10.1155/2008/384171>.
- [118] F.L. Toma, G. Bertrand, S. Begin, C. Meunier, O. Barres, D. Klein, C. Coddet, Microstructure and environmental functionalities of TiO<sub>2</sub>-supported photocatalysts obtained by suspension plasma spraying, *Appl Catal B*. 68 (2006) 74–84. <https://doi.org/10.1016/j.apcatb.2006.07.009>.
- [119] A. Feuerstein, J. Knapp, T. Taylor, A. Ashary, A. Bolcavage, N. Hitchman, Technical and economical aspects of current thermal barrier coating systems for gas turbine engines by thermal spray and EB-PVD: A review, *Journal of Thermal Spray Technology*. 17 (2008) 199–213. <https://doi.org/10.1007/s11666-007-9148-y>.
- [120] A. Bacciochini, G. Montavon, J. Ilavsky, A. Denoirjean, P. Fauchais, Porous architecture of SPS thick YSZ coatings structured at the nanometer scale, *Journal of Thermal Spray Technology*. 19 (2010) 198–206. <https://doi.org/10.1007/s11666-009-9429-8>.
- [121] E.S.C. Fan, O. Kesler, Deposition of lanthanum strontium cobalt ferrite (LSCF) using suspension plasma spraying for oxygen transport membrane applications, *Journal of Thermal Spray Technology*. 24 (2015) 1081–1092. <https://doi.org/10.1007/s11666-015-0269-4>.
- [122] L. Pawlowski, Suspension and solution thermal spray coatings, *Surf Coat Technol.* 203 (2009) 2807–2829. <https://doi.org/10.1016/J.SURFCOAT.2009.03.005>.
- [123] and L.B. Pierre Fauchais, Vincent Rat, Cédric Delbos, Jean François Coudert, Thierry Chartier, Understanding of Suspension DC Plasma Spraying of Finely Structured Coatings for SOFC, (n.d.). <http://ieeexplore.ieee.org/stamp/stamp.jsp?arnumber=1420645> (accessed October 30, 2017).
- [124] H. Kassner, R. Siegert, D. Hathiramani, R. Vassen, D. Stoeber, Application of suspension plasma spraying (SPS) for manufacture of ceramic coatings, *Journal of Thermal Spray Technology*. 17 (2008) 115–123. <https://doi.org/10.1007/s11666-007-9144-2>.
- [125] B. Bernard, A. Quet, L. Bianchi, V. Schick, A. Joulia, A. Malié, B. Rémy, Effect of Suspension Plasma-Sprayed YSZ Columnar Microstructure and Bond Coat Surface Preparation on Thermal Barrier Coating Properties, *Journal of Thermal Spray Technology*. 26 (2017) 1025–1037. <https://doi.org/10.1007/s11666-017-0584-z>.
- [126] J.G. Odhiambo, W.G. Li, Y.T. Zhao, C.L. Li, Porosity and its significance in plasma-sprayed coatings, *Coatings*. 9 (2019) 1–19. <https://doi.org/10.3390/coatings9070460>.
- [127] P. Fauchais, R. Etchart-Salas, C. Delbos, M. Tognonvi, V. Rat, J.F. Coudert, T. Chartier, Suspension and solution plasma spraying of finely structured layers: potential application to SOFCs, *J. Phys. D: Appl. Phys.* 40 (2007) 2394–2406. <https://doi.org/10.1088/0022-3727/40/8/S19>.

- [128] P. Fauchais, V. Rat, J.F. Coudert, R. Etchart-Salas, G. Montavon, Operating parameters for suspension and solution plasma-spray coatings, *Surf Coat Technol.* 202 (2008) 4309–4317. <https://doi.org/10.1016/j.surfcoat.2008.04.003>.
- [129] R. Vaen, H. Kaner, G. Mauer, D. Stöver, Suspension plasma spraying: Process characteristics and applications, in: *Journal of Thermal Spray Technology*, 2010: pp. 219–225. <https://doi.org/10.1007/s11666-009-9451-x>.
- [130] P. Fauchais, R. Etchart-Salas, V. Rat, J.F. Coudert, N. Caron, K. Wittmann-Ténèze, Parameters controlling liquid plasma spraying: Solutions, sols, or suspensions, *Journal of Thermal Spray Technology*. 17 (2008) 31–59. <https://doi.org/10.1007/s11666-007-9152-2>.
- [131] P. Fauchais, Understanding plasma spraying, *J Phys D Appl Phys.* 37 (2004). <https://doi.org/10.1088/0022-3727/37/9/R02>.
- [132] A. Joulia, W. Duarte, S. Goutier, M. Vardelle, A. Vardelle, S. Rossignol, Tailoring the Spray Conditions for Suspension Plasma Spraying, *Journal of Thermal Spray Technology*. 24 (2014) 24–29. <https://doi.org/10.1007/s11666-014-0184-0>.
- [133] F. Tarasi, E. Alebrahim, A. Dolatabadi, C. Moreau, A Comparative study of YSZ suspensions and coatings, *Coatings*. 9 (2019) 188. <https://doi.org/10.3390/COATINGS9030188>.
- [134] R. Rampon, O. Marchand, C. Filiatre, G. Bertrand, Influence of suspension characteristics on coatings microstructure obtained by suspension plasma spraying, *Surf Coat Technol.* 202 (2008) 4337–4342. <https://doi.org/10.1016/j.surfcoat.2008.04.006>.
- [135] A.A. Kulkarni, S. Sampath, A. Goland, H. Herman, A.J. Allen, J. Ilavsky, W. Gong, S. Gopalan, Plasma spray coatings for producing next-generation supported membranes, *Top Catal.* 32 (2005) 241–249. <https://doi.org/10.1007/s11244-005-2905-6>.
- [136] X. Ma, J. Dai, H. Zhang, J. Roth, T.D. Xiao, D.E. Reisner, Solid Oxide Fuel Cell Development by Using Novel Plasma Spray Techniques, *J Fuel Cell Sci Technol.* 2 (2005) 190. <https://doi.org/10.1115/1.1928928>.
- [137] R. Hui, J.O. Berghaus, C. Decès-Petit, W. Qu, S. Yick, J.G. Legoux, C. Moreau, High performance metal-supported solid oxide fuel cells fabricated by thermal spray, *J Power Sources*. 191 (2009) 371–376. <https://doi.org/10.1016/j.jpowsour.2009.02.067>.
- [138] E.S.C. Fan, J. Kuhn, O. Kesler, Suspension plasma spraying of La<sub>0.6</sub>Sr<sub>0.4</sub>Co<sub>0.2</sub>Fe<sub>0.8</sub>O<sub>3-δ</sub> cathodes: influence of carbon black pore former on performance and degradation, *J Power Sources*. 316 (2016) 72–84. <https://doi.org/10.1016/j.jpowsour.2016.02.075>.
- [139] K.L. Tung, C.C. Hsiung, T.C. Ling, K.S. Chang, T.T. Wu, Y.L. Li, C.H. Kang, W.Y. Chen, D. Nanda, Preparation and characterization of aluminum oxide cermet microfiltration membrane using atmospheric plasma spraying, *Desalination*. 245 (2009) 408–421. <https://doi.org/10.1016/j.desal.2009.02.004>.
- [140] Y.F. Lin, K.L. Tung, Y.S. Tzeng, J.H. Chen, K.S. Chang, Rapid atmospheric plasma spray coating preparation and photocatalytic activity of macroporous titania nanocrystalline membranes, *J Memb Sci*. 389 (2012) 83–90. <https://doi.org/10.1016/j.memsci.2011.10.018>.

- [141] K.-L. Tung, K.L. Tung, C.J. Chuang, C.C. Hsiung, T.C. Ling, Al<sub>2</sub>O<sub>3</sub> MICROPOROUS MEMBRANES PREPARED ON WET SUBSTRATE BY PLASMA SPRAY COATING TECHNOLOGY Membrane filtration View project Al<sub>2</sub>O<sub>3</sub> MICROPOROUS MEMBRANES PREPARED ON WET SUBSTRATE BY PLASMA SPRAY COATING TECHNOLOGY, n.d. <https://www.researchgate.net/publication/267917756> (accessed November 11, 2018).
- [142] F.L. Toma, L.M. Berger, D. Jacquet, D. Wicky, I. Villaluenga, Y.R. de Miguel, J.S. Lindeløv, Comparative study on the photocatalytic behaviour of titanium oxide thermal sprayed coatings from powders and suspensions, *Surf Coat Technol.* 203 (2009) 2150–2156. <https://doi.org/10.1016/j.surfcoat.2008.10.022>.
- [143] G. Mauer, A. Guignard, R. Vaßen, Plasma spraying of efficient photoactive TiO<sub>2</sub> coatings, *Surf Coat Technol.* 220 (2013) 40–43. <https://doi.org/10.1016/j.surfcoat.2012.08.042>.
- [144] R. Jaworski, L. Pawlowski, F. Roudet, S. Kozerski, A. Le Maguer, Influence of suspension plasma spraying process parameters on TiO<sub>2</sub> coatings microstructure, *Journal of Thermal Spray Technology.* 17 (2008) 73–81. <https://doi.org/10.1007/S11666-007-9147-Z/TABLES/7>.
- [145] F.L. Toma, D. Sokolov, G. Bertrand, D. Klein, C. Coddet, C. Meunier, Comparison of the photocatalytic behavior of TiO<sub>2</sub> coatings elaborated by different thermal spraying processes, in: *Proceedings of the International Thermal Spray Conference, 2006*: pp. 576–581. <https://doi.org/10.1361/105996306X147225>.
- [146] E. Bannier, G. Darut, E. Sanchez, A. Denoirjean, M.C. Bordes, M.D. Salvador, E. Rayan, H. Ageorges, Microstructure and photocatalytic activity of suspension plasma sprayed TiO<sub>2</sub> coatings on steel and glass substrates, *Surf Coat Technol.* 206 (2011) 378–386. <https://doi.org/10.1016/j.surfcoat.2011.07.039>.
- [147] H. Khatibnezhad, F. Ambriz-Vargas, F. Ben Ettouil, C. Moreau, Role of phase content on the photocatalytic performance of TiO<sub>2</sub> coatings deposited by suspension plasma spray, *J Eur Ceram Soc.* 42 (2022) 2905–2920. <https://doi.org/10.1016/j.jeurceramsoc.2022.02.010>.
- [148] J.H. Huang, M.S. Wong, Structures and properties of titania thin films annealed under different atmosphere, *Thin Solid Films.* 520 (2011) 1379–1384. <https://doi.org/10.1016/J.TSF.2011.08.094>.
- [149] A. Ohmori, K.C. Park, M. Inuzuka, Y. Arata, K. Inoue, N. Iwamoto, Electrical conductivity of plasma-sprayed titanium oxide (rutile) coatings, *Thin Solid Films.* 201 (1991) 1–8. [https://doi.org/10.1016/0040-6090\(91\)90149-R](https://doi.org/10.1016/0040-6090(91)90149-R).
- [150] S. Wang, J. Cai, J. Mao, S. Li, J. Shen, S. Gao, J. Huang, X. Wang, I.P. Parkin, Y. Lai, Defective black Ti<sup>3+</sup> self-doped TiO<sub>2</sub> and reduced graphene oxide composite nanoparticles for boosting visible-light driven photocatalytic and photoelectrochemical activity, *Appl Surf Sci.* 467–468 (2019) 45–55. <https://doi.org/10.1016/j.apsusc.2018.10.138>.
- [151] F. Amano, M. Nakata, A. Yamamoto, T. Tanaka, Rutile titanium dioxide prepared by hydrogen reduction of Degussa P25 for highly efficient photocatalytic hydrogen evolution, *Catal Sci Technol.* 6 (2016) 5693–5699. <https://doi.org/10.1039/c6cy00296j>.

- [152] I. Burlacov, J. Jirkovský, M. Müller, R.B. Heimann, Induction plasma-sprayed photocatalytically active titania coatings and their characterisation by micro-Raman spectroscopy, *Surf Coat Technol.* 201 (2006) 255–264. <https://doi.org/10.1016/J.SURFCOAT.2005.11.117>.
- [153] J.R. Werber, C.O. Osuji, M. Elimelech, Materials for next-generation desalination and water purification membranes, *Nat Rev Mater.* 1 (2016). <https://doi.org/10.1038/natrevmats.2016.18>.
- [154] S. Barredo-Damas, M.I. Alcaina-Miranda, A. Bes-Piá, M.I. Iborra-Clar, A. Iborra-Clar, J.A. Mendoza-Roca, Ceramic membrane behavior in textile wastewater ultrafiltration, *Desalination.* 250 (2010) 623–628. <https://doi.org/10.1016/j.desal.2009.09.037>.
- [155] M. Sun, I. Zucker, D.M. Davenport, X. Zhou, J. Qu, M. Elimelech, Reactive, Self-Cleaning Ultrafiltration Membrane Functionalized with Iron Oxychloride Nanocatalysts, *Environ Sci Technol.* 52 (2018) 8674–8683. <https://doi.org/10.1021/acs.est.8b01916>.
- [156] E. Bet-Moushoul, Y. Mansourpanah, K. Farhadi, M. Tabatabaei, TiO<sub>2</sub> nanocomposite based polymeric membranes: A review on performance improvement for various applications in chemical engineering processes, *Chemical Engineering Journal.* 283 (2016) 29–46. <https://doi.org/10.1016/J.CEJ.2015.06.124>.
- [157] H. Verweij, Ceramic membranes: Morphology and transport, *J Mater Sci.* 38 (2003) 4677–4695. <https://doi.org/10.1023/A:1027410616041>.
- [158] Y. Kang, S. Jiao, Y. Zhao, B. Wang, Z. Zhang, W. Yin, Y. Tan, G. Pang, High-flux and high rejection TiO<sub>2</sub> nanofibers ultrafiltration membrane with porous titanium as supporter, *Sep Purif Technol.* 248 (2020) 117000. <https://doi.org/10.1016/J.SEPPUR.2020.117000>.
- [159] X. Liu, K. Wen, C. Deng, K. Yang, C. Deng, M. Liu, K. Zhou, Nanostructured Photocatalytic TiO<sub>2</sub> Coating Deposited by Suspension Plasma Spraying with Different Injection Positions, *Journal of Thermal Spray Technology.* 27 (2018) 245–254. <https://doi.org/10.1007/s11666-018-0693-3>.
- [160] R.S. Lima, B.R. Marple, Thermal spray coatings engineered from nanostructured ceramic agglomerated powders for structural, thermal barrier and biomedical applications: A review, *Journal of Thermal Spray Technology.* 16 (2007) 40–63. <https://doi.org/10.1007/s11666-006-9010-7>.
- [161] F. Ghadami, M.A. Davoudabadi, S. Ghadami, Cyclic Oxidation Properties of the Nanocrystalline AlCrFeCoNi High-Entropy Alloy Coatings Applied by the Atmospheric Plasma Spraying Technique, *Coatings.* 12 (2022) 372. <https://doi.org/10.3390/coatings12030372>.
- [162] F. Ghadami, A. Sabour, R. Aghdam, S. Ghadami, A comprehensive study on the microstructure evolution and oxidation resistance of conventional and nanocrystalline MCrAlY coatings, *Scientific Reports |.* 11 (123AD) 875. <https://doi.org/10.1038/s41598-020-79323-w>.
- [163] M.R. Al-Mamun, S. Kader, M.S. Islam, M.Z.H. Khan, Photocatalytic activity improvement and application of UV-TiO<sub>2</sub> photocatalysis in textile wastewater treatment: A review, *J Environ Chem Eng.* 7 (2019) 103248. <https://doi.org/10.1016/j.jece.2019.103248>.
- [164] E.O. Onah, M.A. Onuorah, S.U. Offiah, R.M. Obodo, O. V Ekechukwu, P.E. Ugwuoke, F.I. Ezema, Effects of annealing temperature on TiO<sub>2</sub> photoelectrodes of dye-sensitized solar cells using

- lxora coccenia dye extract, *Journal of Nanoparticle Research*. 23 (2021). <https://doi.org/10.1007/s11051-021-05335-w>.
- [165] A.M. Ali, M.A. Sayed, H. Algarni, V. Ganesh, M. Aslam, A.A. Ismail, H.M. El-Bery, Synthesis, characterization and photoelectric properties of Fe<sub>2</sub>O<sub>3</sub> incorporated TiO<sub>2</sub> photocatalyst nanocomposites, *Catalysts*. 11 (2021). <https://doi.org/10.3390/catal11091062>.
- [166] Y. Fu, Y. Liu, H. Li, Onion-like carbon-modified TiO<sub>2</sub> coating by suspension plasma spray with enhanced photocatalytic performances, *Journal of Nanoparticle Research*. 21 (2019). <https://doi.org/10.1007/s11051-019-4633-z>.
- [167] Z. Miao, G. Wang, L. Li, C. Wang, X. Zhang, Fabrication of black TiO<sub>2</sub>/TiO<sub>2</sub> homojunction for enhanced photocatalytic degradation, *J Mater Sci*. 54 (2019) 14320–14329. <https://doi.org/10.1007/s10853-019-03900-2>.
- [168] K.M. Reddy, S. V Manorama, A.R. Reddy, Bandgap studies on anatase titanium dioxide nanoparticles, *Mater Chem Phys*. 78 (2003) 239–245. [https://doi.org/10.1016/S0254-0584\(02\)00343-7](https://doi.org/10.1016/S0254-0584(02)00343-7).
- [169] R. Yue, B. Raisi, J. Rahmatinejad, Z. Ye, B. Barbeau, M.S. Rahaman, A photo-Fenton nanocomposite ultrafiltration membrane for enhanced dye removal with self-cleaning properties, *J Colloid Interface Sci*. 604 (2021) 458–468. <https://doi.org/10.1016/j.jcis.2021.06.157>.
- [170] J.O. Berghaus, J.G. Legoux, C. Moreau, R. Hui, D. Ghosh, Suspension plasma spaying of intermediate temperature SOFC components using an axial injection DC torch, *Materials Science Forum*. 539–543 (2007) 1332–1337. <https://doi.org/10.4028/www.scientific.net/msf.539-543.1332>.
- [171] C.E. Mancini, C.C. Berndt, L. Sun, A. Kucuk, Porosity determinations in thermally sprayed hydroxyapatite coatings, *J Mater Sci*. 36 (2001) 3891–3896. <https://doi.org/10.1023/A:1017905818479>.
- [172] S.M. Samaei, S. Gato-Trinidad, A. Altaee, The application of pressure-driven ceramic membrane technology for the treatment of industrial wastewaters – A review, *Sep Purif Technol*. 200 (2018) 198–220. <https://doi.org/10.1016/j.seppur.2018.02.041>.
- [173] Z. Pala, E. Shaw, J.W. Murray, N. Senin, T. Hussain, Suspension high velocity oxy-fuel spraying of TiO<sub>2</sub>: A quantitative approach to phase composition, *J Eur Ceram Soc*. 37 (2017) 801–810. <https://doi.org/10.1016/j.jeurceramsoc.2016.08.030>.
- [174] P. Fauchais, J.F. Coudert, M. Vardelle, Diagnostics in Thermal Plasma Processing, in: *Plasma Diagnostics*, Academic Press, 1989: pp. 349–446. <https://doi.org/10.1016/b978-0-12-067635-4.50012-0>.
- [175] F.L. Toma, G. Bertrand, S.O. Chwa, C. Meunier, D. Klein, C. Coddet, Comparative study on the photocatalytic decomposition of nitrogen oxides using TiO<sub>2</sub> coatings prepared by conventional plasma spraying and suspension plasma spraying, *Surf Coat Technol*. 200 (2006) 5855–5862. <https://doi.org/10.1016/j.surfcoat.2005.08.148>.

- [176] J. Oberste Berghaus, S. Bouaricha, J.G. Legoux, C. Moreau, Injection conditions and in-flight particle states in suspension plasma spraying of alumina and zirconia nano-ceramics, in: The International Thermal Spray Conference (ITSC) Basel, Switzerland, 2005: pp. 1434–1440.
- [177] J. Oberste-Berghaus, S. Bouaricha, J.-G. Legoux, C. Moreau, Injection conditions and in-flight particles states in suspension plasma spraying of alumina and zirconia nano-ceramics, Thermal Spray 2005: Proceedings of the International Thermal Spray Conference. (2005) 512–518.
- [178] A. Bacciochini, J. Ilavsky, G. Montavon, A. Denoirjean, F. Ben-ettouil, S. Valette, P. Fauchais, K. Wittmann-teneze, Quantification of void network architectures of suspension plasma-sprayed (SPS) yttria-stabilized zirconia (YSZ) coatings using Ultra-small-angle X-ray scattering (USAXS), *Materials Science and Engineering: A*. 528 (2010) 91–102. <https://doi.org/10.1016/J.MSEA.2010.06.082>.
- [179] R. R. Bhave, J. Guibaud, R. Rumeau, *Inorganic membranes synthesis, characteristics and applications*, 1st ed., Van Nostrand Reinhold, New York, 1991. <https://doi.org/10.1007/978-94-011-6547-1>.
- [180] P. Galizia, G. Maizza, C. Galassi, Heating rate dependence of anatase to rutile transformation, *Processing and Application of Ceramics*. 10 (2016) 235–241. <https://doi.org/10.2298/PAC1604235G>.
- [181] C. Lee, H. Choi, C. Lee, H. Kim, Photocatalytic properties of nano-structured TiO<sub>2</sub> plasma sprayed coating, *Surf Coat Technol.* 173 (2003) 192–200. [https://doi.org/10.1016/S0257-8972\(03\)00509-7](https://doi.org/10.1016/S0257-8972(03)00509-7).
- [182] S. Kozerski, F.L. Toma, L. Pawlowski, B. Leupolt, L. Latka, L.M. Berger, Suspension plasma sprayed TiO<sub>2</sub> coatings using different injectors and their photocatalytic properties, *Surf Coat Technol.* 205 (2010) 980–986. <https://doi.org/10.1016/j.surfcoat.2010.04.068>.
- [183] Y. Li, T. Ishigaki, Thermodynamic analysis of nucleation of anatase and rutile from TiO<sub>2</sub> melt, *J Cryst Growth*. 242 (2002) 511–516. [https://doi.org/10.1016/S0022-0248\(02\)01438-0](https://doi.org/10.1016/S0022-0248(02)01438-0).
- [184] Y.F. Chen, C.Y. Lee, M.Y. Yeng, H.T. Chiu, The effect of calcination temperature on the crystallinity of TiO<sub>2</sub> nanopowders, *J Cryst Growth*. 247 (2003) 363–370. [https://doi.org/10.1016/S0022-0248\(02\)01938-3](https://doi.org/10.1016/S0022-0248(02)01938-3).
- [185] M. Klaus, K. Peter, Comparison between different presentations of pore size distribution in porous materials, *Fresenius J Anal Chem.* 363 (1999) 174–178.
- [186] M.M. Cortalezzi, J. Rose, G.F. Wells, J.Y. Bottero, A.R. Barron, M.R. Wiesner, Ceramic membranes derived from ferroxane nanoparticles: A new route for the fabrication of iron oxide ultrafiltration membranes, *J Memb Sci.* 227 (2003) 207–217. <https://doi.org/10.1016/j.memsci.2003.08.027>.
- [187] R. Sondhi, R. Bhave, G. Jung, Applications and benefits of ceramic membranes, *Membrane Technology*. 2003 (2003) 5–8. [https://doi.org/10.1016/S0958-2118\(03\)11016-6](https://doi.org/10.1016/S0958-2118(03)11016-6).
- [188] M. Ben Ali, N. Hamdi, M.A. Rodriguez, K. Mahmoudi, E. Srasra, Preparation and characterization of new ceramic membranes for ultrafiltration, *Ceram Int.* 44 (2018) 2328–2335. <https://doi.org/10.1016/J.CERAMINT.2017.10.199>.

- [189] L. Yu, M. Kanezashi, H. Nagasawa, T. Tsuru, Phase inversion/sintering-induced porous ceramic microsheet membranes for high-quality separation of oily wastewater, *J Memb Sci.* 595 (2020) 117477. <https://doi.org/10.1016/J.MEMSCI.2019.117477>.
- [190] F.L. Toma, L.M. Berger, C.C. Stahr, T. Naumann, S. Langner, Microstructures and functional properties of suspension-sprayed Al<sub>2</sub>O<sub>3</sub> and TiO<sub>2</sub> coatings: An overview, *Journal of Thermal Spray Technology.* 19 (2010) 262–274. <https://doi.org/10.1007/s11666-009-9417-z>.
- [191] F.-L. Toma, S. Alamri, B. Leupolt, T. Kunze, M. Barbosa, Functionalization of Suspension Sprayed HVOF TiO<sub>2</sub> Coatings by Direct Laser Interference Patterning, (n.d.). <https://doi.org/10.1007/s11666-021-01181-3>.
- [192] J. Wang, P. Yang, B. Huang, Self-doped TiO<sub>2-x</sub> nanowires with enhanced photocatalytic activity: Facile synthesis and effects of the Ti<sup>3+</sup>, *Appl Surf Sci.* 356 (2015) 391–398. <https://doi.org/10.1016/j.apsusc.2015.08.029>.
- [193] C. Li, T. Sun, D. Zhang, X. Zhang, Y. Qian, Y. Zhang, X. Lin, J. Liu, L. Zhu, X. Wang, Z. Shi, Q. Lin, Fabrication of ternary Ag/La-black TiO<sub>2-x</sub> photocatalyst with enhanced visible-light photocatalytic activity for tetracycline degradation, *J Alloys Compd.* 891 (2022). <https://doi.org/10.1016/j.jallcom.2021.161960>.
- [194] H. Herman, S. Sampath, R. Mccune, Thermal spray: current status and future trends, *MRS Bull.* 25 (2000) 17–25.
- [195] P.L. Fauchais, J.V.R. Heberlein, M.I. Boulos, *Thermal Spray Fundamentals*, 2014. <https://doi.org/10.1007/978-0-387-68991-3>.
- [196] E. Dalir, A. Dolatabadi, J. Mostaghimi, Modeling of Suspension Plasma Spraying Process Including Arc Movement Inside the Torch, *Journal of Thermal Spray Technology.* 28 (2019) 1105–1125. <https://doi.org/10.1007/s11666-019-00883-z>.
- [197] M. Aghasibeig, F. Tarasi, R.S. Lima, A. Dolatabadi, C. Moreau, A Review on Suspension Thermal Spray Patented Technology Evolution, *Journal of Thermal Spray Technology.* 28 (2019) 1579–1605. <https://doi.org/10.1007/s11666-019-00904-x>.
- [198] O. Marchand, P. Bertrand, J. Mougín, C. Comminges, M.P. Planche, G. Bertrand, Characterization of suspension plasma-sprayed solid oxide fuel cell electrodes, *Surf Coat Technol.* 205 (2010) 993–998. <https://doi.org/10.1016/j.surfcoat.2010.06.001>.
- [199] E. Alebrahim, M.S. Rahaman, C. Moreau, TiO<sub>2</sub> Photocatalytic Ultrafiltration Membrane Developed with Suspension Plasma Spray Process, *Coatings.* 12 (2022) 1764. <https://doi.org/10.3390/coatings12111764>.
- [200] Y. Zhao, Y. Wang, F. Peyraut, M.P. Planche, J. Ilavsky, H. Liao, G. Montavon, A. Lasalle, A. Allimant, Z. Yu, M.P. Planche, A. Lasalle, A. Allimant, G. Montavon, H. Liao, Parametric analysis and modeling for the porosity prediction in suspension plasma-sprayed coatings, *Journal of Thermal Spray Technology.* 29 (2020) 51–59. <https://doi.org/10.1007/s11666-019-00966-x>.
- [201] Y. Zhao, F. Peyraut, M.P. Planche, J. Ilavsky, H. Liao, A. Lasalle, A. Allimant, G. Montavon, Experiments, Statistical Analysis, and Modeling to Evaluate the Porosity Influence in SPS Coatings,

- Journal of Thermal Spray Technology. 28 (2019) 76–86. <https://doi.org/10.1007/s11666-018-0749-4>.
- [202] M. Cuglietta, J. Kuhn, O. Kesler, A novel hybrid axial-radial atmospheric plasma spraying technique for the fabrication of solid oxide fuel cell anodes containing Cu, Co, Ni, and samaria-doped ceria, *Journal of Thermal Spray Technology*. 22 (2013) 609–621. <https://doi.org/10.1007/s11666-013-9918-7>.
- [203] G. Bolelli, A. Candeli, L. Lusvarghi, A. Ravoux, K. Cazes, A. Denoirjean, S. Valette, C. Chazelas, E. Meillot, L. Bianchi, Tribology of NiCrAlY+Al<sub>2</sub>O<sub>3</sub> composite coatings by plasma spraying with hybrid feeding of dry powder+suspension, *Wear*. 344–345 (2015) 69–85. <https://doi.org/10.1016/j.wear.2015.10.014>.
- [204] B.T. Hazel, J.L. Serra, X. Liu, ( 12 ) Patent Application Publication ( 10 ) Pub . No . : US 2017 / 0116693 A1 Complete Patent Application Publication, 2017.
- [205] S. Björklund, S. Goel, S. Joshi, Function-dependent coating architectures by hybrid powder-suspension plasma spraying: Injector design, processing and concept validation, *Mater Des*. 142 (2018) 56–65. <https://doi.org/10.1016/j.matdes.2018.01.002>.
- [206] M. Nowakowska, P. Sokolowski, T. Tesar, R. Musalek, T. Kielczawa, Al<sub>2</sub>O<sub>3</sub>-TiO<sub>2</sub> coatings deposition by intermixed and double injection SPS concepts, *Materials Science- Poland*. 39 (2021) 599–614. <https://doi.org/10.2478/msp-2021-0046>.
- [207] S. Mahade, A. Mulone, S. Björklund, U. Klement, S. Joshi, Incorporation of graphene nano platelets in suspension plasma sprayed alumina coatings for improved tribological properties, *Appl Surf Sci*. 570 (2021). <https://doi.org/10.1016/j.apsusc.2021.151227>.
- [208] Y. Liu, J. Huang, X. Feng, H. Li, Thermal-Sprayed Photocatalytic Coatings for Biocidal Applications: A Review, *Journal of Thermal Spray Technology*. (2020). <https://doi.org/10.1007/s11666-020-01118-2>.
- [209] S. Kozerski, F.L. Toma, L. Pawlowski, B. Leupolt, L. Latka, L.M. Berger, Suspension plasma sprayed TiO<sub>2</sub> coatings using different injectors and their photocatalytic properties, *Surf Coat Technol*. 205 (2010) 980–986. <https://doi.org/10.1016/j.surfcoat.2010.04.068>.
- [210] G. Mittal, S. Paul, Suspension and Solution Precursor Plasma and HVOF Spray: A Review, *Journal of Thermal Spray Technology*. 31 (2022) 1443–1475. <https://doi.org/10.1007/s11666-022-01360-w>.
- [211] V. Carnicer, M.J. Orts, R. Moreno, E. Sánchez, Influence of solids concentration on the microstructure of suspension plasma sprayed Y-TZP/Al<sub>2</sub>O<sub>3</sub>/SiC composite coatings, *Surf Coat Technol*. 371 (2019) 143–150. <https://doi.org/10.1016/j.surfcoat.2019.01.078>.
- [212] K. VanEvery, M.J.M. Krane, R.W. Trice, Parametric study of suspension plasma spray processing parameters on coating microstructures manufactured from nanoscale yttria-stabilized zirconia, *Surf Coat Technol*. 206 (2012) 2464–2473. <https://doi.org/10.1016/j.surfcoat.2011.10.051>.

- [213] S. Mohammadi, Particle Image Velocimetry of Suspension Plasma Spray in the Vicinity of a Substrate, Thesis (Masters), Concordia University, 2020. <https://spectrum.library.concordia.ca/id/eprint/987775/>.
- [214] Z. Chen, R.W. Trice, M. Besser, X. Yang, D. Sordelet, Air-plasma spraying colloidal solutions of nanosized ceramic powders, *J Mater Sci.* 39 (2004) 4171–4178. <https://link.springer.com/content/pdf/10.1023%2FB%3AJMSC.0000033396.51316.8b.pdf> (accessed July 11, 2018).
- [215] F.L. Toma, L.M. Berger, T. Naumann, S. Langner, Microstructures of nanostructured ceramic coatings obtained by suspension thermal spraying, *Surf Coat Technol.* 202 (2008) 4343–4348. <https://doi.org/10.1016/j.surfcoat.2008.04.007>.
- [216] P. Sokolowski, L. Pawlowski, D. Dietrich, T. Lampke, D. Jech, Advanced Microscopic Study of Suspension Plasma-Sprayed Zirconia Coatings with Different Microstructures, *Journal of Thermal Spray Technology.* 25 (2016) 94–104. <https://doi.org/10.1007/s11666-015-0310-7>.
- [217] G. Mauer, R. Vaßen, Coatings with Columnar Microstructures for Thermal Barrier Applications, *Adv Eng Mater.* 22 (2020) 1–9. <https://doi.org/10.1002/adem.201900988>.
- [218] P. Fauchais, M. Vardelle, A. Vardelle, S. Goutier, What Do We Know, What are the Current Limitations of Suspension Plasma Spraying?, *Journal of Thermal Spray Technology.* 24 (2015) 1120–1129. <https://doi.org/10.1007/s11666-015-0286-3>.
- [219] G.D. Scott, D.M. Kilgour, The density of random close packing of spheres, *J Phys D Appl Phys.* 2 (1969) 863–866. <https://doi.org/10.1088/0022-3727/2/6/311>.
- [220] P. Fauchais, R. Etchart-Salas, V. Rat, J.F. Coudert, N. Caron, K. Wittmann-Ténéze, Parameters controlling liquid plasma spraying: Solutions, sols, or suspensions, *Journal of Thermal Spray Technology.* 17 (2008) 31–59. <https://doi.org/10.1007/s11666-007-9152-2>.
- [221] F. Tarasi, M. Medraj, A. Dolatabadi, J. Oberste-Berghaus, C. Moreau, Effective parameters in axial injection suspension plasma spray process of alumina-zirconia ceramics, *Journal of Thermal Spray Technology.* 17 (2008) 685–691. <https://doi.org/10.1007/s11666-008-9259-0>.
- [222] P. Fauchais, V. Rat, C. Delbos, J.F. Coudert, T. Chartier, L. Bianchi, Understanding of suspension DC plasma spraying of finely structured coatings for SOFC, *IEEE Transactions on Plasma Science.* 33 (2005) 920–930. <https://doi.org/10.1109/TPS.2005.845094>.
- [223] K. Vanevery, M.J.M. Krane, R.W. Trice, H. Wang, W. Porter, M. Besser, D. Sordelet, J. Ilavsky, J. Almer, Column formation in suspension plasma-sprayed coatings and resultant thermal properties, *Journal of Thermal Spray Technology.* 20 (2011) 817–828. <https://doi.org/10.1007/s11666-011-9632-2>.
- [224] Y. Li, T. Ishigaki, Thermodynamic analysis of nucleation of anatase and rutile from TiO<sub>2</sub> melt, *J Cryst Growth.* 242 (2002) 511–516. [https://doi.org/10.1016/S0022-0248\(02\)01438-0](https://doi.org/10.1016/S0022-0248(02)01438-0).
- [225] J.R. Colmenares-Angulo, V. Cannillo, L. Lusvarghi, A. Sola, S. Sampath, Role of process type and process conditions on phase content and physical properties of thermal sprayed TiO<sub>2</sub> coatings, *J Mater Sci.* 44 (2009) 2276–2287. <https://doi.org/10.1007/s10853-008-3044-9>.

- [226] S. Zhao, L. Shen, Editorial: Advanced Membrane Science and Technology for Sustainable Environmental Applications, *Front Chem.* 8 (2020) 609774. <https://doi.org/10.3389/FCHEM.2020.609774/BIBTEX>.
- [227] H. Xu, K. Xiao, X. Wang, S. Liang, C. Wei, X. Wen, X. Huang, Outlining the Roles of Membrane-Foulant and Foulant-Foulant Interactions in Organic Fouling During Microfiltration and Ultrafiltration: A Mini-Review, *Front Chem.* 8 (2020) 538277. <https://doi.org/10.3389/FCHEM.2020.00417/BIBTEX>.
- [228] S.L. Sandhya Rani, R.V. Kumar, Insights on applications of low-cost ceramic membranes in wastewater treatment: A mini-review, *Case Studies in Chemical and Environmental Engineering.* 4 (2021) 100149. <https://doi.org/10.1016/J.CSCEE.2021.100149>.
- [229] A. Abdullayev, M.F. Bekheet, D.A.H. Hanaor, A. Gurlo, Materials and applications for low-cost ceramic membranes, *Membranes (Basel).* 9 (2019). <https://doi.org/10.3390/membranes9090105>.
- [230] Q. Liu, S. Huang, Y. Zhang, S. Zhao, Comparing the antifouling effects of activated carbon and TiO<sub>2</sub> in ultrafiltration membrane development, *J Colloid Interface Sci.* 515 (2018) 109–118. <https://doi.org/10.1016/j.jcis.2018.01.026>.
- [231] H. Yang, X. Yu, J. Liu, Z. Tang, T. Huang, Z. Wang, Y. Zhong, Z. Long, L. Wang, A Concise Review of Theoretical Models and Numerical Simulations of Membrane Fouling, *Water (Switzerland).* 14 (2022) 3537. <https://doi.org/10.3390/w14213537>.
- [232] R.Y. Yue, P.C. Yuan, C.M. Zhang, Z.H. Wan, S.G. Wang, X. Sun, Robust self-cleaning membrane with superhydrophilicity and underwater superoleophobicity for oil-in-water separation, *Chemosphere.* 330 (2023) 138706. <https://doi.org/10.1016/j.chemosphere.2023.138706>.
- [233] M. Bekbolet, A.S. Suphandag, C.S. Uyguner, An investigation of the photocatalytic efficiencies of TiO<sub>2</sub> powders on the decolourisation of humic acids, *J Photochem Photobiol A Chem.* 148 (2002) 121–128. [https://doi.org/10.1016/S1010-6030\(02\)00081-3](https://doi.org/10.1016/S1010-6030(02)00081-3).
- [234] M. Rawat, V.K. Bulasara, Synthesis and characterization of low-cost ceramic membranes from fly ash and kaolin for humic acid separation, *Korean Journal of Chemical Engineering.* 35 (2018) 725–733. <https://doi.org/10.1007/s11814-017-0316-6>.
- [235] C.S. Uyguner, M. Bekbolet, Evaluation of humic acid photocatalytic degradation by UV-vis and fluorescence spectroscopy, in: *Catal Today, Elsevier, 2005: pp. 267–274.* <https://doi.org/10.1016/j.cattod.2005.03.011>.
- [236] M. Qadafi, R.T. Rosmalina, M.M. Pitoi, D.R. Wulan, Chlorination disinfection by-products in Southeast Asia: A review on potential precursor, formation, toxicity assessment, and removal technologies, *Chemosphere.* 316 (2023) 137817. <https://doi.org/10.1016/j.chemosphere.2023.137817>.
- [237] Y.H. Teow, B.S. Ooi, A.L. Ahmad, J.K. Lim, Investigation of anti-fouling and uv-cleaning properties of PVDF/TiO<sub>2</sub> mixed-matrix membrane for humic acid removal, *Membranes (Basel).* 11 (2021) 1–22. <https://doi.org/10.3390/membranes11010016>.

- [238] L. Zhang, T.C.A. Ng, X. Liu, Q. Gu, Y. Pang, Z. Zhang, Z. Lyu, Z. He, H.Y. Ng, J. Wang, Hydrogenated TiO<sub>2</sub> membrane with photocatalytically enhanced anti-fouling for ultrafiltration of surface water, *Appl Catal B*. 264 (2020) 118528. <https://doi.org/10.1016/j.apcatb.2019.118528>.
- [239] C. Li, W. Sun, Z. Lu, X. Ao, C. Yang, S. Li, Systematic evaluation of TiO<sub>2</sub>-GO-modified ceramic membranes for water treatment: Retention properties and fouling mechanisms, *Chemical Engineering Journal*. 378 (2019) 122138. <https://doi.org/10.1016/j.cej.2019.122138>.
- [240] C. Delbos, J. Fazilleau, V. Rat, J.F. Coudert, P. Fauchais, B. Pateyron, Phenomena involved in suspension plasma spraying part 2: Zirconia particle treatment and coating formation, *Plasma Chemistry and Plasma Processing*. 26 (2006) 393–414. <https://doi.org/10.1007/s11090-006-9020-8>.
- [241] H. Khatibnezhad, F. Ambriz-Vargas, F. Ben Ettouil, C. Moreau, An investigation on the photocatalytic activity of sub-stoichiometric TiO<sub>2</sub>-x coatings produced by suspension plasma spray, *J Eur Ceram Soc*. 41 (2021) 544–556. <https://doi.org/10.1016/j.jeurceramsoc.2020.08.017>.
- [242] A. Vardelle, C. Moreau, J. Akedo, H. Ashrafizadeh, C.C. Berndt, J.O. Berghaus, M. Boulos, J. Brogan, A.C. Bourtsalas, A. Dolatabadi, M. Dorfman, T.J. Eden, P. Fauchais, G. Fisher, F. Gaertner, M. Gindrat, R. Henne, M. Hyland, E. Irissou, E.H. Jordan, K.A. Khor, A. Killinger, Y.C. Lau, C.J. Li, L. Li, J. Longtin, N. Markocsan, P.J. Masset, J. Matejicek, G. Mauer, A. McDonald, J. Mostaghimi, S. Sampath, G. Schiller, K. Shinoda, M.F. Smith, A.A. Syed, N.J. Themelis, F.L. Toma, J.P. Trelles, R. Vassen, P. Vuoristo, The 2016 Thermal Spray Roadmap, *Journal of Thermal Spray Technology*. 25 (2016) 1376–1440. <https://doi.org/10.1007/s11666-016-0473-x>.
- [243] K.C. Khulbe, C.Y. Feng, T. Matsuura, *Synthetic Polymeric Membranes*, Springer Berlin Heidelberg, Berlin, 2008.
- [244] C.P. Holliday, T.C. Rasmussen, W.P. Miller, Establishing the Relationship Between Turbidity and Total Suspended Sediment Concentration, *Proceedings of the 2003 Georgia Water Resources Conference*. (2003) 23-24 April.
- [245] A. Hannouche, G. Chebbo, G. Ruban, B. Tassin, B.J. Lemaire, C. Joannis, Relationship between turbidity and total suspended solids concentration within a combined sewer system, *Water Science and Technology*. 64 (2011) 2445–2452. <https://doi.org/10.2166/wst.2011.779>.
- [246] R. Yue, B. Raisi, J. Rahmatinejad, Z. Ye, B. Barbeau, M.S. Rahaman, A photo-Fenton nanocomposite ultrafiltration membrane for enhanced dye removal with self-cleaning properties, *J Colloid Interface Sci*. 604 (2021) 458–468. <https://doi.org/10.1016/j.jcis.2021.06.157>.
- [247] Y.H. Kotp, Enhancement of Industrial Effluents Quality by Using Nanocomposite Mg/Al LDH Ultrafiltration Membranes, *J Inorg Organomet Polym Mater*. 30 (2020) 5244–5260. <https://doi.org/10.1007/s10904-020-01608-4>.
- [248] L. Yan, X. Yang, Y. Li, R. Song, Y. Lin, Q. Huang, L. Shao, Acid-resistant supramolecular nanofibrous hydrogel membrane with core-shell structure for highly efficient oil/water separation, *J Memb Sci*. 679 (2023) 121705. <https://doi.org/10.1016/J.MEMSCI.2023.121705>.

- [249] Y.F. Lin, K.L. Tung, Y.S. Tzeng, J.H. Chen, K.S. Chang, Rapid atmospheric plasma spray coating preparation and photocatalytic activity of macroporous titania nanocrystalline membranes, *J Memb Sci.* 389 (2012) 83–90. <https://doi.org/10.1016/j.memsci.2011.10.018>.
- [250] A.D. Sabde, M.K. Trivedi, V. Ramachandhran, M.S. Hanra, B.M. Misra, Casting and characterization of cellulose acetate butyrate based UF membranes, *Desalination.* 114 (1997) 223–232. [https://doi.org/10.1016/S0011-9164\(98\)00014-9](https://doi.org/10.1016/S0011-9164(98)00014-9).
- [251] M. Hossein Razzaghi, A. Safekordi, M. Tavakolmoghadam, F. Rekabdar, M. Hemmati, Morphological and separation performance study of PVDF/CA blend membranes, *J Memb Sci.* 470 (2014) 547–557. <https://doi.org/10.1016/j.memsci.2014.07.026>.
- [252] E. Arkhangelsky, A. Duek, V. Gitis, Maximal pore size in UF membranes, *J Memb Sci.* 394–395 (2012) 89–97. <https://doi.org/10.1016/j.memsci.2011.12.031>.
- [253] S. Singh, K.C. Khulbe, T. Matsuura, P. Ramamurthy, Membrane characterization by solute transport and atomic force microscopy, *J Memb Sci.* 142 (1998) 111–127. [https://doi.org/10.1016/S0376-7388\(97\)00329-3](https://doi.org/10.1016/S0376-7388(97)00329-3).
- [254] Y. Wang, L. Li, Y. Wei, J. Xue, H. Chen, L. Ding, J. Caro, H. Wang, Water Transport with Ultralow Friction through Partially Exfoliated g-C<sub>3</sub>N<sub>4</sub> Nanosheet Membranes with Self-Supporting Spacers, *Angewandte Chemie - International Edition.* 56 (2017) 8974–8980. <https://doi.org/10.1002/anie.201701288>.
- [255] T. Urase, K. Yamamoto, S. Ohgaki, Effect of pore structure of membranes and module configuration on virus retention, *J Memb Sci.* 115 (1996) 21–29. [https://doi.org/10.1016/0376-7388\(95\)00269-3](https://doi.org/10.1016/0376-7388(95)00269-3).
- [256] C.M. Tam, A.Y. Tremblay, Membrane pore characterization-comparison between single and multicomponent solute probe techniques, *J Memb Sci.* 57 (1991) 271–287. [https://doi.org/10.1016/S0376-7388\(00\)80683-3](https://doi.org/10.1016/S0376-7388(00)80683-3).
- [257] A.D. Syafei, C.F. Lin, C.H. Wu, Removal of natural organic matter by ultrafiltration with TiO<sub>2</sub>-coated membrane under UV irradiation, *J Colloid Interface Sci.* 323 (2008) 112–119. <https://doi.org/10.1016/j.jcis.2008.03.037>.
- [258] Y. Chung, D. Park, H. Kim, S.E. Nam, S. Kang, Novel method for the facile control of molecular weight cut-off (MWCO) of ceramic membranes, *Water Res.* 215 (2022) 118268. <https://doi.org/10.1016/j.watres.2022.118268>.
- [259] M. Nyström, K. Ruohomäki, L. Kaipia, Humic acid as a fouling agent in filtration, *Desalination.* 106 (1996) 79–87. [https://doi.org/10.1016/S0011-9164\(96\)00095-1](https://doi.org/10.1016/S0011-9164(96)00095-1).
- [260] J. Wiszniowski, D. Robert, J. Surmacz-Gorska, K. Miksch, J.V. Weber, Photocatalytic decomposition of humic acids on TiO<sub>2</sub>. Part I: Discussion of adsorption and mechanism, *J Photochem Photobiol A Chem.* 152 (2002) 267–273. [https://doi.org/10.1016/S1010-6030\(02\)00022-9](https://doi.org/10.1016/S1010-6030(02)00022-9).

- [261] S. Liu, M. Lim, R. Fabris, C. Chow, K. Chiang, M. Drikas, R. Amal, Removal of humic acid using TiO<sub>2</sub> photocatalytic process - Fractionation and molecular weight characterisation studies, *Chemosphere*. 72 (2008) 263–271. <https://doi.org/10.1016/j.chemosphere.2008.01.061>.
- [262] O. Carp, C.L. Huisman, A. Reller, Photoinduced reactivity of titanium dioxide, *Progress in Solid State Chemistry*. 32 (2004) 33–177. <https://doi.org/10.1016/j.progsolidstchem.2004.08.001>.
- [263] J. Wiszniowski, D. Robert, J. Surmacz-Gorska, K. Miksch, S. Malato, J.V. Weber, Solar photocatalytic degradation of humic acids as a model of organic compounds of landfill leachate in pilot-plant experiments: influence of inorganic salts, *Appl Catal B*. 53 (2004) 127–137. <https://doi.org/10.1016/J.APCATB.2004.04.017>.
- [264] N. Corin, P. Backhand, M. Kulovaara, Degradation products formed during UV-irradiation of humic waters, *Chemosphere*. 33 (1996) 245–255. [https://doi.org/10.1016/0045-6535\(96\)00167-1](https://doi.org/10.1016/0045-6535(96)00167-1).
- [265] A. Mills, An overview of the methylene blue ISO test for assessing the activities of photocatalytic films, *Appl Catal B*. 128 (2012) 144–149. <https://doi.org/10.1016/J.APCATB.2012.01.019>.
- [266] A. Houas, H. Lachheb, M. Ksibi, E. Elaloui, C. Guillard, J.M. Herrmann, Photocatalytic degradation pathway of methylene blue in water, *Appl Catal B*. 31 (2001) 145–157. [https://doi.org/10.1016/S0926-3373\(00\)00276-9](https://doi.org/10.1016/S0926-3373(00)00276-9).
- [267] X. Wang, S. Li, P. Chen, F. Li, X. Hu, T. Hua, Photocatalytic and antifouling properties of TiO<sub>2</sub>-based photocatalytic membranes, *Mater Today Chem*. 23 (2022) 100650. <https://doi.org/10.1016/j.mtchem.2021.100650>.
- [268] S.S. Madaeni, S. Zinadini, V. Vatanpour, A new approach to improve antifouling property of PVDF membrane using in situ polymerization of PAA functionalized TiO<sub>2</sub> nanoparticles, *J Memb Sci*. 380 (2011) 155–162. <https://doi.org/10.1016/j.memsci.2011.07.006>.
- [269] E.S.C. Fan, O. Kesler, Deposition of lanthanum strontium cobalt ferrite (LSCF) using suspension plasma spraying for oxygen transport membrane applications, *Journal of Thermal Spray Technology*. 24 (2015) 1081–1092. <https://doi.org/10.1007/s11666-015-0269-4>.
- [270] E. Arkhangelsky, Y. Sefi, B. Hajaj, G. Rothenberg, V. Gitis, Kinetics and mechanism of plasmid DNA penetration through nanopores, *J Memb Sci*. 371 (2011) 45–51. <https://doi.org/10.1016/j.memsci.2011.01.014>.
- [271] M.M. Cortalezzi, J. Rose, A.R. Barron, M.R. Wiesner, Characteristics of ultrafiltration ceramic membranes derived from alumoxane nanoparticles, *J Memb Sci*. 205 (2002) 33–43. [https://doi.org/10.1016/S0376-7388\(02\)00049-2](https://doi.org/10.1016/S0376-7388(02)00049-2).

## **Appendix1: Supplementary Material to Chapter 5**

This document contains supplementary information related to Chapter 5 “A Comparative Study of the Self-cleaning and Filtration Performance of Suspension Plasma Sprayed TiO<sub>2</sub> Ultrafiltration and Microfiltration Membranes”. The below-mentioned sections have been labeled in correspondence with the sections in the chapter, to provide easy navigation and quick access to relevant content.

### **5.2.1 Membrane Preparation (Brief Description of the SPS Membranes According to Previous Works)**

In our previous works, the suspension plasma spray (SPS) process was used to produce membranes with pore sizes in the range of MF and UF. It was observed that in both UF and MF structures, there existed a significant correlation between the particle size of the feedstock material and the resulting average pore size in the membranes. Moreover, it was described that in the SPS membranes, the porosity mainly depended on the space amongst the unmelted inflight particles trapped and surrounded by the microstructure formed from fully melted particles. Hence, the correlation between the feedstock particle size and membrane pore size was attributed to the presence of unmelted feedstock particles within the structure [1,2].

Generally, a high surface roughness is undesirable for membrane application since it could increase membrane fouling [3]. In SPS coatings, columnar features forming bumps on the top surface may develop by the deflection of the smaller inflight particles close to the surface of the substrate during the SPS process. As a result, the coating is built by attaching the deviated particles to the sides of the asperities on the surface of the substrate. As the thickness of the coating increases, bumps may appear on the surface of the coatings, increasing the surface roughness [4]. In the SPS process, the formation of these bumps is influenced by the roughness of the substrate and the size of the feedstock particles. Higher surface roughness and smaller feedstock size could increase the likelihood of the occurrence of this phenomenon [5]. In our previous works, the columnar features were observed only on the surface of the MF membranes, produced with submicron-sized feedstock inflight [2]. On the other hand, in the UF membranes, bumps on the surface were less intense [1]. Although in the UF membrane, the individual particles of the feedstock were around 30 nm, they formed a few micron-sized agglomerates that were less subjected to the drag forces of the plasma [6]. Thus, in the UF membrane, a preferential filling of the pores on the substrate occurred, and less roughness was observed compared to the MF membrane [1,2]. Furthermore, by increasing the thickness of the UF membranes, the surface becomes less susceptible to the form of asperities on the surface of the substrate resulting in lower roughness. On the other hand, in the MF membrane, where the feedstock powder is much smaller with a  $d_{50}$  of around 280 nm, a rougher coating surface was obtained.

### **5.2.3. Membrane Performance**

Figure S1 shows the particle size distribution of the SiO<sub>2</sub> particles used for the rejection efficiency measurements.

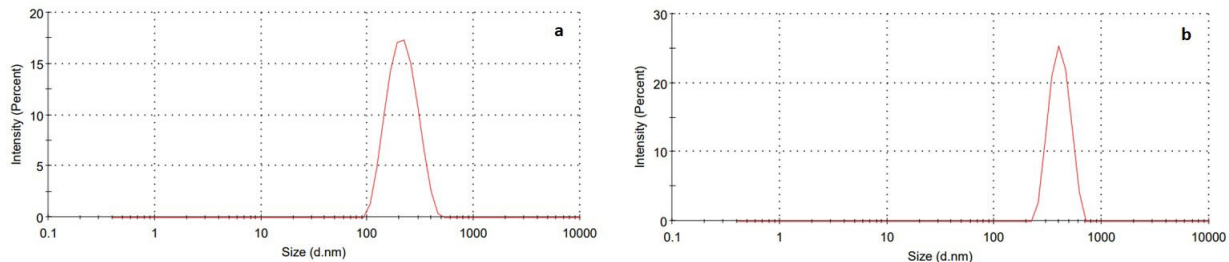


Figure S1 Particle size distribution of the two SiO<sub>2</sub> particles used for characterizing the efficiency of the particle rejection in the membranes showing (a) the particle size distribution of SiO<sub>2</sub> powder with the average particle size of 200 nm, and (b) the particle size distribution of the SiO<sub>2</sub> powder with the average particle size of 400 nm.

### 5.3.2.1. Separation Performance

Figure S2 presents the normalized flux of the UF and MF membranes during the SiO<sub>2</sub> separation process.

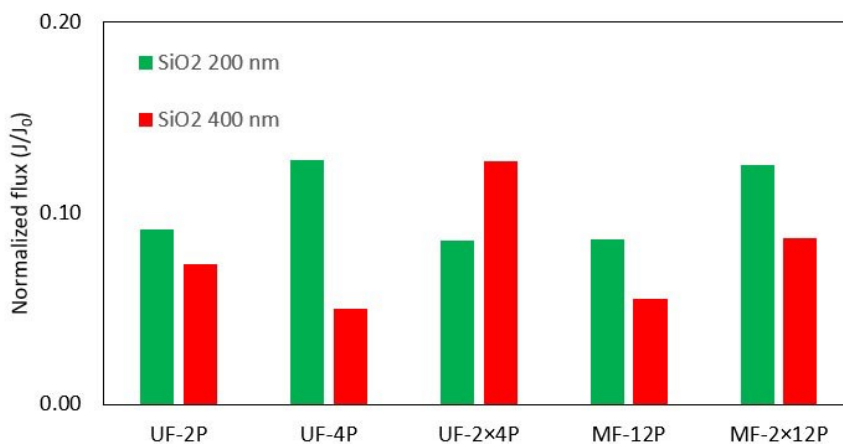


Figure S2 Normalized flux during the SiO<sub>2</sub> separation process for UF and MF membranes

### 5.3.2.2. Self-cleaning and recyclability

Figure S3 shows the photocatalytic efficiency of the UF-2P and MF-12P membranes in degrading an MB solution over the course of 3 cycles.

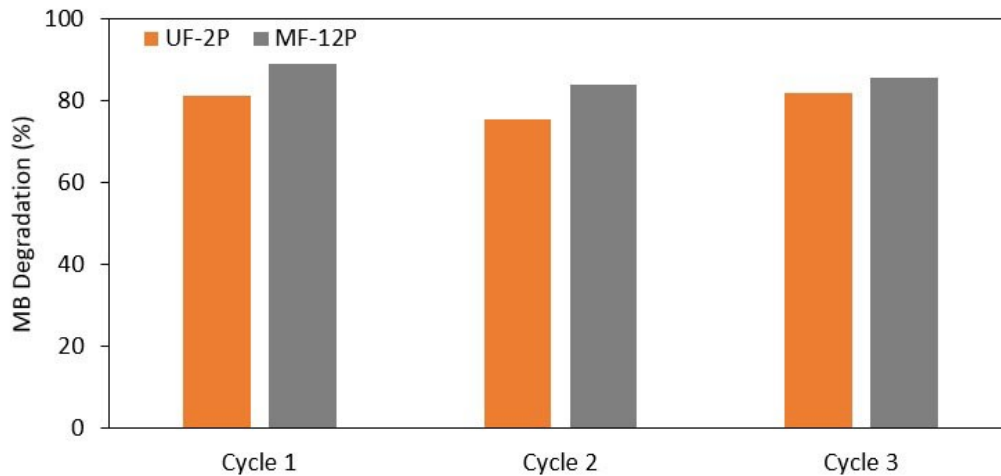


Figure S3 Recyclability of UF-2P and MF-12P in terms of the photocatalytic degradation of MB, showing relatively consistent performance.

## References

- [1] E. Alebrahim, M.S. Rahaman, C. Moreau, TiO<sub>2</sub> Photocatalytic Ultrafiltration Membrane Developed with Suspension Plasma Spray Process, *Coatings*. 12 (2022) 1764. <https://doi.org/10.3390/coatings12111764>.
- [2] E. Alebrahim, F. Tarasi, Md.S. Rahaman, A. Dolatabadi, C. Moreau, Fabrication of titanium dioxide filtration membrane using suspension plasma spray process, *Surf Coat Technol.* 378 (2019) 124927. <https://doi.org/10.1016/j.surfcoat.2019.124927>.
- [3] K.C. Khulbe, C.Y. Feng, T. Matsuura, *Synthetic Polymeric Membranes*, Springer Berlin Heidelberg, Berlin, 2008.
- [4] G. Mauer, C. Moreau, Process Diagnostics and Control in Thermal Spray, *Journal of Thermal Spray Technology*. 31 (2022) 818–828. <https://doi.org/10.1007/s11666-022-01341-z>.
- [5] G. Mauer, R. Vaßen, Coatings with Columnar Microstructures for Thermal Barrier Applications, *Adv Eng Mater.* 22 (2020) 1–9. <https://doi.org/10.1002/adem.201900988>.
- [6] J. Oberste Berghaus, S. Bouaricha, J.G. Legoux, C. Moreau, Injection conditions and in-flight particle states in suspension plasma spraying of alumina and zirconia nano-ceramics, in: *The International Thermal Spray Conference (ITSC) Basel, Switzerland, 2005*: pp. 1434–1440.

## **Appendix 2: A Comparative Study of the Antiviral Properties of Thermally Sprayed Coatings against Human Coronavirus HCoV-229E**

Alebrahim, E., Khatibnezhad, H., Bajgiran, M. M., Solomon, M., Liang, C., Sagan, S. M., ... & Moreau, C. (2023). A Comparative Study of the Antiviral Properties of Thermally Sprayed Coatings against Human Coronavirus HCoV-229E. *Catalysts*, 13(7), 1141.

This research work is a collaboration among the Green-SEAM NSERC Strategic Network (Concordia University, McGill University, National research council of Canada, Metal 7 Inc., SprayWerx Technologies, Hatch, and University of Toronto). The article produced by its results was published in the *Catalysts Journal*.

This work contributed to the investigation of the feasibility of producing antiviral coatings using  $\text{TiO}_2$  and  $\text{Cu}_2\text{O}$ , with anti-pathogenic properties. The primary aim was to inhibit the spread of viral infections, particularly focusing on mitigating the indirect transmission of the SARS-CoV-2 virus. These coatings have the potential to be applied to frequently touched surfaces, such as handrails, doorknobs, elevator buttons, ATM machines, as well as on biomedical appliances within various public and service-oriented facilities like hospitals, schools, and the transportation system. Another potential application lies in air purification within ventilation systems and filtration of the viral species.

# A Comparative Study of the Antiviral Properties of Thermally Sprayed Coatings against Human Coronavirus HCoV-229E

Elnaz Alebrahim <sup>1,†</sup>, Hediye Khatibnezhad <sup>1,†</sup>, Morvarid Mohammadian Bajgiran <sup>1</sup>, Magan Solomon<sup>2</sup>, Chen Liang <sup>2,3</sup>, Selena M. Sagan <sup>3,4</sup>, Rogerio S. Lima <sup>5</sup>, Jörg Oberste Berghaus <sup>5</sup>, Maniya Aghasibeig <sup>5</sup> and Christian Moreau <sup>1\*</sup>

Department of Mechanical, Industrial and Aerospace Engineering, Concordia University, 1455 de Maisonneuve Blvd. W, Montreal, QC H3G 1M8, Canada;

<sup>2</sup>Department of Medicine, Division of Experimental Medicine, McGill University, 3755 Côte Ste-Catherine Road, Montreal, QC H3T 1E2, Canada

<sup>3</sup>Department of Microbiology and Immunology, McGill University, 3775 Rue University, Montreal, QC H3A 2B4, Canada

<sup>4</sup>Department of Biochemistry, McGill University, 3655 Promenade Sir William Osler, Montreal, QC H3G 1Y6, Canada

<sup>5</sup>National Research Council Canada, 75 de Mortagne Blvd., Boucherville, QC J4B 6Y4, Canada

\*Correspondence: christian.moreau@concordia.ca

†These authors contributed equally to this work.

**Abstract:** For decades, novel viral strains of respiratory tract infections have caused human pandemics and initiated widespread illnesses. The recent coronavirus disease 2019 (COVID-19) outbreak caused by the SARS-CoV-2 virus has raised an urgent need to develop novel antiviral coatings as one of the potential solutions to mitigate the transmission of viral pathogens. Titanium dioxide is considered an excellent candidate for viral disinfection under light irradiation, with the potential to be activated under visible light for indoor applications. This research assessed the antiviral performance of thermally sprayed TiO<sub>2</sub> coatings under UVA and ambient light. We also report the antiviral performance of TiO<sub>2</sub> composites with other oxides, such as Cu<sub>2</sub>O and Al<sub>2</sub>O<sub>3</sub>, produced by suspension plasma spray, atmospheric plasma spray, and suspension high-velocity oxygen fuel techniques. To evaluate the antiviral performance of the above coatings in a containment level-2 laboratory, a human common cold coronavirus, HCoV-229E, was initially used as a relevant surrogate for SARS-CoV-2. Coatings were also analyzed using SEM and XRD and were classified based on their surface roughness, porosity, and phase composition. Collectively, the thermally sprayed coatings showed comparable or slightly better antiviral activity compared to copper. The most significant level of activity observed was approximately 20% to 50% higher than that of a pure copper plate.

**Keywords:** TiO<sub>2</sub>; Cu<sub>2</sub>O; photoactivity; contact killing; antiviral coatings; thermal spray; human coronaviruses HCoV-229E; COVID-19

## 1. Introduction

As of March 2020, the widespread and rapid increase in the novel human coronavirus disease (COVID-19), which causes the severe acute respiratory syndrome (SARS) named SARS-CoV-2, has raised worldwide attention toward public health. The World Health Organization reported in June 2023 over 767 million cases of infection, including over 6.9 million deaths, due to the COVID-19 pandemic [1,2]. After SARS coronavirus and Middle East

Respiratory Syndrome (MERS) coronavirus, this is the third highly pathogenic human coronavirus that was spread over the past two decades [1].

Vaccination against SARS-CoV-2 has been developed since 2020 with acceptable success [3]. However, vaccination cannot prevent the emergence of new variants. Infectious pathogens could be transmitted either directly from close person-to-person contact or indirectly through hand-touch contact after deposition on surfaces [4]. Based on the literature, airborne transmission of SARS-CoV-2 virus was the main transmission route [5], but previous studies revealed that the highly contagious COVID-19 virus could remain infectious for days on some surfaces [4]. To inhibit the risk of indirect transmission of infections, coated surfaces with intrinsic antiviral materials could be more effective than frequent cleaning of the environment. Regular cleaning in public places is costly, and re-contamination may occur. An incomplete cleaning process or ineffective cleaning agents may also leave viral residues that may continue to contaminate surfaces [6,7]. Moreover, respiratory disease symptoms such as coughing and mucus production would contaminate the cleaned surfaces frequently and increase the risk of virus transmissions [1]. Accessories in healthcare facilities are mostly made of stainless-steel surfaces as a common material due to its corrosion resistance and clean appearance. However, stainless steel has no antimicrobial capabilities, and pathogens can attach and grow on it easily [8,9]. Thus, the deposition of highly efficient, low-cost, and environmentally friendly antiviral coatings on such surfaces is a reasonable solution to mitigate the transmission of viral diseases. The antimicrobial properties of various metals, particularly copper and silver, have been extensively studied and documented [10]. The COVID-19 pandemic caused a surge in research interest in copper due to its ability to deactivate viruses, which is shown to be directly related to the amount of copper ions released on the surface of the alloy.

Since the antibacterial properties of titanium dioxide ( $\text{TiO}_2$ ) photocatalyst were reported by Matsunaga et al. in 1985 [11],  $\text{TiO}_2$  has attracted ever-growing worldwide attention for antipathogenic applications due to its unique mechanical and chemical resistance [12–15].  $\text{TiO}_2$  can be excited by light irradiation to produce powerful reactive oxygen species (ROS) with strong oxidizing power for airborne pathogen inactivation under ambient conditions. Interaction of the virus with the photocatalytic surface results in substantial changes in the virus structure, leading to the loss of the ability of the virus to attack host cells [13,16].

Among the two main crystalline phases of  $\text{TiO}_2$ , the anatase phase presents the highest activity for photoactive applications. However, previous reports have shown the synergistic effects of the mixture of anatase and rutile phases that could enhance the photoactivity of  $\text{TiO}_2$  photocatalyst [8,17–19]. Furthermore, based on the literature, increasing the surface area could also improve the photoactivity of  $\text{TiO}_2$  photocatalysts by increasing the active sites for reaction initiation and decreasing the charge carrier's recombination rate by introducing some trapping sites [20–22].

Alumina ( $\text{Al}_2\text{O}_3$ ) could be utilized with  $\text{TiO}_2$  to improve the mechanical properties of  $\text{TiO}_2$  coatings [23,24]. Among different alumina phases, the stable corundum phase ( $\alpha\text{-Al}_2\text{O}_3$ ) presents high chemical stability, high electrical resistance, and good thermal and mechanical properties [25].

Copper oxide ( $\text{Cu}_2\text{O}$ ) coatings also show potent antiviral activity, even under dark conditions [4,26,27]. Recent interest in visible light-sensitive  $\text{Cu}_2\text{O-TiO}_2$  nanocomposite has been substantial due to its sustainable antiviral activity under dark conditions.  $\text{Cu}_2\text{O-TiO}_2$  nanocomposite is desirable for indoor environmental remediation applications and also exhibits strong antiviral activity under dark conditions when indoor light instruments are switched off [28,29]. These coatings would be less susceptible to viral contamination and can minimize the spread of the viruses.

TiO<sub>2</sub> films and coatings have been fabricated by various techniques; however, introduction into the market of antiviral coatings relies on the capability of the coating deposition technique for mass production. Thermal spray technology appears as a versatile and rapid processing approach where the large surface area coverage and high deposition rate (up to hundreds of microns in a couple of minutes) make this deposition process compatible with the industry [8,30,31]. Another advantage of thermal spray processes is the flexibility of producing a wide variety of high-quality coatings on substrates with different shapes and sizes [32]. In addition, historically, copper has been more expensive than TiO<sub>2</sub>. Furthermore, the price can vary depending on various factors, such as global demand, supply, economic conditions, and market dynamics. Thus, using copper-based materials on a large scale during a pandemic could be more costly.

Based on our previous work [17,33], thermally sprayed sub-stoichiometric TiO<sub>2-x</sub> coatings presented remarkable photocatalytic performance under visible light. These coatings were deposited using the suspension plasma spray (SPS) process. The results indicated the effect of the oxygen deficiency and Ti<sup>3+</sup> ions on decreasing the bandgap energy and shifting the absorption edge to the visible light range [33].

In this research work, TiO<sub>2</sub>, Cu<sub>2</sub>O, TiO<sub>2</sub>-Cu<sub>2</sub>O, and TiO<sub>2</sub>-Al<sub>2</sub>O<sub>3</sub> antiviral coatings were produced using different thermal spray processes, including atmospheric plasma spray (APS), suspension plasma spray (SPS), and suspension high-velocity oxygen fuel (S-HVOF). To investigate the antiviral activity of the produced coatings, the human common cold coronavirus, HCoV-229E, was used as a surrogate for SARS-CoV-2 in a containment level-2 laboratory.

## 2. Results and Discussion

### 2.1. Phase Composition

XRD patterns and the derived information of TiO<sub>2</sub>, Cu<sub>2</sub>O, TiO<sub>2</sub>-Cu<sub>2</sub>O, and TiO<sub>2</sub>-Al<sub>2</sub>O<sub>3</sub> coatings are shown in Figure 1 and Table 1. According to the results, various ranges of anatase phase contents were produced in TiO<sub>2</sub> coatings, where T1-SPS and T5-SHVOF coatings presented the highest anatase content.

XRD patterns (Figure 1) show Cu<sub>2</sub>O, CuO, and Cu phases for C-SPS coating and anatase, rutile, Cu<sub>2</sub>O, and Cu phases for TC-SPS coating. According to the literature, copper (Cu) and Cu<sub>2</sub>O are considered antibacterial/antiviral materials by a direct contact mechanism [4,34,35]. On the other hand, the inferior antiviral activity of the CuO phase might be related to the less potential of the CuO phase to adsorb and denature proteins [4]. In TiO<sub>2</sub>-Al<sub>2</sub>O<sub>3</sub> coatings, some part of the active TiO<sub>2</sub> phase was transformed into the TiAl<sub>2</sub>O<sub>5</sub> phase, as shown in Figure 1 and Table 1. The formation of the aluminum titanate phase could be detrimental to the photoactivity of the coatings.

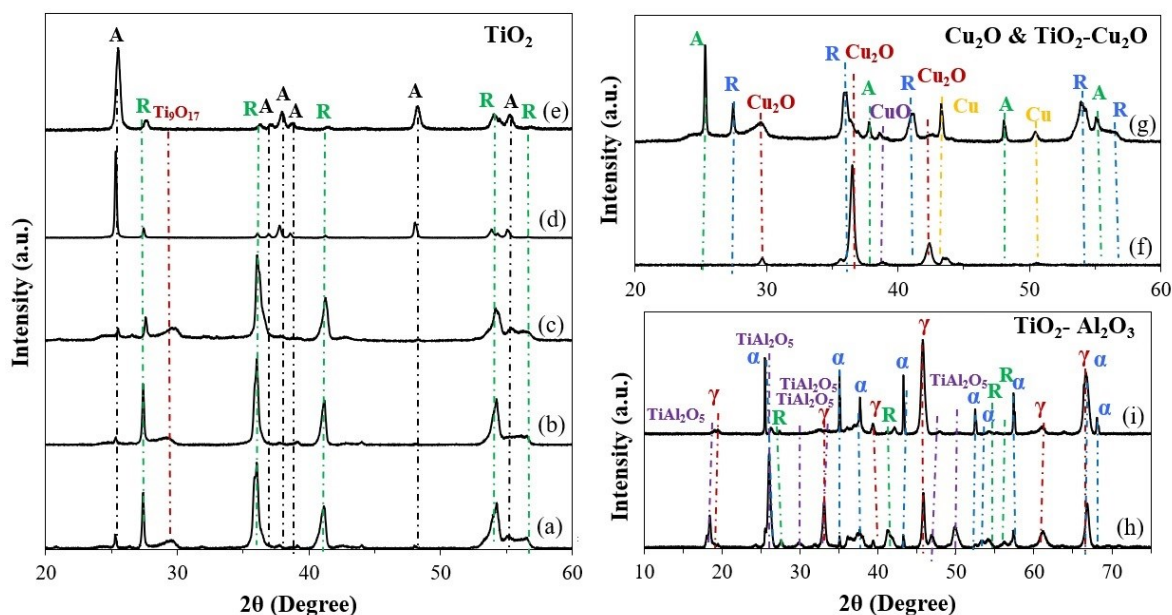


**Figure 1.** XRD patterns of coatings as (a) T2-APS, (b) T3-APS, (c) T4-APS, (d) T1-SPS, (e) T5-SHVOF, and (f) C-SPS, (g) TC-SPS, (h) A40%T-APS, (i) A13%T-APS, in which A denotes anatase phase, R denotes rutile phase,  $\alpha$  is  $\alpha$ -Al<sub>2</sub>O<sub>3</sub>, and  $\gamma$  is  $\gamma$ -Al<sub>2</sub>O<sub>3</sub>.

**Table 1.** Phase content of the coatings derived from Figure 1.

Sample	%Anatase	%Rutile	%Ti <sub>9</sub> O <sub>17</sub>	%Cu <sub>2</sub> O	%CuO	%Cu	% $\alpha$ -Al <sub>2</sub> O <sub>3</sub>	% $\gamma$ -Al <sub>2</sub> O <sub>3</sub>	%TiAl <sub>2</sub> O <sub>5</sub>
T1-SPS	83	17	-	-	-	-	-	-	-
T2-APS	9.5	64.5	26	-	-	-	-	-	-
T3-APS	6	67.5	26.5	-	-	-	-	-	-
T4-APS	28	72	-	-	-	-	-	-	-
T5-SHVOF	82	18	-	-	-	-	-	-	-
C-SPS	-	-	-	65.1	18.2	16.7	-	-	-
TC-SPS	42	19	-	34	-	5	-	-	-
A40%T-APS	-	6	-	-	-	-	32.5	37	24.5
A13%T-APS	-	2	-	-	-	-	55	32	11

## 2.2. Microstructure and Morphology

Three-dimensional (3D) maps of the top surfaces of the coatings taken by a confocal laser microscope are presented in Figure 2. Based on the results, different surface roughness was produced using different thermal spray processes. The T5-SHVOF coating showed the smoothest surface ( $R_a \sim 1.8 \mu\text{m}$ ), and the roughest surface was observed in the TC-SPS coating ( $R_a \sim 9.2 \mu\text{m}$ ).

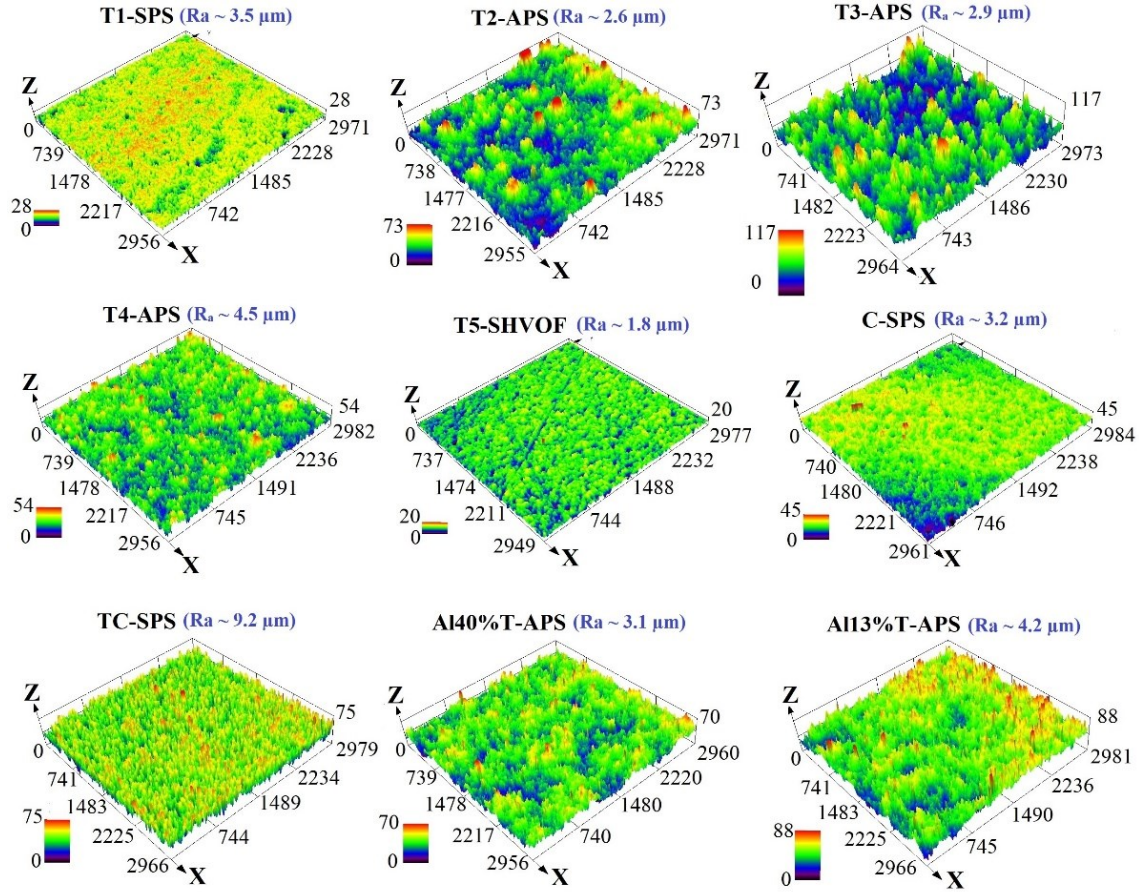


**Figure 2.** Top surface 3D images of the coatings and  $R_a$  provided by the confocal laser microscope.

The SEM micrographs of the coating cross-sections and top surfaces are shown in Figures 3–7. Cross-sectioned SEM images of  $\text{TiO}_2$  coatings in Figure 3 showed mechanically stable coatings well bonded to the surface. It is observed that the T1-SPS and T5-SHVOF have similar microstructural features. In T1-SPS and T5-SHVOF, the melted splats are represented by the light gray zones, while the dark gray zones correspond to finely porous regions formed by unmelted particles from the feedstock suspension and resolidified particles [36,37]. In fact, the color difference between the light and dark gray zones corresponds to the presence of a large number of fine pores in the dark gray regions [38]. Additionally, the black zones are attributed to the larger pores. The origin of the unmelted particles in the T1-SPS coating could arise from the inflight particles traveling within the colder fringe of the plasma plume with lower thermal energy. Moreover, the relatively high vaporization enthalpy of water that was used as the solvent in the feedstock suspension would cool down the plasma jet and increase the ratio of unmelted particles in the coatings compared to APS coatings. The inflight particles in the HVOF process normally have lower temperatures than plasma processes, which, combined with using water as the solvent in the feedstock suspension, may result in preserving the unmelted particles in the T5-SHVOF coating. In addition, finer particles used in SPS and SHVOF processes are prone to resolidify faster within the spray jet and deposit on the surface [17,36,38]. The presence of agglomerated unmelted particles and resolidified particles may enhance the photocatalytic activity of the coatings by increasing the specific surface area of the photocatalyst and increasing the anatase content.

The surface view of the TiO<sub>2</sub> coatings is presented in Figure 4. It is observed that the asperities on the surface of T1-SPS and T5-SHVOF coatings are smaller compared to APS coatings, which could correspond to the finer feedstock powder that was used in the SPS and S-HVOF processes. Moreover, a high magnification view of the surface of T1-SPS and T5-SHVOF coatings in Figure 5 reveals the presence of a significant number of fine pores, unmelted agglomerated particles, and resolidified particles. In contrast, the surface of the APS coatings in Figure 4 shows the presence of mainly well-melted splats with limited porosity.

In Figure 3, the APS coatings also demonstrate comparable microstructures characterized by a typical lamellar arrangement. The lamellar structure results from the flattening of melted or partially melted inflight particles forming splats [39]. Other features that are observed in the APS coatings microstructure include the interlamellar pores and cracks and macro-pores [39,40].

SEM micrographs of C-SPS and TC-SPS are shown in Figure 6. A low plasma power was used to deposit the TC-SPS to maintain the Cu<sub>2</sub>O phase. The C-SPS demonstrates significantly smaller surface asperities compared to TC-SPS, resulting in a notable disparity in surface roughness between the two coatings, as illustrated in Figure 6. Moreover, the TC-SPS coating exhibits a highly porous microstructure.

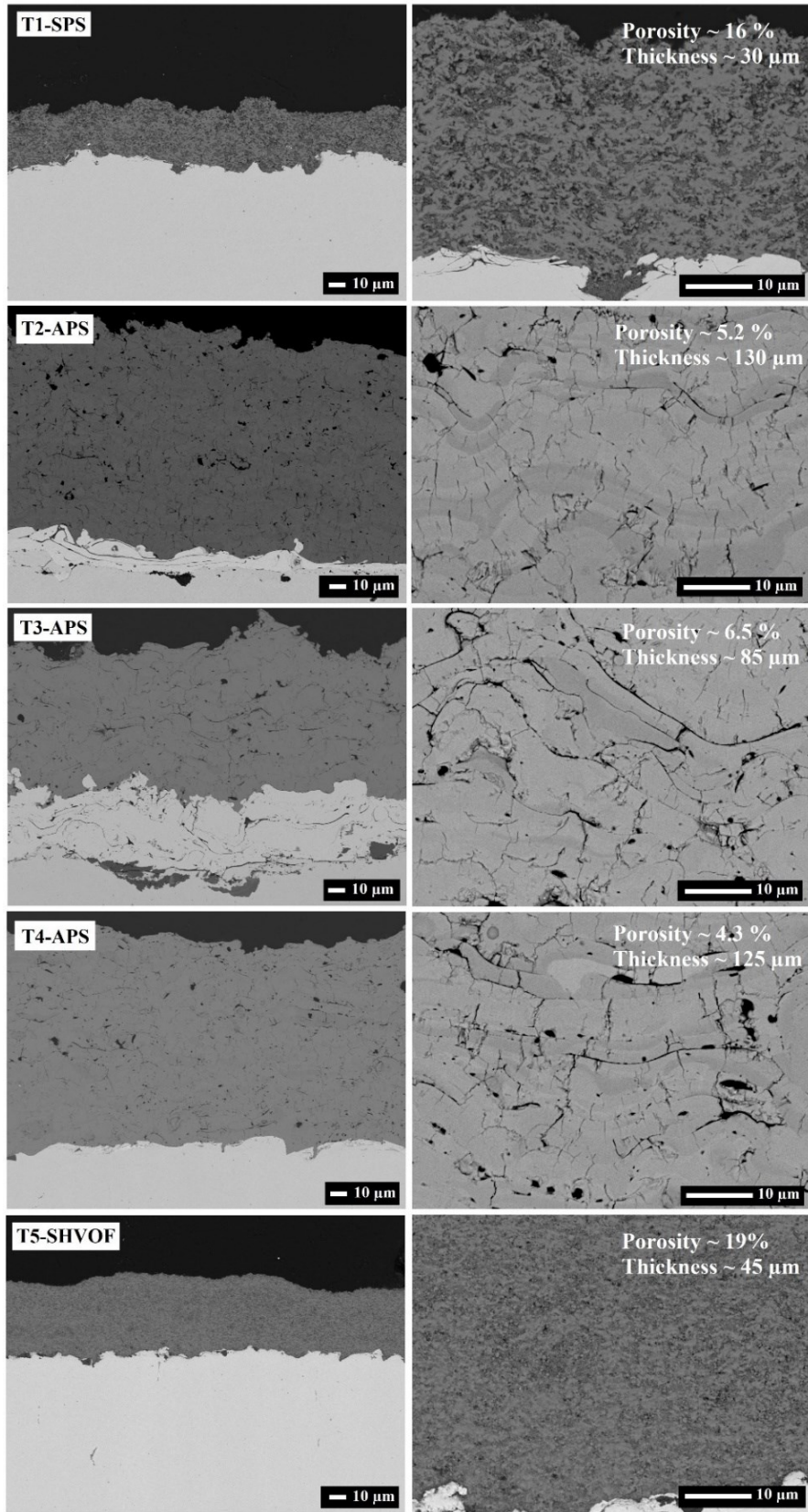


Figure 3. BSE FESEM micrographs of TiO<sub>2</sub> coatings' cross-sections at two magnifications.

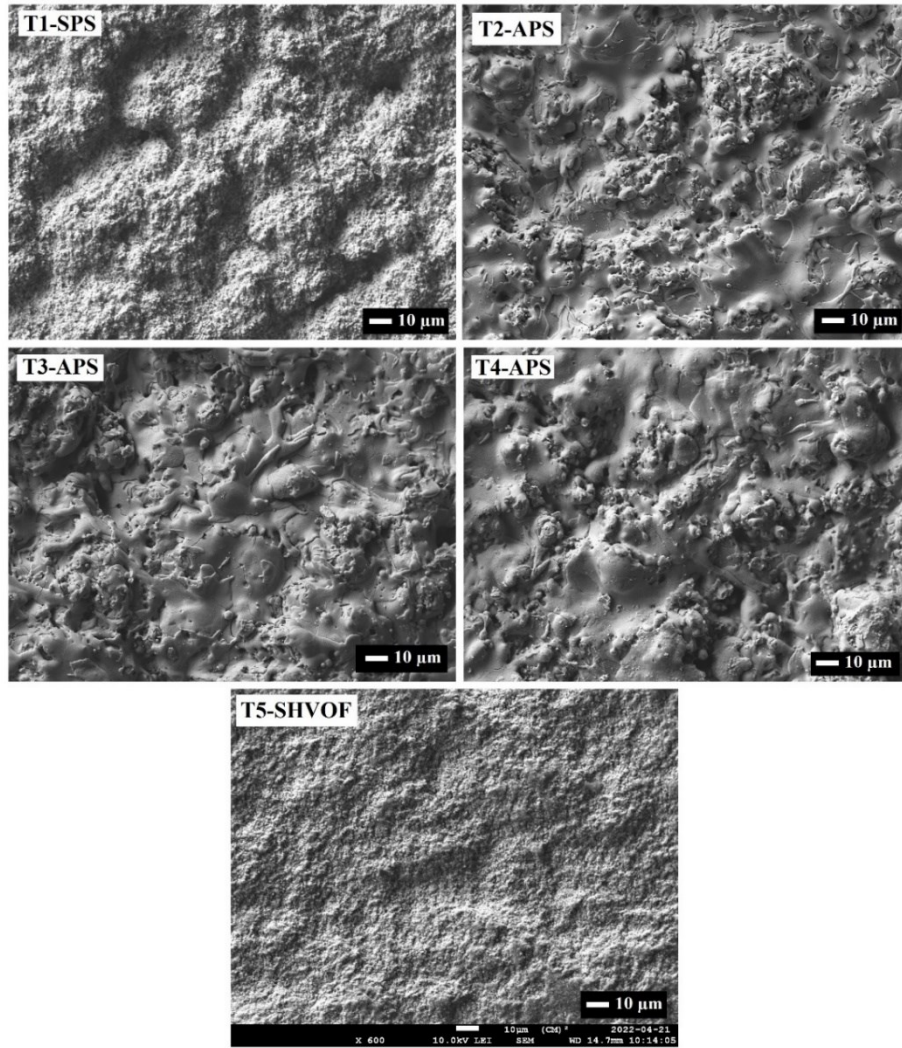


Figure 4. Top surface SE FESEM micrographs of TiO<sub>2</sub> coatings.

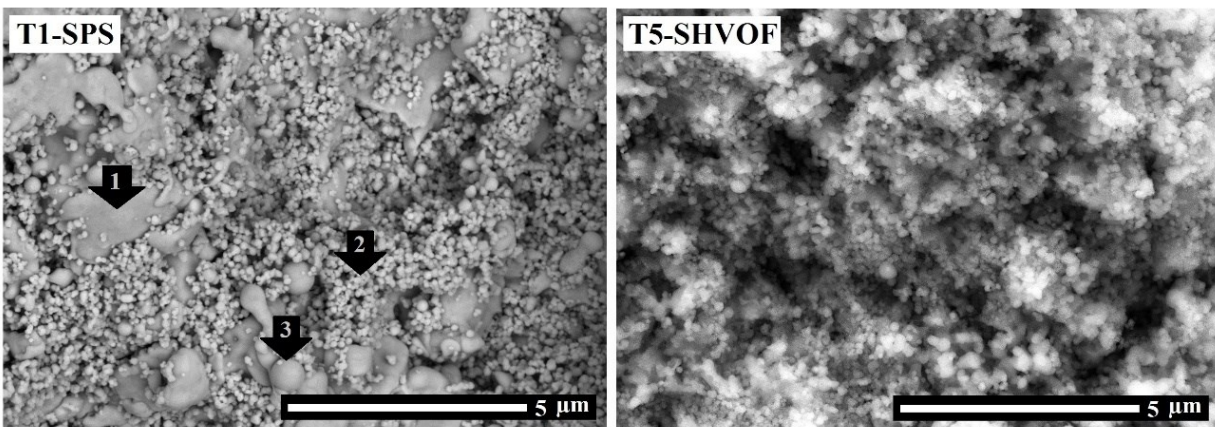
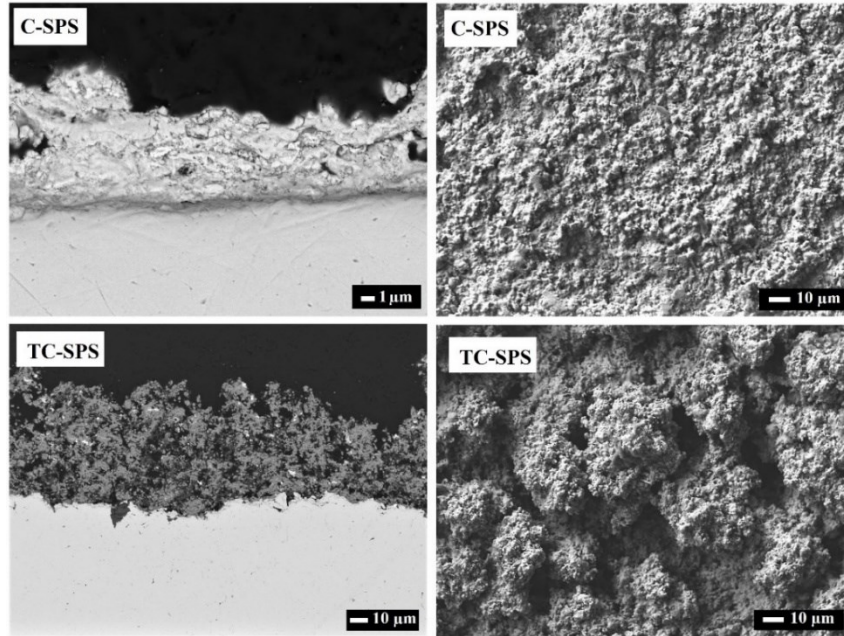
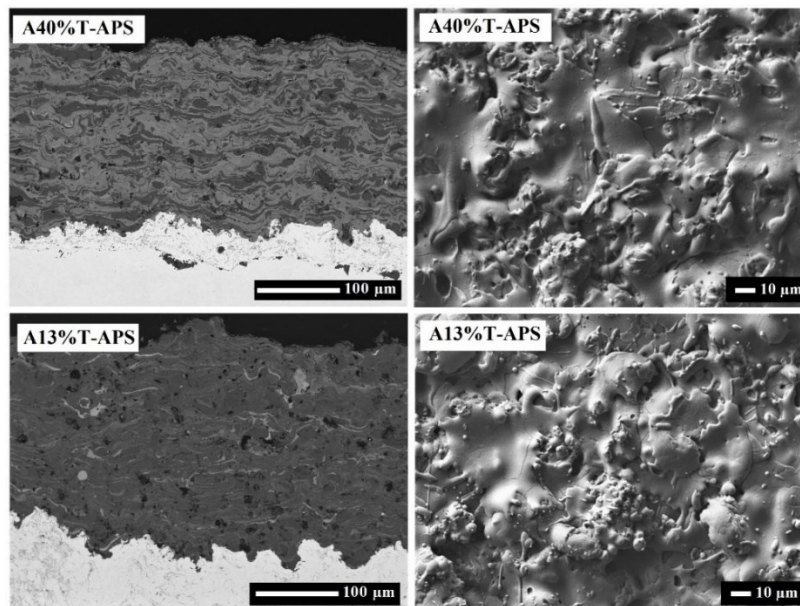


Figure 5. Top surface SE FESEM micrographs of T1-SPS and T5-SHVOF at high magnification, where (1) fully melted particles, (2) unmelted agglomerated particles, and (3) resolidified particles.



**Figure 6.** FESEM micrographs of C-SPS ( $\text{Cu}_2\text{O}$ ) and TC-SPS ( $\text{TiO}_2\text{-Cu}_2\text{O}$ ) coatings, left side: BSE cross-sectioned, right side: SE top surface images.

Figure 7 shows the SEM micrographs of the cross-section and the surface of A40%T-APS and A13%T-APS coatings. Both coatings display surface features resembling the  $\text{TiO}_2$  coatings deposited by the APS process, as depicted in Figure 4, with low porosity (black zones observed on the cross-sectional views). Additionally, in both coatings, the dark gray regions correspond to Al-rich areas, while the light gray regions are attributed to Ti-rich areas, as shown in the EDS images of the coatings in Figure 8. Moreover, The Cu-rich regions in TC-SPS are clearly depicted in the EDS images presented in Figure 8.



**Figure 7.** FESEM micrographs of  $\text{TiO}_2\text{-Al}_2\text{O}_3$  coatings, left side: BSE cross-sectioned, right side: SE top surface images.

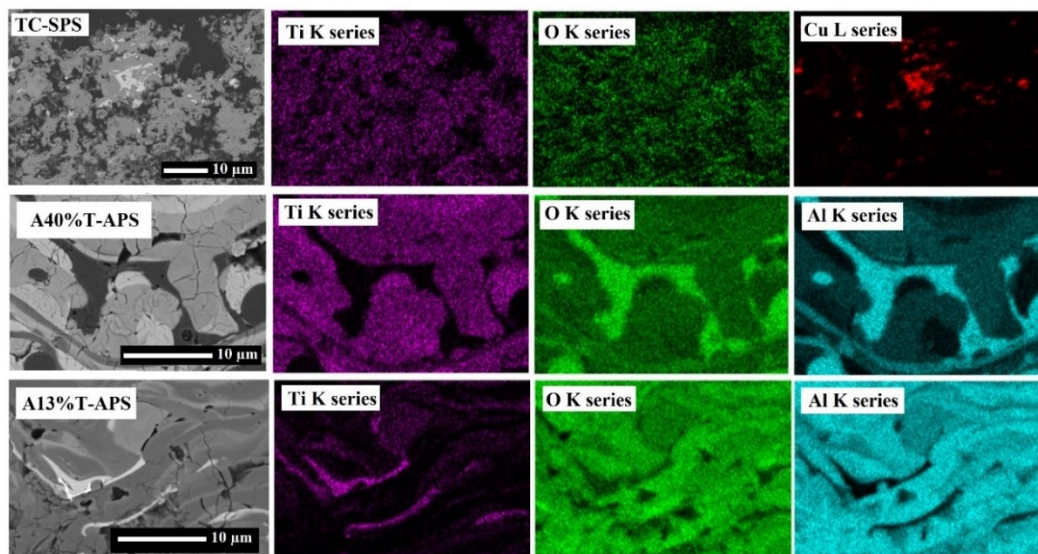
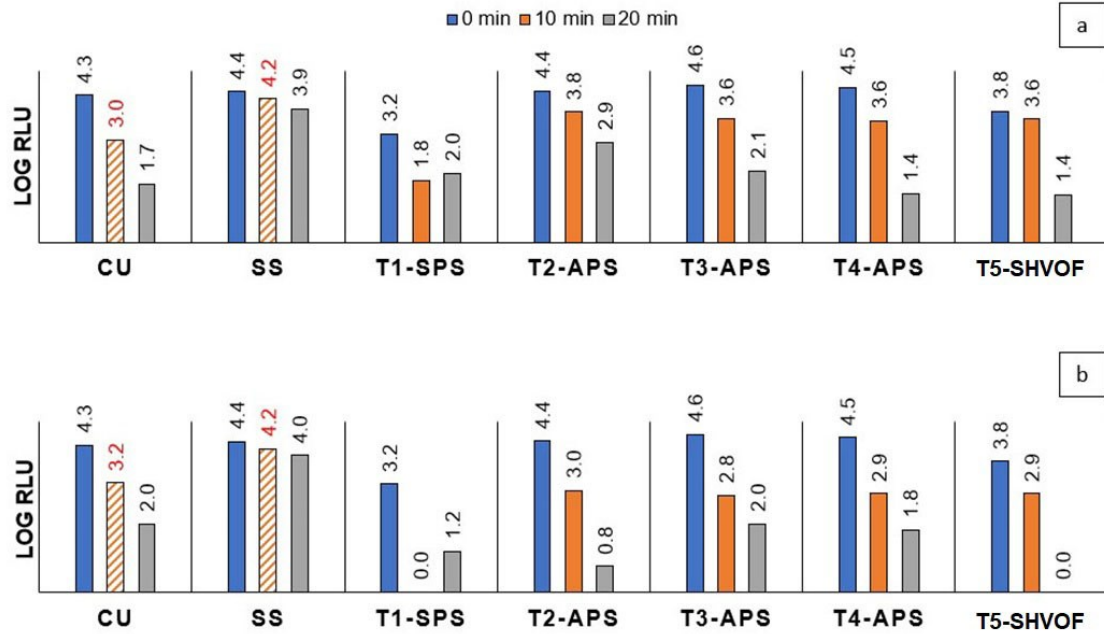


**Figure 8.** FESEM-EDX mapping of the cross-sectional view of  $\text{TiO}_2\text{-Cu}_2\text{O}$  and  $\text{TiO}_2\text{-Al}_2\text{O}_3$  coatings.

## 2.3. Antiviral Activity

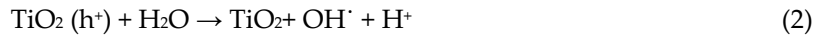
### 2.3.1. $\text{TiO}_2$ Coatings

Figure 9 shows the antiviral activity of the  $\text{TiO}_2$  coatings produced with SPS, APS, and S-HVOF processes under ambient light and UVA illumination. Overall, the antiviral activity of the coatings appears to be comparable or slightly enhanced under UVA light compared to ambient light, whereas T4-APS and T5-SHVOF show a rather higher activity level. Interestingly, the antiviral activity of the coatings under UVA and ambient light, regardless of the thermal spray production process, is comparable or slightly superior to that of the copper sample. Despite the minor fluctuation, which could correspond to the specific surface characteristics of the samples in this work, a consistent trend can be observed in the results.



**Figure 9.** Antiviral activity assessment of TiO<sub>2</sub> coatings under (a) ambient light, (b) UVA light. Cu-10 min and SS-10 min were calculated by linear interpolation.

The antiviral activity of TiO<sub>2</sub> is due to the photocatalytic oxidation property [17,41]. When TiO<sub>2</sub> is exposed to photons with more energy than its bandgap, an electron (e<sup>-</sup>) is excited from the valence band (VB) to the conduction band (CB), and a hole (h<sup>+</sup>) is generated in the valence band. At the surface of the photocatalyst, these charge carriers interact with oxygen and water to produce highly reactive oxygen species (ROS) such as hydroxyl radicals (OH<sup>·</sup>), O<sub>2</sub><sup>·-</sup>, HO<sub>2</sub><sup>·</sup>, H<sub>2</sub>O<sub>2</sub>, etc. [42]. Equations (1)–(5) show the mechanisms of producing some ROS [42].



ROS such as OH<sup>·</sup>, O<sub>2</sub><sup>·-</sup>, HO<sub>2</sub><sup>·</sup>, and H<sub>2</sub>O<sub>2</sub> have been suggested to be responsible for the degradation of viruses [41,42]. These ROS could damage the lipid membrane of the virus and degrade the capsid proteins or the envelope of the virus. Consequently, nucleic acid leakage occurs following virus destruction due to the decomposition of its genetic material [42,43].

Generally, the photogenerated electron-hole pairs in TiO<sub>2</sub> are produced under UV illumination due to their 3–3.2 eV bandgap energy [44]. However, thermal-sprayed coatings show photocatalytic activity under visible light due to the presence of oxygen vacancy and Ti<sup>3+</sup> ions in the coatings [33,37,45].

In general, anatase content in TiO<sub>2</sub> is believed to be the most important factor for photocatalytic activity [15,19,46]. However, other parameters, such as oxygen vacancy and surface morphology, could also play a critical role in the photocatalytic performance of thermally sprayed coatings [17,44].

It can be seen that after 20 min, T1-SPS and T5-SHVOF, with around 80% anatase, show rather similar or slightly lower Log RLU values than copper under both ambient and UVA illuminations. Notably, the Log RLU value of these two samples at 0 min, which determines the amount of the re-collectible virus from the coatings' surface, is lower than the other coatings and the dense control samples. The T1-SPS and T5-SHVOF samples have a relatively high surface porosity, as shown in Figure 5. This porosity allows a fraction of the virus to penetrate through the coatings almost immediately upon contact with the surface. The presence of sponge-like features in the coatings corresponding to the high surface porosity is not necessarily undesirable. This is due to the limited survival time of the coronavirus, which can last up to a few days [47]. Therefore, when the virus penetrates below the touchable section of the surface, it is unable to transmit infection and eventually decomposes. In addition, the high porosity and asperities on the surface create a larger photocatalytically reactive surface area, which, combined with the anatase content, could lead to a more efficient photocatalytic performance. Thus, in porous TiO<sub>2</sub> coatings, the antiviral activity depends on the combined effect of the efficient photocatalytic oxidation on the surface and displacement of the virus from the surface.

Likewise, in samples T2-APS, T3-APS, and T4-APS, the antiviral activity could be explained through a combined effect of several parameters. Figure 10 shows the color of the TiO<sub>2</sub> coatings produced with different thermal spray processes. It is seen that the APS coatings are much darker than SPS and S-HVOF coatings. It was shown previously that the darker the sub-stoichiometric TiO<sub>2-x</sub> coating in SPS coatings, the higher the oxygen vacancy content [17,33]. Furthermore, the level of darkness in sub-stoichiometric coatings is related to the concentration of the Ti<sup>3+</sup> ions [48–50].

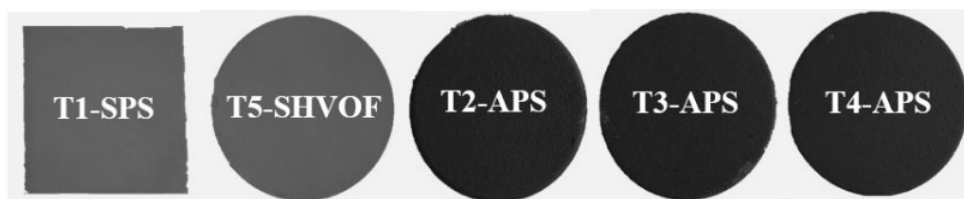


**Figure 10.** The color difference between TiO<sub>2</sub> coatings produced by various thermal spray processes.

In the thermal spray process, a high-temperature heat source is utilized to melt and accelerate feedstock material (such as powder or suspension) to form the coating. Oxygen vacancy could form during the intense heating of the particles, and its quantity is associated with the temperature of the in-flight particles. Notably, the presence of hydrogen as a reductive gas could promote the formation of oxygen vacancy [8,51,52]. Therefore, Ti<sup>4+</sup> could be reduced to Ti<sup>3+</sup> by accepting electrons from the reducing gas, and oxygen vacancies, or even by receiving the photogenerated electrons under UVA and ambient lights [53]. Oxygen vacancies and Ti<sup>3+</sup> ions generate new energy levels below the conduction band, inhibiting charge carrier recombination and enhancing photocatalytic activity [54].

Consequently, the dark APS coatings may include higher levels of oxygen vacancy and Ti<sup>3+</sup> ions, resulting in the enhancement of antiviral performance. On the other hand, the lighter color in SPS and HVOF coatings could be due to a lower level of oxygen vacancy. Using water-based suspension feedstock for T1-SPS and T5-SHVOF would cool down the plasma jet due to the high vaporization enthalpy of water ( $2.3 \times 10^6 \text{ J kg}^{-1}$ ), decreasing the chance of producing

oxygen vacancy in the coatings. Finally, it is worth mentioning that the synergetic effect between anatase and rutile in TiO<sub>2</sub> coatings may also promote photocatalytic reactivity by decreasing the recombination rate of the charge carriers [54].

The rather comparable antiviral activity for TiO<sub>2</sub> coatings under both UVA and ambient light could propose a more sustainable solution for indoor applications by using the commonly used visible light systems and for outdoor applications where the sunlight consists of around 53% visible light [55].

### 2.3.2. TiO<sub>2</sub>-Cu<sub>2</sub>O and Cu<sub>2</sub>O Coatings

The suggested mechanism for virus deactivation by Cu<sub>2</sub>O is the direct contact of the virus with solid-state Cu<sub>2</sub>O compounds through valence-state Cu(I) species, resulting in the denaturation or degradation of its biomolecules. Therefore, Cu<sub>2</sub>O shows antiviral activity independent of optical absorption and in the dark environment [4,56]. The drawback lies in the oxidation of Cu(I) to Cu(II) under ambient conditions, which does not show significant antiviral activity [56]. In TiO<sub>2</sub>-Cu<sub>2</sub>O composite, a combination of copper species with photogenerated holes in the valence band of TiO<sub>2</sub> under light irradiation can cause membrane damage, which is followed by protein oxidation and DNA degradation [28,29]. Furthermore, it was suggested that the photogenerated electrons in TiO<sub>2</sub> could be received by Cu(II), suppressing the self-oxidation of Cu(I) and ensuring a sustainable antiviral property of Cu<sub>2</sub>O [64,65].

Figure 11 shows the antiviral activity of the Cu<sub>2</sub>O and TiO<sub>2</sub>-Cu<sub>2</sub>O coatings produced with SPS processes under ambient light, UVA illumination, and dark.

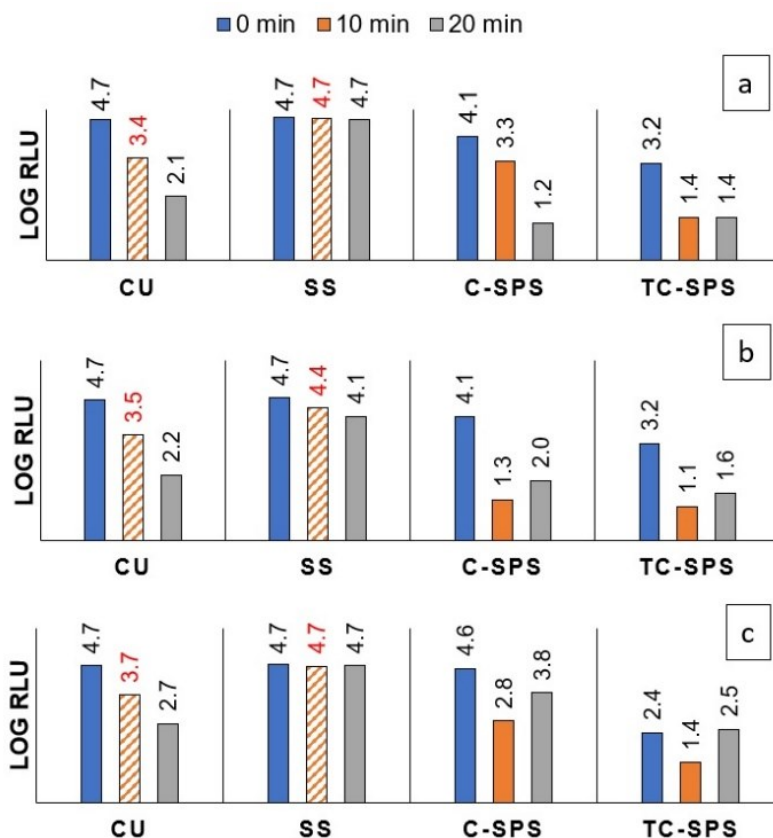


**Figure 11.** Antiviral activity assessment of TiO<sub>2</sub>-Cu<sub>2</sub>O coatings under (a) ambient light, (b) UVA light, and (c) dark. Cu-10 min and SS-10 min were calculated by linear interpolation.

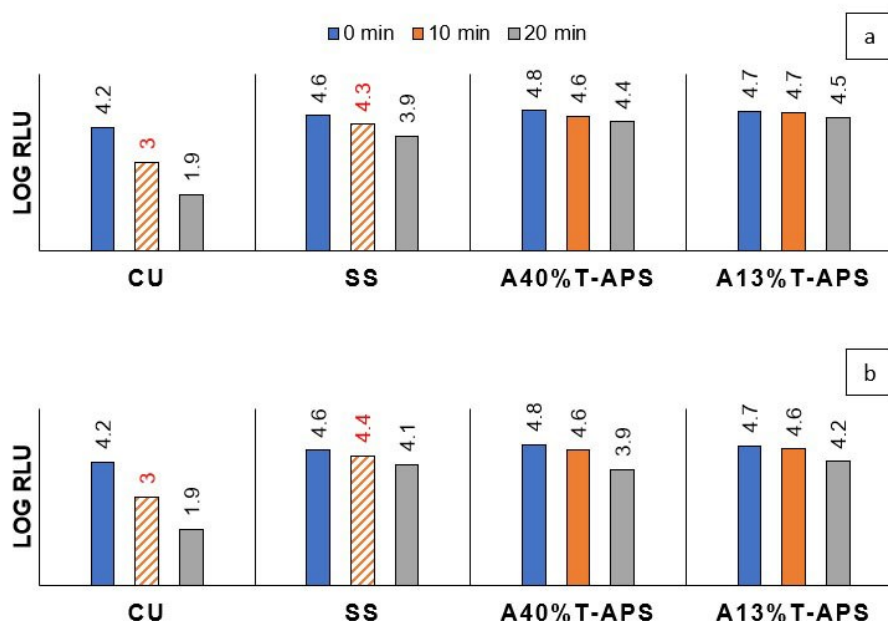
In Figure 11a,b, C-SPS and TC-SPS coatings demonstrate a relatively similar antiviral activity under both UVA and ambient lights, almost comparable to or slightly higher than that of the pure copper control sample. The Log RLU value of TC-SPS at 0 min shows that the quantity of re-collected virus was lower than C-SPS. The lower quantity of re-collected virus is due to the high porosity observed on the surface of TC-SPS shown in Figure 9. Therefore, the antiviral performance in TC-SPS could be linked to the combined effects of photocatalytic reactivity of  $\text{TiO}_2$ , penetration of the virus below the top surface of the coating due to porosity, and direct contact with  $\text{Cu}_2\text{O}$ . However, as seen in Figure 8, the Cu species are enveloped by  $\text{TiO}_2$ , which might have limited the antiviral activity due to the reduced direct contact with solid-state  $\text{Cu}_2\text{O}$ .

Figure 11c shows the antiviral activity of C-SPS and TC-SPS in dark conditions. It seems that the antiviral activity of C-SPS coating in the dark is lower than that that under UVA and ambient light. This outcome was not unexpected, since the direct-contact virus-killing mechanism in  $\text{Cu}_2\text{O}$  is independent of photon energy [4,56].

Interestingly, at 20 min, the TC-SPS coating in dark conditions shows a significant decrease in the quantity of the viable virus, which is close to that of the copper sample. However, the Log RLU values for TC-SPS coating at 0, 10, and 20 min are somewhat similar. As mentioned earlier, this close similarity in Log RLU values indicates that the observed antiviral activity could correspond to penetration of the virus through the porous structure of the coating and its removal from the top surface. It can be assumed that optimizing the proportion of  $\text{Cu}_2\text{O}$  in the  $\text{TiO}_2$ - $\text{Cu}_2\text{O}$  coating might probably be advantageous in terms of increasing the efficiency of antiviral activity in the dark.

### 2.3.3. $\text{Al}_2\text{O}_3$ - $\text{TiO}_2$ Coatings

Figure 12 shows the antiviral activity of A40%T-APS and A13%T-APS coatings under UVA and ambient light. The coatings showed almost no antiviral activity in both cases, which is similar to the stainless-steel control sample. In  $\text{Al}_2\text{O}_3$ - $\text{TiO}_2$  coatings, as shown in Section 3.1, most of the  $\text{TiO}_2$  in the feedstock was transformed into  $\text{TiAl}_2\text{O}_5$  in the coatings. Furthermore, the EDS images of  $\text{Al}_2\text{O}_3$ - $\text{TiO}_2$  coatings in Figure 8 showed the photocatalytically active surface of  $\text{TiO}_2$  covered with inert Al-rich regions, resulting in the suppression of the photocatalytic activity in these coatings.



**Figure 12.** Antiviral activity assessment of Al<sub>2</sub>O<sub>3</sub>-TiO<sub>2</sub> coatings under (a) ambient light, (b) UVA light. Cu-10 min and SS-10 min were calculated by linear interpolation.

### 3. Materials and Methods

#### 3.1. Preparation of Antiviral Coatings

Submicron-sized TiO<sub>2</sub> (TKB Trading, Oakland, CA, USA), micron-sized TiO<sub>2</sub> (Metco 102-Metco Oerlikon, Fort Saskatchewan, AB, Canada), nanostructured TiO<sub>2</sub> spray-dried (NEOXID T101 nano, Millidyne, Finland), Cu<sub>2</sub>O (PI-KEM, Tamworth, UK), Al<sub>2</sub>O<sub>3</sub>-40%TiO<sub>2</sub> (Amdry 6257- Metco Oerlikon, Fort Saskatchewan, AB, Canada), and Al<sub>2</sub>O<sub>3</sub>-13%TiO<sub>2</sub> (Metco 130-Metco Oerlikon, Fort Saskatchewan, AB, Canada) powders were used as feedstock materials to deposit coatings. SEM micrographs of the feedstock powders are shown in Figure 13. A diverse range of powder sizes is essential in the context of the different thermal spray processes. In the APS process, powders with particle sizes ranging from 10 to 100 μm are commonly used to avoid injection clogging [36]. On the other hand, sub-micron-sized powders are used in the SPS system.

Different thermal spray processes and systems were applied to produce the antiviral coatings on the grit-blasted 304 stainless steel coupons (1-inch diameter). The objective was to produce a range of coatings with different surface roughness, porosity, anatase content, and microstructures. To this end, three APS systems with low, medium, and high power were used. In addition, using the SPS process allows producing porous coatings with finer microstructures [57]. Furthermore, S-HVOF systems may preserve a higher fraction of anatase in the coatings due to the lower flame temperature [58]. The influence of various coating parameters is discussed in the following sections.

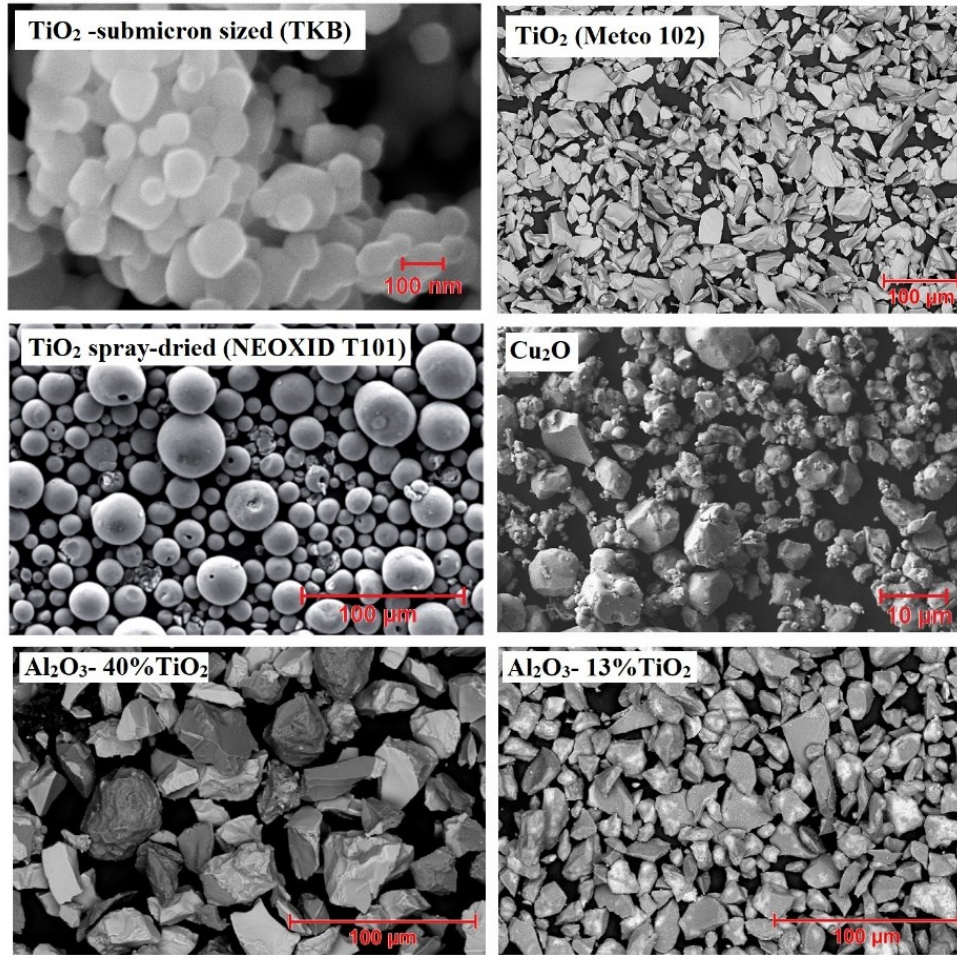


**Figure 13.** SEM micrographs of TiO<sub>2</sub> powder (Metco 102), Al<sub>2</sub>O<sub>3</sub>-40%TiO<sub>2</sub>, and Al<sub>2</sub>O<sub>3</sub>-40%TiO<sub>2</sub> are taken from the data sheets provided by Metco Oerlikon.

Details of the operating parameters are summarized in Tables 2 and 3. Five different types of TiO<sub>2</sub> coatings were produced to provide various microstructure, roughness, porosity, and anatase phase contents. The 10 wt.% water-based TiO<sub>2</sub> suspensions without any dispersing agent were used as the feedstock material to deposit T1-SPS and T5-SHVOF coatings by SPS and S-HVOF processes, respectively. An Axial IIITM APS torch (Northwest Mettech Corp., Surrey, BC, Canada) and ID-Nova Mk6 (Spraywerx technologies, North Vancouver, BC, Canada) HVOF system were used for producing the T1-SPS and T5-SHVOF coatings, respectively. ID-Nova is a compact hydrogen-fueled HVOF system designed to spray coatings onto the internal surfaces of the components. A hydrogen flow rate of 390 lpm and an oxygen flow rate of 190 lpm were used for the deposition of the T5-SHVOF coating. T2-APS, T3-APS, and T4-APS TiO<sub>2</sub> coatings were deposited by APS using SG-100 (Praxair Surface Technologies, Indianapolis, IN, USA), 100HE (Progressive Surface, Grand Rapids, MI, USA), and 3MB (Oerlikon Metco, Wohlen, Switzerland) plasma guns, respectively. The T2-APS, T4-APS, A40%-T-APS, and A13%-T-APS coatings were sprayed on the top of a bond coat to enhance the adhesion of the coating to the substrate. The presence of the bond coat does not affect the antiviral activity of the coatings.

**Table 2.** Thermal spray deposition parameters.

Sample	Feedstock Material	Thermal Spray Process	Spray System	Powder Feed Rate (g/min)	Suspension Feed Rate (mL/min)	Current (A)	Spray Distance (mm)	Power(kW)
T1-SPS	TiO <sub>2</sub> -TKB	SPS	Axial III <sup>TM</sup>	-	30	220	75	77
T2-APS	TiO <sub>2</sub> -Metco 102	APS	SG-100	25	-	1000	100	35
T3-APS	TiO <sub>2</sub> -Metco 102	APS	100 HE	100	-	400	115	95
T4-APS	TiO <sub>2</sub> -NEOXID T101	APS	3 MB	20	-	500	75	29
T5-SHVOF	TiO <sub>2</sub> -TKB	S-HVOF	ID-Nova	-	37	-	30	-
C-SPS	Cu <sub>2</sub> O-PI-KEM	SPS	3MB	-	35	500	50	17.5
TC-SPS	TiO <sub>2</sub> - 25%Cu <sub>2</sub> O-TKB	SPS	3 MB	-	35	500	50	20
A40%T-APS	Al <sub>2</sub> O <sub>3</sub> - 40%TiO <sub>2</sub> (Amdry 6257)	APS	F4	30	-	480	120	30
A13%T-APS	Al <sub>2</sub> O <sub>3</sub> - 13%TiO <sub>2</sub> (Metco 130)	APS	100 HE	90	-	260	115	65

**Table 3.** Primary and secondary gas flow rates for plasma-sprayed APS and SPS coatings.

Sample	Ar Flow Rate (L/min)	Secondary Gas Flow Rate (L/min)		
		H <sub>2</sub>	He	N <sub>2</sub>
T1-SPS	Gas flow (SLPM): 223, Gas mixture (%): Ar: 82/N <sub>2</sub> : 11/H <sub>2</sub> : 7			
T2-APS	42.7	-	27.4	-
T3-APS	85	66	-	66
T4-APS	40	8	-	-
C-SPS	50	-	10	-
TC-SPS	50	1	-	-
A40%T-APS	40	8	-	-
A13%T-APS	86	56	-	56

Cu<sub>2</sub>O (C-SPS) and TiO<sub>2</sub>-25%Cu<sub>2</sub>O (TC-SPS) coatings were deposited by the SPS method with a 3MB plasma torch. Here, 10 wt.% ethanol-based suspensions containing a small quantity of polyvinylpyrrolidone (PVP) (Sigma-Aldrich, Oakville, ON, Canada) (5 wt.% corresponding to the solid content) as a dispersing agent were used to deposit the coatings. A roller mill was utilized for five days to increase the homogeneity of the suspensions and to break down large agglomerates. The particle size distribution of the suspensions was measured by a Spraytec particle size analyzer unit (Malvern Instruments, Malvern, UK), as shown in Figure 14.

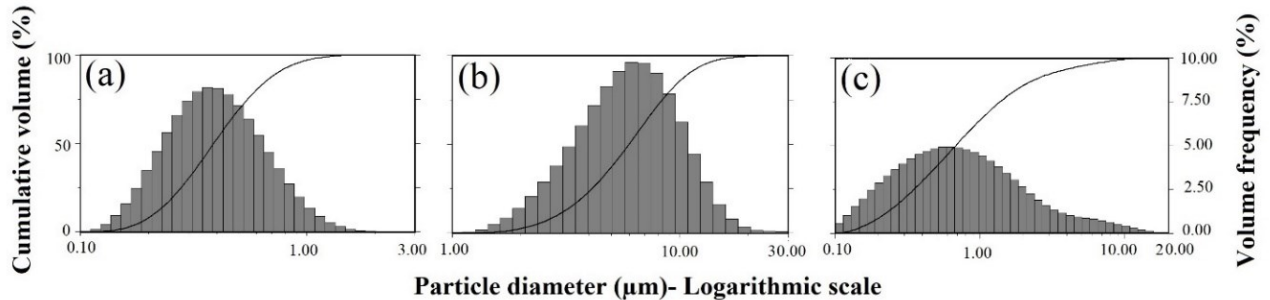


**Figure 14.** Particle size distribution of the suspensions: (a) TiO<sub>2</sub>: d<sub>10</sub> = 0.2 μm, d<sub>50</sub> = 0.39 μm, d<sub>90</sub> = 0.75 μm, (b) Cu<sub>2</sub>O: d<sub>10</sub> = 2.9 μm, d<sub>50</sub> = 5.9 μm, d<sub>90</sub> = 11 μm, (c) TiO<sub>2</sub>-Cu<sub>2</sub>O: d<sub>10</sub> = 0.2 μm, d<sub>50</sub> = 0.68 μm, d<sub>90</sub> = 2.8 μm, to deposit T1-SPS/T5-SHVOF, C-SPS, and TC-SPS coatings, respectively.

To evaluate the role of the TiO<sub>2</sub> content on the antiviral activity of the coatings, TiO<sub>2</sub>-Al<sub>2</sub>O<sub>3</sub> composite coatings were manufactured by spraying two feedstock powders containing different quantities of TiO<sub>2</sub> (A40%T-APS: 40%TiO<sub>2</sub> and A13%T-APS: 13% TiO<sub>2</sub>) using F4 (Oerlikon Metco, Wholen, Switzerland) and 100HE plasma torches.

### 3.2. Characterization of the Coatings

The morphology of the powders, the top surface of the coatings, and the polished cross-section of the coatings were observed with a field-emission scanning electron microscope (FESEM JSM 7600TFE, JEOL, Japan) in secondary electron and backscattered electron modes. The arithmetic average surface roughness (Ra) and topography of the coatings were evaluated with a confocal laser microscope (LEXT OLS4000 Olympus, Toronto, ON, Canada). The phase analysis of the coatings was carried out by the X-ray diffraction (XRD) technique (X'Pert pro, PANalytical, Philips, The Netherlands) in a range of 10–75° with Cu K $\alpha$  radiation and a step size of 0.02°. The phase content was quantified by the tabulated reference intensity ratio using DIFFRACT.EVA software (Bruker, Billerica, MA, USA) and the PDF-2 database (international center for diffraction data).

### 3.3. Antiviral Activity Assessment

The antiviral performance of selected coatings was assessed in a containment level 2 bio lab under UVA light (Fisher Scientific, Canada), ambient light, and dark conditions. Two UVA ( $\lambda = 365$  nm) lamps with a power of 15 W each with the illumination of around 500 lux were used. The intensity of UVA light was reduced by decreasing the transmission to 1% using 2.0 OD UV-NIR Neutral Density Filters (88-275, Edmund Optics Inc., USA) to eliminate the impact of UVA illumination, killing the virus directly. The distance between the surface of the samples and UVA lights was around 7 cm, and the distance between the surface of the samples and the UV-NIR filters was around 2 cm, allowing normal air circulation over the surface of the samples. The ambient light was provided using white LED lights, which was generally used to illuminate inside the fume hood. The intensity of the ambient light was measured at around 500 lux using a light meter (LANTEX LM-50KL, Woodbridge, ON, Canada).

The antiviral activity of the coatings was assessed using the HCoV-229E-Luc virus as a surrogate for the SARS-CoV-2 virus [59]. The HCoV-229E-Luc virus contains a Luciferase reporter gene allowing quantification of the relative amount of the viable virus in terms of relative luminescence unit (RLU), which was determined by measuring the luminescence signal using a Luciferase assay [60].

HCoV-229E-Luc stocks containing 1000 Plaque-Forming Units (PFUs) were prepared in Dulbecco's Modified Eagle Medium (DMEM) containing 2% Fetal Bovine Serum (FBS). First, 50  $\mu$ L of the virus solution was put on the surface of the coatings. The coatings were exposed to ambient/UVA light or kept in the dark. The virus was recollected from the coating surface by pipetting 100  $\mu$ L of media (Dulbecco's Modified Eagle Medium) at the coating's surface at three time points of 0 min, 10 min, and 20 min after exposure. A fresh coating was used for the test at each time point. The retrieved virus was then used to infect Huh7 cells in triplicates. Huh7 cells are human epithelial liver cell lines derived from hepatoma tissue, which supports HCoV-229E replication. A Renilla-Glo Luciferase Assay System (catalogue number E2720, Promega), with a Perkin Elmer plate reader (Ensign, Perkin Elmer), was used to quantify virus infection in terms of relative luminescence unit (RLU), and the logarithmic value of the average of the triplicate RLU measurements was reported. Furthermore, a copper plate (Cu), with high antiviral activity, and a stainless steel 304 plate (SS) with no antiviral activity were used as positive and negative control samples, respectively [61,62]. The antiviral activity of each coating can be determined by

comparing its activity at 20 min to the activity of the same coating at 0 min. Subsequently, the antiviral activity of the coatings was compared to that of the control samples. For each day of the antiviral activity assessment experiment, independent control samples were used. The antiviral activity of the control samples followed a consistent trend during the whole duration of the experiment. To compare the results from the tests carried out on different days, the average values of the activity of the control samples were used. The schematic of the antiviral activity assessment process is shown in Figure 15.

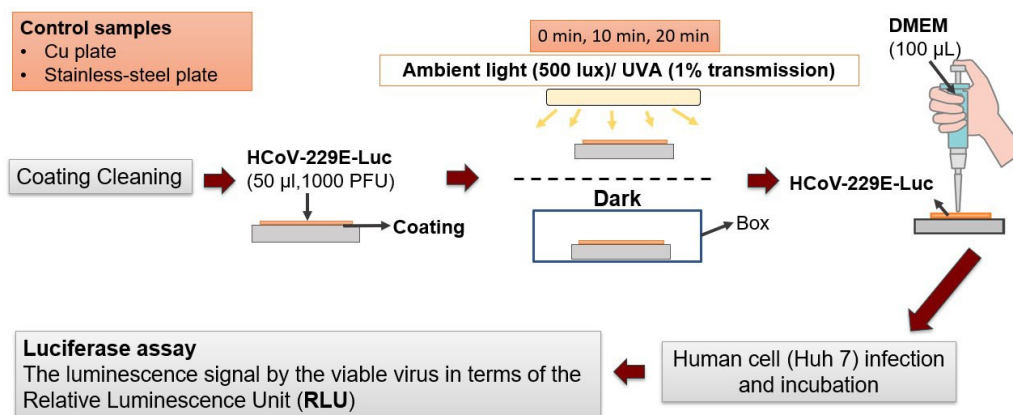


Figure 15. Schematic of the antiviral activity assessment process.

#### 4. Conclusions

The antiviral activity of thermally sprayed coatings was assessed under ambient light, UVA, and dark conditions.  $\text{TiO}_2$ ,  $\text{Cu}_2\text{O}$ ,  $\text{TiO}_2\text{-Cu}_2\text{O}$ , and  $\text{Al}_2\text{O}_3\text{-TiO}_2$  coatings were produced by APS, SPS, and S-HVOF processes. Regardless of the coating fabrication process, the  $\text{TiO}_2$  coatings demonstrated relatively similar or somewhat enhanced antiviral activity compared to copper under visible light and UVA light. Furthermore, the  $\text{TiO}_2\text{-Cu}_2\text{O}$  coating showed antiviral activity comparable to that of copper under visible light, UVA light. Results showed that the antiviral performance of the coatings corresponded to the collective influence of various parameters, including the photocatalytic activity of  $\text{TiO}_2$ , direct contact of  $\text{Cu}_2\text{O}$  components, and surface properties of the coatings, such as porosity and roughness. The surface porosity resulted in the transportation of a significant quantity of the virus beneath the touchable surface of the coatings, hindering its potential to cause infection. Although the regular cleaning processes of touched surfaces with high roughness and porosity could be challenging, an optimized level of surface properties could be beneficial to the total antiviral performance of the coatings through the combined effect of inactivating the virus and removing the virus from the surface.

Our results show that thermally sprayed coatings can offer a promising and potentially cost-effective approach for producing effective antiviral coatings using stable  $\text{TiO}_2$ . Other benefits include the absence of surface oxidation that occurs on copper, which can diminish its antiviral activity. The thermally sprayed coatings can be used on high-touch surfaces for indoor applications under ambient light, in the dark, and outdoor applications under sunlight.

**Author Contributions:** Conceptualization, C.M.; Data curation, E.A., H.K. and M.S.; Formal analysis, E.A., H.K., C.L. and C.M.; Funding acquisition, C.M.; Investigation, E.A., H.K., M.M.B. and M.S.; Methodology, E.A., H.K., M.S., C.L., R.S.L., J.O.B., M.A. and C.M.; Project administration, C.M.; Resources, C.L., S.S., R.S.L., J.O.B., M.A. and C.M.; Supervision, C.M.; Writing—original draft, E.A. and H.K.; Writing—review and editing, E.A., H.K., M.M.B., C.L., S.S., R.S.L., J.O.B., M.A. and C.M. All authors have read and agreed to the published version of the manuscript.

**Funding:** This study was financially supported by the Alliance Program of the Natural Sciences and Engineering Research Council of Canada (NSERC) and the Accelerate Program of Mitacs.

**Acknowledgments:** The authors extend their appreciation to David Kwan and Lan Huong Nguyen from Concordia University, Bruno M. H. Guerreiro from National Research Council Canada, Alan Burgess from Sprywerx Technologies, Steve Beaudin, Marc-Andre Ringuet, Adam Truchon, and Alexandre Gonçalves Andrade from Metal 7, Murray Pearson from Hatch, and Maurice Ringuette from University of Toronto.

**Conflicts of Interest:** The authors declare no conflict of interest.

## References

1. Kampf, G.; Todt, D.; Pfaender, S.; Steinmann, E. Persistence of coronaviruses on inanimate surfaces and their inactivation with biocidal agents. *J. Hosp. Infect.* **2020**, *104*, 246–251. <https://doi.org/10.1016/j.jhin.2020.01.022>.
2. World Health Organization. *COVID-19 Weekly Epidemiological Update*; World Health Organization: Singapore, 2022; pp. 1–33.
3. Haas, E.J.; Angulo, F.J.; McLaughlin, J.M.; Anis, E.; Singer, S.R.; Khan, F.; Brooks, N.; Smaja, M.; Mircus, G.; Pan, K.; et al. Impact and effectiveness of mRNA BNT162b2 vaccine against SARS-CoV-2 infections and COVID-19 cases, hospitalisations, and deaths following a nationwide vaccination campaign in Israel: An observational study using national surveillance data. *Lancet* **2021**, *397*, 1819–1829. [https://doi.org/10.1016/s0140-6736\(21\)00947-8](https://doi.org/10.1016/s0140-6736(21)00947-8).
4. Sunada, K.; Minoshima, M.; Hashimoto, K. Highly efficient antiviral and antibacterial activities of solid-state cuprous compounds. *J. Hazard. Mater.* **2012**, *235–236*, 265–270. <https://doi.org/10.1016/j.jhazmat.2012.07.052>.
5. Morawska, L.; Cao, J. Airborne transmission of SARS-CoV-2: The world should face the reality. *Environ. Int.* **2020**, *139*, 105730. <https://doi.org/10.1016/j.envint.2020.105730>.
6. Scully, J.R. The COVID-19 Pandemic, Part 1: Can Antimicrobial Copper-Based Alloys Help Suppress Infectious Transmission of Viruses Originating from Human Contact with High-Touch Surfaces? *Corrosion* **2020**, *76*, 523–527. <https://doi.org/10.5006/3568>.
7. Warnes, S.L.; Little, Z.R.; Keevil, C.W. Human Coronavirus 229E Remains Infectious on Common Touch Surface Materials. *mBio* **2015**, *6*, e01697-15. <https://doi.org/10.1128/mbio.01697-15>.
8. George, N.; Mahon, M.; McDonald, A. Bactericidal Performance of Flame-Sprayed Nanostructured Titania-Copper Composite Coatings. *J. Therm. Spray Technol.* **2010**, *19*, 1042–1053. <https://doi.org/10.1007/s11666-010-9503-2>.
9. Versoza, M.; Jung, W.; Barabad, M.L.; Ko, S.; Kim, M.; Park, D. Reduction of *Escherichia Coli* Using Metal Plates with the Influenced of Applied Low Current and Physical Barrier of Filter Layers. *Int. J. Environ. Res. Public Health* **2019**, *16*, 3887. <https://doi.org/10.3390/ijerph16203887>.
10. Rakowska, P.D.; Tiddia, M.; Faruqui, N.; Bankier, C.; Pei, Y.; Pollard, A.J.; Zhang, J.; Gilmore, I.S. Antiviral surfaces and coatings and their mechanisms of action. *Commun. Mater.* **2021**, *2*, 53. <https://doi.org/10.1038/s43246-021-00153-y>.
11. Matsunaga, T.; Tomoda, R.; Nakajima, T.; Wake, H. Photoelectrochemical sterilization of microbial cells by semiconductor powders. *FEMS Microbiol. Lett.* **1985**, *29*, 211–214. <https://doi.org/10.1111/j.1574-6968.1985.tb00864.x>.
12. Zhang, C.; Li, Y.; Shuai, D.; Shen, Y.; Wang, D. Progress and challenges in photocatalytic disinfection of waterborne Viruses: A review to fill current knowledge gaps. *Chem. Eng. J.* **2019**, *355*, 399–415. <https://doi.org/10.1016/j.cej.2018.08.158>.
13. Cui, H.; Jiang, J.; Gu, W.; Sun, C.; Wu, D.; Yang, T.; Yang, G. Photocatalytic Inactivation Efficiency of Anatase Nano-TiO<sub>2</sub> Sol on the H9N2 Avian Influenza Virus. *Photochem. Photobiol.* **2010**, *86*, 1135–1139. <https://doi.org/10.1111/j.1751-1097.2010.00763.x>.
14. Kikuchi, Y.; Sunada, K.; Iyoda, T.; Hashimoto, K.; Fujishima, A. Photocatalytic bactericidal effect of TiO<sub>2</sub> thin films: Dynamic view of the active oxygen species responsible for the effect. *J. Photochem. Photobiol. A: Chem.* **1997**, *106*, 51–56. [https://doi.org/10.1016/s1010-6030\(97\)00038-5](https://doi.org/10.1016/s1010-6030(97)00038-5).
15. Prakash, J.; Cho, J.; Mishra, Y.K. Photocatalytic TiO<sub>2</sub> nanomaterials as potential antimicrobial and antiviral agents: Scope against blocking the SARS-COV-2 spread. *Micro Nano Eng.* **2022**, *14*, 100100–100100. <https://doi.org/10.1016/j.mne.2021.100100>.
16. Hajkova, P.; Spatenka, P.; Horsky, J.; Horska, I.; Kolouch, A. Photocatalytic Effect of TiO<sub>2</sub> Films on Viruses and Bacteria. *Plasma Process. Polym.* **2007**, *4*, S397–S401. <https://doi.org/10.1002/ppap.200731007>.
17. Khatibnezhad, H.; Ambriz-Vargas, F.; Ben Ettouil, F.; Moreau, C. Role of phase content on the photocatalytic performance of TiO<sub>2</sub> coatings deposited by suspension plasma spray. *J. Eur. Ceram. Soc.* **2022**, *42*, 2905–2920. <https://doi.org/10.1016/j.jeurceramsoc.2022.02.010>.
18. Wagstaffe, M.; Noei, H.; Stierle, A. Elucidating the Defect-Induced Changes in the Photocatalytic Activity of TiO<sub>2</sub>. *J. Phys. Chem. C* **2020**, *124*, 12539–12547. <https://doi.org/10.1021/acs.jpcc.0c02809>.
19. Luttrell, T.; Halpegamage, S.; Tao, J.; Kramer, A.; Sutter, E.; Batzill, M. Why is anatase a better photocatalyst than rutile?—Model studies on epitaxial TiO<sub>2</sub> films. *Sci. Rep.* **2014**, *4*, 4043. <https://doi.org/10.1038/srep04043>.
20. Rauf, M.; Meetani, M.; Hisaindee, S. An overview on the photocatalytic degradation of azo dyes in the presence of TiO<sub>2</sub> doped with selective transition metals. *Desalination* **2011**, *276*, 13–27. <https://doi.org/10.1016/j.desal.2011.03.071>.

21. Shayegan, Z.; Haghghat, F.; Lee, C.-S.; Bahloul, A.; Huard, M. Effect of surface fluorination of P25-TiO<sub>2</sub> on adsorption of indoor environment volatile organic compounds. *Chem. Eng. J.* **2018**, *346*, 578–589. <https://doi.org/10.1016/j.cej.2018.04.043>.
22. Hanaor, D.A.H.; Sorrell, C.C. Review of the anatase to rutile phase transformation. *J. Mater. Sci.* **2010**, *46*, 855–874. <https://doi.org/10.1007/s10853-010-5113-0>.
23. Stengl, V.; Ageorges, H.; Ctibor, P.; Murafa, N. Atmospheric plasma sprayed (APS) coatings of Al<sub>2</sub>O<sub>3</sub>-TiO<sub>2</sub> system for photocatalytic application. *Photochem. Photobiol. Sci.* **2009**, *8*, 733–738. <https://doi.org/10.1039/b817199h>.
24. Choi, H.; Stathatos, E.; Dionysiou, D.D. Sol-gel preparation of mesoporous photocatalytic TiO<sub>2</sub> films and TiO<sub>2</sub>/Al<sub>2</sub>O<sub>3</sub> composite membranes for environmental applications. *Appl. Catal. B Environ.* **2006**, *63*, 60–67. <https://doi.org/10.1016/j.apcatb.2005.09.012>.
25. Toma, F.-L.; Berger, L.-M.; Stahr, C.C.; Naumann, T.; Langner, S. Microstructures and Functional Properties of Suspension-Sprayed Al<sub>2</sub>O<sub>3</sub> and TiO<sub>2</sub> Coatings: An Overview. *J. Therm. Spray Technol.* **2010**, *19*, 262–274. <https://doi.org/10.1007/s11666-009-9417-z>.
26. Borkow, G.; Zhou, S.S.; Page, T.; Gabbay, J. A Novel Anti-Influenza Copper Oxide Containing Respiratory Face Mask. *PLoS ONE* **2010**, *5*, e11295. <https://doi.org/10.1371/journal.pone.0011295>.
27. Borkow, G. Safety of Using Copper Oxide in Medical Devices and Consumer Products. *Curr. Chem. Biol.* **2012**, *6*, 86–92. <https://doi.org/10.2174/2212796811206010086>.
28. Qiu, X.; Miyauchi, M.; Sunada, K.; Minoshima, M.; Liu, M.; Lu, Y.; Li, D.; Shimodaira, Y.; Hosogi, Y.; Kuroda, Y.; et al. Hybrid Cu<sub>x</sub>O/TiO<sub>2</sub> Nanocomposites As Risk-Reduction Materials in Indoor Environments. *ACS Nano* **2012**, *6*, 1609–1618. <https://doi.org/10.1021/nn2045888>.
29. Liu, M.; Sunada, K.; Hashimoto, K.; Miyauchi, M. Visible-light sensitive Cu(ii)-TiO<sub>2</sub> with sustained anti-viral activity for efficient indoor environmental remediation. *J. Mater. Chem. A* **2015**, *3*, 17312–17319. <https://doi.org/10.1039/c5ta03756e>.
30. Jeffery, B.; Pepller, M.; Lima, R.S.; McDonald, A. Bactericidal Effects of HVOF-Sprayed Nanostructured TiO<sub>2</sub> on *Pseudomonas aeruginosa*. *J. Therm. Spray Technol.* **2010**, *19*, 344–349. <https://doi.org/10.1007/s11666-009-9369-3>.
31. Vardelle, A.M.; Moreau, C.; Akedo, J.; Ashrafizadeh, H.; Berndt, C.; Berghaus, J.O.; Boulos, M.; Brogan, J.; Bourtsalas, A.C.; Dolatabadi, A.; et al. The 2016 Thermal Spray Roadmap. *J. Therm. Spray Technol.* **2016**, *25*, 1376–1440. <https://doi.org/10.1007/s11666-016-0473-x>.
32. Du, L.; Coyle, T.W.; Chien, K.; Pershin, L.; Li, T.; Golozar, M. Titanium Dioxide Coating Prepared by Use of a Suspension-Solution Plasma-Spray Process. *J. Therm. Spray Technol.* **2015**, *24*, 915–924. <https://doi.org/10.1007/s11666-015-0251-1>.
33. Khatibnezhad, H.; Ambriz-Vargas, F.; Ben Ettouil, F.; Moreau, C. An investigation on the photocatalytic activity of sub-stoichiometric TiO<sub>2-x</sub> coatings produced by suspension plasma spray. *J. Eur. Ceram. Soc.* **2020**, *41*, 544–556. <https://doi.org/10.1016/j.jeurceramsoc.2020.08.017>.
34. Selvamani, V.; Zareei, A.; Elkashif, A.; Maruthamuthu, M.K.; Chittiboyina, S.; DeLisi, D.; Li, Z.; Cai, L.; Pol, V.G.; Seleem, M.; et al. Hierarchical Micro/Mesoporous Copper Structure with Enhanced Antimicrobial Property via Laser Surface Texturing. *Adv. Mater. Interfaces* **2020**, *7*, 1901890. <https://doi.org/10.1002/admi.201901890>.
35. Vincent, M.; Duval, R.E.; Hartemann, P.; Engels-Deutsch, M. Contact killing and antimicrobial properties of copper. *J. Appl. Microbiol.* **2018**, *124*, 1032–1046. <https://doi.org/10.1111/jam.13681>.
36. Alebrahim, E.; Tarasi, F.; Rahaman, S.; Dolatabadi, A.; Moreau, C. Fabrication of titanium dioxide filtration membrane using suspension plasma spray process. *Surf. Coat. Technol.* **2019**, *378*, 124927. <https://doi.org/10.1016/j.surfcoat.2019.124927>.
37. Alebrahim, E.; Rahaman, S.; Moreau, C. TiO<sub>2</sub> Photocatalytic Ultrafiltration Membrane Developed with Suspension Plasma Spray Process. *Coatings* **2022**, *12*, 1764. <https://doi.org/10.3390/coatings12111764>.
38. Toma, F.-L.; Bertrand, G.; Begin, S.; Meunier, C.; Barres, O.; Klein, D.; Coddet, C. Microstructure and environmental functionalities of TiO<sub>2</sub>-supported photocatalysts obtained by suspension plasma spraying. *Appl. Catal. B Environ.* **2006**, *68*, 74–84. <https://doi.org/10.1016/j.apcatb.2006.07.009>.
39. Li, G.-R.; Lv, B.-W.; Yang, G.-J.; Zhang, W.-X.; Li, C.-X.; Li, C.-J. Relationship between Lamellar Structure and Elastic Modulus of Thermally Sprayed Thermal Barrier Coatings with Intra-splat Cracks. *J. Therm. Spray Technol.* **2015**, *24*, 1355–1367. <https://doi.org/10.1007/s11666-015-0292-5>.
40. Ramakrishnan, G.; Dwivedi, G.; Sampath, S.; Orlov, A. Development and optimization of thermal sprayed ceramic microfiltration membranes. *J. Membr. Sci.* **2015**, *489*, 106–111. <https://doi.org/10.1016/j.memsci.2015.03.094>.
41. Bono, N.; Ponti, F.; Punta, C.; Candiani, G. Effect of UV Irradiation and TiO<sub>2</sub>-Photocatalysis on Airborne Bacteria and Viruses: An Overview. *Materials* **2021**, *14*, 1075. <https://doi.org/10.3390/ma14051075>.
42. Gong, M.; Xiao, S.; Yu, X.; Dong, C.; Ji, J.; Zhang, D.; Xing, M. Research progress of photocatalytic sterilization over semiconductors. *RSC Adv.* **2019**, *9*, 19278–19284. <https://doi.org/10.1039/c9ra01826c>.
43. Han, R.; Coey, J.D.; O'Rourke, C.; Bamford, C.G.; Mills, A. Flexible, disposable photocatalytic plastic films for the destruction of viruses. *J. Photochem. Photobiol. B Biol.* **2022**, *235*, 112551–112551. <https://doi.org/10.1016/j.jphotobiol.2022.112551>.
44. Kozerski, S.; Toma, F.-L.; Pawlowski, L.; Leupolt, B.; Latka, L.; Berger, L.-M. Suspension plasma sprayed TiO<sub>2</sub> coatings using different injectors and their photocatalytic properties. *Surf. Coat. Technol.* **2010**, *205*, 980–986. <https://doi.org/10.1016/j.surfcoat.2010.04.068>.

45. Fu, Y.; Liu, Y.; Li, H. Onion-like carbon-modified TiO<sub>2</sub> coating by suspension plasma spray with enhanced photocatalytic performances. *J. Nanopart. Res.* **2019**, *21*, 182. <https://doi.org/10.1007/s11051-019-4633-z>.
46. Zhang, J.; Zhou, P.; Liu, J.; Yu, J. New understanding of the difference of photocatalytic activity among anatase, rutile and brookite TiO<sub>2</sub>. *Phys. Chem. Chem. Phys.* **2014**, *16*, 20382–20386. <https://doi.org/10.1039/c4cp02201g>.
47. Fiorillo, L.; Cervino, G.; Matarese, M.; D'Amico, C.; Surace, G.; Paduano, V.; Fiorillo, M.T.; Moschella, A.; La Bruna, A.; Romano, G.L.; et al. COVID-19 Surface Persistence: A Recent Data Summary and Its Importance for Medical and Dental Settings. *Int. J. Environ. Res. Public Health* **2020**, *17*, 3132. <https://doi.org/10.3390/ijerph17093132>.
48. Justicia, I.; Ordejón, P.; Canto, G.; Mozos, J.L.; Fraxedas, J.; Battiston, G.A.; Gerbasi, R.; Figueras, A. Designed self-doped titanium oxide thin films for efficient visible-light photocatalysis. *Adv. Mater.* **2002**, *14*, 1399–1402. [https://doi.org/https://doi.org/10.1002/1521-4095\(20021002\)14:19<1399::AID-ADMA1399>3.0.CO;2-C](https://doi.org/https://doi.org/10.1002/1521-4095(20021002)14:19<1399::AID-ADMA1399>3.0.CO;2-C).
49. Ager, F.; Justicia, I.; Gerbasi, R.; Battiston, G.; McSporry, N.; Figueras, A. RBS analysis of substoichiometric TiO<sub>2</sub>-anatase thin films for visible-light photocatalysis. *Nucl. Instrum. Methods Phys. Res. Sect. B Beam Interact. Mater. Atoms* **2006**, *249*, 490–492. <https://doi.org/10.1016/j.nimb.2006.03.037>.
50. Vu, P.; Otto, N.; Vogel, A.; Kern, F.; Killinger, A.; Gadow, R. Efficiently quantifying the anatase content and investigating its effect on the photocatalytic activity of titania coatings by suspension plasma spraying. *Surf. Coat. Technol.* **2018**, *371*, 117–123. <https://doi.org/10.1016/j.surfcoat.2018.07.064>.
51. Colmenares-Angulo, J.R.; Cannillo, V.; Lusvarghi, L.; Sola, A.; Sampath, S. Role of process type and process conditions on phase content and physical properties of thermal sprayed TiO<sub>2</sub> coatings. *J. Mater. Sci.* **2009**, *44*, 2276–2287. <https://doi.org/10.1007/s10853-008-3044-9>.
52. Toma, F.-L.; Sokolov, D.; Bertrand, G.; Klein, D.; Coddet, C.; Meunier, C. Comparison of the Photocatalytic Behavior of TiO<sub>2</sub> Coatings Elaborated by Different Thermal Spraying Processes. *J. Therm. Spray Technol.* **2006**, *15*, 576–581. <https://doi.org/10.1361/105996306x147225>.
53. Xiong, L.-B.; Li, J.-L.; Yang, B.; Yu, Y. Ti<sup>3+</sup> in the Surface of Titanium Dioxide: Generation, Properties and Photocatalytic Application. *J. Nanomater.* **2012**, *2012*, 831524. <https://doi.org/10.1155/2012/831524>.
54. Amano, F.; Nakata, M.; Yamamoto, A.; Tanaka, T. Rutile titanium dioxide prepared by hydrogen reduction of Degussa P25 for highly efficient photocatalytic hydrogen evolution. *Catal. Sci. Technol.* **2016**, *6*, 5693–5699. <https://doi.org/10.1039/c6cy00296j>.
55. Yamasaki, R.S. Intensity variations of ultraviolet, visible, and near infrared bands of terrestrial solar radiation. *J. Paint Technol.* **1971**, *43*, 75–83.
56. Miyauchi, M.; Sunada, K.; Hashimoto, K. Antiviral Effect of Visible Light-Sensitive Cu<sub>x</sub>O/TiO<sub>2</sub> Photocatalyst. *Catalysts* **2020**, *10*, 1093. <https://doi.org/10.3390/catal10091093>.
57. Vaßen, R.; Kaßner, H.; Mauer, G.; Stöver, D. Suspension Plasma Spraying: Process Characteristics and Applications. *J. Therm. Spray Technol.* **2009**, *19*, 219–225. <https://doi.org/10.1007/s11666-009-9451-x>.
58. Pala, Z.; Shaw, E.; Murray, J.; Senin, N.; Hussain, T. Suspension high velocity oxy-fuel spraying of TiO<sub>2</sub>: A quantitative approach to phase composition. *J. Eur. Ceram. Soc.* **2017**, *37*, 801–810. <https://doi.org/10.1016/j.jeurceramsoc.2016.08.030>.
59. Meunier, T.; Desmarets, L.; Bordage, S.; Bamba, M.; Hervouet, K.; Rouillé, Y.; François, N.; Decossas, M.; Sencio, V.; Trottein, F.; et al. A Photoactivable Natural Product with Broad Antiviral Activity against Enveloped Viruses, Including Highly Pathogenic Coronaviruses. *Antimicrob. Agents Chemother.* **2022**, *66*, e01581-21. <https://doi.org/10.1128/aac.01581-21>.
60. Smale, S.T. Luciferase Assay. *Cold Spring Harb. Protoc.* **2010**, *2010*, 54. <https://doi.org/10.1101/pdb.prot5421>.
61. Noyce, J.O.; Michels, H.; Keevil, C.W. Inactivation of Influenza A Virus on Copper versus Stainless Steel Surfaces. *Appl. Environ. Microbiol.* **2007**, *73*, 2748–2750. <https://doi.org/10.1128/aem.01139-06>.
62. Mehtar, S.; Wiid, I.; Todorov, S. The antimicrobial activity of copper and copper alloys against nosocomial pathogens and Mycobacterium tuberculosis isolated from healthcare facilities in the Western Cape: An in-vitro study. *J. Hosp. Infect.* **2008**, *68*, 45–51. <https://doi.org/10.1016/j.jhin.2007.10.009>.

**Disclaimer/Publisher's Note:** The statements, opinions and data contained in all publications are solely those of the individual author(s) and contributor(s) and not of MDPI and/or the editor(s). MDPI and/or the editor(s) disclaim responsibility for any injury to people or property resulting from any ideas, methods, instructions or products referred to in the content.